3-23-2017

Military Space Mission Design and Analysis in a Multi-Body Environment: An Investigation of High-Altitude Orbits as Alternative Transfer Paths, Parking Orbits for Reconstitution, and Unconventional Mission Orbits

John N. Brick

MILITARY SPACE MISSION DESIGN AND ANALYSIS IN A MULTI-BODY ENVIRONMENT: AN INVESTIGATION OF HIGH-ALTITUDE ORBITS AS ALTERNATIVE TRANSFER PATHS, PARKING ORBITS FOR RECONSTITUTION, AND UNCONVENTIONAL MISSION ORBITS

THESIS

John N. Brick, 2d Lt, USAF

AFIT-ENY-MS-17-M-246

DEPARTMENT OF THE AIR FORCE
AIR UNIVERSITY

AIR FORCE INSTITUTE OF TECHNOLOGY

Wright-Patterson Air Force Base, Ohio

AFIT-ENY-MS-17-M-246

MILITARY SPACE MISSION DESIGN AND ANALYSIS IN A MULTI-BODY ENVIRONMENT: AN INVESTIGATION OF HIGH-ALTITUDE ORBITS AS ALTERNATIVE TRANSFER PATHS, PARKING ORBITS FOR RECONSTITUTION, AND UNCONVENTIONAL MISSION ORBITS

THESIS

Presented to the Faculty

Department of Aeronautics and Astronautics

Graduate School of Engineering and Management

Air Force Institute of Technology

Air University

Air Education and Training Command

in Partial Fulfillment of the Requirements for the

Degree of Master of Science in Astronautical Engineering

John N. Brick, B.S.

2d Lt, USAF

March 2017

AFIT-ENY-MS-17-M-246

MILITARY SPACE MISSION DESIGN AND ANALYSIS IN A MULTI-BODY ENVIRONMENT: AN INVESTIGATION OF HIGH-ALTITUDE ORBITS AS ALTERNATIVE TRANSFER PATHS, PARKING ORBITS FOR RECONSTITUTION, AND UNCONVENTIONAL MISSION ORBITS

THESIS

John N. Brick, B.S.
2d Lt, USAF

Committee Membership:

Lt Col Christopher D. Geisel, Ph.D.
Chair

William E. Wiesel, Ph.D.
Member

Richard G. Cobb, Ph.D.
Member

Lt Col Stuart A. Stanton, Ph.D.
Member

Abstract

High-altitude satellite trajectories (traveling well above the altitude of a geostationary orbit) and their military applications are analyzed in the Earth-Moon circular restricted three-body problem. The equations of motion for this dynamical model possess no known closed-form analytical solution; therefore, various solutions are computed using numerical methods. To gain insight into the dynamics of high-altitude trajectories in this multi-body dynamical environment, periapsis Poincaré maps of the invariant manifolds associated with periodic, resonant orbits are generated at particular values of the Jacobi Constant, which is the only known integral of the motion. These maps are employed as visual aids to generate initial guesses for orbital transfers and to determine the predictability of the long term behavior of a spacecraft's trajectory. Differential corrections schemes are then implemented to target feasible solutions to two-point boundary value problems involving orbital transfer. Next, a numerical optimization algorithm is implemented to search for locally optimal orbital transfers in terms of the required ΔV. Results of the current investigation demonstrate that alternative, high-altitude transfers may be performed for comparable, and in some cases significantly less, ΔV than conventional transfers. Additionally, transfers are found that are more timely than a launch-on-demand capability that requires 30 days lead time. Analysis of these low-ΔV and timely transfers implies that such high-altitude solutions could be an effective means of reconstitution for conventional constellations. Therefore, reconstitution scenarios from high-altitude resonant parking orbits, including multi-satellite solutions, are examined. Additionally, the ability of satellites in such orbits to provide remote sensing coverage of the surface of the Earth is assessed. The overall capability of satellites in such high-altitude orbits to remotely

sense the surface of the Earth is found to be low relative to that of a satellite at geostationary altitude (35,786 km); however, intervals of high performance are found, indicating that a satellite in such an orbit may effectively perform remote sensing of the Earth's surface at specific times during the satellite's trajectory. Finally, periapsis maps are used to categorize the long term behavior of trajectories. Insight from these maps may be exploited either by a mission planner (to design trajectories) or by an observer (to predict the long term behavior of an observed satellite's trajectory). The current investigation demonstrates not only the potential utility of high-altitude satellite trajectories for military applications but also an effective implementation of methods from dynamical systems theory.

Acknowledgments

First, I would like to thank my advisor, Lt Col Geisel, for the support and direction throughout this graduate program. Your feedback and insight were invaluable during this research. I would also like to thank the rest of my committee for the insightful conversations and feedback along the way.

Additionally, I would like to thank all of my fellow classmates for helping me in both classes and my research. I want to also thank my parents and brothers for all of the encouragement. Finally, I would like to thank my wife for the endless support during this rigorous program.

John N. Brick

Table of Contents

Page

Page

Page

Page

Page

Page

List of Figures

List of Tables

List of Abbreviations

MILITARY SPACE MISSION DESIGN AND ANALYSIS IN A MULTI-BODY ENVIRONMENT: AN INVESTIGATION OF HIGH-ALTITUDE ORBITS AS ALTERNATIVE TRANSFER PATHS, PARKING ORBITS FOR RECONSTITUTION, AND UNCONVENTIONAL MISSION ORBITS

1. Introduction

1.1 Overview

The current investigation explores and analyzes the military applications of satellites in alternative, high-altitude orbits (traveling well above the altitude of a geostationary orbit). These potential military applications include the utilization of high-altitude alternative trajectories to transfer from one conventional orbit to another, the ability to reconstitute a conventional constellation from a high-altitude parking orbit, and the ability of satellites in these high-altitude trajectories to remotely sense the surface of the Earth. Additionally, the ability to predict the long term behavior of a spacecraft's trajectory is investigated. The preliminary design and analysis of these orbits are performed in a multi-body dynamical environment that includes the gravitational effects of the Earth and the Moon. To understand the complex dynamical behavior of this multi-body environment, methods from dynamical systems theory are implemented.

1.2 Motivation

Space-based capabilities have become critical in today's society, both commercially and militarily. According to *JP 3-14*, a document published by the U.S. Joint Chiefs

of Staff in 2013, the capabilities provided by space operations include, but are not limited to, global communications, positioning, navigation, environmental monitoring, surveillance, and reconnaissance [1]. The U.S. military considers these capabilities to be ''significant force multipliers'' [1]. *JP 3-14* defines a ''significant force multiplier'' as a capability that greatly improves the effectiveness of military operations [1]. However, due to the U.S. military's reliance on space-based capabilities, the U.S. military is becoming ''increasingly dependent'' on space operations [1]. Further, the U.S. military is not the only entity that has become dependent on space-based operations. The commercial sectors of the U.S. and other nations are also dependent on space-based systems. Additionally, the ''congested, contested, and competitive'' environment of space-based operations has created a potential vulnerability for these space-based systems [1]. Because of the global dependence of space-based operations and the vulnerability of these operations, there is interest in ensuring the continued operation of critical space assets. This interest may include seeking alternative trajectories to accomplish missions, becoming unpredictable in space operations, increasing the space domain mission assurance, and increasing the operational agility of space users. Additionally, because of the high costs to launch a satellite into orbit, space missions should be accomplished in the most cost-effective manner possible.

The current space-based architecture has led to a ''congested, contested, and competitive'' environment [1]. Space users consistently find themselves competing with other nations, commercial companies, and even themselves for desirable orbits in space. For example, one type of desirable orbit in space is a geostationary orbit—a circular, equatorial orbit that has a period of one sidereal day. The Advanced Extremely High Frequency system is one example of a U.S. military satellite system that utilizes geostationary orbits [2]. Commercially, geostationary orbits are also exploited for communications purposes [3]. Geostationary orbits are desirable because

a spacecraft placed in this type of orbit will remain fixed over the same position on the equator. This fixed position, relative to the rotating Earth, is beneficial for communication purposes because continuous coverage to a specific region of the Earth may be provided by a single satellite [4]. However, because of the high demand of this orbit, the geostationary belt has become heavily congested [4]. Also, low Earth orbit (LEO) satellites are frequently employed by many nations and commercial companies. This congested LEO environment has even led to collisions in space between two satellites. An example of this occurred in 2009 when the U.S. satellite Iridium 33 collided with the Russian satellite Cosmos 2251 [5]. It is estimated that this collision created over 500 pieces of debris that posed a threat to other satellites [5]. An overall increase in debris and satellites may eventually cause even more collisions resulting in more debris [6]. This domino effect is known as Kessler's syndrome [6]. This overpopulation of space may eventually force space users out of traditional orbits of operation.

Another problem with the current space-based architecture is the predictability of conventional mission orbits [1]. For example, when a satellite is launched into a geostationary orbit, a Hohmann-type transfer is typically employed. This type of transfer utilizes a transfer ellipse to maneuver from one orbit to another. Because of the extensive implementation and simplicity of Hohmann-type transfers, the intent of the satellite may be known almost immediately after the transfer has begun. Additionally, at altitudes below a geostationary orbit, a perturbed two-body model is typically implemented for preliminary design [7, 8]. A perturbed two-body model assumes a conic solution as a reference solution of a satellite's trajectory and assumes that deviations from this conic solution, due to disturbing forces, are small [9]. If the deviations from the conic solution become too large, the results may become ''invalid'' [9]. Because of this requirement, preliminary designs generated with a

perturbed two-body model may be similar to the reference conic solutions. This design method may result in predictable orbits. This conventional approach may hinder the ability to be unpredictable in the space domain.

Because space-based operations are essential to the U.S. military and commercial companies and these operations are increasingly vulnerable, an increase in mission assurance is required [10]. According to the Office of the Assistant Secretary of Defense for Homeland Defense and Global Security, space domain mission assurance is defined as the process to ensure the functionality of space based assets [11]. One method of increasing space domain mission assurance is through reconstitution. [11]. Reconstitution is defined as the ability to restore a compromised capability through the deployment of an asset [11]. Currently, reconstitution of a constellation requires the launch of a new satellite to restore the degraded capability. However, the launch of a new satellite requires an operational launch site as well as a fully prepared satellite and rocket. Such resources may not always be immediately available. Additionally, assuming a satellite and rocket are prepared, launch campaigns typically require weeks to months of lead time to execute [1]. However, other methods of reconstitution may allow for a more timely response time and an increase in space domain mission assurance.

In addition to an increase in mission assurance, the U.S. Air Force has also been tasked with increasing its operational agility [12]. The U.S. Air Force's ''Air Force Future Operating Concept'' defines operational agility as ''the ability to rapidly generate—and shift among—multiple solutions to a given challenge'' [12]. This agility is critical in a space environment that is increasingly contested. The ability to respond in multiple ways is not only beneficial to the U.S. military but also to all space users. In a contested environment, it is imperative to have a multitude of solutions to

any given problem. This flexibility is needed to allow decision-makers in the space community to respond appropriately to any circumstance.

Space users are also interested in accomplishing their missions with cost-effectiveness; due to the cost of launch, each kilogram of a satellite is critical [1]. One method to potentially decrease the cost of launch is to reduce the amount of fuel needed by a satellite to perform its mission. In order to achieve potential fuel savings, alternative trajectories that may reduce the fuel requirements of a satellite may be explored. Ocampo showcased this possibility through the ''rescue'' mission of AsiaSat-3. In 1997, this spacecraft was originally tasked to perform a transfer into a geostationary orbit; however, the planned final burn failed to complete the transfer and the spacecraft was ''stranded'' in an ''unusable,'' highly elliptical orbit with a large inclination with respect to Earth's equatorial plane [13]. The spacecraft did not possess enough fuel on-board to perform a conventional transfer to the desired geostationary orbit. At this point, Asia Satellite Communications Ltd. declared the mission a failure [13]. A ''rescue'' mission was later proposed to Hughes Spacecraft Company by representatives of Innovative Orbital Design and Microcosm Inc. [13]. This proposal led to the development of the ''rescue'' mission performed by Hughes Global Services and the renaming of AsiaSat-3 to HGS-1 [13]. HGS-1 then performed two lunar fly-bys to help change its inclination and to position itself in a nearly equatorial geosynchronous orbit [13]. Because of the exploitation of the gravitational effects of the Moon, the fuel requirements were well within the capabilities of the spacecraft [13]. The success of the HGS-1 ''rescue'' mission demonstrated the potential fuel savings of high-altitude alternative trajectories when compared to conventional transfer methods. This example demonstrates the need for space users to explore similar alternative preliminary design methods. Figure 1 shows a notional depiction of the highly elliptical transfer orbit that the spacecraft was ''stranded'' in and the final geostationary orbit that the spacecraft was eventually

transferred to through the use of lunar fly-bys. This figure also depicts the planned ΔV location of the final burn that could no longer be performed after this burn failed.

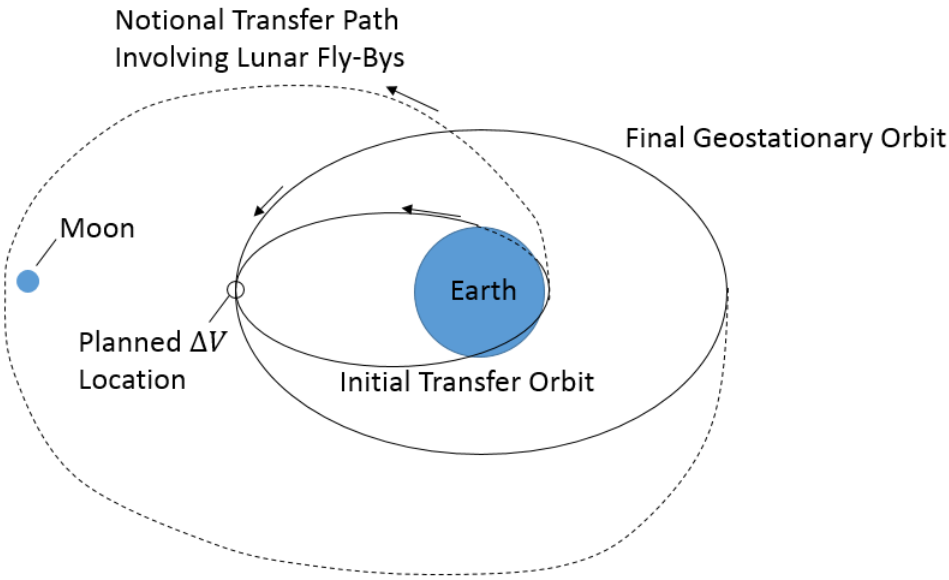

Figure 1. A Notional Depiction of the Highly Elliptical Orbit with an Inclination of 51.619 Degrees Where AsiaSat-3 Was "Stranded" and the Final Geostationary Orbit with an Inclination of 0 Degrees That the Spacecraft Transferred to Through the Use of Lunar Fly-Bys, Adapted from Wilmer [14]

In order for space users to continue to accomplish their missions in a contested environment, alternative mission design methods may be required. These alternative design methods may expand the preliminary design space. The ability to expand the design options may allow for innovative and alternative trajectories that are able to accomplish current mission objectives in a less congested, more unpredictable, and cost-effective manner. These trajectories may also provide an opportunity to increase space domain mission assurance and operational agility. To design these alternative trajectories, the current investigation performs preliminary design in the Earth-Moon circular restricted three-body problem (CR3BP). This higher-fidelity, dynamical model includes the Moon's gravitational effects, as well as the Earth's, on the dynamics of a spacecraft [15]. Two-body perturbation methods may also be implemented to approximate the gravitational effects of a third body. However,

these perturbation methods assume the gravitational effect of the third body is a small deviation from a reference conic solution. This assumption is fundamental to perturbation theory, but, given the effects of lunar gravity, may not be valid at high altitudes [9]. The Earth-Moon CR3BP is a fundamentally different dynamical model than a perturbed two-body model, in that the Earth-Moon CR3BP is a higher-fidelity model that incorporates the gravitational effects of the Earth and the Moon without assuming the change in dynamical behavior is a small perturbation from a two-body reference solution.

1.3 Military Relevance of the Circular Restricted Three-Body Problem

Due to the contested nature of space-based operations, there is interest in increasing the space domain mission assurance and operational agility of such operations, while performing missions in a cost-effective manner. Conventional mission design processes may lead to the positioning of spacecraft in heavily contested and congested regions of space. For example, two conventionally desirable regions of space, LEO and the geostationary belt, have become heavily congested [4, 6]. Because of this congestion, the applications of alternative trajectories should be explored. One possible alternative may be to investigate the applications of high-altitude trajectories. However, a perturbed two-body model may not be sufficient at these high altitudes to accurately predict the behavior of a spacecraft's trajectory. Above the altitude of a geostationary orbit, the dominating disturbing forces are third-body gravitational effects from the Sun and Moon [7,8]. If these disturbing forces become too large, a perturbed two-body model may no longer be adequate to predict the trajectory of a spacecraft. However, by performing preliminary design in the Earth-Moon CR3BP, the gravitational effects of the Moon on the spacecraft are included without assuming such effects are small. This higher-fidelity model may provide more insight than a perturbed two-body model

into the true dynamical environment at high altitudes. However, the addition of a third body's gravitational effects results in a dynamical model that possesses no known closed-form analytical solution; therefore, solutions to the equations of motion require a numerical exploration [3]. Additionally, this multi-body dynamical environment possesses chaotic behavior, which means that a small change in the initial state may lead to a large change in the final state. This sensitivity may make it impossible for an observer to accurately predict the long term behavior of a spacecraft's trajectory. On the other hand, the lack of a known closed-form analytical solution in the CR3BP and presence of chaos may allow for alternative design techniques and innovative mission design that addresses the needs of space users. In particular, the presence of chaos may allow for low-ΔV transfers to be performed.

The additional perspective provided by the CR3BP may provide insight into high-altitude trajectories in unconventional regions of space, such as trajectories near Lagrange points, or equilibrium points, in the CR3BP (see Section 2.10). Some missions have been developed to exploit such trajectories. For example, in 1978, ISEE-3 was the first spacecraft to be positioned at a Lagrange point [15, 16]. This spacecraft was placed in an orbit about the Sun-Earth L_1 point [16, 17]. In this orbit, the satellite investigated the boundary of Earth's magnetosphere [16]. The design of this type of orbit cannot be performed by solely analyzing two-body dynamics because an orbit about a Lagrange point is not a solution to the two-body problem. Various other Lagrange point missions have been performed since 1978 and are discussed in detail in Section 2.1.

Because of the complexity of the dynamical model, the CR3BP yields an ''infinitely complex'' solution space [3]. This solution space may allow for the preliminary design of unpredictable orbits. Since no known closed-form analytical solution is available, if one was to attempt to predict the intent of a high-altitude satellite, precise numerical

integration would be required. However, the presence of chaos in certain regions of the phase space may make it impossible to accurately predict the long term behavior of a spacecraft's dynamics. This unpredictability may be desirable to some mission planners.

Preliminary design in the Earth-Moon CR3BP may lead to the design of trajectories that increase space domain mission assurance. High-altitude parking orbits may exist that allow a satellite to effectively reconstitute a capability in a cost-effective and timely manner. Because of the chaos present in the CR3BP, the intent of these orbits may not be clear to an observer. In fact, a single satellite in one of these high-altitude parking orbits may be able to reconstitute a variety of different conventional orbits. This ability to reconstitute an orbit may increase the mission assurance of desired capabilities.

In addition to an increase in mission assurance, an increase in operational agility may also be possible by performing preliminary design in the Earth-Moon CR3BP. Alternative trajectories that exploit the insight gained from the Earth-Moon CR3BP may provide more options to a decision-maker. The decision-maker may be able to weigh conventional options designed in a two-body model with unconventional high-altitude options designed in a three-body model. The appropriate decision may then be determined by the response time, unpredictability, and cost-effectiveness of each option. Additionally, a satellite in a high-altitude parking orbit designed in the Earth-Moon CR3BP to reconstitute a specific capability may also possess the flexibility to reconstitute other capabilities. The decision-maker may then have the adaptability to decide which capability needs to be reconstituted. This flexibility may allow for decision-makers to act in the most effective manner instead of the most conventional manner.

The implementation of the Earth-Moon three-body model may provide insight into less costly transfers than conventional methods. Through an analysis of the same scenario as the ‘‘stranded’’ AsiaSat-3 spacecraft, Wilmer found an alternative transfer path that required less fuel than a conventional two-body transfer path by performing lunar fly-bys to aid in an inclination change [14]. This mission design was similar to the mission design performed by Ocampo except that Wilmer performed the preliminary design in the Earth-Moon CR3BP [14]. This fuel savings, which could translate to a reduction in spacecraft mass, can reduce the cost of launch. These potential cost savings (in terms of fuel and/or launch costs) may allow for complex missions to be performed in a more cost-effective manner.

Preliminary design in the Earth-Moon CR3BP may provide insight into alternative and innovative solutions. These solutions may increase the unpredictability and cost-effectiveness of a satellite's orbit, while increasing mission assurance and operational agility. Additionally, the unconventional nature of these orbits may allow for missions to be performed in less congested environments than current solutions. However, the implementation of the CR3BP introduces complex behavior into the preliminary design phase that may be difficult to analyze. The lack of a known closed-form analytical solution requires numerical tools to be employed. Numerical integration is required to generate particular solutions in this multi-body dynamical environment. Additionally, differential corrections schemes are implemented to target feasible solutions involving orbital transfers and periodic trajectories. The presence of chaos in this dynamical environment also introduces complexities that can be difficult to analyze. A modern tool to attempt to understand these complexities is known as dynamical systems theory (DST) [3].

1.4 The Application of Dynamical Systems Theory

Due to the presence of chaos and the ‘‘unsolvable’’ nature of some dynamical systems, tools have been developed to understand the possible solutions and behavior of dynamical systems [9]. Developments beginning in the late 1970s in the study of dynamical systems have led to breakthroughs in the modern field of DST [3, 18]. These new tools may be employed to understand the possible solutions through a geometrical approach of a dynamical system by analyzing the natural ‘‘flow’’ of a dynamical system [19]. One such tool is the analysis of invariant manifolds, which are tube-like structures in the phase space that asymptotically approach some periodic solutions. Knowledge of the natural ‘‘flow’’ of these manifolds may be exploited to identify desirable solutions to dynamical problems [19]. Another tool that may be employed for analysis is the Poincaré surface of section, or Poincaré map. This map may be used to reduce the dimension of a dynamical system by only investigating a ‘‘slice’’ of the phase space [9, 20]. This tool may also be utilized as a visual aid to understand the global behavior of a dynamical system [9, 19, 20]. In general, these tools may be employed in any dynamical system to gain insight into the global behavior of a dynamical system and reduce the dimension of the problem. In the Earth-Moon CR3BP, these methods may be implemented to aid in the design of trajectories that are cost-effective or possess other desirable characteristics [3, 9, 19].

Mission designers may employ DST to understand some of the possible trajectories and behaviors present in the Earth-Moon CR3BP. This insight may aid in the search for trajectories with desirable characteristics that exploit the natural dynamics of the system. Some of these desired characteristics may be stability, periodicity, unpredictability, or the ability to perform transfers for low costs (in terms of fuel) [3, 9]. The potential insight provided by DST may be exploited to design missions that take advantage of the natural ‘‘flow’’ of the CR3BP [3, 19].

One example of a mission designed using DST was the Genesis mission. This spacecraft utilized the natural dynamics present in the Sun-Earth CR3BP to perform a complex mission for a trivially small amount of fuel [3]. In 2001, the Genesis spacecraft left Earth on a trajectory that approached a periodic orbit about the Sun-Earth L_1 point [21, 22]. Solar wind particles were collected in this orbit for approximately two years before the spacecraft transfered to a periodic orbit about the Sun-Earth L_2 point [21, 22]. The spacecraft then returned to Earth for its planned recovery on the surface [21, 22]. The Genesis mission was designed to perform this mission for a deterministic ΔV of less than 36 m/s [21, 22]. The success of this mission showcased the possibilities available to mission designers to perform complex missions for a low cost, in terms of ΔV, through the implementation of methods from DST. Trajectory design using methods from DST, similar to the Genesis mission, may allow for the design of high-altitude alternative trajectories in the CR3BP that meet the needs of a user in a contested space environment.

The implementation of methods from DST may allow for insight into the high-altitude alternative trajectories present in the Earth-Moon CR3BP that possess desirable characteristics for mission planners. However, according to the National Research Council, as of 2012, U.S. Air Force Space Command had not been implementing the modern breakthroughs of DST and were using the same techniques used in the 1960s [18]. The National Research Council also notes that current space systems are subject to chaotic effects due to drag, the oblateness of the Earth, and third body effects that lead to inaccurate predictions [18]. By utilizing DST, the dynamical behavior of a satellite may be better understood [18]. The implementation of DST may allow for the U.S. Air Force and other space users to understand the potential applications of high-altitude alternative trajectories modeled in the Earth-Moon CR3BP.

1.5 Problem Statement

The objective of the current investigation is to explore the implementation of the Earth-Moon CR3BP and DST to perform the preliminary design of military missions. The current investigation examines the potential applications of the high-altitude alternative trajectories modeled in the Earth-Moon CR3BP to perform transfers between conventional, conic orbits in the vicinity of Earth. Additionally, the current investigation examines the ability of high-altitude parking orbits, modeled in the Earth-Moon CR3BP, to increase mission assurance by providing the capability to reconstitute conventional capabilities. Also explored is the capability of satellites in high-altitude orbits to remotely sense the surface of the Earth. Furthermore, the current work investigates the ability to characterize the long term behavior of a spacecraft's trajectory. The current investigation showcases a multitude of design methods and applications of DST to develop feasible, cost-effective solutions with potential real-world applications.

1.6 Previous Contributions

Various other researchers have implemented methods from DST to the design and analysis of possible trajectories in the CR3BP. Specifically, the asymptotic behavior of the invariant manifolds has led to the exploitation of these trajectories in mission design. The first spacecraft mission designed to exploit such manifolds was the Genesis mission launched in 2001 [3,9,21,22]. Koon et al. investigated the connections between invariant manifolds as transfer paths between resonant orbits, which are a type of periodic orbit in the CR3BP, in the Sun-Jupiter CR3BP [23]. Then, Lo and Parker explored the exploitation of the invariant manifolds associated with orbits in the Earth-Moon CR3BP [24]. In 2004, Gómez et al. investigated the utilization of invariant manifolds to transit between periodic orbits in various systems [25].

Haapala also performed trajectory design in the CR3BP using invariant manifolds as transfer trajectories [26, 27]. Additionally, Pavlak investigated transfers in the Earth-Moon CR3BP through the use of invariant manifolds associated with Lagrange point orbits [28]. Davis et al. explored the use of the invariant manifolds to perform transfers from LEO to geosynchronous orbits [29]. Vaquero and Howell exploited invariant manifolds associated with resonant orbits to perform transfers between periodic orbits about various Lagrange points [30, 31, 32]. In 2016, Wilmer explored the use of invariant manifolds to perform transfers in the Earth-Moon CR3BP that remained in the Earth-Moon orbital plane [14].

In addition to research exploring the exploitation of invariant manifolds, previous researchers have also investigated the utilization of Poincaré maps as visual aids. In 1966, Hénon generated Poincaré maps in the planar Copenhagen CR3BP, which is a special case of the CR3BP where the two primaries are of equal mass [33]. Villac and Scheeres then employed the periapsis Poincaré map, which is a type of Poincaré map where an intersection of the hyperplane occurs when the trajectory reaches a periapse [34]. Vaquero and Howell explored the applications of multiple types of Poincaré maps in the planar CR3BP to generate initial guesses for transfers between periodic orbits [30, 31, 32]. Howell, Craig Davis, and Haapala categorized the behavior of a spacecraft's trajectory in the vicinity of the smaller primary through the investigation of periapsis maps [26, 27, 35, 36, 37]. In 2016, Wilmer implemented a similar strategy to explore the long term behavior of trajectories in the vicinity of the Earth in the Earth-Moon CR3BP. Researchers have also investigated the generation and applications of four-dimensional Poincaré maps. Geisel investigated a ''space-plus-color'' method where color represented the fourth dimension of the map [19]. On the other hand, Haapala investigated the implementation of glyphs to represent the fourth dimension [27]. Haapala then utilized these four-dimensional

maps as visual aids to generate transfers between periodic orbits. These contributions provide the context of the current investigation.

The current investigation is a follow-on to the research conducted by Wilmer [14]. Wilmer showcases the implementation of high-altitude transfers modeled in the Earth-Moon CR3BP to transfer between conventional orbits. First, Wilmer demonstrates the application of preliminary design in the Earth-Moon CR3BP to develop a cost-effective transfer similar to the HGS-1 ''rescue'' mission [13]. Then, Wilmer explores the employment of high-altitude transfers modeled in the Earth-Moon CR3BP between conventional orbits that lie in the Earth-Moon orbital plane. In particular, Wilmer investigates such transfers from a highly elliptical orbit to a circular orbit through the employment of the invariant manifolds of a Lyapunov orbit. However, errors in Wilmer's calculations of the required ΔV to perform conventional transfers are found and discussed in Section 3.1.2.1. The current investigation expands upon Wilmer's work by examining high-altitude transfers in the Earth-Moon CR3BP from a highly elliptical geosynchronous orbit in the Earth-Moon orbital plane to various geosynchronous orbits, some of which do not lie in the Earth-Moon orbital plane, through the employment of the invariant manifolds associated with resonant periodic orbits. This initial highly elliptical geosynchronous orbit is chosen to lie in the Earth-Moon orbital plane because it simplifies the analysis of Poincaré maps. Additionally, Wilmer recommends the investigation of high-altitude parking orbits modeled in the Earth-Moon CR3BP as a source of reconstitution. The current investigation explores this recommendation in detail. In particular, resonant orbits in the Earth-Moon orbital plane and their applications as high-altitude parking orbits are investigated. Again, in the current investigation, these parking orbits are chosen to lie in the Earth-Moon orbital plane to simplify the analysis of Poincaré maps.

Another major component of the work conducted by Wilmer was the investigation of periapsis Poincaré maps to characterize the long term behavior of a spacecraft's trajectory. However, Wilmer's limitations include the cost, in terms of time, to generate such maps in MATLAB® [38]. Wilmer recommends the utilization of a more efficient computer program to overcome this obstacle. The current investigation employs Air Force Research Laboratory (AFRL) supercomputing resources to generate periapsis Poincaré maps using MATLAB® in a more timely manner. This resource allows for more maps to be generated with a higher density of periapses. Additionally, the current investigation demonstrates the potential utilization of such a map to calculate low-ΔV transfers.

1.7 Thesis Overview

This thesis consists of five chapters that describe the design processes employed in the current investigation. Chapter 1 provides the context and motivation for the current research. Then, Chapter 2 reviews the necessary background information utilized in the development of the methodology and analysis. Next, Chapter 3 discusses the methodology implemented by the current investigation, as well as the test plan. Chapter 4 then describes and analyzes the results of the current investigation. Finally, Chapter 5 includes discussion of the overall conclusions of the current investigation, as well as some recommendations for future research.

- Chapter 2: A brief historical overview of astrodynamics is described to provide the background information utilized in the current investigation, as well as the history of various Lagrange point missions. A review of astrodynamics is provided, including discussion on the N-body problem, the two-body problem, and the CR3BP. This discussion includes the derivation of each of these problems, including the nondimensionalization of the equations of motion of the CR3BP.

Numerical integration and its applications to the CR3BP are discussed. Then, the equilibrium solutions of the CR3BP and their Lyapunov stability are analyzed. Also, the definition of the single known integral of the motion of the CR3BP, the Jacobi constant, is derived. Next, the existence of zero velocity surfaces, which bound the motion of a spacecraft at a particular value of the Jacobi Constant, is described. The state transition matrix, which relates the final state to the initial state based on a linearization of the equations of motion about a reference solution, is introduced. Next, differential corrections processes that exploit knowledge gained through the computation of the state transition matrix are discussed. Background on numerical optimization is then provided. Next, different types of periodic orbits and their orbital stability, based on a linear analysis, are explained. The invariant manifolds of orbitally unstable periodic orbits, which are made up of trajectories that asymptotically approach or depart a periodic orbit, are then defined. Finally, Poincaré maps and their applications as visual aids are discussed.

- Chapter 3: An overview of the test plan implemented by the current investigation is provided. Then, methodology specific to the investigation is explained. Included in this explanation is the continuation method employed by the current investigation. A continuation scheme uses one periodic orbit as an initial guess to search for a portion of the family of periodic orbits that possess similar behavior. Periapsis Poincaré maps are then discussed, as well the supercomputing resources exploited to generate the maps. Next, the numerical optimization method implemented by the current investigation to search for locally optimal solutions is explained. Finally, metrics are developed that assess the ability of a satellite to remotely sense the surface of the Earth.

- Chapter 4: Results and analysis are provided for each of the test cases described in the test plan portion of Chapter 3. Feasible solutions, as well as some locally optimal solutions, are presented, and their potential utility are discussed. These solutions are found to be comparable to the cost, in terms of ΔV, of performing transfers using a conventional Hohmann-type transfer. In some cases, the high-altitude alternatives are associated with potentially significant cost savings, in terms of ΔV. On the other hand, the overall capability of a satellite in such an orbit to remotely sense the Earth's surface is found to be low relative to that of a satellite at geostationary altitude (35,786 km); however, intervals of high performance are also found. Finally, the ability to predict the long term behavior of a spacecraft's trajectory is explored.

- Chapter 5: A brief summary of the current investigation is provided. Then, conclusions based on the results and analysis presented in Chapter 4 are discussed. Next, limitations of the current investigation are discussed. Finally, recommendations for future work are proposed.

1.8 Chapter 1 Summary

This chapter presents the context and motivation of the current investigation. The essential nature and ''congested, contested, and competitive'' environment of space-based operations is discussed [1]. Because of this contested environment, the potential applications of alternative high-altitude trajectories are introduced. Then, due to the high-altitudes of these trajectories, the relevance of the CR3BP is discussed. However, since the CR3BP does not possess a closed-form analytical solution, numerical methods and alternative methods of analysis, such as DST, are discussed. Next, a problem statement is presented as well as a brief discussion of some previous contributions. Finally, a thesis overview is provided that details the current work.

2. Background

This chapter provides the necessary background for the current investigation. First, a historical overview of astrodynamics is presented. Then, the 2BP, N-body problem, and the CR3BP are discussed. Next, the equations of motion for the CR3BP are presented as well as some of their characteristics, such as the Lagrange points and the Jacobi Constant. Additionally, numerical methods are discussed, including numerical integration, differential corrections schemes, and numerical optimization. Multiple types of stability are then discussed and applied to the Lagrange points and periodic trajectories based on a linear analysis of the variational equations. Finally, aspects of DST are discussed, including invariant manifolds and Poincaré maps.

2.1 Historical Overview

One could argue that the study of dynamics began in ancient Greece when Aristotle began attempting to explain the motion of an arbitrary body. His efforts provided an early attempt to describe what would later be defined as gravity. Aristotle believed that all bodies tended toward a ‘‘natural place’’ at the center of the Earth and would approach this place if nothing impeded the progress of the body [39]. However, Aristotle incorrectly asserted that this ‘‘natural place’’ existed at the center of the Earth [39]. In the second century A.D., Ptolemy introduced the idea that planets orbited Earth with circular trajectories, and that these circular orbits contained epicycles [3]. This geocentric Ptolemaic scheme became a ‘‘close approximation’’ to an elliptical orbit [3]. The geocentric model was widely accepted until Copernicus, in 1543, adjusted Aristotle's assertions and repositioned the ‘‘natural place’’ to the center of the Sun in a heliocentric model [3, 39]. Galileo then claimed to prove that his telescopic observations of 1610 verified Copernicus's heliocentric model [3, 40].

Galileo also introduced the idea of acceleration being related to force, rather than velocity as was previously believed [39]. This Copernican revolution continued with the publications of Kepler's three laws [40]:

1. ''The orbit of each planet is an ellipse, with the sun at a focus.'' (published in 1609) [40]

2. ''The line joining the planet to the sun sweeps out equal areas in equal times.'' (published in 1609) [40]

3. ''The square of the period of a planet is proportional to the cube of its mean distance to the sun.'' (published in 1619) [40]

These kinematical relationships accurately reflected the observational data of the time. However, these laws did not provide a description of the cause of motion. These causes were later described by Newton in 1687 [40]. Newton's three laws of motion were able to describe dynamics of falling bodies [40]:

1. ''Every body continues in its state of rest or of uniform motion in a straight line unless it is compelled to change that state by forces impressed upon it.'' [40]

2. The rate of change of momentum is proportional to the force impressed and is in the same direction as that force.'' [40]

3. ''To every action there is always opposed an equal reaction.'' [40]

These three laws have become the foundation of classical mechanics. Newton's discoveries also eliminated the need to define a ''natural place'' as had originally been done by Aristotle [39]. Newton's Universal Law of Gravitation, sometimes referred to as Newton's fourth law, was also defined in his publication of *Principia* in 1687 [40]. This law states that the magnitude of the attractive force experienced by one mass due

to the gravitational effects of another mass is proportional to the product of the masses and inversely proportional to the square of the distance between the masses [39, 40]. This relationship is defined mathematically in equation (1).

$$F = G\frac{m_1 m_2}{r^2} \tag{1}$$

The universal gravitational constant, G, has been estimated to be approximately $6.67408 \times 10^{-11} \frac{\mathrm{m}^3}{\mathrm{kg}\cdot\mathrm{s}^2}$ [40, 41]. With his three laws of motion and law of gravitation, Newton was able to derive Kepler's laws and determine that the solution of the two-body problem could be written in terms of conics [3, 39, 40, 42, 43]. Newton's solution to the two-body problem inspired the desire to accurately predict the location of the Moon [44]. A precise knowledge of the Moon's location would allow for accurate naval navigation [44]. However, Newton was never able to accurately predict the Moon's behavior [45].

In 1753, Euler published his first lunar theory, which exploited the method of the variation of parameters to account for the perturbations on lunar motion caused by the Sun [45]. Then, in 1772, he published his second lunar theory with Lagrange [15, 45]. This lunar theory was implemented to develop a lunar ephemeris by the British navy for navigational purposes [44]. This work with Lagrange also introduced the CR3BP based on a rotating frame [15, 45]. The publication also explained the discovery of the five equilibrium points in the CR3BP, or Lagrange points (see Section 2.10) [15, 45]. Euler was responsible for discovering the collinear points in 1765, while Lagrange discovered the equilateral points in 1772 [15, 19, 45]. Further insight into the CR3BP was gained in 1836 when Jacobi discovered the existence of the only known integral of the motion admitted by the equations of motion of the CR3BP—the Jacobi Constant [15, 45]. This discovery of the Jacobi Constant implied the existence of ''forbidden'' regions enclosed by zero-velocity surfaces, which were first discovered by Hill in 1878 [15, 45].

With the publication of the three volumes of *Méthodes Nouvelles de la Mécanique Céleste*, the final of which was published in 1899, Poincaré had proven that the CR3BP possesses no known closed-form analytical solution [3, 44]. This discovery led Poincaré to approach the CR3BP with a more qualitative approach [45]. Poincaré explored periodic orbits in this dynamical system to attempt to analyze the global dynamics of the CR3BP [3, 9]. This pursuit led him to define the ''surface of section,'' which would later be known as the Poincaré map [3, 9]. His prediction of the types of behavior seen on a ''surface of section'' of a nonintegrable system, such as the CR3BP, may have been the first description of chaotic behavior [3, 9]. Poincaré's innovative research laid the foundation of modern DST [3, 9]. Further attempts to find a ''solution'' to the CR3BP were continued by Sundman, but were unsuccessful. In 1912, Sundman ''solved'' the CR3BP with a convergent, infinite power series [45, 46]. However, this ''solution'' provided no information about the qualitative behavior of the CR3BP and converged too slowly to be of practical use [45]. Additional work was accomplished by Szebelehy, leading to his definitive text on the CR3BP, published in 1967, *Theory of Orbits* [15]. In fact, Wiesel claims that no reference is required for the CR3BP ''beyond Szebelehy's magnificent book'' [3]. To this day no known closed-form analytical solution to the CR3BP exists.

Since Szebelehy's publication of *Theory of Orbits*, various Lagrange point missions have been performed. The first mission to a Lagrange point occurred in 1978 when ISEE-3 was positioned in an orbit about the Sun-Earth L_1 point [17]. This spacecraft investigated the boundary of Earth's magnetosphere and was also the first spacecraft to investigate near-Earth solar wind [16, 17]. In 1994, another spacecraft, WIND, was also inserted into an orbit about the Sun-Earth L_1 point [47]. WIND investigated the upstream interplanetary medium as well as other aspects of the solar wind [47]. Then, in 1995, SOHO was placed in an orbit about the Sun-Earth L_1 point where

it investigated the structure of the Sun's corona [48]. In 1997, ACE was inserted into a trajectory about the Sun-Earth L_1 point [49, 50]. The ACE spacecraft studied coronal mass ejections and served as an early warning system of adverse space weather [49]. In 2001, the Genesis spacecraft and the WMAP spacecraft were both launched [21, 22, 51, 52]. The Genesis spacecraft traveled to both the Sun-Earth L_1 and L_2 points before returning to Earth in 2004 [21, 22, 51]. This spacecraft collected solar wind samples at the Sun-Earth L_1 and returned them to Earth for further study [22, 51]. The WMAP spacecraft was inserted into an orbit near the Sun-Earth L_2 point, where it measured background microwave radiation [52]. In 2009, the Herschel Space Observatory and the Planck Space Observatory were both inserted into orbits about the Sun-Earth L_2 point [53, 54]. The Herschel Space Observatory was tasked to investigate the coldest regions of space using infrared light [53]. The Planck Space Observatory investigated the universe's cosmic microwave background radiation [54]. Also, in 2009, the ARTEMIS missions began [55]. These missions repurposed two spacecraft from the THEMIS mission and transferred the spacecraft into orbits about the Earth-Moon L_1 and L_2 points [55, 56]. These spacecraft were the first to visit Lagrange points in the Earth-Moon system where they studied the behavior of energetic particles near the Moon [55].

2.2 The N-Body Problem

The N-body problem is a dynamical model describing the motion of N masses subject to their mutual gravitational attraction according to Newton's three laws of motion and Newton's law of universal gravitation. The fundamental assumptions of the N-body problem are that the only forces acting upon each of the N bodies are the mutual gravitational forces due to the other $N - 1$ bodies and that each mass possesses a spherically symmetric mass distribution [3, 40]. Since it is assumed that

each mass possesses a spherically symmetric mass distribution, each mass may be modeled as a point mass [3, 40]. This system of N points (P_i) each with mass (m_i) is shown with respect to an arbitrary inertial frame $(\hat{i}\hat{j}\hat{k})$ in Figure 2. Each point (P_i)

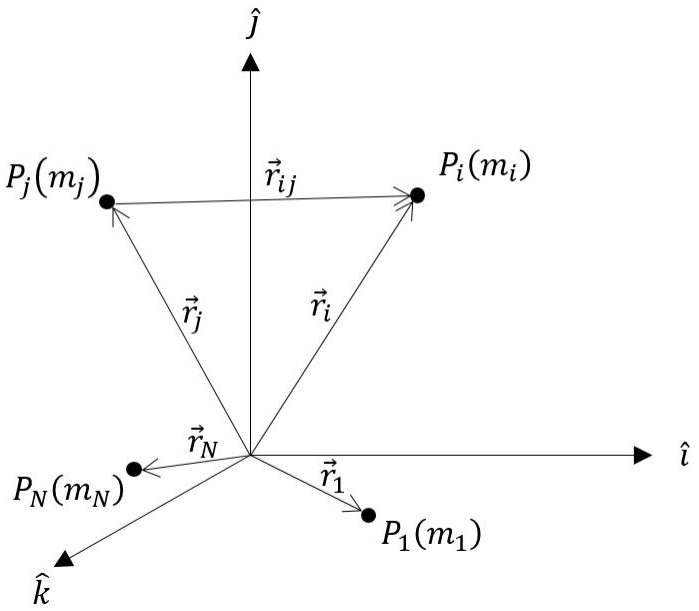

Figure 2. The N-Body Problem Displayed in an Inertial Frame

may be described by a position vector defined relative to the origin labeled $\vec{r}_i$. In addition to this position, the relative position of each point (P_i) is defined relative to each other point (P_j) and labeled $\vec{r}_{ij}$, such that $\vec{r}_{ij} = \vec{r}_i - \vec{r}_j$. The equations of motion for each of the N points are then described by applying Newton's laws in equation (2) [3].

$$\ddot{\vec{r}}_i = -G \sum_{\substack{j=1 \\ j \neq i}}^{N} m_j \left(\frac{\vec{r}_{ij}}{||\vec{r}_{ij}||^3} \right) \qquad for\ i = 1, 2, \ldots, N \tag{2}$$

In general, the N-body problem consists of $6N$ first-order equations of motion, which would require $6N$ integrals of the motion to possess a closed-form analytical solution [9, 57]. However, the N-body problem, in general, only possesses ten integrals of the motion: the conservation of linear momentum (six), the conservation of angular momentum (three), and the conservation of total mechanical energy (one) [9]. If

$N \geq 2$, then the general N-body problem possesses no known closed-form analytical solution [9]. However, when $N = 2$, the general two-body problem may be reformulated as a relative problem that does possess a closed-form analytical solution in terms of conics [3, 9, 39, 40].

2.3 The Two-Body Problem

The two-body problem (2BP) is a special case of the N-body problem where $N = 2$. As formulated in an inertial frame, the general 2BP possesses 10 integrals of the motion; however, 12 integrals of the motion would be required for this dynamical model to possess a closed-form analytical solution. On the other hand, the general 2BP may be reformulated as the relative 2BP, which does possess a closed-form analytical solution in terms of conics [3, 39, 40, 42, 43]. First, the equations of motion for each of the two bodies (P_1 and P_2) may be described by equation (2) and combined to produce the relative second-order differential equation of motion of P_2 relative to P_1 as seen in equation (3) in terms of a gravitational parameter, μ, where $\mu = G(m_1 + m_2)$.

$$\ddot{\vec{r}} = \ddot{\vec{r}}_2 - \ddot{\vec{r}}_1 = -\mu \frac{\vec{r}}{||\vec{r}||^3} \tag{3}$$

This relative formulation requires six integrals of the motion to possess a closed-form solution. The law of energy conservation may be derived by performing a dot product of the relative velocity, $\dot{\vec{r}}$, with both sides of equation (3) [3]. This operation results in a scalar equation known as the ‘‘vis-viva’’ equation [58]. This relationship is defined in equation (4) in terms of the conserved quantity: specific mechanical energy (ε).

$$\varepsilon = \frac{||\dot{\vec{r}}||^2}{2} - \frac{\mu}{||\vec{r}||} \tag{4}$$

In the general two-body problem, ε is the quantity of total mechanical energy per $m_{reduced}$, where $m_{reduced} = \frac{m_1 m_2}{m_1 + m_2}$. The conservation of angular momentum may then be derived by performing a cross product of the relative velocity with both sides of equation (3) [3]. This operation results in the conserved angular momentum vector, $\vec{H}$, which is defined in equation (5).

$$\vec{H} = \vec{r} \times \dot{\vec{r}} \tag{5}$$

The angular momentum vector defines the orbital plane of the two bodies. Since the position and velocity vectors must always be orthogonal to the angular momentum vector, according to equation (5), the motion of the two bodies must remain in an orbital plane. Additionally, since the conserved entity is a three-dimensional vector, three integrals of the motion are described by the angular momentum vector. The final two integrals of the motion are unique to the 2BP. These integrals of the motion may be derived by performing a cross product between the angular momentum vector and both sides of equation (3) [3]. This operation reveals the conservation of the eccentricity vector, $\vec{e}$, as seen in equation (6) [3].

$$\dot{\vec{r}} \times \vec{H} - \mu \frac{\vec{r}}{||\vec{r}||} = \mu \vec{e} \tag{6}$$

At first glance, equation (6) appears to provide three additional integrals of the motion because the conserved eccentricity vector is three-dimensional. However, since the eccentricity vector must lie in the orbital plane, only two of the three components of the eccentricity vector are independent of the three integrals of the motion provided by the angular momentum vector. Despite this realization, the total number of integrals of the motion in the relative formulation of the 2BP derived in the current investigation is now six. These six integrals of the motion imply that a closed-form

analytical solution of the relative 2BP exists. Accordingly, the dot product of both sides of equation (6) with the relative position vector may be taken. This operation results in equation (7), which is known as the ‘‘trajectory’’ equation [3, 40].

$$||\vec{r}|| = \frac{||\vec{H}||^2/\mu}{1 + ||\vec{e}||cos\nu} \tag{7}$$

The true anomaly, ν, is defined as the angle between the eccentricity vector and the relative position vector. Because equation (7) is expressed in the ‘‘*polar form of a conic section*’’ [emphasis in the original] [3], this equation implies that the solution of the 2BP may be written in terms of conics [39, 40, 42, 43]. Conic sections include circles, ellipses, parabolas, and hyperbolas. The trajectory of one body relative to another in the relative 2BP will trace out one of these conic sections in the configuration space, with the other body located at a focus of the conic section [3]. The type of conic section is determined by the eccentricity, $e = ||\vec{e}||$. If $e = 0$, the conic section is a circle. If $0 < e < 1$, the conic section is an ellipse. If $e = 1$, the conic section is a parabola, degenerate parabola, degenerate ellipse, or degenerate hyperbola. And finally, if $e > 1$, the conic section is a hyperbola. Many transformations exist between the dynamical quantities of the 2BP and the geometric quantities of the conic solutions. One example is the relationship between the magnitude of the angular momentum vector, $\vec{H}$, the semimajor axis, a, and the semi-latus rectum, p, described in equation (8).

$$\frac{||\vec{H}||^2}{\mu} = a(1 - e^2) = p \tag{8}$$

Another example is the relationship between the specific mechanical energy, ε, and the semimajor axis, a.

$$\varepsilon = \frac{-\mu}{2a} \tag{9}$$

Figure 3 shows an example of a nominal elliptical orbit describing some of the geometric quantities of an elliptical trajectory. P_1 is located at one focus of the ellipse, while the other focus is vacant. The motion of P_2 then traces the ellipse. The period, P, of an

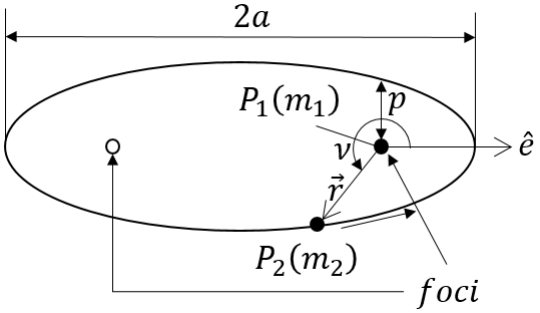

Figure 3. Elliptical Orbit

elliptical orbit may be described in terms of the semimajor axis and the gravitational parameter of the system. This definition is seen in equation (10) [3].

$$P = 2\pi\sqrt{\frac{a^3}{\mu}} \tag{10}$$

Additionally, it is possible to define the mean motion, n, of an orbit, which is also the angular frequency of the orbit [3].

$$n = \frac{2\pi}{P} = \sqrt{\frac{\mu}{a^3}} \tag{11}$$

The mean anomaly, M, is then defined as an angle that increases linearly with time at a rate equal to the mean motion [3].

$$M(t) = M(t_0) + n(t - t_0) \tag{12}$$

A common variant of the general 2BP is the restricted two-body problem (R2BP). This variant assumes that one mass, m_1, is much larger than the other, $m_1 \gg m_2$. This assumption slightly alters the definition of the gravitational parameter, $\mu =$

$G(m_1 + m_2) \approx Gm_1$. This assumption is valid for many applications of astrodynamics. For example, the dynamics of a spacecraft in the vicinity of the Earth may be approximated using the R2BP, since, in general, the spacecraft will have a negligible gravitational effect on Earth [3]. Additionally, in the R2BP, the specific mechanical energy of the spacecraft, as defined in equation (4), is the total mechanical energy of the spacecraft per unit mass of the spacecraft, instead of per unit reduced mass.

2.3.1 Orbital Transfers

In order to insert a spacecraft into a desired orbit, orbital transfers must be performed. The optimal two-burn transfer between coplanar circular orbits is the Hohmann transfer [42, 59]. This transfer employs a coplanar transfer ellipse and requires two impulsive changes in velocity, ΔV. The first of these ΔVs transfers the spacecraft from a circular orbit to the apse of an elliptical transfer orbit. After one half of the period of the transfer ellipse, the spacecraft is at the other apse of the transfer ellipse. At this apse, a second impulsive maneuver is performed to transfer the spacecraft from an elliptical orbit to a circular orbit at a new altitude. A multitude of sources provide an in-depth explanation and derivation for calculating the required ΔV to perform a Hohmann transfer [3, 40, 42, 43]. Figure 4 displays a nominal Hohmann transfer between two circular orbits. In addition to an altitude raising transfer, it may be desirable to perform a transfer between two noncoplanar circular orbits. A Hohmann-type transfer may be employed in this instance. This Hohmann-type transfer would incorporate a combined plane change to change the satellite's inclination and speed simultaneously. Such a maneuver would typically be performed at the apoapse of the transfer ellipse because it is more cost-effective to change the inclination of a spacecraft when the speed is low [42]. However, while on-orbit maneuverability is possible through the use of Hohmann-type transfers, Hohmann-type transfers may be

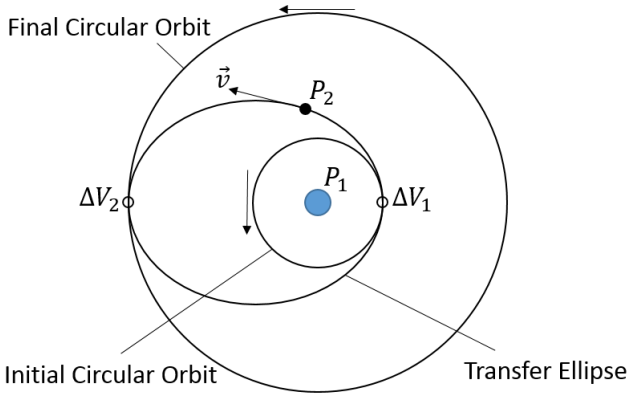

Figure 4. A Nominal Hohmann Transfer Between Two Coplanar Circular Orbits

more costly in terms of fuel than alternative, high-altitude transfers. The AsiaSat-3/HGS-1 mission demonstrates the potential cost savings associated with high-altitude transfers between conventional constellations that exploit the gravitational effects of the Moon (see Section 1.2) [13].

2.3.2 The Classical Orbital Elements

A common set of coordinates for describing an orbit in the R2BP are the classical orbital elements (COEs). These coordinates are capable of fully describing the state of a satellite modeled in the R2BP as a function of time. One of the COEs is the semimajor axis, a, of the orbit. This COE describes the size and period of an orbit in the R2BP. Another COE is known as the eccentricity, e. This quantity describes the shape of the solution in terms of conics. Then, the inclination, i, is defined to be the angle between a fixed reference plane and the orbital plane of the trajectory. In an Earth-satellite system, the inclination is typically defined as the angle between Earth's equatorial plane and the orbital plane of the satellite. This inclination may also be defined as the angle between a reference vector, the North pole direction, and the angular momentum vector of the satellite's orbit. The right ascension of the ascending node, Ω, is then defined as the angle between another fixed reference vector

and the line of nodes, $\hat{n}$. In an Earth-satellite system, this fixed reference vector is typically defined as the vernal equinox, or first point of Aries, Υ [3]. This vernal equinox direction is defined as the direction towards the Sun as it passes through Earth's equatorial plane from south to north on the first day of spring [3]. Next, the argument of periapse, ω, is defined as the angle between the line of nodes and the eccentricity vector. Finally, the true anomaly is defined as the angle, measured in the direction of motion, from the eccentricity vector to the satellite's position vector. Figure 5 details the relationships between the COEs and a satellite's position in space relative to Earth. The six classical orbital elements fully describe an orbit in the R2BP.

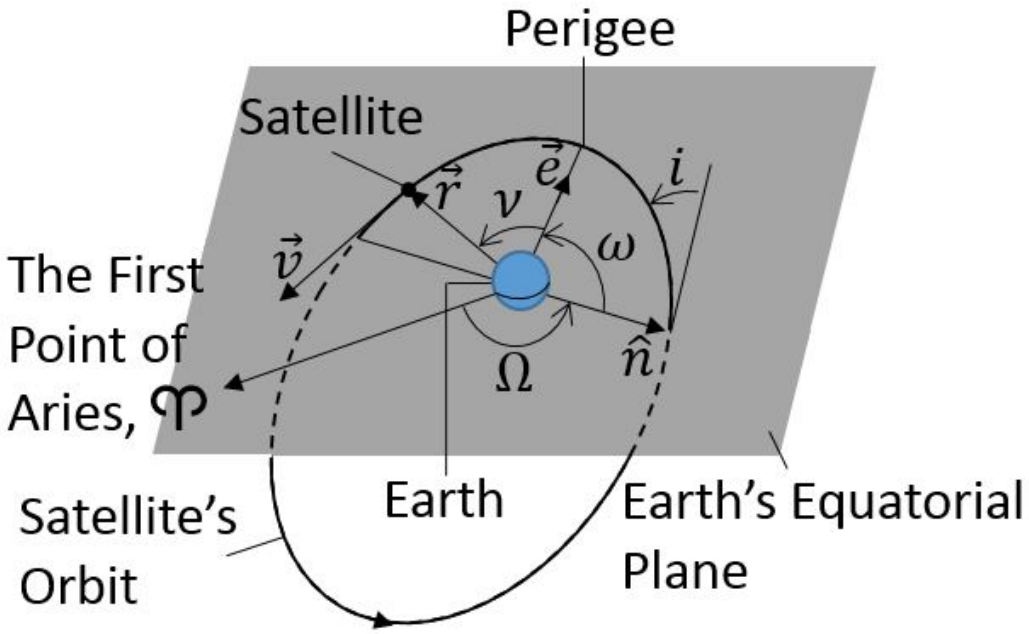

Figure 5. Classical Orbital Elements

The first five COEs—semimajor axis, eccentricity, inclination, right ascension of the ascending node, and argument of periapse—are constants in the R2BP. However, the true anomaly is a function of time, dependent upon the satellite's position in the orbit.

Under certain circumstances, some of the classical orbital elements may be undefined. In this case, alternative orbital elements may be introduced to unambiguously

describe an orbit modeled in the R2BP. If the inclination is zero, the longitude of periapsis, Π, may be introduced, which is the angle from the vernal equinox to the eccentricity vector [40]. On the other hand, if the orbit is circular, the argument of latitude, u, may be defined as the angle from the line of nodes to the satellite's position vector [40]. In the special case of a circular orbit with zero inclination, the true longitude, l, may be defined [40]. This quantity measures the angle between the vernal equinox and the satellite's position vector [40].

2.3.3 The Gravitational Effects of an Oblate Earth

The closed-form analytical solution of the R2BP in terms of conics is based on the assumption that the central body possesses a spherically symmetric mass distribution and may therefore be modeled as a point mass; however, a higher-fidelity approximation could include the effects of a nonspherical mass distribution. For example, the Earth is often modeled as spherical, but does possess an equatorial bulge [3]. This oblateness can affect the trajectory of a satellite as it orbits Earth. One such effect is known as the regression of the nodes, $\dot{\Omega}$ [3]. This effect causes a secular change in the right ascension of the ascending node of a satellite.

$$\Omega(t) = \Omega(t_0) + \dot{\Omega} \cdot (t - t_0) \tag{13}$$

Another effect of this oblateness is known as the advance of perigee, $\dot{\omega}$ [3]. Similarly, this effect causes a secular change in the argument of perigee of a satellite.

$$\omega(t) = \omega(t_0) + \dot{\omega} \cdot (t - t_0) \tag{14}$$

In the R2BP, prior to considering the effects of an oblate Earth, both the right ascension of the ascending node and the argument of perigee were constant. However,

when considering the oblateness effects of the Earth, both of these quantities change linearly with time. The rate of change for both of these COEs can be calculated using the relationships described in equations (15)-(16) where a, e, and i are the COEs, while n and $R_\oplus$ are the mean motion and radius of the Earth, respectively [3].

$$\dot{\Omega} = -\frac{3nJ_2R_\oplus^2}{2a^2(1-e^2)^2}cos(i) \tag{15}$$

$$\dot{\omega} = -\frac{3nJ_2R_\oplus^2}{2a^2(1-e^2)^2}\left(\frac{5}{2}sin^2(i) - 2\right) \tag{16}$$

The constant J_2 defines the oblateness of the central body. For Earth, $J_2 = 0.001082$ [3]. Note that as the size of the semimajor axis, a, is increased the oblateness effects decrease. Additionally, at the critical inclinations of approximately 63.4 degrees and 116.6 degrees, there is no advance of perigee. Without an advance of perigee, a satellite's apogee would remain above the same hemisphere for all time.

Some satellite orbits exploit the oblateness effects of the Earth. One example of such an orbit is known as a Tundra orbit. A Tundra orbit is a highly elliptical geosynchronous orbit at a critical inclination, typically 63.4 degrees, with an argument of perigee equal to 270 degrees or 90 degrees [60]. A satellite in a Tundra orbit will complete one period per day, while spending most of its time near apogee above the hemisphere of interest. If the argument of perigee is equal to 270 degrees, the satellite will dwell near apogee above the Northern hemisphere. Alternatively, if the argument of perigee is equal to 90 degrees the satellite will dwell near apogee above the southern hemisphere. In general the argument of perigee will change linearly with time due to the oblateness of the Earth. However, since this Tundra orbit is at a critical inclination, the argument of perigee will remain fixed. A constellation of three Tundra orbits is capable of providing continuous coverage to a desired hemisphere [60]. These highly inclined orbits also provide other advantages. Since the orbits are highly

inclined, coverage of the higher latitudes of Earth is possible. This high-latitude coverage may not be possible from a geostationary satellite. Additionally, insertion into a geostationary orbit requires an inclination change unless the launch site is located on the equator. On the other hand, insertion into a Tundra orbit may not require an inclination change if the launch site is located between the latitudes of 63.4 degrees north and 63.4 degrees south. This lack of inclination change may be desirable for space users that do not have access to a low-latitude launch site.

2.4 Numerical Integration

The 2BP possesses a closed-form analytical solution in terms of conics, so any future state may be described algebraically in terms of the COEs. This closed-form analytical solution circumvents the need for numerical integration. Note that it is still possible to numerically integrate the equations of motion for the 2BP (equation (3)) directly using a numerical integrator. However, some equations of motion, for example, the N-body problem when $N > 2$, do not possess a known closed-form analytical solution. These types of systems require numerical integration to predict a future state based on an initial state. Cowell and Cromellin showcased the ability to accurately numerically integrate the trajectory of a comet by predicting the 1910 return of Halley's comet [3]. This type of direct numerical integration provides a particular solution and is known as Cowell's method [9].

Since numerical integration is a numerical process, error is present. Local round-off error is the total round-off error gained during one integration step [61]. This round-off error occurs because of the imprecision of the machine used to perform the numerical integration. The only method to decrease this type of error is to increase the precision of each arithmetic operation. For example, a single-precision operation is accurate to about 7 decimal places, while a double-precision operation is accurate to about

15 decimal places. Round-off error is only dependent on the number of arithmetical operations and the precision of the machine, so the numerical integrator does not directly affect the local round-off error. However, the other type of error present with a numerical integrator, known as local truncation error, is dependent upon the numerical integration method. The local truncation error is the error caused by the truncation of an infinite series. This quantity varies depending on the method chosen, and accuracy may be increased by truncating the series after more calculations; however, this method may result in additional round-off error. As a numerical integration is performed, the local round-off errors and local truncation errors accumulate into the global round-off error and global truncation error. The sum of these global errors is the total global error. If a machine existed that was able to perform each operation with infinite precision without the need to truncate an infinite series, the ''true'' solution may be found. However, this process would also require infinite compute time [61]. Instead, errors must be accepted and accounted for. This reality is especially troublesome in systems that possess chaotic regions of the phase space, such as the CR3BP, where small errors in the initial state may lead to large errors in the final state. Accordingly, because of the accumulation of global errors, short term integrations may be accurate, but as the time interval increases, the accuracy of the numerical integration will deteriorate. This loss of accuracy is present in the numerical integration of all systems, not just chaotic systems.

The current investigation performs numerical integrations using MATLAB® [38]. Specifically, the built-in MATLAB® function *ode45* is employed to numerically integrate trajectories modeled in the CR3BP [62]. This function is an explicit Runge-Kutta code that utilizes a Dormand-Prince (4,5) pair [63]. A Runge-Kutta method takes multiple steps forward in the integration and averages the slopes of each step [64]. Then, the method steps forward to the next point in the integration using

the average slope [64]. An absolute and relative integration error tolerance is chosen to be 2.22045×10^{-14} for all numerical integrations in the current investigation. This tolerance is the smallest quantity *ode45* will tolerate and corresponds to position and velocity errors in the Earth-Moon CR3BP of 0.0085 mm and 2.275×10^{-8} mm/s, respectively.

2.5 The Circular Restricted Three-Body Problem

When $N = 3$, the N-body problem possesses no known closed-form analytical solution. In order for such a solution to exist, 18 integrals of the motion would be required, but only 10 are present. One variant of the three-body problem is known as the CR3BP. The CR3BP was first introduced by Euler and Lagrange in 1772 [15, 45]. The CR3BP is based on three basic assumptions [15].

1. Each of the three bodies possess spherically symmetric gravity fields.
2. The mass of P_3 is negligible relative to the masses of P_1 and P_2 ($m_3 \ll m_1$ *and* m_2).
3. The primaries, P_1 and P_2, are in circular orbits about their common barycenter and about each other.

The first assumption allows for each of the bodies to be modeled as point masses [40]. The second assumption requires the mass of P_3 to be much less than the masses of P_1 and P_2. This assumption allows the motion of P_1 and P_2 to be modeled according to the 2BP. Thus, the motion of P_1 and P_2 may be described in terms of conic sections. This assumption may be a valid approximation in many applications of astrodynamics. For example, the motion of the Moon may be modeled in the Sun-Earth CR3BP, the motion of a comet may be modeled in the Sun-Jupiter system, and the motion of a spacecraft in the Earth-Moon vicinity may be modeled in the Earth-Moon CR3BP. In

all three cases, the mass of the third body has a negligible gravitational effect on the motion of the primaries. Finally, the third assumption requires the primaries to be in circular orbits about their common barycenter. This third assumption is the defining assumption of the CR3BP; however, other variants exist. For example, the elliptical restricted three-body problem models the motion of the primaries as ellipses about their common barycenter [15].

2.6 The Equations of Motion of the CR3BP

The purpose of the CR3BP is to model the motion of the third body [15]. Since the primaries' motions are described in terms of the 2BP, their motion is known for all of time. To describe the motion of the third body, the equations of motion for P_3 are first described in the inertial frame with Newton's Law of Universal Gravitation. Figure 6 shows the three bodies in an inertial frame with the barycenter of the primaries located at the origin. It is defined that the mass of P_1 is greater than or equal to the mass of P_2. The inertial frame is then defined such that the motion of the primaries remains in the $\hat{i} - \hat{j}$ plane. In other words, the angular momentum vector, describing the motion of the primaries is parallel to the $\hat{k}$-axis. Note that the motion of P_3 is, in general, not constrained to the $\hat{i} - \hat{j}$ plane. The equations of motion for P_3 are then described by equation (2) when $N = 3$. Also, note that in the current investigation derivatives taken with respect to dimensional time are denoted as $\vec{p}\,'$, as seen in equation (17). Additionally, the dimensional universal gravitational constant is defined as $\tilde{G}$.

$$m_3\ {}^I\vec{p}\,'' = -\frac{\tilde{G}m_1m_3}{D^3}\vec{D} - \frac{\tilde{G}m_2m_3}{R^3}\vec{R} \tag{17}$$

Next, a barycentric rotating frame is introduced to describe the motion of P_3. This rotating frame was first introduced by Euler in 1772 [45]. The $\hat{x}$-axis of this rotating

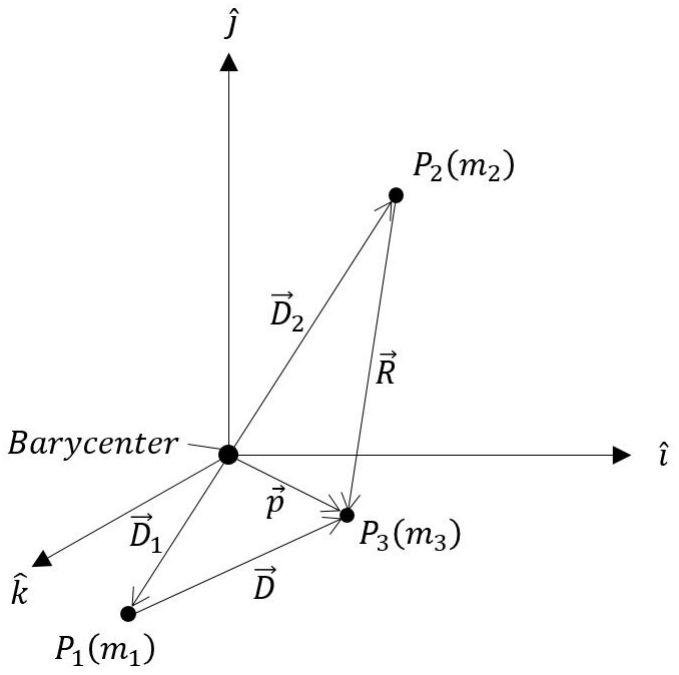

Figure 6. The CR3BP in a Barycentric Inertial Frame

frame is defined to be parallel to $\vec{D}_2$, so this axis points from the larger primary (P_1) to the smaller primary (P_2). This axis is sometimes referred to as the line of syzygy [65]. Then, the $\hat{z}$-axis of the rotating frame is defined to be parallel to the $\hat{k}$-axis of the inertial frame. Finally, the $\hat{y}$-axis is defined such that it completes the right hand rule with the $\hat{x}$ and $\hat{z}$ axes. The rotating frame rotates with respect to the inertial frame with the angular frequency N, the mean motion of the primaries as defined by equation (11). The angle between the $\hat{\imath}$-axis and the $\hat{x}$-axis is defined as θ, where $\theta = Nt$. This relationship implies that the frames are aligned when $t = 0$ or t is a multiple of 2π. The relationship between the barycentric inertial frame and the rotating frame is seen in Figure 7. The inertial time derivative of $\vec{p}$ may be computed using time derivatives of $\vec{p}$ in the rotating frame by employing the transport theorem described in equation (18) where $\vec{\omega}^{RI}$ is the angular velocity vector of a rotating frame, R, with respect to an inertial frame, I [9].

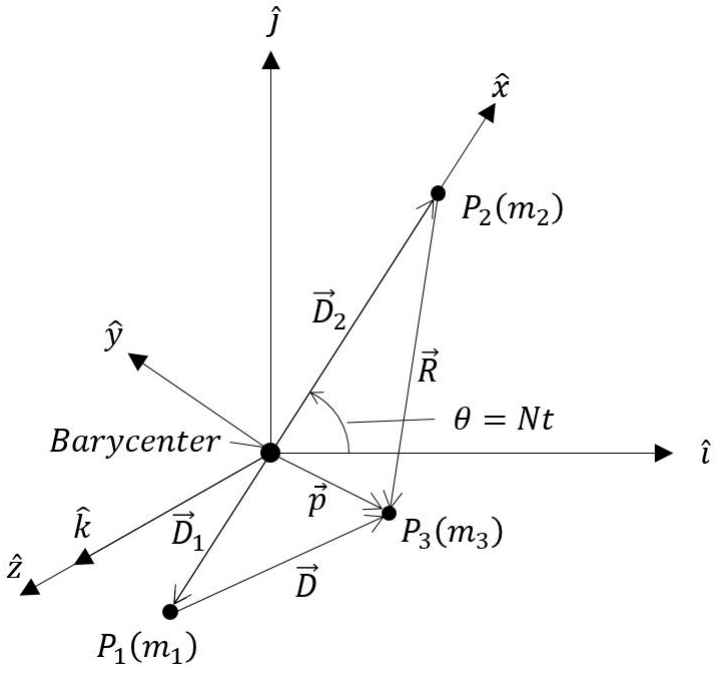

Figure 7. The Relationship Between the Barycentric Inertial Frame and the Barycentric Rotating Frame

$$ {}^{I}\frac{d}{dt}(\ ) = {}^{R}\frac{d}{dt}(\ ) + \vec{\omega}^{RI} \times (\ ) \tag{18} $$

This transport theorem may then be applied to relate the first derivative of $\vec{p}$ in the inertial and rotating frames.

$$ {}^{I}\vec{p}\,' = {}^{R}\vec{p}\,' + \vec{\omega}^{RI} \times \vec{p} \tag{19} $$

Likewise, the second derivatives in the inertial and rotating frames may be related through a second utilization of the transport theorem.

$$ {}^{I}\vec{p}\,'' = {}^{R}\vec{p}\,'' + 2\vec{\omega}^{RI} \times {}^{R}\vec{p}\,' + \vec{\omega}'^{RI} \times \vec{p} + \vec{\omega}^{RI} \times \vec{\omega}^{RI} \times \vec{p} \tag{20} $$

Equations (17)-(20) may be combined, resulting in equation (21).

$$m_3 \left({}^{R}\vec{p}\,'' + 2\vec{\omega}^{RI}\times {}^{R}\vec{p}\,' + \vec{\omega}'^{RI}\times\vec{p} + \vec{\omega}^{RI}\times\vec{\omega}^{RI}\times\vec{p} \right) = -\frac{\tilde{G}m_1 m_3}{D^3}\vec{D} - \frac{\tilde{G}m_2 m_3}{R^3}\vec{R} \quad (21)$$

However, since $\vec{\omega}^{RI}$ describes the angular of velocity of the rotating frame with respect to the inertial frame, $\vec{\omega}'^{RI} = 0$, because the mean motion of the primaries is constant in the CR3BP. Additionally, since m_3 is a scalar multiplier on both sides of the equation and the mass of the third primary is not zero, both sides of equation (21) may be divided by this mass. Accordingly, equation (21) may be reformulated as equation (22).

$${}^{R}\vec{p}\,'' = -2\vec{\omega}^{RI}\times {}^{R}\vec{p}\,' - \vec{\omega}^{RI}\times\vec{\omega}^{RI}\times\vec{p} - \frac{\tilde{G}m_1 m_3}{D^3}\vec{D} - \frac{\tilde{G}m_2 m_3}{R^3}\vec{R} \quad (22)$$

The vector $\vec{p}$ is now expressed in terms of its components in the rotating frame.

$$\vec{p} = X\hat{x} + Y\hat{y} + Z\hat{z} \quad (23)$$

And the angular velocity vector is expressed in terms of the mean motion of the primaries, N.

$$\vec{\omega}^{RI} = N\hat{z} = \sqrt{\frac{\tilde{G}(m_1 + m_2)}{a^3}}\hat{z} \quad (24)$$

where a is the semimajor axis of the motion of the primaries and, equivalently, the distance from P_1 to P_2. Next, the cross products in equation (22) are performed.

$$\vec{\omega}^{RI}\times {}^{R}\vec{p}\,' = N\hat{z}\times(X'\hat{x} + Y'\hat{y} + Z'\hat{z}) = N\left(-Y'\hat{x} + X'\hat{y}\right) \quad (25)$$

and

$$\vec{\omega}^{RI}\times\vec{\omega}^{RI}\times\vec{p} = N\hat{z}\times N\hat{z}\times(X\hat{x} + Y\hat{y} + Z\hat{z}) = N^2\left(-X\hat{x} - Y\hat{y}\right) \quad (26)$$

Then, these results are substituted into equation (22).

$$ {}^{R}\vec{p}'' = -2N\left(-Y'\hat{x} + X'\hat{y}\right) - N^2\left(-X\hat{x} - Y\hat{y}\right) - \frac{\tilde{G}m_1m_3}{D^3}\vec{D} - \frac{\tilde{G}m_2m_3}{R^3}\vec{R} \tag{27} $$

Also, recall from Figure 7 that $\vec{R} = \vec{p} - \vec{D}_2 = (X - D_2)\hat{x} + Y\hat{y} + Z\hat{z}$ and $\vec{D} = \vec{p} - \vec{D}_1 = (X - D_1)\hat{x} + Y\hat{y} + Z\hat{z}$. The three scalar, dimensional, second-order equations of motion for P_3 in the CR3BP may now be written in the rotating frame.

$$ X'' = 2NY' + N^2X - \frac{\tilde{G}m_1}{D^3}(X + D_1) - \frac{\tilde{G}m_2}{R^3}(X - D_2) \tag{28} $$

$$ Y'' = -2NX' + N^2Y - \frac{\tilde{G}m_1}{D^3}Y - \frac{\tilde{G}m_2}{R^3}Y \tag{29} $$

$$ Z'' = -\frac{\tilde{G}m_1}{D^3}Z - \frac{\tilde{G}m_2}{R^3}Z \tag{30} $$

where $D = \sqrt{(X + D_1)^2 + Y^2 + Z^2}$ and $R = \sqrt{(X - D_2)^2 + Y^2 + Z^2}$.

2.7 Nondimensional Equations of Motion

In numerical processes, it is often convenient to scale equations of motion such that each of the states is on the same order of magnitude [66]. In astrodynamics, the states of interest are often orders of magnitude apart. For example, a satellite in a geostationary orbit has an altitude of approximately 35,786 km but a velocity of approximately 3.075 km/s [8]. These differences in magnitude may lead to poorly scaled problems [66]. This poor scaling may hinder the ability for numerical algorithms to converge [66]. Additionally, the nondimensionalization of the equations of motion allows for comparisons and insights between different systems. For example, two different CR3BP systems may be orders of magnitude apart in dimensional units but comparable in nondimensional units.

In the CR3BP, characteristic quantities for length, mass, and time (l^*, m^*, and t^*, respectively) are chosen to nondimensionalize the equations of motion. The characteristic length is chosen to be the distance between the primaries, $l^* = D_1 + D_2$. The characteristic length is also equal to the semimajor axis of the motion of the primaries. The characteristic mass is the system mass, $m^* = m_1 + m_2$. And the characteristic time unit is selected such that the primaries complete one revolution about their common barycenter in $2\pi t^*$ time units. In other words, the characteristic time quantity is the amount of time it takes the primaries to travel one radian about their common barycenter, which is equal to the inverse of their dimensional mean motion, N. These characteristic quantities are defined in Table 1, and values of the quantities are listed for the Earth-Moon system. The nondimensional period of the

Table 1. Characteristic Quantities of the CR3BP

Quantity	Symbol	Definition	Earth-Moon System
length	l^*	$D_1 + D_2$	$384,400$ km
mass	m^*	$m_1 + m_2$	$6.04582568497830324 \times 10^{24}$ kg
time	t^*	$\frac{1}{N}$	4.342479844022600 days

primaries, P, may be found by dividing the dimensional period, which was previously defined as $2\pi t^*$ time units, by the characteristic time quantity.

$$P = \frac{2\pi t^*}{t^*} = 2\pi \ nondimensional \ units \tag{31}$$

Since the nondimensional period of the primaries is 2π nondimensional time units, the nondimensional mean motion, n, is equal to one nondimensional unit. The equation for n is described in equation (32) in terms of the nondimensional universal gravitational constant, G, where $G = \frac{\tilde{G} m^* t^{*2}}{l^{*3}}$.

$$n = 1 = Nt^* = \sqrt{\frac{\tilde{G}m^*t^{*2}}{l^{*3}}} = \sqrt{G} \tag{32}$$

So, the nondimensional universal gravitational constant is equal to one nondimensional unit, based on the chosen characteristic quantities. Additionally, a mass ratio is defined as $\mu = \frac{m_2}{m_1+m_2}$. For the Earth-Moon system, the current investigation assumes a mass ratio equal to 0.012150586550569 nondimensional units. Note that this μ is different than the gravitational parameter, μ, defined in the formulation of the 2BP. The μ defined in the CR3BP is nondimensional and varies between 0 and 0.5.

Each of the dimensional quantities in the three scalar, dimensional, second-order, differential equations of motion described in equations (28)-(30) may then be nondimensionalized using the characteristic quantities. Note that dimensional time is denoted as t, while nondimensional time is denoted as τ.

$$\begin{array}{cccc}
x = \frac{X}{l^*} & y = \frac{Y}{l^*} & z = \frac{Z}{l^*} & \tau = \frac{t}{t^*} \\
\dot{x} = \frac{X't^*}{l^*} & \dot{y} = \frac{Y't^*}{l^*} & \dot{z} = \frac{Z't^*}{l^*} & n = Nt^* \\
\ddot{x} = \frac{X''t^{*2}}{l^*} & \ddot{y} = \frac{Y''t^{*2}}{l^*} & \ddot{z} = \frac{Z''t^{*2}}{l^*} & G = 1 \\
d = \frac{D}{l^*} & r = \frac{R}{l^*} & (1-\mu) = \frac{m_1}{m^*} & \mu = \frac{m_2}{m^*} \\
 & \mu = \frac{D_1}{l^*} & (1-\mu) = \frac{D_2}{l^*} &
\end{array} \tag{33}$$

For clarity, Figure 8 describes the barycentric rotating frame in terms of the nondimensional quantities where the nondimensional position of P_3 in this frame is described by $\vec{\rho} = x\hat{x} + y\hat{y} + z\hat{z}$.

The equations of motion may then be nondimensionalized by the characteristic quantities to yield the scalar, nondimensional, second-order equations of motion for P_3 (equations (34)-(36)).

$$\ddot{x} = 2\dot{y} + x - \frac{(1-\mu)(x+\mu)}{d^3} - \frac{\mu(x-1+\mu)}{r^3} \tag{34}$$

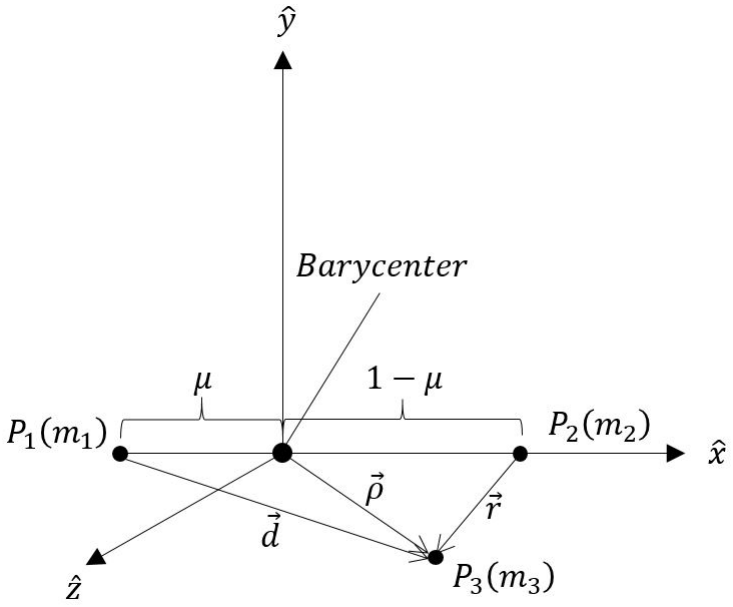

Figure 8. The Barycentric Rotating Frame

$$\ddot{y} = -2\dot{x} + y - \frac{(1-\mu)y}{d^3} - \frac{\mu y}{r^3} \tag{35}$$

$$\ddot{z} = -\frac{(1-\mu)z}{d^3} - \frac{\mu z}{r^3} \tag{36}$$

where $d = \sqrt{(x+\mu)^2 + y^2 + z^2}$ and $r = \sqrt{(x-1+\mu)^2 + y^2 + z^2}$. Also, note that the equations of motion are dependent on the mass ratio, μ. This parameter is dependent on the system, so different types of solutions exist depending on the value of the parameter of various systems. Additionally, the motion of P_3 is, in general, three-dimensional. However, if the motion of P_3 begins in the plane of the primaries, $z = 0$, with $\dot{z} = 0$, then $\ddot{z} = 0$ and the motion of P_3 will remain in the plane of the primaries for all finite time, unless an external force is applied. When P_3 remains in the plane of the primaries, the CR3BP may be referred to as the planar CR3BP. However, when P_3 leaves the plane of the primaries, the CR3BP may be referred to as the spatial CR3BP. Another feature of the nondimensional equations of motion for the CR3BP is that time does not explicitly appear in the equations of motion. This feature implies that the system is autonomous, which means that solutions are

not dependent on their start time [67]. This time invariance may be exploited when designing trajectories with the CR3BP because an epoch time may not need to be defined prior to the design of a trajectory. Alternatively, these equations of motion may be described in terms of a pseudopotential U^* as seen in equations (37)-(40).

$$U^* = \frac{1-\mu}{d} + \frac{\mu}{r} + \frac{1}{2}(x^2 + y^2) \tag{37}$$

$$\ddot{x} = 2\dot{y} + \frac{\partial U^*}{\partial x} = 2\dot{y} + U_x^* \tag{38}$$

$$\ddot{y} = -2\dot{x} + \frac{\partial U^*}{\partial y} = -2\dot{x} + U_y^* \tag{39}$$

$$\ddot{z} = \frac{\partial U^*}{\partial z} = U_z^* \tag{40}$$

where $U_x^* = \frac{\partial U^*}{\partial x}$, $U_y^* = \frac{\partial U^*}{\partial y}$, and $U_z^* = \frac{\partial U^*}{\partial z}$.

2.8 Coordinate Transformations between the Barycentric Rotating Frame and an Earth-Centered Inertial Frame

Once a solution is numerically integrated in the CR3BP, it may be beneficial to observe the trajectory from a primary-centered inertial frame. Specifically, the current investigation is concerned with observing trajectories in an Earth-centered inertial frame. First, using Figure 7 as a reference, a rotation matrix, R, is defined to transform a position vector with components defined in the rotating frame, $\vec{a}_{\hat{x}\hat{y}\hat{z}} = [a_x, a_y, a_z]^T$, to a position vector with components defined in a barycentric inertial frame, $\vec{a}_{\hat{i}\hat{j}\hat{k}} = [a_i, a_j, a_k]^T$ [68]. This development follows the description provided by Haapala as well as Wilmer [14, 26].

$$\vec{a}_{\hat{i}\hat{j}\hat{k}} = \begin{Bmatrix} a_i \\ a_j \\ a_k \end{Bmatrix} = R\vec{a}_{\hat{x}\hat{y}\hat{z}} = \begin{bmatrix} cos(t) & -sin(t) & 0 \\ sin(t) & cos(t) & 0 \\ 0 & 0 & 1 \end{bmatrix} \begin{Bmatrix} a_x \\ a_y \\ a_z \end{Bmatrix} \tag{41}$$

Then, the time derivative of equation (41) is taken with respect to nondimensional time using the product rule.

$$\begin{Bmatrix} \dot{a}_i \\ \dot{a}_j \\ \dot{a}_k \end{Bmatrix} = \dot{R} \begin{Bmatrix} a_x \\ a_y \\ a_z \end{Bmatrix} + R \begin{Bmatrix} \dot{a}_x \\ \dot{a}_y \\ \dot{a}_z \end{Bmatrix} \tag{42}$$

where $\dot{R}$ is defined in equation (43).

$$\dot{R} = \begin{bmatrix} -sin(t) & -cos(t) & 0 \\ cos(t) & -sin(t) & 0 \\ 0 & 0 & 0 \end{bmatrix} \tag{43}$$

Finally, equation (44) may be defined as the combination of equations (41)-(43) to transform a state vector containing position and velocity from the barycentric rotating frame to a barycentric inertial frame.

$$\begin{Bmatrix} a_i \\ a_j \\ a_k \\ \dot{a}_i \\ \dot{a}_j \\ \dot{a}_k \end{Bmatrix} = \begin{bmatrix} cos(t) & -sin(t) & 0 & 0 & 0 & 0 \\ sin(t) & cos(t) & 0 & 0 & 0 & 0 \\ 0 & 0 & 1 & 0 & 0 & 0 \\ -sin(t) & -cos(t) & 0 & cos(t) & -sin(t) & 0 \\ cos(t) & -sin(t) & 0 & sin(t) & cos(t) & 0 \\ 0 & 0 & 0 & 0 & 0 & 1 \end{bmatrix} \begin{Bmatrix} a_x \\ a_y \\ a_z \\ \dot{a}_x \\ \dot{a}_y \\ \dot{a}_z \end{Bmatrix} \tag{44}$$

In order to perform a transformation from a barycentric rotating frame to a Earth-centered inertial frame in the Earth-Moon system, a translation of the origin is needed prior to the rotation. To perform this translation, the mass ratio is summed with the x-component of $\vec{a}$. Then, the rotation may be performed. This relationship is described in equation (45), which transforms a state vector from the barycentric rotating frame to an Earth-centered inertial frame in the Earth-Moon system.

$$\begin{Bmatrix} a_i \\ a_j \\ a_k \\ \dot{a}_i \\ \dot{a}_j \\ \dot{a}_k \end{Bmatrix} = \begin{bmatrix} cos(t) & -sin(t) & 0 & 0 & 0 & 0 \\ sin(t) & cos(t) & 0 & 0 & 0 & 0 \\ 0 & 0 & 1 & 0 & 0 & 0 \\ -sin(t) & -cos(t) & 0 & cos(t) & -sin(t) & 0 \\ cos(t) & -sin(t) & 0 & sin(t) & cos(t) & 0 \\ 0 & 0 & 0 & 0 & 0 & 1 \end{bmatrix} \begin{Bmatrix} a_x + \mu \\ a_y \\ a_z \\ \dot{a}_x \\ \dot{a}_y \\ \dot{a}_z \end{Bmatrix} \tag{45}$$

Additionally, a state vector in an Earth-centered inertial frame may be transformed into the barycentric rotating frame by performing the inverse of equation (45).

2.9 Symmetries in the CR3BP

The equations of motion for the CR3BP in the barycentric rotating frame possess two symmetries. The first of these symmetries is a reflection across the $x-z$ plane and time. This symmetry implies that a numerically integrated solution in the CR3BP, which may be described as $[x(t)\ y(t)\ z(t)\ \dot{x}(t)\ \dot{y}(t)\ \dot{z}(t)]^T$, may be reflected across the $x-z$ plane and time to generate another solution, $[x(-t)\ -y(-t)\ z(-t)\ -\dot{x}(-t)\ \dot{y}(-t)\ -\dot{z}(-t)]^T$ [15]. This symmetry may be exploited to find symmetric periodic orbits in the CR3BP by targeting a trajectory which begins and ends at perpendicular crossings of the $x-z$ plane [69]. This method for computing periodic orbits is explained in further detail in Section 2.17.1.

The other symmetry present in the CR3BP is a reflection across the plane of the primaries. This symmetry may be described through the following transformation $[x(t)\ y(t)\ z(t)\ \dot{x}(t)\ \dot{y}(t)\ \dot{z}(t)]^T \rightarrow [x(t)\ y(t)\ -z(t)\ \dot{x}(t)\ \dot{y}(t)\ -\dot{z}(t)]^T$. This symmetry allows for trajectories to be reflected across the x-y plane to generate ''northern'' and ''southern'' trajectories [19]. However, some trajectories, such as planar orbits and the collinear vertical orbits, may be invariant across this symmetry [70].

2.10 Equilibrium Solutions

The equations of motion of the CR3BP as formulated in the rotating frame yield five equilibrium solutions, known as the Lagrange points or libration points [15]. The three collinear points were discovered by Euler in 1765 prior to Lagrange's discovery of the two equilateral points in 1772 [3, 19, 58]. A spacecraft exactly located at one of these equilibrium points, with no velocity in the rotating frame, would remain stationary in the rotating frame for all of finite time.

In order for equilibrium solutions to exist in a nonlinear system of ordinary differential equations, $\dot{\vec{X}} = f(\vec{X})$, where $\vec{X}$ is the state vector, the first derivatives of the state vector with respect to time must be equal to the zero vector [71]. In the CR3BP, the state vector consists of the positions and velocities of P_3 in the rotating frame. In order for an equilibrium solution in the CR3BP to be found, the first derivatives of each state must be equal to zero as seen in equation (46). Note that in order for an equilibrium solution to be present, according to equation (46), $\dot{z} = 0$ and $\ddot{z} = 0$. These conditions can only be met when $z = 0$, so all five of the Lagrange points lie in the plane of the primaries.

$$\vec{X} = \begin{Bmatrix} x \\ y \\ z \\ \dot{x} \\ \dot{y} \\ \dot{z} \end{Bmatrix} \quad \dot{\vec{X}} = \begin{Bmatrix} \dot{x} \\ \dot{y} \\ \dot{z} \\ \ddot{x} \\ \ddot{y} \\ \ddot{z} \end{Bmatrix} = \vec{0} \tag{46}$$

These requirements for an equilibrium solution may be substituted into the equations of motion in the barycentric rotating frame to show that the condition for an equilibrium point is that the partials of the pseudopotential must be equal to zero, where the pseudopotential is defined in equation (37) [15].

$$\begin{array}{rcll} \ddot{x} = 2\dot{y} + U_x^* & & 0 = U_x^* & \\ \ddot{y} = -2\dot{x} + U_y^* & \rightarrow & 0 = U_y^* & or \quad \vec{\nabla} U^* = \vec{0} \\ \ddot{z} = U_z^* & & 0 = U_z^* & \end{array} \tag{47}$$

The first three points discovered by Euler in 1765 are labeled the collinear points because they are collinear to the primaries in the rotating frame [15, 19, 72]. In other words, the collinear points lie on the line of syzygy [65]. The first of the three collinear Lagrange points, L_1, lies between P_1 and P_2 at a distance γ_1 from P_2. The second point, L_2, lies on the far side of P_2 from P_1 at a distance γ_2 from P_2. And the third point, L_3 lies on the far side of P_1 from P_2 at a distance γ_3 from P_1, as seen in Figure 9 [15, 19]. By definition, in the rotating frame, the collinear Lagrange points require that $y = 0$ and $z = 0$ [15].

The x-coordinates of each of the Lagrange points may be found by examining the partial of the pseudopotential with respect to x, which will be equal to zero at each equilibrium point.

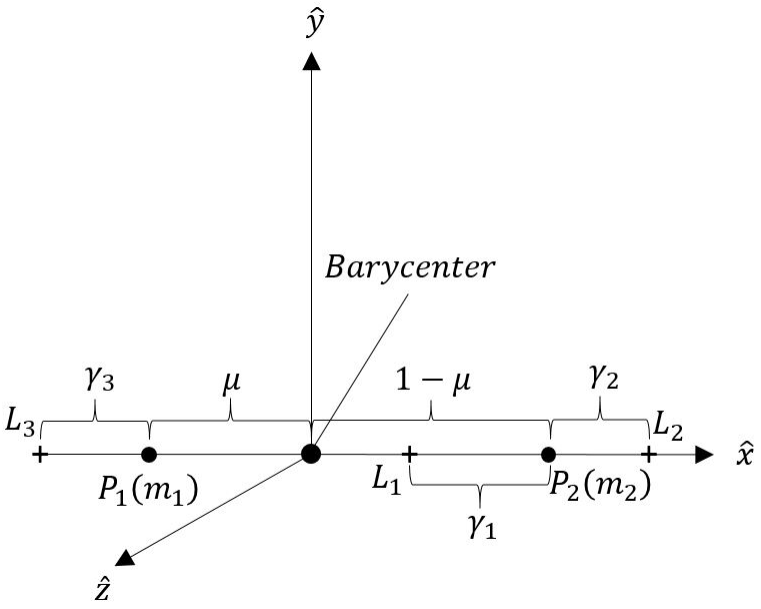

Figure 9. Notional Representation of the Collinear Lagrange Points in the CR3BP

$$U_x^* = 0 = x - \frac{(1-\mu)(x+\mu)}{d^3} - \frac{\mu(x-1+\mu)}{r^3} \tag{48}$$

For the first Lagrange point, the x-coordinate may be defined in terms of γ_1.

$$x_{L_1} = 1 - \mu - \gamma_1 \tag{49}$$

Also, based on Figure 9, d_{L_1} and r_{L_1} may be defined in terms of γ_1.

$$d_{L_1} = 1 - \gamma_1 \quad and \quad r_{L_1} = \gamma_1 \tag{50}$$

Equations (48)-(50) may be combined to yield equation (51).

$$0 = 1 - \mu - \gamma_1 - \frac{1-\mu}{(1-\gamma_1)^2} + \frac{\mu}{\gamma_1^2} = f(\gamma_1) \tag{51}$$

A Newton-Raphson algorithm may now be used to iteratively solve for $f(\gamma_1) = 0$ [73].

$$\gamma_1^{(n+1)} = \gamma_1^{(n)} - \frac{f(\gamma_1)}{f'(\gamma_1)} \tag{52}$$

This algorithm is iterated until a solution has converged within 10^{-15} nondimensional units (3.844×10^{-4} mm). For L_1, an initial guess, $\gamma_1^{(1)}$, is based on the approximate radius of the Hill sphere, r_H, described in equation (53) [68]. The radius of the Hill sphere is the distance from P_2 to L_1 in the CR3BP as $\mu \to 0$.

$$\gamma_1^{(1)} = \left(\frac{\mu}{3}\right)^{1/3} \approx r_H \tag{53}$$

A similar process may be employed to find the other collinear points. Table 2 provides the general methods used to find the location of the collinear points in any system.

Table 2. Collinear Lagrange Points

L_i	$x_{L_i}(\gamma_i)$	d_{L_i}	r_{L_i}	$f(\gamma_i)$	$\gamma_i^{(1)}$
L_1	$1-\mu-\gamma_1$	$1-\gamma_1$	γ_1	$1-\mu-\gamma_1-\frac{1-\mu}{(1-\gamma_1)^2}+\frac{\mu}{\gamma_1^2}$	$\left(\frac{\mu}{3}\right)^{1/3}$
L_2	$1-\mu+\gamma_2$	$1+\gamma_2$	γ_2	$1-\mu+\gamma_2-\frac{1-\mu}{(1+\gamma_2)^2}-\frac{\mu}{\gamma_2^2}$	$\left(\frac{\mu}{3}\right)^{1/3}$
L_3	$-\mu-\gamma_3$	γ_3	$1+\gamma_3$	$-\mu-\gamma_3+\frac{1-\mu}{\gamma_3^2}+\frac{\mu}{(1+\gamma_3)^2}$	$1-\frac{7}{12}\mu$ [68]

The triangular points or equilateral points were first discovered by Lagrange in 1772 [3]. Like the collinear points, these points lie in the plane of the primaries ($z = 0$) but not on the line of syzygy ($y \neq 0$). The equilateral points may be determined analytically by examining the partials of the pseudopotential with respect to x and y. These partials must be equal to zero at an equilibrium point. First, the partial of the pseudopotential with respect to y is examined in equation (54).

$$U_y^* = y - \frac{(1-\mu)y}{d^3} - \frac{\mu y}{r^3} = y\left(1 - \frac{1-\mu}{d^3} - \frac{\mu}{r^3}\right) \tag{54}$$

For an equilateral point, $y \neq 0$, so equation (55) must be satisfied at an equilateral point.

$$1 - \frac{1-\mu}{d^3} - \frac{\mu}{r^3} = 0 \tag{55}$$

Next, equation (48) is expanded as seen in equation (56).

$$0 = x - \frac{(1-\mu)(x+\mu)}{d^3} - \frac{\mu(x-1+\mu)}{r^3} = x - \frac{x - x\mu + \mu - \mu^2}{d^3} - \frac{x\mu - \mu + \mu^2}{r^3} \tag{56}$$

Then, equation (56) may be rearranged to the form shown in equation (57).

$$\frac{\mu - \mu^2}{d^3} + \frac{\mu^2 - \mu}{r^3} = x\left(1 - \frac{1-\mu}{d^3} - \frac{\mu}{r^3}\right) \tag{57}$$

Finally, equation (55) may be substituted into equation (57) to cancel out the right side of equation (57). The resulting equation is rearranged and shown in equation (58).

$$\frac{\mu(1-\mu)}{d^3} = \frac{\mu(1-\mu)}{r^3} \tag{58}$$

For any nonzero and nonunity mass ratio, equation (58) results in the solution $d = r$ at the locations of the equilateral points. This condition is true for any two finite, nonzero primary masses. By setting $d = r$ with $z = 0$, it may be seen that $x_{L_4,L_5} = \frac{1}{2} - \mu$ and $y_{L_4,L_5} = \pm\frac{\sqrt{3}}{2}$ [15]. Note that the L_4 and L_5 points each serve as a vertex of an equilateral triangle with the two primaries located at the other two vertices [74]. Figure 10 and Table 3 show the locations of the Lagrange points in the Earth-Moon system.

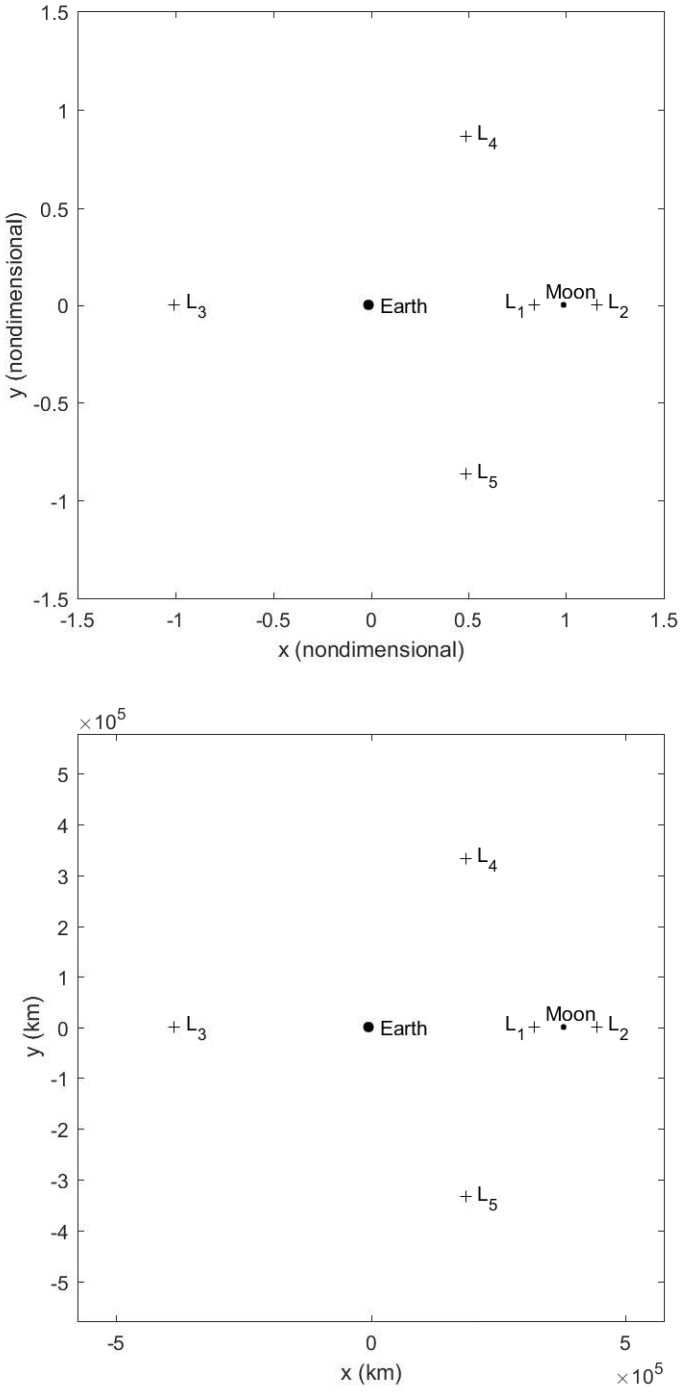

Figure 10. The Lagrange Points of the Earth-Moon CR3BP (Top: Displayed in Nondimensional Distance Units; Bottom: Displayed in Kilometers)

Table 3. The Locations of the Earth-Moon Lagrange Points in the Barycentric Rotating Frame

Lagrange Point	x-coordinate	y-coordinate	Units
L_1	0.836915121142417	0	Nondimensional
	321710.1725671450	0	Kilometers
L_2	1.155682169063842	0	Nondimensional
	444244.2257881407	0	Kilometers
L_3	-1.005062646202315	0	Nondimensional
	-386346.0812001700	0	Kilometers
L_4	0.487849413449431	0.866025403784439	Nondimensional
	187529.3145299614	332900.1652147382	Kilometers
L_5	0.487849413449431	-0.866025403784439	Nondimensional
	187529.3145299614	-332900.1652147382	Kilometers

2.11 The Integral of the Motion

The three second-order equations of motion of the CR3BP imply a six-dimensional phase space. In order for a closed-form analytical solution to exist for this system, six integrals of the motion must exist [75]. However, in the CR3BP only one known integral of the motion exists, the Jacobi Constant [3, 9, 15, 68]. The Jacobi Constant was first discovered by Jacobi in 1836 [15, 45]. This integral of the motion may be derived by analyzing the equations of motion in terms of the pseudopotential as seen in equations (38)-(40).

The dot product of the velocity vector and the acceleration vector of P_3 in the rotating frame may be performed.

$$\dot{\vec{r}} \cdot \ddot{\vec{r}} = \dot{x}\ddot{x} + \dot{y}\ddot{y} + \dot{z}\ddot{z} = \dot{x}U_x^* + \dot{y}U_y^* + \dot{z}U_z^* \tag{59}$$

Now it may be recognized that both sides of the above equation represent the time derivative of separate quantities.

$$\frac{1}{2}\frac{d}{dt}\left(\dot{x}^2+\dot{y}^2+\dot{z}^2\right)=\dot{x}\ddot{x}+\dot{y}\ddot{y}+\dot{z}\ddot{z}=\dot{x}U_x^*+\dot{y}U_y^*+\dot{z}U_z^*=\frac{dU^*}{dt} \tag{60}$$

Equation (60) may be rearranged to show a conserved quantity, $U^*-\frac{1}{2}v^2$, where $v^2=\dot{x}^2+\dot{y}^2+\dot{z}^2$. Thus, v is the speed of the spacecraft relative to the rotating frame.

$$\frac{d}{dt}\left(U^*-\frac{1}{2}v^2\right)=0 \tag{61}$$

The Jacobi Constant, JC, is then defined in equation (62) to be a scalar multiple of the conserved quantity [15]. The Jacobi Constant is an ''energy''-like quantity; however, this integral of the motion is not equal to the total mechanical energy of a spacecraft's trajectory.

$$JC=2U^*-v^2 \tag{62}$$

It is important to note that, as the ''energy'' level of the system increases, the value of the Jacobi Constant decreases. This relationship means that a large value of the Jacobi Constant corresponds to a low ''energy''-level trajectory, while a lesser value of the Jacobi Constant corresponds to a higher ''energy''-level trajectory. Table 4 shows the values of the Jacobi Constant associated with each of the Lagrange points in the Earth-Moon CR3BP.

In lieu of an analytical solution, a useful method to track the accuracy of an integration is to track the value of the Jacobi Constant throughout the numerical integration. The true trajectory would conserve the value of the Jacobi Constant. However, numerical integration will cause the value of the Jacobi Constant to change throughout the numerical integration due to the accumulation of error. This metric may provide an indication of how representative the numerical integration is of the

Table 4. The Values of the Jacobi Constant Associated with each of the Lagrange Points in the Earth-Moon CR3BP

Lagrange Point (L_i)	The Value of the Jacobi Constant (JC_{L_i})
L_1	$JC_{L_1} = 3.188341126426104$
L_2	$JC_{L_2} = 3.172160468395109$
L_3	$JC_{L_3} = 3.012147151620889$
L_4	$JC_{L_4} = 2.987997050202954$
L_5	$JC_{L_5} = 2.987997050202954$

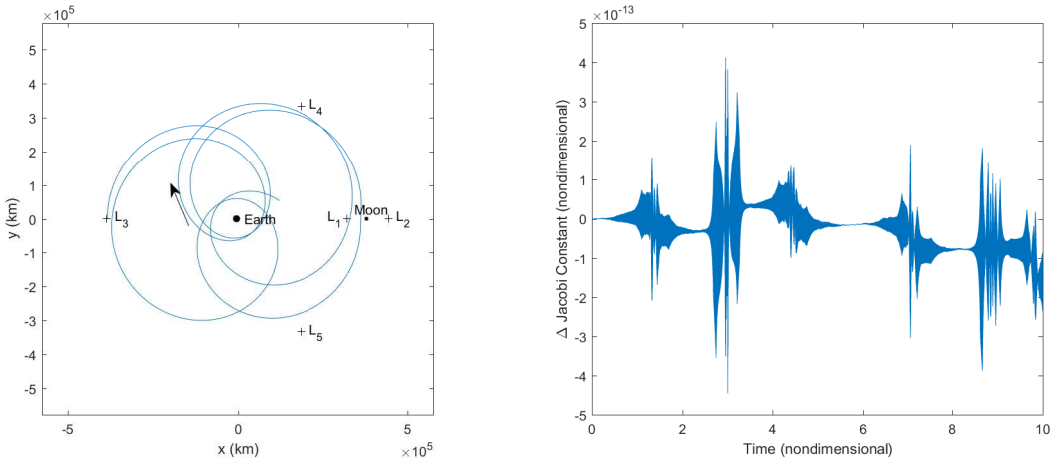

Figure 11. An Example of Tracking the Error in the Value of the Jacobi Constant Throughout a Numerical Integration in the Earth-Moon CR3BP (Left: Trajectory Numerically Integrated for 10 Nondimensional Units—Approximately 43.4 Days; Right: The Change in the Value of the Jacobi Constant During the Numerical Integration)

true behavior of a spacecraft's dynamics. Figure 11 shows a trajectory numerically integrated in the CR3BP, while the error in the value of the Jacobi Constant is tracked.

Figure 11 shows that throughout this trajectory, the value of the Jacobi Constant remains approximately constant: the maximum change in the value of the Jacobi Constant is approximately 4.5×10^{-13} nondimensional units. However, one must also note that the large changes in the value of the Jacobi Constant correspond to close

approaches with one of the primaries. These drastic changes to the value of the Jacobi Constant occur because the center of each primary corresponds to a singularity. Local truncation errors tend to be largest when the trajectory passes near singularities [9,61].

As the length of the numerical integration is increased, the accumulation of error will, in general, also increase due to the accumulation of round-off and truncation errors [61]. Figure 12 shows a trajectory with the same initial conditions as Figure 11, but numerically integrated for 1,000 nondimensional units (about 11.9 years). Due to

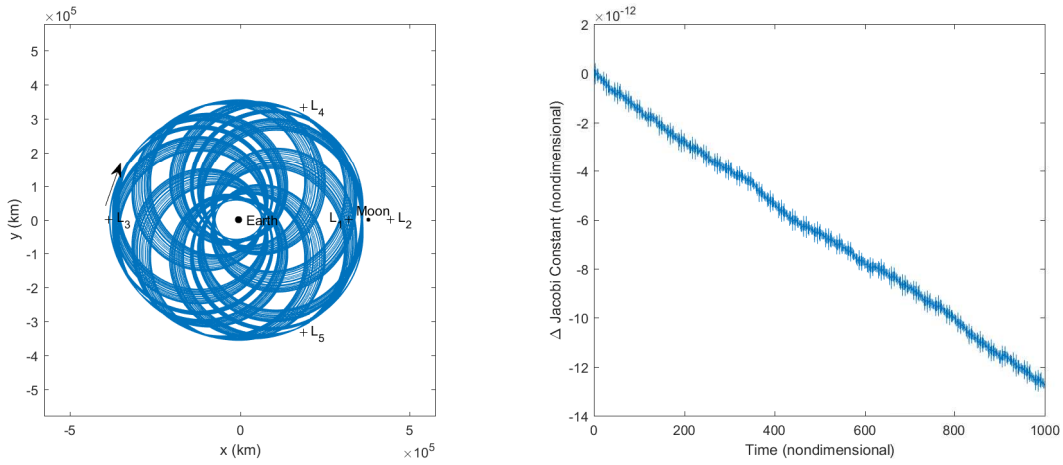

Figure 12. An Example of Tracking the Error in the Value of the Jacobi Constant Throughout a Numerical Integration in the Earth-Moon CR3BP (Left: Trajectory Numerically Integrated for 1,000 Nondimensional Units—Approximately 11.9 Years; Right: The Change in the Value of the Jacobi Constant During the Numerical Integration)

the length of this numerical integration, the error in the value of the Jacobi Constant reached a maximum of approximately 13×10^{-12} nondimensional units. It is also evident, from Figure 12, that the error in the value of Jacobi Constant is trending away from zero as the integration moves through time. One would expect this trend to continue as the length of integration is increased even further.

2.12 Zero Velocity Surfaces

The definition of the Jacobi Constant implies the existence of accessible regions and inaccessible regions separated by zero velocity surfaces (ZVSs) [15]. At a particular value of Jacobi Constant, regions of the configuration space are forbidden (for physical solutions). A trajectory within a forbidden region at a particular value of the Jacobi Constant would require imaginary velocity components, which would be nonphysical. The boundaries between the accessible and inaccessible regions are defined by surfaces in the three-dimensional configuration space with zero velocity in the barycentric rotating frame, based on a particular value of the Jacobi Constant. This property is defined in equation (63).

$$JC = 2U^* \tag{63}$$

Figure 13 provides some examples of ZVSs at varying values of the Jacobi Constant in the Earth-Moon CR3BP.

At the intersection of the ZVSs and the x-y plane, zero velocity curves (ZVCs) may be defined. These curves define the boundary between accessible and inaccessible regions in the planar version of the CR3BP. These ZVCs, Hill curves, or Hill's limiting surfaces, were first defined by Hill in 1878 [68, 74, 76]. Figure 14 shows some examples of ZVCs at varying values of the Jacobi Constant in the Earth-Moon CR3BP. Figures 13 and 14 show that as the value of the Jacobi Constant is decreased (as the ''energy'' level is increased), the configuration space becomes more accessible. When the value of the Jacobi Constant is greater than the value of the Jacobi Constant of L_1, as seen in example (a), L_1 is in the inaccessible region. A trajectory at this value of the Jacobi constant would never be able to access L_1 without a change in the value of the Jacobi Constant. Additionally, at this value of the Jacobi Constant, three separate accessible regions exist: one in the vicinity of the Earth, one in the vicinity of the Moon, and an

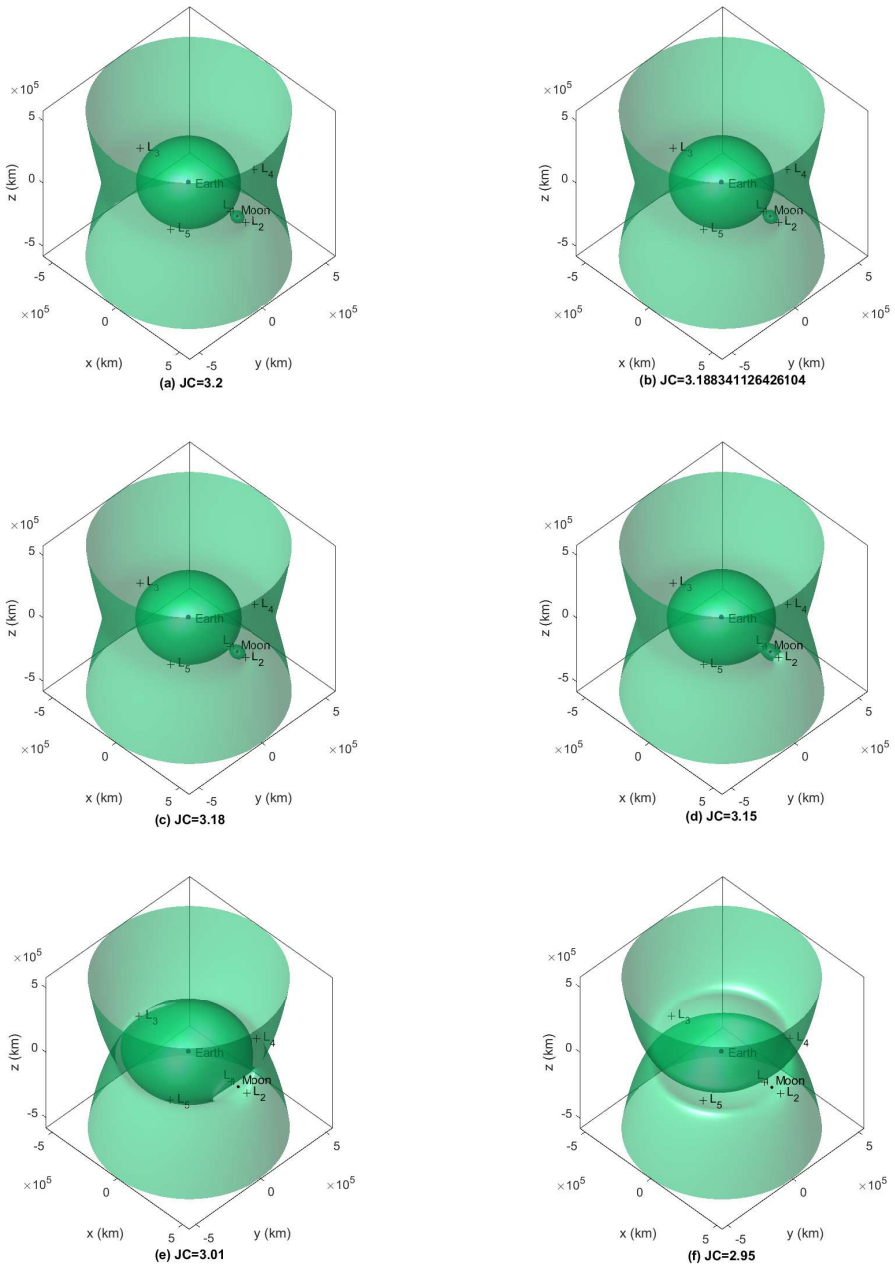

Figure 13. Examples of the ZVSs at Varying Values of the Jacobi Constant in the Earth-Moon Barycentric Frame: (a) $JC = 3.2 > JC_{L_1}$**, (b)** $JC = 3.188341126426104 = JC_{L_1}$**, (c)** $JC = 3.18 < JC_{L_1}$**, (d)** $JC = 3.15 < JC_{L_2}$**, (e)** $JC = 3.01 < JC_{L_3}$**, (f)** $JC = 2.95 < JC_{L_{4,5}}$

exterior region. However, a trajectory at this value of the Jacobi Constant would be unable to travel between the different accessible regions without changing its value of the Jacobi Constant. In example (b), the value of the Jacobi Constant is exactly

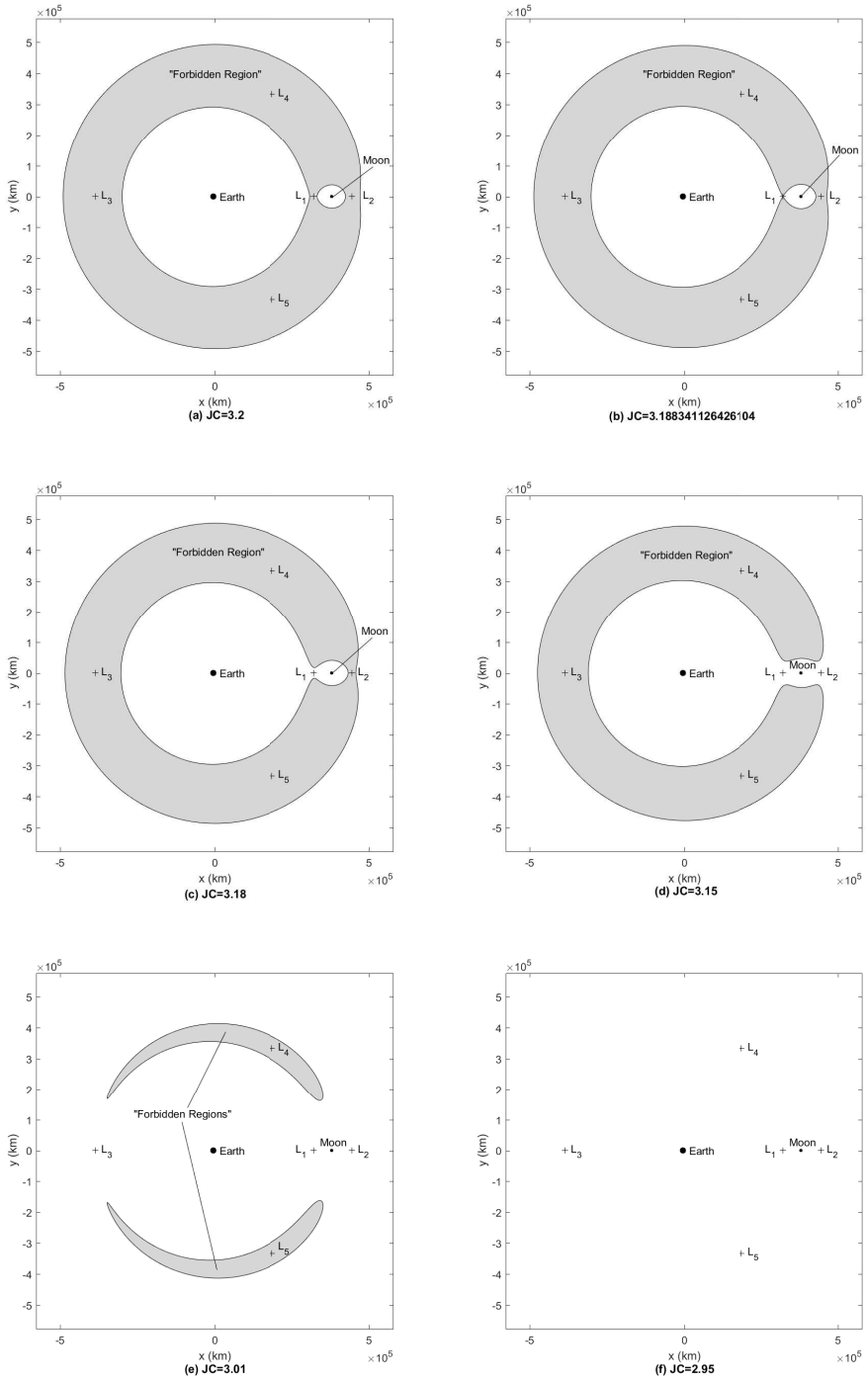

Figure 14. Examples of the ZVCs at Varying Values of the Jacobi Constant in the Earth-Moon Barycentric Frame: (a) $JC = 3.2 > JC_{L_1}$**, (b)** $JC = 3.188341126426104 = JC_{L_1}$**, (c)** $JC = 3.18 < JC_{L_1}$**, (d)** $JC = 3.15 < JC_{L_2}$**, (e)** $JC = 3.01 < JC_{L_3}$**, (f)** $JC = 2.95 < JC_{L_{4,5}}$

the value of the Jacobi Constant associated with L_1. In this example, the Earth and Moon accessible regions have intersected at one point, L_1. In example (c), the value of the Jacobi Constant is less than the value of the Jacobi Constant associated with L_1. The Earth and Moon accessible regions have combined into one accessible region with a gateway between the two regions at L_1. However, a trajectory in this interior region is still unable to transfer to the exterior region without changing its value of the Jacobi Constant. In examples (a)-(c), a trajectory in the Earth-Moon interior region is unable to escape to the exterior region regardless of the integration time. This type of boundedness is known as Hill stability [68]. On the other hand, example (d) shows an example of the ZVSs and ZVCs where the L_2 gateway is open. In this case, transfers from the interior region to the exterior region are possible by passing through the L_2 gateway. Example (e) has a value of the Jacobi Constant that is less than the value of the Jacobi Constant of L_3. This value of the Jacobi Constant opens the gateway at L_3 and allows for transfers between the interior and exterior regions through either the L_2 or L_3 gateway. Finally, example (f) shows the ZVSs for a trajectory with a value of the Jacobi Constant that is less than the value of the Jacobi Constant associated with the equilateral points. In this example, the entire $\hat{x} - \hat{y}$ plane is accessible; however, forbidden regions still exist in the spatial problem as seen in Figure 13. In other words, at this value of the Jacobi Constant, there are no ZVCs but there are ZVSs.

2.13 Stability of the Lagrange Points

In a dynamical system, at an equilibrium point, $\vec{X}_{eq}$, a solution is Lyapunov stable if for any $\varepsilon > 0$ there exists a $\delta > 0$ such that if $||\vec{X}(0) - \vec{X}_{eq}|| < \delta$, then $||\vec{X}(t) - \vec{X}_{eq}(t)|| < \varepsilon$ for all $t > 0$ [77]. Additionally, if $||\vec{X}(t) - \vec{X}_{eq}(t)|| \to 0$ as $t \to \infty$, then the equilibrium point is asymptotically stable [77]. The Lyapunov stability of

the Lagrange points in the CR3BP may be examined through an isochronous linear stability analysis [15]. This analysis is known as Lyapunov's first method [77].

$$X_{eq} = \begin{Bmatrix} x_{eq} \\ y_{eq} \\ z_{eq} \\ \dot{x}_{eq} \\ \dot{y}_{eq} \\ \dot{z}_{eq} \end{Bmatrix} \tag{64}$$

To perform this analysis, first, the nonlinear equations of motion must be linearized to determine the equations of variation. This linearization is accomplished by defining the initial state, $\vec{X}(t)$, as being perturbed from the equilibrium solution, $\vec{X}_{eq}$.

$$\vec{X}(t) = \vec{X}_{eq} + \delta\vec{X}(t) \tag{65}$$

where the perturbation of the state, $\delta\vec{X}(t)$, and its derivative are defined in equation (66).

$$\delta\vec{X}(t) = \begin{Bmatrix} \xi(t) \\ \eta(t) \\ \zeta(t) \\ \dot{\xi}(t) \\ \dot{\eta}(t) \\ \dot{\zeta}(t) \end{Bmatrix} \qquad \delta\dot{\vec{X}}(t) = \begin{Bmatrix} \dot{\xi}(t) \\ \dot{\eta}(t) \\ \dot{\zeta}(t) \\ \ddot{\xi}(t) \\ \ddot{\eta}(t) \\ \ddot{\zeta}(t) \end{Bmatrix} \tag{66}$$

Next, the equations of variation are defined by substituting equation (65) into the equations of motion and expanding in a first-order Taylor series expansion about the equilibrium solution [9, 73].

$$\ddot{x}_{eq}+\ddot{\xi}(t)-2\dot{y}_{eq}-2\dot{\eta} = \left.\frac{\partial U^*}{\partial x}\right|_{\vec{X}_{eq}} + \left.\frac{\partial^2 U^*}{\partial^2 x}\right|_{\vec{X}_{eq}} \xi(t) + \left.\frac{\partial^2 U^*}{\partial x \partial y}\right|_{\vec{X}_{eq}} \eta(t) + \left.\frac{\partial^2 U^*}{\partial x \partial z}\right|_{\vec{X}_{eq}} \zeta(t) \quad (67)$$

$$\ddot{y}_{eq}+\ddot{\eta}(t)+2\dot{x}_{eq}+2\dot{\xi} = \left.\frac{\partial U^*}{\partial y}\right|_{\vec{X}_{eq}} + \left.\frac{\partial^2 U^*}{\partial y \partial x}\right|_{\vec{X}_{eq}} \xi(t) + \left.\frac{\partial^2 U^*}{\partial^2 y}\right|_{\vec{X}_{eq}} \eta(t) + \left.\frac{\partial^2 U^*}{\partial y \partial z}\right|_{\vec{X}_{eq}} \zeta(t) \quad (68)$$

$$\ddot{z}_{eq} + \ddot{\zeta}(t) = \left.\frac{\partial U^*}{\partial z}\right|_{\vec{X}_{eq}} + \left.\frac{\partial^2 U^*}{\partial z \partial x}\right|_{\vec{X}_{eq}} \xi(t) + \left.\frac{\partial^2 U^*}{\partial z \partial y}\right|_{\vec{X}_{eq}} \eta(t) + \left.\frac{\partial^2 U^*}{\partial^2 z}\right|_{\vec{X}_{eq}} \zeta(t) \quad (69)$$

These variational equations of motion are further simplified by substituting in the nonlinear equations of motion evaluated at an equilibrium point. For example, from the nonlinear equations of motion, $\ddot{x} - 2\dot{y} = U_x^*$, so these terms cancel out in equation (67). Similar cancellations are performed in equations (68)-(69). Additionally, it is recognized that $\frac{\partial^2 U^*}{\partial x \partial y}() = \frac{\partial^2 U^*}{\partial y \partial x}()$, $\frac{\partial^2 U^*}{\partial x \partial z}() = \frac{\partial^2 U^*}{\partial z \partial x}()$, and $\frac{\partial^2 U^*}{\partial y \partial z}() = \frac{\partial^2 U^*}{\partial z \partial y}()$ because the mixed partials of U^* are continuous [78]. The resulting simplified variational equations of motion about the equilibrium point are described in equations (70)-(72).

$$\ddot{\xi}(t) - 2\dot{\eta} = \left.\frac{\partial^2 U^*}{\partial^2 x}\right|_{\vec{X}_{eq}} \xi(t) + \left.\frac{\partial^2 U^*}{\partial x \partial y}\right|_{\vec{X}_{eq}} \eta(t) + \left.\frac{\partial^2 U^*}{\partial x \partial z}\right|_{\vec{X}_{eq}} \zeta(t) \quad (70)$$

$$\ddot{\eta}(t) + 2\dot{\xi} = \left.\frac{\partial^2 U^*}{\partial x \partial y}\right|_{\vec{X}_{eq}} \xi(t) + \left.\frac{\partial^2 U^*}{\partial^2 y}\right|_{\vec{X}_{eq}} \eta(t) + \left.\frac{\partial^2 U^*}{\partial y \partial z}\right|_{\vec{X}_{eq}} \zeta(t) \quad (71)$$

$$\ddot{\zeta}(t) = \left.\frac{\partial^2 U^*}{\partial x \partial z}\right|_{\vec{X}_{eq}} \xi(t) + \left.\frac{\partial^2 U^*}{\partial y \partial z}\right|_{\vec{X}_{eq}} \eta(t) + \left.\frac{\partial^2 U^*}{\partial^2 z}\right|_{\vec{X}_{eq}} \zeta(t) \quad (72)$$

The variational equations of motion may now be described in matrix form.

$$\dot{\delta\vec{X}}(t) = \begin{bmatrix} 0 & 0 & 0 & 1 & 0 & 0 \\ 0 & 0 & 0 & 0 & 1 & 0 \\ 0 & 0 & 0 & 0 & 0 & 1 \\ U^*_{xx}|_{\vec{X}_{eq}} & U^*_{xy}\big|_{\vec{X}_{eq}} & U^*_{xz}|_{\vec{X}_{eq}} & 0 & 2 & 0 \\ U^*_{xy}\big|_{\vec{X}_{eq}} & U^*_{yy}\big|_{\vec{X}_{eq}} & U^*_{yz}\big|_{\vec{X}_{eq}} & -2 & 0 & 0 \\ U^*_{xz}|_{\vec{X}_{eq}} & U^*_{yz}\big|_{\vec{X}_{eq}} & U^*_{zz}|_{\vec{X}_{eq}} & 0 & 0 & 0 \end{bmatrix} \delta\vec{X}(t) = A\delta\vec{X}(t) \tag{73}$$

where A is the system matrix [9]. Note that in general $A = A(t)$, but when evaluated at an equilibrium point, the system matrix is constant. Also, since each of the equilibrium points exist in the plane of the primaries where $z_{eq} = 0$ and $\dot{z}_{eq} = 0$, $U^*_{xz}|_{\vec{X}_{eq}} = U^*_{yz}\big|_{\vec{X}_{eq}} = 0$. The variational equations about the equilibrium point may be simplified further as described in equation (74).

$$\dot{\delta\vec{X}}(t) = \begin{bmatrix} 0 & 0 & 0 & 1 & 0 & 0 \\ 0 & 0 & 0 & 0 & 1 & 0 \\ 0 & 0 & 0 & 0 & 0 & 1 \\ U^*_{xx}|_{\vec{X}_{eq}} & U^*_{xy}\big|_{\vec{X}_{eq}} & 0 & 0 & 2 & 0 \\ U^*_{xy}\big|_{\vec{X}_{eq}} & U^*_{yy}\big|_{\vec{X}_{eq}} & 0 & -2 & 0 & 0 \\ 0 & 0 & U^*_{zz}|_{\vec{X}_{eq}} & 0 & 0 & 0 \end{bmatrix} \delta\vec{X}(t) = A\delta\vec{X}(t) \tag{74}$$

Note that the in-plane motion and out-of-plane motion in the vicinity of the equilibrium points is entirely decoupled based on the linearization of the variational equations [15]. In fact, the linearized out-of-plane motion near an equilibrium point is described in equation (75) in the form of a simple harmonic oscillator [15, 71].

$$\ddot{\zeta} = U^*_{zz}|_{\vec{X}_{eq}}\,\zeta \tag{75}$$

The frequency of this harmonic oscillator is $\omega = \sqrt{U^*_{zz}|_{\vec{X}_{eq}}}$ and the period is $T = \frac{2\pi}{|\omega|}$. For all equilibrium points in the CR3BP, $U^*_{zz}|_{\vec{X}_{eq}} < 0$, so each of the equilibrium points is linearly Lyapunov stable to out-of-plane perturbations [15]. This type of oscillatory behavior associated with the equilibrium point is known as a center [67]. However, since the conclusion based on the linear analysis is marginal stability, or center-type behavior, no conclusions may be made about the Lyapunov stability in the nonlinear equations of motion.

2.13.1 Stability of the Collinear Points

Since the equilibrium points in the CR3BP were previously determined to be linearly Lyapunov stable to out-of-plane perturbations, the in-plane variational equations of motion can be considered separately, and are shown in equation (76).

$$\begin{Bmatrix} \dot{\xi} \\ \dot{\eta} \\ \ddot{\xi} \\ \ddot{\eta} \end{Bmatrix} = \begin{bmatrix} 0 & 0 & 1 & 0 \\ 0 & 0 & 0 & 1 \\ U^*_{xx}|_{\vec{X}_{eq}} & U^*_{xy}\big|_{\vec{X}_{eq}} & 0 & 2 \\ U^*_{xy}\big|_{\vec{X}_{eq}} & U^*_{yy}\big|_{\vec{X}_{eq}} & -2 & 0 \end{bmatrix} \begin{Bmatrix} \xi \\ \eta \\ \dot{\xi} \\ \dot{\eta} \end{Bmatrix} \tag{76}$$

Also, for each of the collinear points $y_{eq} = 0$, so $U^*_{xy} = 0$ [15]. The characteristic equation may then be defined [15].

$$\lambda^4 + 2\beta_1\lambda^2 - \beta_2^2 = 0 = \Lambda^2 + 2\beta_1\Lambda - \beta_2^2 \tag{77}$$

where [15],

$$\beta_1 = 2 - \frac{U^*_{xx}|_{\vec{X}_{eq}} + U^*_{yy}\big|_{\vec{X}_{eq}}}{2} \qquad \beta_2 = -\,U^*_{xx}|_{\vec{X}_{eq}}\, U^*_{yy}\big|_{\vec{X}_{eq}} \tag{78}$$

Next, the four roots of characteristic equation may be found using the quadratic formula [15].

$$\lambda_{1,2} = \pm\sqrt{\Lambda_1} = \pm\sqrt{-\beta_1 + \sqrt{\beta_1^2 + \beta_2^2}} \tag{79}$$

$$\lambda_{3,4} = \pm\sqrt{\Lambda_2} = \pm\sqrt{-\beta_1 - \sqrt{\beta_1^2 + \beta_2^2}} \tag{80}$$

The first two roots, λ_1 and λ_2, are real, while the third and fourth roots, λ_3 and λ_4 are imaginary [15]. Because of this, the first pair of roots are associated with a saddle and the second pair of roots are associated with a center [67]. Recall that the out-of-plane motion is also associated with a center [15]. Based on this linear analysis of the Lyapunov stability of the linear system, each of the collinear Lagrange points may be described as a two-dimensional saddle and four-dimensional center based on a linear analysis. Overall, because of the presence of a saddle, the collinear points are Lyapunov unstable based on the linear analysis. Since the collinear points are Lyapunov unstable based on the linear analysis, it is concluded that such equilibrium points are also Lyapunov unstable in the nonlinear equations of motion.

Next, the linearized motion in the vicinity of the collinear points may be described as a solution of the linear variational equations of motion [15].

$$\xi(t) = \sum_{i=1}^{4} A_i e^{\lambda_i t} \tag{81}$$

$$\eta(t) = \sum_{i=1}^{4} B_i e^{\lambda_i t} \tag{82}$$

Additionally, the coefficients A_i and B_i are not independent [15].

$$B_i = \frac{\lambda_i^2 - U_{xx}^*|_{\vec{X}_{eq}}}{2\lambda_i} A_i = \alpha_i A_i \tag{83}$$

Initial conditions may then be carefully chosen to suppress the saddle behavior of the motion in the vicinity of a collinear Lagrange point based on the linear analysis [15]. The resulting in-plane motion will be elliptical and is based on the initial conditions defined in equation (84) for any ξ_0 and η_0 [15].

$$\dot{\xi}_0 = \frac{\eta_0 \lambda_3}{\alpha_3} \quad and \quad \dot{\eta}_0 = \alpha_3 \xi_0 \lambda_3 \tag{84}$$

It is essential to note that these linearized solutions are only valid based on the linear analysis and are not solutions to the nonlinear equations of motion.

2.13.2 Stability of the Equilateral Points

Recall the out-of-plane period for an equilibrium point in the CR3BP is found to be $P = \frac{2\pi}{|\sqrt{U^*_{zz}|_{\vec{X}_{eq}}}|}$ [15]. For the equilateral points, $U^*_{zz}|_{\vec{X}_{eq}} = -1$, so the out-of-plane period in the vicinity of the equilateral points is 2π nondimensional units, the same as the period of the primaries [15]. The in-plane stability of the equilateral points may be examined in a similar manner to the collinear points. The roots of the characteristic equation for the equilateral points are defined in equations (85)-(86) [15].

$$\lambda_{1,2} = \pm\sqrt{\Lambda_1} = \pm\sqrt{\frac{-1 + \sqrt{1 - 27\mu(1-\mu)}}{2}} \tag{85}$$

$$\lambda_{3,4} = \pm\sqrt{\Lambda_2} = \pm\sqrt{\frac{-1 - \sqrt{1 - 27\mu(1-\mu)}}{2}} \tag{86}$$

Then, a parameter, d, may be defined as $d = 1 - 27\mu(1-\mu)$. The stability of the equilateral points is dependent on the sign of d. The sign changes at the critical mass ratio, μ_0, where $\mu_0 = \frac{1-\sqrt{23/27}}{2} = 0.038520896504551$ nondimensional units. If $\mu < \mu_0$, the equilateral points are marginally Lyapunov stable according to the linear analysis and associated with a six-dimensional center [15] [67]. Also, there will, in general, be

three distinct frequencies: a short period frequency, a long period frequency, and an out-of-plane frequency (which is determined to be the frequency of the primaries) [15]. If $\mu > \mu_0$, the equilateral points are unstable based on the linear analysis, which implies that they are also unstable in the nonlinear system [15]. This behavior is associated with a two-dimensional spiral sink, a two-dimensional spiral source, and a two-dimensional center [67]. If $\mu = \mu_0$, the two in-plane frequencies are equivalent and secular terms are present [15]. Under this condition the equilateral point is Lyapunov unstable in the linear and nonlinear system [15]. In many natural systems, such as the Sun-Earth system, the Earth-Moon system, and the Sun-Jupiter system, the mass ratio is less than the critical mass ratio [3]. Because of the Lyapunov stability of the equilateral Lagrange points in such systems, natural objects may be found near these equilateral points. For example, in the Sun-Jupiter system, the Trojan asteroids are found at the equilateral points [3, 79]. In the Sun-Earth system, 2010 TK7 is an asteroid that librates about L_4 [79]. Additionally, 2010 SO16 is another near-Earth asteroid that librates about the Sun-Earth L_5 point [80]. However, in the Earth-Moon system, no natural object has yet been found in orbit about an equilateral point, perhaps due to the perturbing gravitational effects from the Sun [3].

2.14 The State Transition Matrix

Cowell's method involves a simple and direct numerical integration of a set of equations of motion [9] [74]. However, only information about one particular trajectory is determined. Encke's method involves numerically integrating the equations of motion and a state transition matrix (STM) about a reference trajectory, $\vec{X}_{ref}$ to learn about neighboring trajectories based on a linear analysis [9, 74]. The STM, or sensitivity matrix, provides information about the sensitivity of a final state to the initial conditions [58]. The STM is defined as the Jacobian of the final state, $\vec{X}(t)$,

with respect to the initial state, $\vec{X}(t_0)$ based on a linearization about a reference trajectory [9]. This Jacobian for the CR3BP is defined in equation (87).

$$\Phi(t,t_0) = \left[\begin{array}{cccccc} \frac{\partial x(t)}{\partial x(t_0)} & \frac{\partial x(t)}{\partial y(t_0)} & \frac{\partial x(t)}{\partial z(t_0)} & \frac{\partial x(t)}{\partial \dot{x}(t_0)} & \frac{\partial x(t)}{\partial \dot{y}(t_0)} & \frac{\partial x(t)}{\partial \dot{z}(t_0)} \\ \frac{\partial y(t)}{\partial x(t_0)} & \frac{\partial y(t)}{\partial y(t_0)} & \frac{\partial y(t)}{\partial z(t_0)} & \frac{\partial y(t)}{\partial \dot{x}(t_0)} & \frac{\partial y(t)}{\partial \dot{y}(t_0)} & \frac{\partial y(t)}{\partial \dot{z}(t_0)} \\ \frac{\partial z(t)}{\partial x(t_0)} & \frac{\partial z(t)}{\partial y(t_0)} & \frac{\partial z(t)}{\partial z(t_0)} & \frac{\partial z(t)}{\partial \dot{x}(t_0)} & \frac{\partial z(t)}{\partial \dot{y}(t_0)} & \frac{\partial z(t)}{\partial \dot{z}(t_0)} \\ \frac{\partial \dot{x}(t)}{\partial x(t_0)} & \frac{\partial \dot{x}(t)}{\partial y(t_0)} & \frac{\partial \dot{x}(t)}{\partial z(t_0)} & \frac{\partial \dot{x}(t)}{\partial \dot{x}(t_0)} & \frac{\partial \dot{x}(t)}{\partial \dot{y}(t_0)} & \frac{\partial \dot{x}(t)}{\partial \dot{z}(t_0)} \\ \frac{\partial \dot{y}(t)}{\partial x(t_0)} & \frac{\partial \dot{y}(t)}{\partial y(t_0)} & \frac{\partial \dot{y}(t)}{\partial z(t_0)} & \frac{\partial \dot{y}(t)}{\partial \dot{x}(t_0)} & \frac{\partial \dot{y}(t)}{\partial \dot{y}(t_0)} & \frac{\partial \dot{y}(t)}{\partial \dot{z}(t_0)} \\ \frac{\partial \dot{z}(t)}{\partial x(t_0)} & \frac{\partial \dot{z}(t)}{\partial y(t_0)} & \frac{\partial \dot{z}(t)}{\partial z(t_0)} & \frac{\partial \dot{z}(t)}{\partial \dot{x}(t_0)} & \frac{\partial \dot{z}(t)}{\partial \dot{y}(t_0)} & \frac{\partial \dot{z}(t)}{\partial \dot{z}(t_0)} \end{array}\right]\Bigg|_{\vec{X}_{ref}(t)} \tag{87}$$

Based on the linear analysis $\delta\vec{X}(t) = \Phi(t,t_0)\delta\vec{X}(t_0)$ [9]. However, it must be noted that this approximation is based on a linear analysis and, in order to find the true variation in the final state based on a variation in the initial state, the new initial conditions must be numerically integrated in the full nonlinear system.

In order to compute the STM along a reference trajectory, the STM must be numerically integrated in parallel with the trajectory, which, in general, requires the numerical integration of $N + N^2$ first-order equations of motion [9]. The governing equation for the STM is based on the variational equations and defined in equation (88) [9].

$$\dot{\Phi}(t,t_0) = A(t)\Phi(t,t_0) \tag{88}$$

The system matrix, $A(t)$, is similar to the system matrix used in the linear analysis of the Lagrange points; however, in the context of numerically integrating the STM, the system matrix is a function of time and must be evaluated at each step of the trajectory [9]. The system matrix is defined as the Jacobian of the equations of motion, $\dot{\vec{X}}(t) = \vec{f}(\vec{X}(t))$, with respect to a reference trajectory, $\vec{X}(t)_{ref}$, in equation (89) [9].

$$A(t) = \left. \frac{\partial \vec{f}\left(\vec{X}(t)\right)}{\partial \vec{X}(t)} \right|_{\vec{X}_{ref}(t)} \tag{89}$$

The system matrix for the CR3BP is defined in equation (90).

$$A(t) = \left. \begin{bmatrix} 0 & 0 & 0 & 1 & 0 & 0 \\ 0 & 0 & 0 & 0 & 1 & 0 \\ 0 & 0 & 0 & 0 & 0 & 1 \\ U^*_{xx} & U^*_{xy} & U^*_{xz} & 0 & 2 & 0 \\ U^*_{xy} & U^*_{yy} & U^*_{yz} & -2 & 0 & 0 \\ U^*_{xz} & U^*_{yz} & U^*_{zz} & 0 & 0 & 0 \end{bmatrix} \right|_{\vec{X}_{ref}(t)} \tag{90}$$

The STM is then numerically integrated using the governing equation described in equation (88) and the initial conditions described in equation (91) [9].

$$\Phi(t_0, t_0) = I \tag{91}$$

The STM possesses three important characteristics that are exploited by the current investigation. The first two characteristics are defined in equations (92)-(93) [9].

$$\Phi(t_2, t_0) = \Phi(t_2, t_1)\Phi(t_1, t_0) \tag{92}$$

$$\Phi(t_1, t_0) = \Phi(t_0, t_1)^{-1} \tag{93}$$

The third characteristic of the STM in the CR3BP is the invariance of its determinant along a trajectory [9]. This characteristic is described by Liouville's theorem [9, 57]. If the divergence of a system of first-order differential equations is equal to zero, $\vec{\nabla} \cdot \vec{f}(\vec{X}(t)) = 0$, then Liouville's theorem applies [57]. This criteria is analogous to

an incompressible phase fluid [57]. The determinant remains constant because of the Jacobi-Liouville formula expressed in equation (94) [39].

$$det\left(\Psi(t)\right) = det\left(\Psi(t_0)\right) exp\left[\int_{t_0}^{t} tr\left(A(s)\right) ds\right] \tag{94}$$

where $\Psi(t)$ is any matrix subject to the first-order matrix differential equation $\dot{\Psi}(t) = A(t)\Psi(t)$ [39]. The governing equation for the STM in the CR3BP (equation (88)) fits this description. Additionally, the trace of the system matrix defined for the CR3BP in equation (90), is zero. This result means Liouville's theorem applies according to equation (95), which states that the divergence of the system of first-order differential equations is equal to the trace of the system matrix [81].

$$tr(A(t)) = \vec{\nabla} \cdot \vec{f}(\vec{X}(t)) \tag{95}$$

Now, by applying the Jacobi-Liouville formula, the determinant of the STM must be constant, because the trace of the system matrix is zero. Since the determinant of the initial conditions described in equation (91) is one, the determinant of the STM for all time along a trajectory in the CR3BP will be one. Similar to the value of the Jacobi Constant, the determinant of the STM will remain invariant if the trajectory is integrated with no error. However, due to the need to numerically integrate trajectories, the determinant of the STM will only be approximately constant. In fact, the determinant of the STM along a trajectory could be tracked to assess the error of a numerical integration, similar to the tracking of the value of the Jacobi Constant [14, 19].

2.15 Differential Corrections

Differential corrections schemes are implemented throughout the current investigation to solve two-point boundary value problems in the CR3BP within a desired convergence tolerance. Such boundary value problems involve orbital transfers and periodic orbits. The differential corrections processes, or targeting algorithms, employed leverage numerically integrated STMs along trajectories. The development of the differential corrections schemes in the current investigation follows the development by Pavlak [28, 82]. First, n independent variables are chosen. These independent design variables are listed as a column vector, $\vec{X}$. An initial guess for $\vec{X}$ must also be generated and is labeled as $\vec{X}^{(0)}$. Next, m constraints are defined in the column vector $\vec{F}$, where $\vec{F}$ is a function of $\vec{X}$. The constraints defined in $\vec{F}$ may be enforced (such that $\vec{F} = \vec{0}$) at the initial state or anywhere along a trajectory. Note, if $n = m$, a unique solution, in general, exists. Additionally, if $n > m$, an infinite number of solutions, in general, exist. However, if $n < m$, the problem is over-constrained and, in general, no solutions exist.

A Newton-Raphson method is employed to iteratively drive each of the constraints to zero [9]. This method requires a Jacobian of the constraint vector with respect to the independent variables. This Jacobian is size $m \times n$ and is described in equation (96).

$$D\vec{F}(\vec{X}) = \frac{\partial \vec{F}}{\partial \vec{X}} = \begin{bmatrix} \frac{\partial F_1}{\partial X_1} & \cdots & \frac{\partial F_1}{\partial X_n} \\ \vdots & \ddots & \vdots \\ \frac{\partial F_m}{\partial X_1} & \cdots & \frac{\partial F_m}{\partial X_n} \end{bmatrix} \tag{96}$$

For a small change in $\vec{X}$, the new $\vec{F}$ may be approximated using a first-order Taylor series approximation [73]. This approximation is described in equation (97).

$$\vec{F}^{(i+1)} \approx \vec{F}^{(i)} + D\vec{F}(\vec{X}^{(i)}) \left(\vec{X}^{(i+1)} - \vec{X}^{(i)} \right) \tag{97}$$

Since it is desired to drive the constraint vector to zero, $\vec{F}^{(i+1)}$ is set equal to zero and equation (97) is rearranged to form the update equation described in equation (98).

$$\vec{X}^{(i+1)} = \vec{X}^{(i)} - \left[D\vec{F}(\vec{X}^{(i)})\right]^{-1} \vec{F}^{(i)} \tag{98}$$

If $n > m$, then the system is underdetermined and the inverse of $D\vec{F}(\vec{X}^{(i)})$ cannot be found since the Jacobian is not square. Instead, a pseudo-inverse is utilized and the update equation is described in equation (99).

$$\vec{X}^{(i+1)} = \vec{X}^{(i)} - D\vec{F}(\vec{X}^{(i)})^T \left[D\vec{F}(\vec{X}^{(i)})D\vec{F}(\vec{X}^{(i)})^T\right]^{-1} \vec{F}^{(i)} \tag{99}$$

The pseudo-inverse used in the current investigation is a Moore-Penrose pseudo-inverse [83]. This pseudo-inverse calculates the minimum-L^2-norm solution based on the Taylor series approximation described in equation (97) [83]. This pseudo-inverse only calculates one possible solution to the Taylor series approximation, but, in general, an infinite number of solutions exist when $n > m$. The appropriate update equation from equations (98)-(99) is then employed to update $\vec{X}$ until $||\vec{F}|| < \varepsilon$. In the current investigation a tolerance of $\varepsilon = 10^{-12}$ is utilized. In the Earth-Moon CR3BP, this tolerance corresponds to a position error of 0.3844 mm and a velocity error of $1.024546856607337 \times 10^{-6}$ mm/s.

The constraint vector is composed of equality constraints. However, it is possible to define inequality constraints through the use of slack variables. An inequality is first written in the form seen in equation (100) as a function of the independent variables, $\vec{X}$.

$$f(\vec{X}) \geq 0 \tag{100}$$

Then, equation (100) may be rewritten in terms of a slack variable, β, as seen in equation (101).

$$f(\vec{X}) - \beta^2 = 0 \tag{101}$$

This inequality constraint may then be added to the constraint vector while the slack variable becomes an additional independent variable, which requires an initial guess.

One type of differential corrections process is known as single-shooting. Single-shooting algorithms numerically integrate a single arc and utilize an update equation, as described in equations (98)-(99). A notional representation of this type of targeting algorithm is shown in Figure 15.

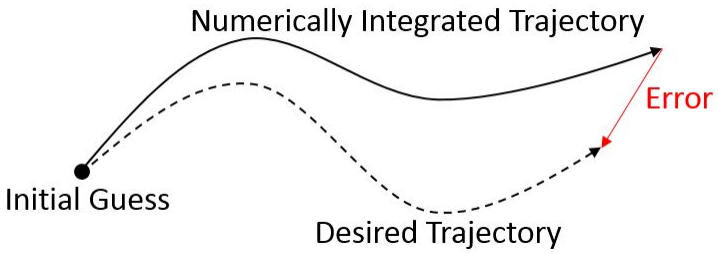

Figure 15. Notional Representation of a Single-Shooting Algorithm

Another type of targeting algorithm is known as multiple-shooting. This type of targeting algorithm numerically integrates multiple arcs connected by patch points. A notional representation of a multiple-shooting algorithm is shown in Figure 16.

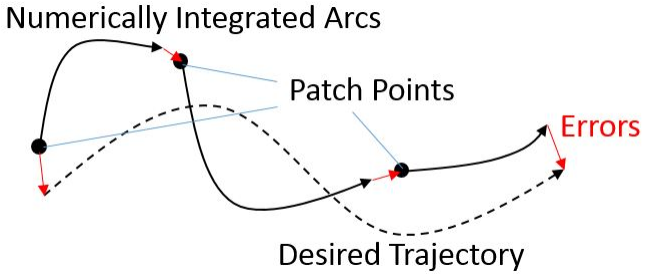

Figure 16. Notional Representation of a Multiple-Shooting Algorithm

The appropriate update equation may then be employed to attempt to drive each of the errors to zero. Multiple advantages may exist through the use of a

multiple-shooting algorithm rather than a single-shooting algorithm. First, since both single-shooting and multiple-shooting methods rely on linearized variational equations to approximate how changes in the initial states will affect the final states, the approximations provided by single-shooting algorithms may be less accurate than those provided by multiple-shooting algorithms [82]. Accuracy is, in general, lost as the length of numerical integration is increased. By dividing the arc into multiple segments, the linear approximations provided by a multiple-shooting algorithm may be more representative of the true nonlinear behavior, since the integration time of each arc is decreased [82]. The employment of multiple-shooting algorithms also spreads the dynamical sensitivity across multiple patch points, which may aid in the convergence of a solution. Another advantage offered by multiple-shooting algorithms is the ability to add or relax constraints at the patch points [82]. For example, an altitude constraint may be added as a constraint at a patch point or velocity continuity may be relaxed at a patch point. The latter example would imply a ΔV along the trajectory. This added control may allow the user to more easily target solutions with desired characteristics.

2.16 Numerical Optimization

In the current investigation, the numerical optimization algorithm *fmincon*, a function in the MATLAB® Optimization Toolbox, is employed to search for locally optimal solutions [84]. Similar to the differential corrections processes described in Section 2.15, n independent design variables may be listed as $\vec{X}$. Likewise, m equality constraints may be listed as $\vec{F}$. Again, if $n = m$, in general, a unique solution exists. And if $n > m$, then an infinite number of solutions exist, in general. In an optimization process, it is generally desired for $n > m$, so that an infinite number of solutions exist, allowing an optimization process to find a locally optimal solution. Additionally, p

inequality constraints may be listed as $\vec{G}$. The cost function may then be defined as the scalar function $f(\vec{X})$. The optimization problem may then be stated as follows:

$$min\ f(\vec{X})\ subject\ to\ \vec{G}(\vec{X}) \leq \vec{0}\ and\ \vec{F}(\vec{X}) = \vec{0}$$

An auxiliary Lagrangian function is then defined as $L(\vec{X}, \vec{\lambda}_p, \vec{\lambda}_m)$, where $\vec{\lambda}_p$ and $\vec{\lambda}_m$ are Lagrange multiplier vectors of length p and m, respectively [84].

$$L(\vec{X}, \vec{\lambda}_p, \vec{\lambda}_m) = f(\vec{X}) + \vec{\lambda}_p \cdot \vec{G}(\vec{X}) + \vec{\lambda}_m \cdot \vec{F}(\vec{X}) \tag{102}$$

The function *fmincon* searches for a locally optimal solution, in terms of the cost function, where the first-order optimality conditions are driven to zero within the desired tolerances. These tolerances are discussed in Section 3.4. The first-order optimality conditions in *fmincon* are defined as the Karusch-Kuhn-Tucker (KKT) conditions [66, 84]. These conditions are defined in equations (103)-(107).

$$\nabla_{\vec{X}} L(\vec{X}, \vec{\lambda}_p, \vec{\lambda}_m) = \vec{0} \tag{103}$$

$$\lambda_{pi} G_i(\vec{X}) = 0 \qquad for\ i = 1 \ldots p \tag{104}$$

$$\vec{G}(\vec{X}) \leq \vec{0} \tag{105}$$

$$\vec{F}(\vec{X}) = \vec{0} \tag{106}$$

$$\vec{\lambda}_p(\vec{X}) \geq \vec{0} \tag{107}$$

2.17 Periodic Orbits

In the CR3BP, periodic solutions are possible within a desired tolerance. These periodic solutions may be targeted using a differential corrections strategy, either single-

shooting or multiple-shooting. In the current investigation, two different methods are employed to approximate periodic orbits. The first method exploits a symmetry in the CR3BP, as described in Section 2.9, that allows for only half of a periodic orbit to be calculated. The second method may be implemented to target asymmetric periodic orbits and employs a differential corrections scheme to target periodicity. However, both methods require an initial guess that is close enough to the periodic orbit to allow convergence.

Additionally, once a periodic orbit is found in the CR3BP, the periodic orbit may be continued to find neighboring periodic orbits with similar characteristics. Together, these periodic orbits form a periodic orbit family. The continuation method employed by the current investigation to compute portions of periodic orbit families is discussed in Section 3.2. The periodic orbits of a given family lie on the same hodograph, which is a curve in the six-dimensional phase space that represents initial conditions for each member in the family [85, 86]. Various methods exist to perform the continuation of a periodic orbit family [14, 28]. Section 3.2 discusses the continuation scheme employed in the current investigation.

2.17.1 Symmetric Periodic Orbits

Symmetric periodic orbits in the CR3BP exploit the first symmetry described in Section 2.9. This symmetry may be described as a reflection across the $x-z$ plane and time. This transformation may be described as seen in equation (108) [15].

$$[x(t), y(t), z(t), \dot{x}(t), \dot{y}(t), \dot{z}(t)]^T \rightarrow [x(-t), -y(-t), z(-t), -\dot{x}(-t), \dot{y}(-t), -\dot{z}(-t)]^T \tag{108}$$

A trajectory that begins with a perpendicular crossing of the $x-z$ plane and ends with a perpendicular crossing of the $x-z$ plane may be reflected across the $x-z$

plane and time to generate another trajectory that is the other half of a periodic orbit [15, 87]. Roy further separates this type of periodic orbit into two different categories [87]. The first is the spatial version of a symmetric periodic orbit, while the second is the planar version of this symmetry [87]. Once a spatial version of this type of symmetry is found, the second symmetry discussed in Section 2.9 may be applied, in general, to find both the ''northern'' and ''southern'' versions of this symmetric periodic orbit. However, the planar version of this type of symmetry is invariant to the second type of symmetry discussed in Section 2.9. Roy describes both types of symmetries as ''mirror configurations'' [87]. In fact, Roy generalizes this symmetry even further to describe the N-body problem [87]. He states, ''If n point masses are acted upon by their mutual gravitational forces only, and at a certain epoch each radius vector from the centre of mass of the system is perpendicular to every velocity vector, then the orbit of each mass after that epoch is a mirror image of its orbit prior to that epoch'' [87]. He then claims that if this configuration occurs at two separate epochs, then the orbits are periodic [87].

This type of symmetry may be exploited by employing differential corrections schemes in the CR3BP that target trajectories with two distinct, perpendicular crossings of the $x-z$ plane. For example, a trajectory targeted with the initial state $\vec{X} = [x_1(t_1),\ 0,\ z_1(t_1),\ 0,\ \dot{y}_1(t_1),\ 0]^T$ and the final state $\vec{X} = [x_2(t_2),\ 0,\ z_2(t_2),\ 0,\ \dot{y}_2(t_2),\ 0]^T$ may be reflected about the $x-z$ plane and time to find a trajectory with the initial state $\vec{X} = [x_2(-t_2),\ 0,\ z_2(-t_2),\ 0,\ \dot{y}_2(-t_2),\ 0]^T$ and the final state $\vec{X} = [x_1(-t_1),\ 0,\ z_1(-t_1),\ 0,\ \dot{y}_1(-t_1),\ 0]^T$. Because of the time invariance of the CR3BP, the epochs of the second trajectory may be shifted forward in time by $2t_2$ resulting in a trajectory with the initial state $\vec{X} = [x_2(t_2),\ 0,\ z_2(t_2),\ 0,\ \dot{y}_2(t_2),\ 0]^T$ and the final state $\vec{X} = [x_1(2t_2 - t_1),\ 0,\ z_1(2t_2 - t_1),\ 0,\ \dot{y}_1(2t_2 - t_1),\ 0]^T$. This trajectory combined with the original targeted trajectory now form a periodic orbit that is continuous in

position, velocity, and time. A notional example of a trajectory with two perpendicular crossings of the $x-z$ plane that is reflected across the $x-z$ plane and time is shown in Figure 17. An example of this type of symmetric periodic orbit modeled in the Earth-Moon CR3BP is shown in Figure 18.

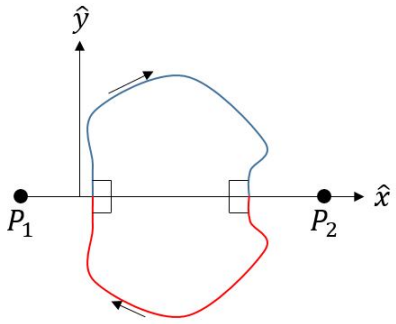

Figure 17. A Notional Symmetric Periodic Orbit in the CR3BP (Red: Trajectory with Two Perpendicular Crossings of the $x-z$ Plane; Blue: A Reflection of the Red Trajectory Across the $x-z$ Plane and Time)

Figure 18 shows a Lyapunov orbit about L_1 in the Earth-Moon system. A Lyapunov orbit is a type of planar periodic trajectory in the CR3BP that orbits a Lagrange point. This periodic orbit is found using a single-shooting algorithm. The initial guess for this periodic orbit is generated by using the linear approximation for motion near a collinear Lagrange point as discussed in Section 2.13.1. The exploitation of symmetry not only makes it easier to find periodic orbits, but it also may decrease the amount of numerical error in the approximation of a periodic orbit. Since the integration time is effectively halved, the accumulation of local round-off and truncation errors may be decreased.

Once a symmetric periodic orbit is targeted using the method described above, it may be convenient to generate the full-cycle monodromy matrix (the STM of a periodic orbit that has been numerically integrated through one period) to assess the orbital stability of the periodic orbit as described in Section 2.18 [9, 19, 69]. One method to compute the full-cycle monodromy matrix would be to utilize the converged solution

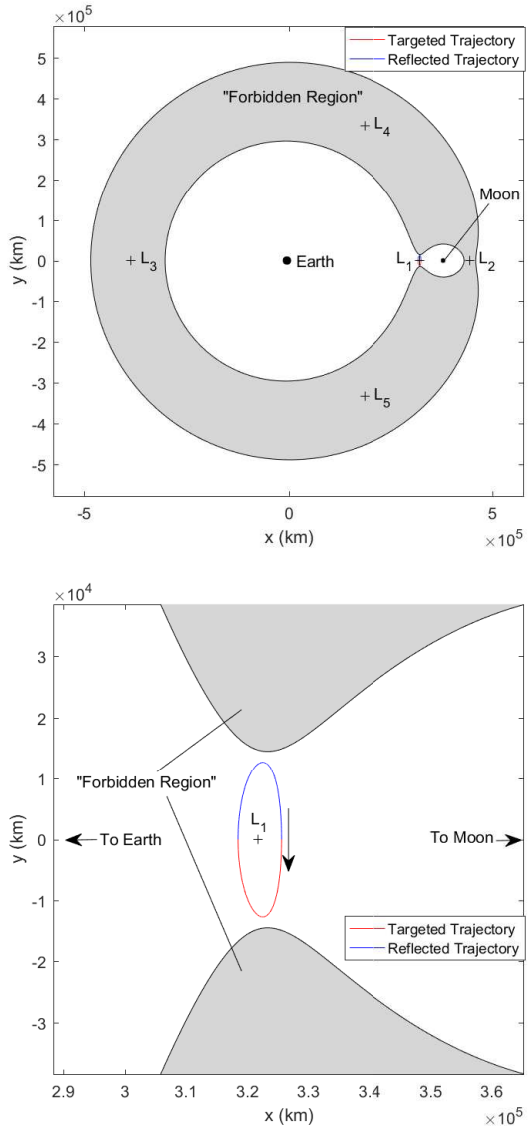

Figure 18. Symmetric Lyapunov Orbit About L_1 in the Earth-Moon CR3BP (Left: A Zoomed-Out View of the Lyapunov Orbit Showing the ZVCs Associated With the Periodic Orbit; Right: A Zoomed-In View of the Lyapunov Orbit Showing the Symmetry Exploited to Target the Symmetric Periodic Orbit)

of one half of a symmetric periodic orbit and numerically integrate the STM for a full period. However, Howell derives a method to compute the full-cycle monodromy matrix with the half-cycle monodromy matrix through the exploitation of this symmetry in her 1984 paper ‘‘Three-Dimensional, Periodic, ‘Halo’ Orbits’’ [69]. This method may decrease the amount of numerical error in the approximated monodromy matrix by

halving the integration time. Howell's final result may be summarized by equation (109) [69].

$$\Phi(T,0) = A \begin{bmatrix} 0 & -I \\ I & -2\Omega \end{bmatrix} \Phi^T(T/2,0) \begin{bmatrix} -2\Omega & I \\ -I & 0 \end{bmatrix} A\Phi^T(T/2,0) \tag{109}$$

where A, I, and Ω are defined in equation (110) and $\Phi^T(T/2,0)$ is the half-cycle STM.

$$A = \begin{bmatrix} 1 & 0 & 0 & 0 & 0 & 0 \\ 0 & -1 & 0 & 0 & 0 & 0 \\ 0 & 0 & 1 & 0 & 0 & 0 \\ 0 & 0 & 0 & -1 & 0 & 0 \\ 0 & 0 & 0 & 0 & 1 & 0 \\ 0 & 0 & 0 & 0 & 0 & -1 \end{bmatrix} \qquad I = \begin{bmatrix} 1 & 0 & 0 \\ 0 & 1 & 0 \\ 0 & 0 & 1 \end{bmatrix} \qquad \Omega = \begin{bmatrix} 0 & 1 & 0 \\ -1 & 0 & 0 \\ 0 & 0 & 1 \end{bmatrix} \tag{110}$$

2.17.2 Asymmetric Periodic Orbits

A more direct approach is needed to target asymmetric periodic orbits in the CR3BP. These types of orbits must be targeted by an algorithm that requires position and velocity continuity between the initial and final states. However, it is only necessary/appropriate to target continuity between five of the six initial and final states [19, 28]. If one were to require continuity between all six states, the targeting algorithm would be overconstrained because the conservation of the value of the Jacobi Constant is an implicit constraint [19, 28]. Typically, continuity of a velocity component is relaxed. In other words, if five of the final six states possess continuity, then the final sixth state must also be continuous with the initial state because of the conservation of the value of the Jacobi Constant. It is possible that the relaxed

velocity component may possess the opposite sign at the final state because velocity appears as a magnitude in the definition of the Jacobi Constant. To ensure the final state possesses the proper sign, an inequality constraint may be defined as described in equation (101) [19, 28]. This method to target asymmetric periodic orbits may also be employed to calculate symmetric periodic orbits, if desired [28]. However, as discussed in Section 2.17.1, the method to target symmetric periodic orbits that exploits symmetry in the CR3BP may decrease the numerical error of a targeted solution.

2.17.3 Resonant Orbits

One special type of periodic orbit in the CR3BP is known as a resonant orbit. These orbits may be symmetric or asymmetric, but their defining characteristic is that if P_3 is in a resonant orbit, then P_3 will complete p revolutions about P_1 in the inertial frame in approximately the same amount of time as it takes P_2 to complete q revolutions about P_1 in the inertial frame [14, 31, 32, 68]. Resonant orbits are then identified by their $p : q$ ratio. To generate resonant orbits, first, an initial guess must be generated. Initial guesses may be generated using conic arcs calculated in the R2BP that are approximately in resonance with the Moon as described by Vaquero [31, 32]. Resonant orbits may then be targeted with one of the methods described in Sections 2.17.1 and 2.17.2. Figure 19 provides an example of a periodic 4:3 resonant orbit in the Earth-Moon CR3BP.

A resonant orbit is a periodic orbit in the barycentric rotating frame; however, a resonant orbit is not, in general, periodic in the inertial frame. A resonant orbit will, in general, not be periodic in the inertial frame because the time it takes P_3 to complete p revolutions is only approximately equal to the time it takes for P_2 to

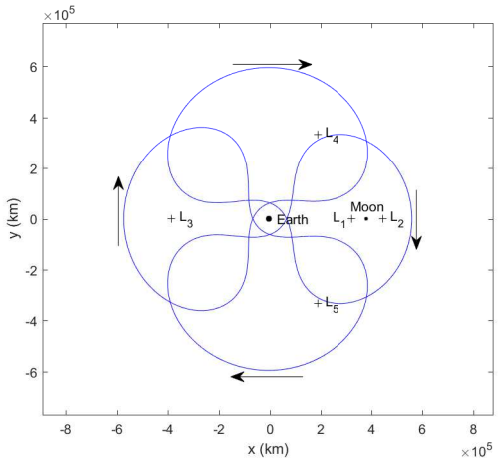

Figure 19. A 4:3 Resonant Orbit in the Earth-Moon CR3BP Plotted in the Barycentric Rotating Frame

complete q revolutions. If these times were exactly equal, then the resonant orbit would be periodic in both the barycentric rotating frame and the inertial frame.

If $p > q$, the resonant orbit is defined as an interior resonant orbit [14,31,32]. This type of resonant trajectory orbits P_1 $p - q$ times in the rotating frame in the prograde direction. If $p < q$, the resonant orbit is defined as an exterior resonant orbit [14,31,32]. An exterior resonant trajectory orbits P_1 in the rotating frame $q - p$ times in the retrograde direction. Both types of resonant orbits orbit P_1 in the prograde direction in the inertial frame. Also, a p:q resonant orbit typically possesses p loops in the rotating frame as seen in Figure 19; however, Vaquero provides some examples of resonant orbits that do not possess this behavior [14, 32]. Vaquero also provides examples of multiple families of periodic orbits in the Earth-Moon CR3BP [31, 32].

Many natural objects exist in resonant orbits. Three of Jupiter's moons exist in resonant orbits [68]. Jupiter's moon Io is in a 2:1 resonant orbit with Europa, while Europa is in a 2:1 orbit with Ganymede [68]. In other words, in the time it takes Ganymede to complete one orbit about Jupiter, Europa completes approximately two orbits and Io completes approximately four orbits. Additionally, on a larger scale, Jupiter's orbit about the Sun is in approximately a 5:2 resonance with the

orbit of Saturn [68]. Some of the moons of Saturn are also in resonant orbits with each other [68]. In addition to natural objects, some spacecraft have been inserted into nearly resonant orbits. In 2008, the spacecraft IBEX was launched into a highly eccentric high-altitude orbit about Earth to study the termination shock [88, 89]. The termination shock is where solar wind particles slow down as they reach the interstellar medium [90]. This spacecraft was subject to large disturbances due to the Sun and Moon that required large amounts of stationkeeping [88]. In 2011, this spacecraft was maneuvered into a 3:1 resonant orbit in the Earth-Moon CR3BP [31,88]. This transfer extended the original mission of the spacecraft by decreasing the stationkeeping requirements [88]. Also, the TESS spacecraft is scheduled to be launched in 2017 into a 2:1 resonant orbit in the Earth-Moon CR3BP [91]. This spacecraft will catalog exoplanets in an attempt to find potentially habitable planets [91].

2.18 Stability of Periodic Orbits

After the computation of a periodic orbit in the CR3BP, it may be convenient to determine the stability of the periodic trajectory. To determine the stability of a periodic trajectory in the CR3BP, the concept of orbital stability is introduced [15, 77]. Unlike the isochronous linear stability assessment used to determine the stability of the Lagrange points, orbital stability utilizes a linearized normal correspondence [15, 77]. A normal correspondence measures the ‘‘distance’’ between two trajectories at their nearest points rather than the ‘‘distance’’ between two trajectories measured at the same time [77]. The latter correspondence is known as an isochronous correspondence [77]. Figure 20 illustrates the difference between an isochronous correspondence and a normal correspondence. A periodic trajectory may then be labeled as orbitally stable if nearby trajectories remain ‘‘close’’ to the periodic, reference trajectory [77]. This criteria may be expressed mathematically as follows: if for any $\varepsilon > 0$ there exists a δ

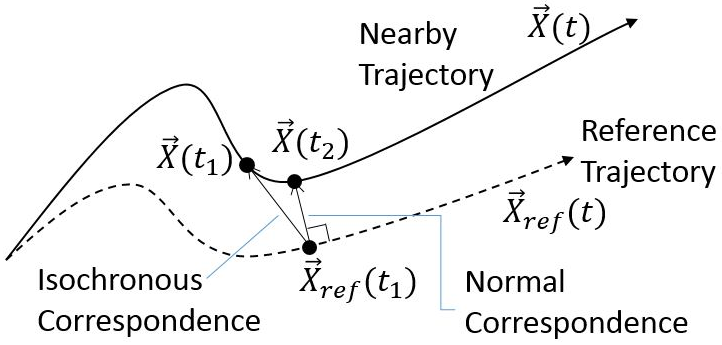

Figure 20. An Illustration of the Difference Between a Normal Correspondence and an Isochronous Correspondence

such that if $min||\vec{X}(t_0) - \vec{X}_{ref}(\tau_0)|| < \delta$, then $min||\vec{X}(t) - \vec{X}_{ref}(\tau)|| < \varepsilon$ for all $t \geq 0$ [77]. Additionally, asymptotic orbital stability is possible if $min||\vec{X}(t) - \vec{X}_{ref}(\tau)|| \to 0$ as $t \to \infty$ [77].

In the current investigation, the orbital stability of a periodic orbit, in the linear sense, is determined with Floquet theory [9, 92]. Floquet theory states that the full-cycle STM, $\Phi(T, 0)$, also known as the monodromy matrix, may be expressed in terms of the periodic matrix, $F(t)$, and the matrix J, which is a Jordan normal form matrix that contains the frequencies of the periodic trajectory [9, 14, 19]. This relationship is described in equation (111) [9].

$$\Phi(T, 0) = F(T)e^{JT}F^{-1}(0) \tag{111}$$

Since $F(t)$ is periodic, and the period of the trajectory is defined to be T, $F(T) = F(0)$ [9]. Equation (111) may then be rearranged to show that $F(0)$ is the eigenvector matrix of the monodromy matrix [9].

$$e^{JT} = F(0)\Phi(T, 0)F^{-1}(0) \tag{112}$$

Next, the eigenvalues, λ_i, known as the characteristic multipliers, of the monodromy matrix may be described in terms of the diagonal components of J as seen in equation (113), where ω_i are the diagonal components of J [9]. These diagonal components of J are also known as the Poincaré exponents [9].

$$\lambda_i = e^{\omega_i T} \tag{113}$$

In a Hamiltonian system, such as the CR3BP, the eigenvalues of the monodromy matrix of a periodic trajectory must appear in complex conjugate pairs and they must appear in reciprocal pairs [9, 14, 19, 65]. These requirements are described in equation (114), where, in general, j may be equal to k [9].

$$\lambda_i = a_i + b_i i \qquad \lambda_j = a_i - b_i i \qquad \lambda_k = \frac{1}{\lambda_i} \tag{114}$$

Additionally, since the trajectories of interest are periodic, at least one of the eigenvalues must be equal to one [19, 92]. This requirement exists because perturbations in the direction of periodicity will neither expand nor contract [92]. And because of the conjugate and reciprocal pair requirements described in equation (114), at least one other eigenvalue must also be equal to one [14, 19, 65].

The orbital stability, in the linear sense, of a periodic orbit in the CR3BP may be determined by examining the eigenvalues of the monodromy matrix described in equation (113) [9]. The phase space of the CR3BP is six-dimensional, so an eigenvalue analysis of the monodromy matrix associated with a periodic trajectory will yield six eigenvalues. As previously noted, two of these eigenvalues will be equal to one. The other four eigenvalues may exist anywhere on the complex plane as long as they satisfy the relationships described in equation (114). If all six of the eigenvalues were to exist inside the unit circle, the periodic orbit would be classified as asymptotically orbitally

stable, in the linear sense [77]. However, since two of the eigenvalues must equal one, a periodic orbit in the CR3BP orbit cannot be asymptotically stable and is at best marginally orbitally stable, in the linear sense [19]. Additionally, when an eigenvalue does exist inside of the unit circle, one must also lie outside of the unit circle according to the requirement that eigenvalues occur as reciprocal pairs [9, 14, 86]. This type of behavior may be described as a non-stable saddle [19, 65, 93]. A non-stable saddle is associated with orbitally unstable behavior, in the linear sense, so the periodic orbit may be classified as unstable in the nonlinear system. When a pair of eigenvalues does lie on a unit circle, the behavior may be described as a center [93]. A center is associated with marginal orbital stability, in the linear sense, so no conclusions may be made about the behavior in the nonlinear system. Since the linear orbital stability of all periodic orbits in the CR3BP may at best be associated with the behavior of a center, no periodic orbit in the CR3BP that is generated in the current investigation can be claimed to be orbitally stable in the nonlinear system.

The behavior of a periodic orbit may be classified in terms of its orbital stability. Each of the three eigenvalue pairs will determine the type of behavior associated with the periodic orbit of interest. At best, marginal orbital stability, in the linear sense, may be concluded if the behavior associated with the periodic orbit is that of a 2D center X 2D center X 2D center (6D center). If only one pair of eigenvalues is associated with a non-stable saddle, the orbital stability, in the linear sense, may be described as a 2D saddle X 2D center X 2D center (2D saddle X 4D center). If two pairs of eigenvalues are associated with non-stable saddles, the orbital stability, in the linear sense, of the periodic orbit may be described as 2D saddle X 2D saddle X 2D center (4D saddle X 2D center). Additionally, the in-plane and out-of-plane orbital stability, in the linear sense, of a periodic orbit that lies in the plane of the primaries are decoupled. For example, a 2D center may be associated with out-of-plane perturbations,

while a 2D center X 2D saddle may be associated with in-plane perturbations based on the linear analysis.

As discussed in Section 2.17, families of periodic orbits in the CR3BP may be found via a continuation method. The continuation method employed by the current investigation is discussed in Section 3.2. As one moves along the hodograph of a periodic orbit family in the CR3BP, which is a curve in the six-dimensional phase space that represents initial conditions for each member in the family, the eigenvalues of the monodromy matrix and the type of stability associated with the periodic orbit may change [86, 94]. An example of a hodograph is shown in Section 3.2. The point along a hodograph that is associated with this change in stability is known as a bifurcation point [86, 94]. Additionally, a bifurcation may also be associated with the intersection of two hodographs [86, 94]. This type of intersection implies that two families of periodic orbits intersect and share a periodic orbit at the bifurcation point [86, 94]. Doedel et. al provide a bifurcation diagram of some of the bifurcations between Lagrange point orbits and other orbits that exist in the Earth-Moon CR3BP [70].

2.19 Invariant Manifolds

The stability analysis of equilibrium points, as described in Section 2.13, provides information about the ‘‘flow’’ local to the Lagrange points [19]. In the CR3BP, this ‘‘flow’’ local to an equilibrium point may be described in terms of invariant manifolds [9]. These invariant manifolds are a collection of trajectories that make up a ‘‘surface of lower dimension imbedded within the phase space’’ [9]. The manifolds may be described as invariant for two reasons. First, if a spacecraft is on an invariant manifold, then it will be on the manifold for all finite time. And second, the CR3BP is an autonomous system, which means that particular solutions are independent of their start time [9]. Additionally, the invariant manifolds associated with a Lagrange

point possess the same value of Jacobi Constant as that associated with the Lagrange point [19]. The ''flow'' in the vicinity of the Lagrange point in the CR3BP may be associated with center-type behavior and saddle-type behavior as discussed in Section 2.13. Center-type behavior is associated with marginal Lyapunov stability, in the linear sense, and saddle-type behavior is associated with unstable behavior. Center-type behavior is associated with center manifolds [9]. The trajectories that lie on the center manifold remain near the marginally stable Lagrange point based on the linear analysis [9]. Non-stable saddles are associated with stable and unstable manifolds [9,19]. Trajectories that lie on the stable manifolds asymptotically approach the equilibrium point as $t \to \infty$, while trajectories that lie on the unstable manifold asymptotically approach the equilibrium point as $t \to -\infty$ [9,19].

The stable and unstable invariant manifolds associated with unstable Lagrange points in the CR3BP may be approximated from a linear analysis of the equilibrium point. As discussed in Section 2.13, the eigenvalues of the system matrix, as defined in equation (73), determine the Lyapunov stability of the equilibrium point, in the linear sense. The eigenvectors ($\vec{v}_i$) associated with the system matrix may then be calculated. Note that the system matrix is, in general, time-varying; however, when evaluated at an equilibrium point the system matrix is constant [19]. Each eigenvector is associated with its corresponding eigenvalue. Eigenvectors that are associated with eigenvalues that possess a negative real part correspond to the stable subspace of the equilibrium point (E^S) [20,71,92,93]. Likewise, eigenvectors that are associated with eigenvalues that possess a positive real part correspond to the unstable subspace of the equilibrium point (E^U) [20,71,92,93]. On the hand, when eigenvalues exist with zero real part, the associated eigenvectors correspond to the center subspace (E^C) [20,71,92,93].

These eigenspaces represent the manifolds of an equilibrium point based on a linear analysis [95]. This linear analysis may not be adequate to describe the true nonlinear behavior of the invariant manifolds of an equilibrium point in the CR3BP. However, the local stable and unstable manifolds may be defined in terms of the stable and unstable eigenspaces [20, 71, 92, 93]. The local stable manifold (W^S_{local}) is defined to be tangent to the stable eigenspace (E^S) at the equilibrium point $\vec{X}_{eq}$ [20, 71, 92, 93]. The positive local stable half-manifold (W^{S+}_{local}) asymptotically approaches the equilibrium point along the positive stable eigenvector ($\vec{v}_S$) as $t \to \infty$. Likewise the negative local stable half-manifold (W^{S-}_{local}) asymptotically approaches the equilibrium point along the negative stable eigenvector ($-\vec{v}_S$) as $t \to \infty$. Together, the positive and negative local stable half-manifolds form the local stable manifold. Additionally, the local unstable manifold (W^U_{local}) is defined to be tangent to the unstable eigenspace (E^U) at the equilibrium point $\vec{X}_{eq}$ [20, 71, 92, 93]. The positive local unstable half-manifold (W^{U+}_{local}) asymptotically approaches the equilibrium point along the positive unstable eigenvector ($\vec{v}_U$) as $t \to -\infty$. Likewise, the negative local unstable half-manifold (W^{U-}_{local}) asymptotically approaches the equilibrium point along the negative unstable eigenvector ($-\vec{v}_U$) as $t \to -\infty$. Figure 21 shows the relationship between the eigenvectors, eigenspaces, and half-manifolds. As the stable half-manifolds are propagated in reverse time, and the unstable half-manifolds are propagated in forward time, the global stable and unstable invariant manifolds may be defined, W^S and W^U, respectively.

The representation shown in Figure 21 shows the stable and unstable half-manifolds associated with an equilibrium point in the CR3BP; however, periodic trajectories in the CR3BP also possess similar manifold behavior [3, 9, 19]. The orbital stability of a periodic orbit, in the linear sense, is first determined through the use of Floquet theory as described in Section 2.18. The full-cycle monodromy matrix is then numerically

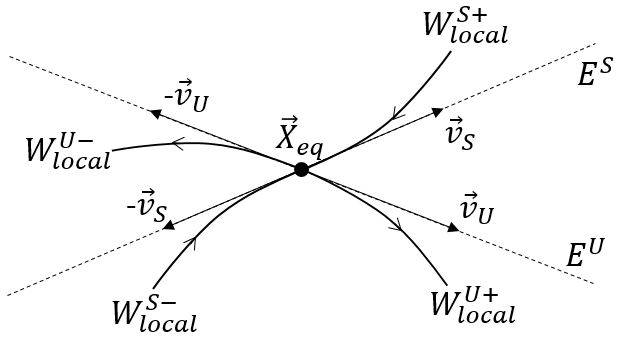

Figure 21. An Illustration of the Relationship Between the Eigenvectors, Eigenspaces, and Half-Manifolds Associated With the Equilibrium Point $\vec{X}_{eq}$

integrated for one period, beginning at a fixed point, $\vec{X}^*(t_0)$, along the periodic orbit. This initial condition is known as a fixed point because the periodic orbit returns to this point every period. The orbital stability, in the linear sense, of the periodic orbit is then determined by examining the eigenvalues (λ_i) of the full-cycle monodromy matrix. Next, the eigenvectors ($\vec{v}_i$) associated with the monodromy matrix may be calculated. Then, a procedure similar to that used for an equilibrium point is employed. Eigenvectors that are associated with eigenvalues that lie inside of the unit circle correspond the stable subspace of the periodic orbit (E^S) [20, 71, 92, 93]. On the other hand, eigenvectors that are associated with eigenvalues that lie outside of the unit circle correspond to the unstable subspace of the periodic orbit (E^U) [20, 71, 92, 93]. When eigenvalues exist on the unit circle, the associated eigenvectors correspond to the center subspace (E^C) [20, 71, 92, 93]. Note that for a periodic orbit in the CR3BP, at least two eigenvalues will lie on the unit circle [19, 92]. The local stable and unstable manifolds are tangent to the stable and unstable eigenspaces at the fixed point [20, 71, 92, 93]. However, a periodic trajectory in the CR3BP possesses an ‘‘infinite number of fixed points’’ [19]. Each of these fixed points possesses associated stable and unstable eigenspaces and half-manifolds. The invariant manifolds of a periodic orbit consist of each half-manifold associated with each fixed point. The

collection of these trajectories results in surfaces that define the invariant manifolds of a periodic orbit.

It is not practical to generate the manifold trajectories associated with every fixed point along a periodic orbit. Instead, a finite number of fixed points is chosen. It is also important to note that the eigenvalues associated with the full-cycle monodromy matrix generated from each fixed point do not change along the periodic orbit in the CR3BP [19]. In other words, the orbital stability characteristics of a periodic orbit in the CR3BP do not change depending on the starting point along a periodic orbit. However, the eigenvectors associated with each fixed point will, in general, change as one moves along the fixed points of a periodic orbit. Despite this fact, it is not necessary to compute the monodromy matrix for each fixed point to find the eigenvectors [19]. Instead, the eigenvectors of the fixed point $\vec{X}^*(t_2)$ may be found using the following relationship [19].

$$\vec{v}(t_1) = \Phi(t_1, t_0)\vec{v}(t_0) \tag{115}$$

Once the stable and unstable eigenspaces are defined for each of the fixed points, initial conditions are found along the eigenspaces and numerically integrated to generate approximations of the stable and unstable invariant manifolds. The stable manifold approximations are found by numerically integrated initial conditions along the stable eigenspaces in reverse time, while the unstable manifold approximations are found by numerically integrating initial conditions along the unstable eigenspaces in forward time.

An offset distance, d, is chosen to offset the initial conditions from the fixed points by a specified distance. First, each of the eigenvectors, $\vec{v}_i$, associated with each of the fixed points, $\vec{X}^*$, may be normalized in terms of position, where $\vec{v}_i = [x_i,\ y_i,\ z_i,\ \dot{x}_i,\ \dot{y}_i,\ \dot{z}_i]^T$.

$$\vec{v}_i^P = \frac{\vec{v}_i}{\sqrt{x_i^2 + y_i^2 + z_i^2}} \tag{116}$$

Then, initial conditions are generated using equation (117).

$$\vec{X}_i = \vec{X}^* \pm d\vec{v}_i^P \tag{117}$$

It is imperative that a proper offset distance is chosen. Too large an offset distance may result in manifold approximations that are not representative of the true manifold behavior [19]. Additionally, the true invariant manifolds possess the same value of the Jacobi Constant as the periodic orbit, but a large offset distance may disturb this equality [95]. On the other hand, because of the asymptotic nature of the manifolds, too small of an offset value may result in the manifolds requiring a long integration time to depart the vicinity of the periodic orbit [19,95]. This long integration time may also lead to more accumulation of local round-off and truncation errors resulting in a poor approximation of the invariant manifolds. The current investigation employs an offset value of 50 km in the Earth-Moon CR3BP [14, 19, 96, 97]. Figure 22 provides an example of stable and unstable manifold approximations associated with the periodic Lyapunov orbit shown in Figure 18. For a planar symmetric periodic orbit in the CR3BP, it is only necessary to approximate the stable manifolds, as the unstable manifolds may be approximated as a reflection of the stable manifold approximations across the x-axis and time (or vice versa) [14]. This application of symmetry is exploited to generate the plot shown in Figure 22.

Homoclinic and heteroclinic connections are possible between periodic orbits in the CR3BP [27]. A homoclinic connection is defined when a trajectory that lies on the unstable manifold of a periodic orbit intersects, in the phase space, a trajectory that lies on the stable manifold of the same periodic orbit [19,92]. A homoclinic connection

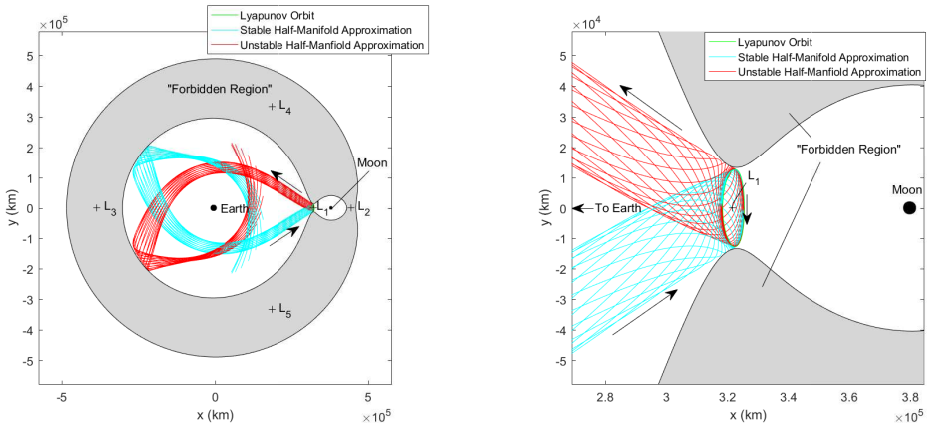

Figure 22. An Example of the Stable and Unstable Half-Manifold Approximations Associated With a Lyapunov Orbit About L_1 in the Earth-Moon CR3BP Numerically Integrated for One Revolution of the Primaries, About 27.3 Days (Left: A Zoomed-Out View of the Stable and Unstable Half-Manifold Approximations; Right: A Zoomed-In View of the Stable and Unstable Half-Manifold Approximations)

in the CR3BP may be utilized by a spacecraft in a periodic orbit to asymptotically depart the periodic orbit on the unstable manifold and then asymptotically return to the same periodic orbit on the stable manifold with theoretically no fuel required. However, a true homoclinic trajectory would require infinite time to complete, since it would require an infinite amount of time to depart asymptotically on the unstable manifold and, similarly, it would take an infinite amount of time to asymptotically return to the original periodic orbit. To perform this transfer in finite time, small ΔVs may be performed to transfer between the homoclinic trajectory and the periodic orbit. Another type of connection between manifolds, known as a heteroclinic connection, also exists in the CR3BP [27]. A heteroclinic connection is an intersection, in the phase space, between the unstable manifold of a periodic orbit and the stable manifold of another periodic orbit [19, 92]. This type of connection allows for the transfer between two different periodic orbits for theoretically zero ΔV. Again, this type of connection would require an infinite transfer time; however, ΔVs may be utilized to perform the transfer in finite time. It is important to note that these homoclinic and heteroclinic connections exist in the CR3BP and may serve as preliminary design to

transition into a higher-fidelity ephemeris model. Once converged in this ephemeris model, these connections may allow for similar, low-ΔV transfers.

Because of the asymptotic nature of the invariant manifolds, many researchers have exploited this behavior in mission design. Unlike a conventional Hohmann-type transfer, as discussed in Section 2.3, where two potentially large, impulsive ΔVs may be needed to perform a transfer, the exploitation of a manifold may only require one large, impulsive ΔV to transfer to a periodic orbit via a stable manifold. This trajectory would then asymptotically approach a periodic orbit in infinite time. A small, impulsive, second ΔV may be performed to transfer to the periodic orbit in a finite amount of time. This may result in fuel savings. The first spacecraft to exploit this possibility in the preliminary design phase was the Genesis mission in 2001 [21,22]. This spacecraft departed Earth on a stable manifold that asymptotically approached a periodic orbit about the Sun-Earth L_1 point [3,9,22]. The spacecraft then exploited a heteroclinic connection as it departed the periodic orbit about the Sun-Earth L_1 point and transferred into a periodic orbit about the Sun-Earth L_2 point [3,9,22]. After that, the spacecraft departed this periodic orbit on an unstable manifold that returned the spacecraft to Earth [3,9,22]. This mission was designed to perform these transfers with a total deterministic ΔV of less than 36 m/s [22]. The Genesis mission showcased the possibilities of performing mission design using DST and exploiting the invariant manifolds. Other researchers have similarly investigated the applications of invariant manifolds to perform mission design. Gómez et al. investigated the use of invariant manifolds to maneuver through the Jovian system [25]. Haapala also investigated the use of invariant manifolds as transfer trajectories [26,27]. Pavlak investigated transfers in the Earth-Moon CR3BP through the use of invariant manifolds associated with Lagrange point orbits [28]. Davis et al. explored the use of the invariant manifolds associated with orbits about the Sun-Earth L_1 point to perform transfers

between conventional orbits about Earth [29]. Wilmer explored the use of invariant manifolds to perform a transfer from a highly elliptical orbit to a circular orbit in the planar Earth-Moon CR3BP [14]. Zurita used invariant manifolds in the planar Earth-Moon CR3BP as initial guesses in an optimization routine to transfer from LEO to a Lagrange point orbit [96]. Koon et al. investigated the use of invariant manifolds and heteroclinic connections to transfer between resonant orbits in the Sun-Jupiter CR3BP [23]. Lo and Parker explored the exploitation of the invariant manifolds associated with unstable resonant orbits in the Earth-Moon CR3BP [24]. Vaquero and Howell exploited resonant manifolds associated with resonant orbits to perform transfers between Lagrange point orbits [30, 31, 32]. These authors demonstrated various techniques and methods to exploit invariant manifolds in a multitude of CR3BP systems.

2.20 Poincaré Maps

The lack of a known analytical solution to the CR3BP has led dynamicists to develop visual tools to aid in the understanding of the dynamical behavior of the CR3BP. One such tool is known as the Poincaré map, or surface of section [9]. In 1892, Poincaré developed this concept; however, because of computational limitations, numerical computation of one of these surfaces did not occur for many years [9,19]. The concept of a Poincaré map may be applied to many dynamical systems. For example, the planar CR3BP possess a four-dimensional phase space. This four-dimensional phase space is reduced to a three-dimensional subspace when a particular value of the Jacobi Constant is chosen. This three-dimensional subspace is then ‘‘sliced’’ with a surface or hyperplane [9]. This ‘‘slice’’ further reduces the three-dimensional subspace to a two-dimensional subspace that may be viewed on a two-dimensional surface [9]. Next, many initial conditions at the particular value of the Jacobi Constant are chosen

and numerically integrated. Each time a trajectory passes through the surface, a point is plotted in the two-dimensional subspace. A one-sided Poincaré map only plots a point if the trajectory passes through the map in a specified direction, while a two-sided map plots a point each time a trajectory passes through the hyperplane regardless of direction. Figure 23 provides a notional example of a one-sided Poincaré map, while Figure 24 provides a notional example of a two-sided Poincaré map. On the one-sided map, a periodic trajectory passes through the map once per period at a single fixed point, while a periodic trajectory on the two-sided map is associated with two fixed points. The implementation of Poincaré maps may provide many

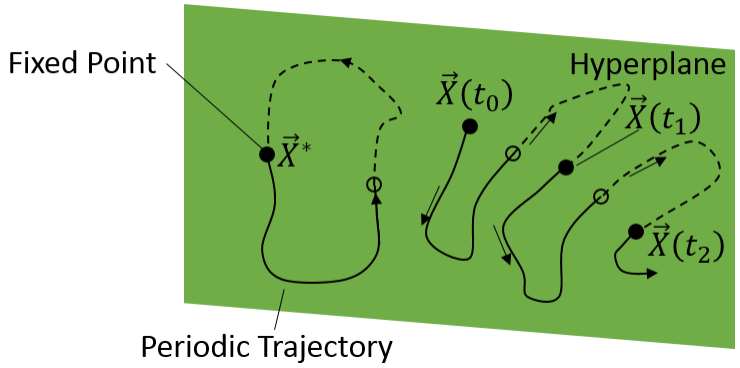

Figure 23. A Notional One-Sided Poincaré Map

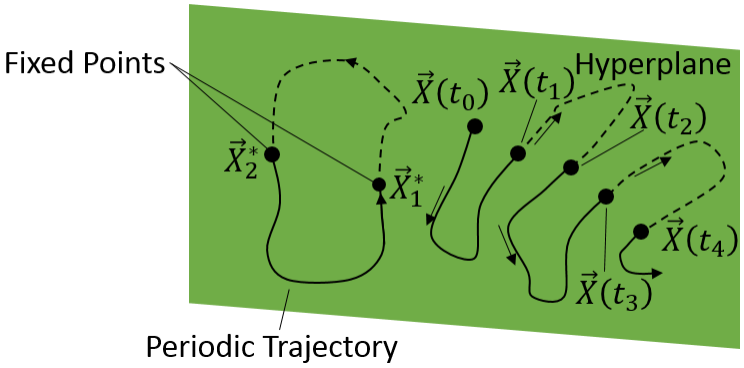

Figure 24. A Notional Two-Sided Poincaré Map

advantages to a dynamicist. Wiggins describes three of the potential advantages of using Poincaré maps [20].

1. ‘‘Dimensional Reduction’’: At least one variable may be removed from the problem through the implementation of a Poincaré map [20].

2. ‘‘Global Dynamics’’: Poincaré maps may provide insight into the global behavior of the dynamics in a dynamical system [20].

3. ‘‘Conceptual Clarity’’: The characteristics of particular trajectories may be easily identified/described through the use of a Poincaré map [20].

Figure 25 provides an example of a Poincaré map generated in the planar Earth-Moon CR3BP. The chosen value of the Jacobi Constant for the map was 3.17. Additionally, the chosen hyperplane is $y = 0$ when $\dot{y} > 0$. This Poincaré map is an example of a one-sided map. This Poincaré Map is generated using the *event* feature

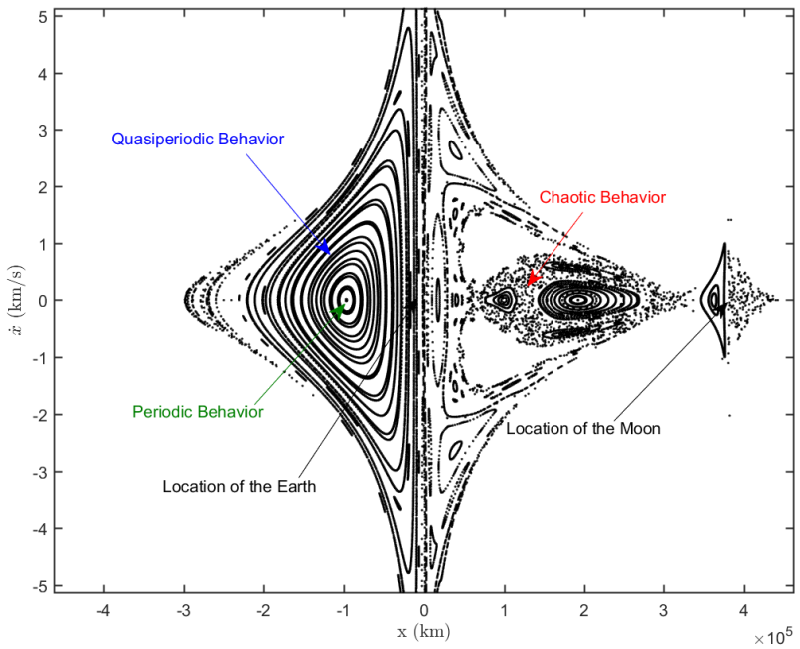

Figure 25. A Poincaré Map of the Planar Earth-Moon CR3BP With a Value of the Jacobi Constant Equal to 3.17, Where the Hyperplane is Defined as $y = 0$ and $\dot{y} > 0$.

of the built-in MATLAB® numerical integrator *ode45* [62]. An absolute and relative integration error tolerance was chosen to be 2.22045×10^{-14}. This tolerance is the

smallest quantity *ode45* will allow and corresponds to position and velocity errors in the Earth-Moon CR3BP of 0.0085 mm and 2.275×10^{-8} mm/s, respectively [62]. Additionally, this map represents the behavior of 78 trajectories that are seeded along the x-axis with $\dot{x} = 0$ and numerically integrated for 159 revolutions of the primaries, about 11.9 years. Many behaviors are evident on this Poincaré map. Fixed points that are enclosed by closed curves imply orbitally stable, in the linear sense, periodic behavior in terms of in-plane perturbations [9]. The closed curves themselves represent quasiperiodic behavior [9]. Finally, chaotic behavior is seen in the ''dusty'' regions [9]. Some outer regions of the map are blank because these regions of the phase space are inaccessible at this value of the Jacobi Constant [33]. Hénon describes the boundary between the accessible region and inaccessible region in the $x - \dot{x}$ plane as the Jacobi limit [33]. However, the internal regions where no points appear are a byproduct of the chosen initial conditions.

Many researchers have implemented Poincaré maps as a visual tool in the CR3BP. In 1966, Hénon investigated the Copenhagen problem (where $\mu = 0.5$) and generated Poincaré maps in the $x - \dot{x}$ plane at multiple values of the Jacobi Constant [33]. Vaquero and Howell generated multiple types of Poincaré maps to construct transfers between periodic orbits in the CR3BP [30, 31, 32]. Howell, Craig-Davis, and Haapala investigated the use of periapsis Poincaré maps near the smaller primary to characterize the long term behavior of the dynamics of a spacecraft in the vicinity of the smaller primary [26, 27, 35, 36, 37]. Wilmer also used periapse maps to construct transfers between a highly elliptical transfer orbit and a circular orbit and to predict the long term behavior of a spacecraft's trajectory near Earth in the Earth-Moon CR3BP [14]. Additionally, many researchers have investigated methods to attempt to visualize higher dimensional Poincaré maps. For example, the spatial CR3BP possesses a six-dimensional phase space. This solution space may be reduced by one dimension by

selecting a value of the Jacobi Constant and reduced by another dimension through the implementation of a surface of section. However, a four-dimensional space remains, and this four-dimensional space may be challenging to visualize. Geisel investigated the employment of a ‘‘space-plus-color’’ method to visualize such a map [19]. Haapala utilized a glyph method to represent the fourth dimension [27]. Clearly, many methods for creating and visualizing Poincaré maps exist.

2.21 Chapter 2 Summary

This chapter provides the foundation and necessary background for the current investigation. A brief historical overview of astrodynamics is provided. Then, the 2BP and its known analytical solution, in terms of conics, is discussed. Next, the nondimensional equations of motion for the CR3BP are derived. Other qualities of the CR3BP are presented, such as the lack of a known closed-form analytical solution, the Jacobi Constant, and the ZVSs. The equilibrium points of the CR3BP are described, as well as their Lyapunov stability based on a linear analysis. Numerical integration and its essential utility in the CR3BP are presented. Additionally, the STM is introduced as a method to predict neighboring trajectories based on a linear analysis of a reference trajectory. The STM leads to the development of targeting algorithms to solve for particular solutions that satisfy desired constraints using an appropriate convergence criterion and within a given tolerance. These targeting methods are applied to compute periodic orbits. Their associated monodromy matrices are shown to contain information about the orbital stability of a periodic orbit based on a linear analysis leveraging Floquet theory. Invariant manifolds in the CR3BP are defined and potential applications are discussed. Finally, Poincaré maps are introduced as a method to understand the global dynamical behavior of the CR3BP at a particular value of the Jacobi Constant.

3. Methodology

This chapter describes the methodology implemented to address the problem statement as defined in Section 1.5. First, a test plan overview is presented that details each of the four test cases explored in the current investigation. Then, the continuation method employed to generate families of periodic orbits is described. Next, periapsis Poincaré maps are discussed in detail, including a description of the applications of such maps to generate initial conditions for resonant orbits. Discussion of the numerical optimization algorithm utilized to search for locally optimal solutions is also included in this chapter. Finally, metrics are introduced to quantify the performance of a satellite based on its ability to remotely sense the surface of the Earth.

The current investigation employs MATLAB® version 8.6.0.267246 (R2015b) with the following benchmark times: 0.1178 0.0721 0.0488 0.1081 0.2358 0.2861 [38]. Additionally, simulations are performed on a Windows 7 computer operating with an Intel(R) Xeon(R) Central Processing Unit E3-1241 version 3 at 3.50 GHz and 32.0 GB of RAM.

3.1 Test Plan Overview

This section outlines the test plan implemented by the current investigation. First, constellations of interest are defined. Then, each of the four test cases are described as well as the subcases associated with each test case. To simplify the explanation of the test plan, a flowchart is presented in Figure 26 to provide a visual explanation of the test plan.

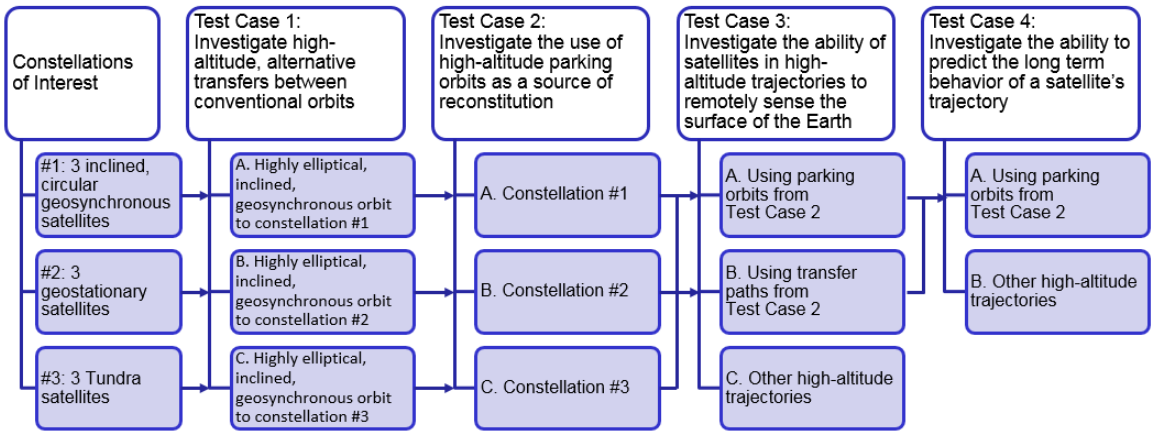

Figure 26. A Flowchart Providing an Overview of the Test Plan Implemented in the Current Investigation

3.1.1 Constellations of Interest

Three different constellations are used as examples in the current investigation. Each of the three constellations of interest consist of three satellites to reflect practical scenarios; however, the results and analysis of the current investigation are not affected by the number of satellites in each constellation. The first constellation consists of three circular, geosynchronous orbits that lie in the Earth-Moon orbital plane. The second constellation consists of three geostationary orbits. And the third constellation consists of three Tundra orbits. The second and third constellations do not lie in the Earth-Moon orbital plane, so these constellations are modeled in the spatial Earth-Moon CR3BP. These three constellations serve as the destinations for alternative transfers in Test Case 1 and as constellations requiring reconstitution in Test Case 2.

3.1.1.1 A Constellation of Three Satellites in Circular, Geosynchronous Orbits that Lie in the Earth-Moon Orbital Plane

The first constellation of interest in the current investigation is a constellation consisting of three circular, geosynchronous orbits that lie in the Earth-Moon orbital plane in the Earth-Moon CR3BP and are equally spaced in argument of latitude.

Three satellites are chosen because continuous coverage of much of the Earth's surface is possible from this type of constellation. Since these orbits are circular, the true anomaly and argument of perigee are undefined, so the argument of latitude is used instead. This constellation lies in the plane of the primaries, $z = 0$ and $\dot{z} = 0$ for all time. In a two-body sense, these orbits may be thought of as inclined geostationary orbits, where the inclinations of these orbits with respect to the Earth's equatorial plane are equal to the inclination of the Moon's orbit. The inclination of the Moon with respect to the Earth's equatorial plane varies between $18°19'$ and $28°35'$ with a period of approximately 18.6 years [40]. In the current investigation, an epoch date of January 1st, 2020 is chosen. Table 5 describe the COEs of the Moon in the J2000 frame according to the Jet Propulsion Laboratory HORIZONS System web-interface [98].

Table 5. The COEs of the Moon in the J2000 Coordinate System on January 1st, 2020

Classical Orbital Element	Value
Semimajor Axis	380,829.3800328925 km
Eccentricity	0.06489698455553032
Inclination	23.25318622894357°
Right Ascension of the Ascending Node	13.35674872265993°
Argument of Perigee	167.5204121678992°
True Anomaly	166.1472628026251°

The COEs of each of the satellites in this constellation are described in Table 6. Note that since the orbits are circular, the argument of latitude is measured instead of the argument of perigee and true anomaly. Also, the argument of latitude of the first satellite, u_0, is arbitrary, but the other satellites may be defined in terms of u_0. Figure 27 shows a screenshot from Systems Tool Kit® (STK) of this constellation of

Table 6. The COEs of a Constellation of Three Circular Geosynchronous Orbits That Lie in the Earth-Moon Orbital Plane in the J2000 Coordinate System on January 1st, 2020

Classical Orbital Element	Satellite #1	Satellite #2	Satellite #3
Semimajor Axis	42,164.17272328596 km		
Eccentricity	0		
Inclination	23.25318622894357°		
Right Ascension of the Ascending Node	13.35674872265993°		
Argument of Latitude	u	$u + 120°$	$u + 240°$

inclined, circular, geosynchronous satellites in the inertial frame [99].

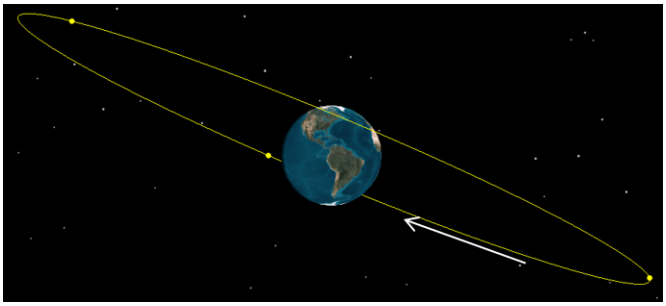

Figure 27. STK Screenshot of A Constellation of Three Satellites in Circular Geosynchronous Orbits Equally Spaced in Argument of Latitude [99]

In a two-body model, this constellation would be periodic in the inertial frame. However, when modeled in the CR3BP, this is no longer the case. The orbits become only approximately periodic. Figure 28 shows the behavior of a trajectory with the initial conditions of a circular geosynchronous orbit that lies in the Earth-Moon orbital plane. In the current investigation, to transition COEs in the J2000 frame to nondimensional position and velocity components in the barycentric rotating frame, the following process is employed. First, the COEs are transitioned into position and velocity components in the J2000 frame using the transformations described by Bate, Mueller, and White [40]. Then, following the development by Pavlak, an

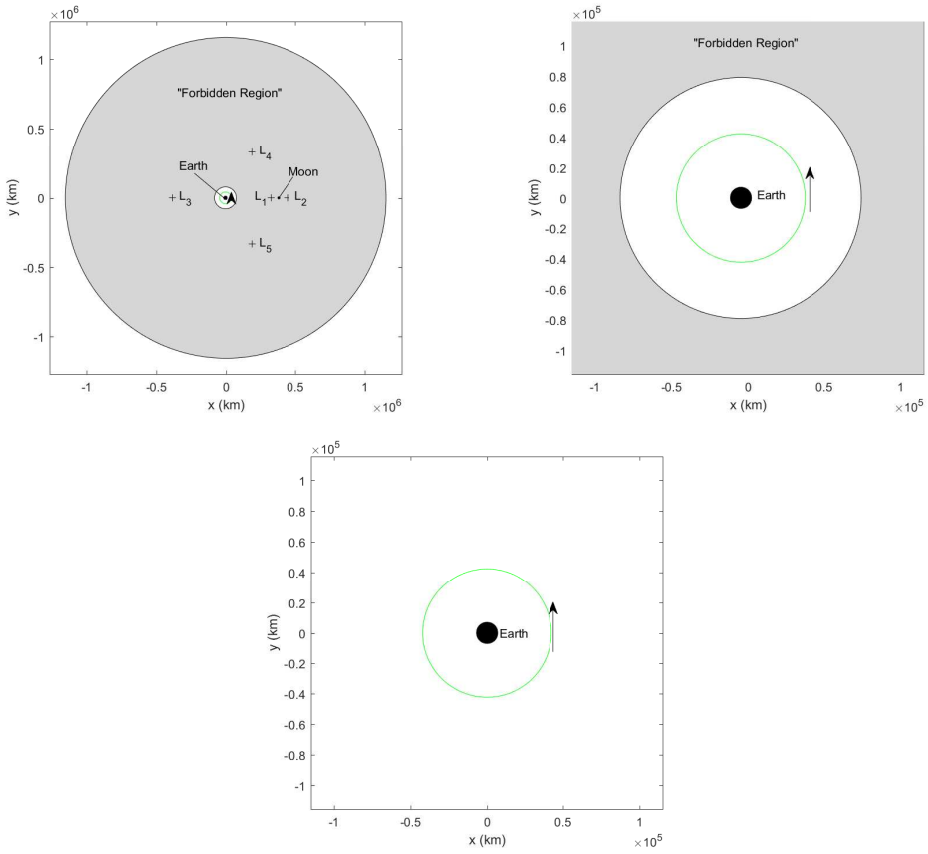

Figure 28. The Initial Conditions of a Satellite in a Circular Geosynchronous Orbit that Lies in the Earth-Moon Orbital Plane Numerically Integrated in the Earth-Moon CR3BP for 10 Nondimensional Time Units, About 43.42 Days (Top Left: Zoomed Out View in the Barycentric Rotating Frame; Top Right: Zoomed in View in the Barycentric Rotating Frame; Bottom Center: Earth-Centered Inertial Frame)

instantaneous barycentric rotating frame is defined in the J2000 frame based on the position and velocity of the Moon in the J2000 frame [28]. Next, a transformation is performed to transform the position and velocity components from the J2000 frame into the instantaneously defined barycentric rotating frame. Finally, the position and velocity components are nondimensionalized using the characteristic quantities [28].

A satellite in a circular geosynchronous orbit that lies in the plane of the primaries appears to be periodic in both the rotating and inertial frame; however, this trajectory is only approximately periodic in both of these frames when modeled in the Earth-

Moon CR3BP. If the gravitational effects of the Moon were not included in this model, then these orbits would be periodic conic solutions.

3.1.1.2 A Constellation of Three Geostationary Satellites

The second constellation of interest is a constellation of three geostationary satellites that are equally spaced in true longitude. This constellation consists of three circular orbits with a period of one sidereal day that lie in the equatorial plane of the Earth. Because of this, the true anomaly, argument of perigee, and right ascension of the ascending node are undefined. Instead, the true longitude is used to describe a satellite's position in such an orbit. Three satellites are chosen because this type of constellation can provide continuous coverage of the Earth's surface between 65 degrees north and 65 degrees south [1]. Unlike the first constellation of interest, this constellation may be defined independently of the position of the Moon. Table 7 describes the COEs of each satellite in this constellation. Note that since these orbits are circular with zero inclination, the true longitude, l, is defined rather than the right ascension of the ascending node, argument of perigee, and true anomaly. Figure 29 shows a screenshot from STK of this constellation of three geostationary satellites in the inertial frame [99].

In a two-body model, this constellation of satellites in geostationary orbits would be periodic in the inertial frame. However, when modeled in the CR3BP, the orbits become only approximately periodic. Figure 30 shows the behavior of a trajectory with the initial conditions of a geostationary orbit modeled in the Earth-Moon CR3BP.

A satellite in a geostationary orbit lies in the equatorial plane of the Earth but does not lie in the Earth-Moon orbital plane. This difference in inclination is evident from the view of such an orbit in the barycentric rotating frame. Unlike the first constellation of interest, this orbit departs the Earth-Moon orbital plane. Additionally,

Table 7. The COEs of a Constellation of Three Satellites in Geostationary Orbits in the J2000 Coordinate System on January 1st, 2020

Classical Orbital Element	Satellite #1	Satellite #2	Satellite #3
Semimajor Axis	42,164.17272328596 km		
Eccentricity	0		
Inclination	0°		
True Longitude	l	$l + 120°$	$l + 240°$

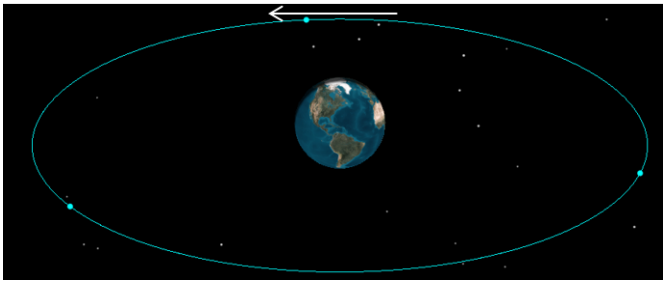

Figure 29. STK Screenshot of A Constellation of Three Satellites in Geostationary Orbits Equally Spaced in True Longitude [99]

when viewed in the inertial frame, this trajectory appears nearly periodic. However, because of the gravitational effects of the Moon, this trajectory is only approximately periodic.

3.1.1.3 A Constellation of Three Tundra Satellites

The third constellation of interest consists of three Tundra satellites that are equally spaced in mean anomaly, M. A Tundra orbit is an elliptical geosynchronous orbit with an inclination of approximately 63.4 degrees. This critical inclination results in a value of zero for the secular change of the argument of perigee due to the oblateness of the Earth. Additionally, the argument of perigee of such an orbit is chosen as 270 degrees or 90 degrees depending on if the constellation is tasked with coverage of the northern hemisphere or southern hemisphere, respectively. Since these

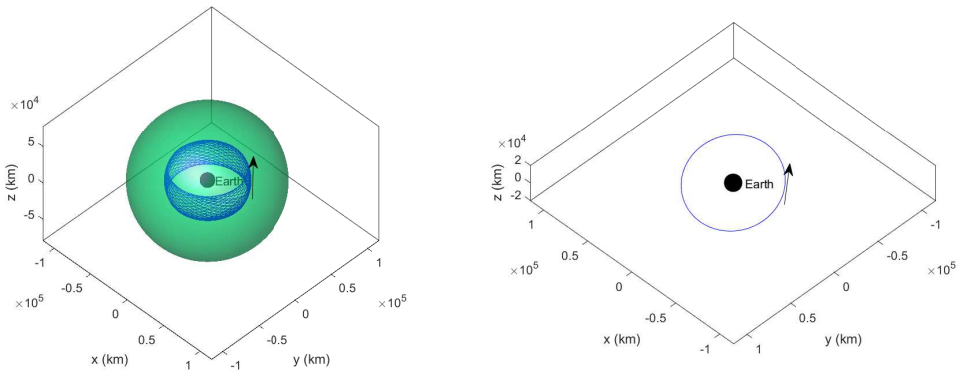

Figure 30. The Initial Conditions of a Satellite in a Geostationary Orbit Numerically Integrated in the Earth-Moon CR3BP for 10 Nondimensional Time Units, About 43.42 Days, with the ZVSs Depicted in Green (Left: Barycentric Rotating Frame; Right: Earth-Centered Inertial Frame)

orbits are elliptical, they will dwell near apogee. Three satellites in Tundra orbits that are equally spaced in mean anomaly are capable of providing continuous coverage to the desired hemisphere [60]. In the current investigation, an argument of perigee equal to 270 degrees is chosen. Figure 31 shows a screenshot from STK of this constellation of three Tundra satellites in the inertial frame [99].

Table 8. The COEs of a Constellation of Three Satellites in Tundra Orbits in the J2000 Coordinate System on January 1st, 2020

Classical Orbital Element	Satellite #1	Satellite #2	Satellite #3
Semimajor Axis	42,164.17272328596 km		
Eccentricity	0.825014116880199		
Inclination	63.4°		
Argument of Perigee	270°		
Mean Anomaly	M	$M + 120°$	$M + 240°$

In a two-body model, this constellation would be periodic in the inertial frame. However, when modeled in the Earth-Moon CR3BP, this is no longer the case. The

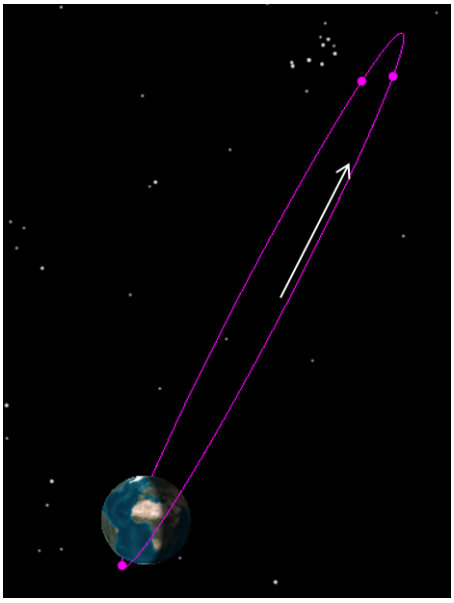

Figure 31. STK Screenshot of A Constellation of Three Satellites in Tundra Orbits Equally Spaced in Mean Anomaly [99]

Tundra orbit modeled in the Earth-Moon CR3BP is only approximately periodic in the inertial frame. Figure 32 shows the behavior of a trajectory with the initial conditions of a Tundra orbit.

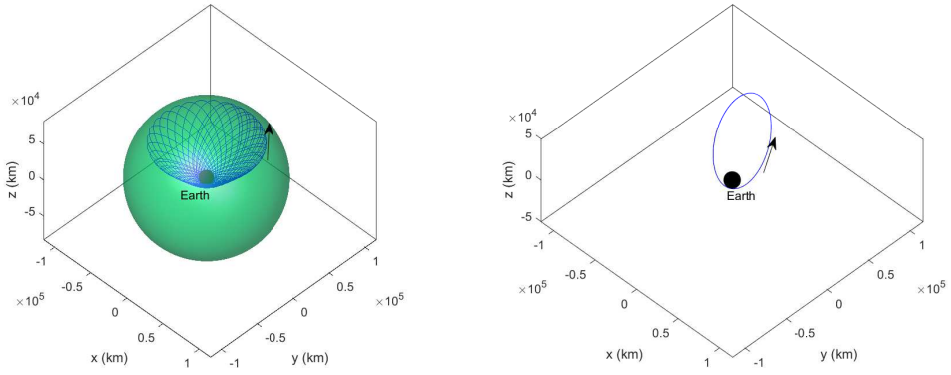

Figure 32. The Initial Conditions of a Satellite in a Tundra Orbit Numerically Integrated in the Earth-Moon CR3BP for 10 Nondimensional Time Units, About 43.42 Days, with the ZVSs Depicted in Green (Left: Barycentric Rotating Frame; Right: Earth-Centered Inertial Frame)

As seen in Figure 32, the Tundra orbit is not a periodic orbit in the barycentric rotating frame. If the numerical integration were to continue, the trajectory would

continue to overlap itself in this frame. However, in the inertial frame, the orbit does appear to be nearly periodic. This near-periodicity occurs because without the gravitational effects of the Moon, this orbit would be periodic. The addition of the gravitational effects of the Moon perturb this trajectory enough such that the orbit is not periodic. Additionally, one of the key features of a Tundra orbit is that the argument of perigee remains constant when modeling the oblateness effects (J_2) of the Earth. These effects are not modeled in the current investigation.

3.1.2 Test Case 1: High-Altitude Alternative Transfers Between Conventional Orbits

In the current investigation, Test Case 1 investigates high-altitude transfers between conventional orbits. The starting orbit for each of these transfers is an elliptical, geosynchronous orbit that lies in the Earth-Moon orbital plane. The semimajor axis and eccentricity of this starting orbit are the same as the semimajor axis and eccentricity of the Tundra orbits defined in the third constellation of interest. However, the inclination and right ascension of the ascending node are defined to be the same inclination and right ascension of the ascending node of the Moon at the epoch time of January 1st, 2020. Table 9 describes the COEs of this starting orbit.

Table 9. The COEs of a Satellite in the Starting Orbit for Test Case 1 in the J2000 Coordinate System on January 1st, 2020

Classical Orbital Element	Starting Orbit
Semimajor Axis	42,164.17272328596 km
Eccentricity	0.825014116880199
Inclination	23.25318622894357°
Right Ascension of the Ascending Node	13.35674872265993°

Alternative transfers are investigated from this starting orbit to each of the three constellations of interest described in Section 3.1.1 using high-altitude trajectories modeled in the Earth-Moon CR3BP. Initial guesses for these high-altitude transfers are developed using a periapsis map (see Section 3.3) of the invariant manifold approximations of a periodic orbit as a visual aid. Feasible solutions are then targeted through the implementation of a multiple-shooting algorithm. Finally, a numerical optimization algorithm is implemented to search for a locally optimal solution in terms of ΔV. Specifically, *fmincon*, a function in the MATLAB® Optimization Toolbox, is employed [84]. The cost of these transfers are compared to conventional Hohmann-type transfers.

3.1.2.1 Test Case 1A: Alternative High-Altitude Transfers from an Elliptical Geosynchronous Orbit that Lies in the Earth-Moon Orbital Plane to a Circular Geosynchronous Orbit that Lies in the Earth-Moon Orbital Plane

In Test Case 1A, high-altitude transfers modeled in the Earth-Moon CR3BP between an elliptical geosynchronous orbit and a circular geosynchronous orbit are investigated. A notional image depicting these two orbits is shown in Figure 33. Both the starting orbit and ending orbit lie in the Earth-Moon orbital plane, so a planar trajectory in the Earth-Moon CR3BP is utilized as a transfer path. Initial guesses are developed using a periapsis map of the invariant manifold approximations of a periodic orbit as a visual aid. Feasible solutions are then generated using a multiple-shooting algorithm. This feasible solution is input as an initial guess into an optimization algorithm employing *fmincon*. Wilmer also investigated high-altitude transfers modeled between two similar orbits [14]. However, Wilmer utilized a periapsis map of the invariant manifold approximations of a Lyapunov orbit in the Earth-Moon

CR3BP [14]. Additionally, Wilmer did not use *fmincon* to locally optimize the transfer in terms of ΔV.

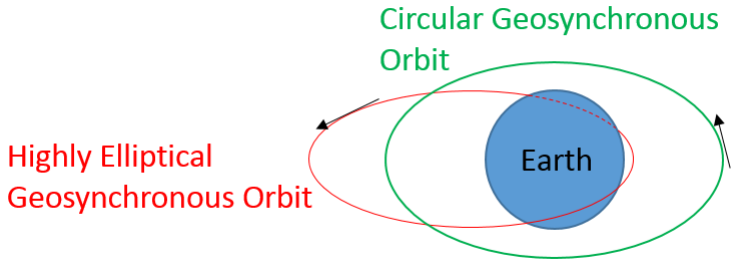

Figure 33. A Notional Depiction of the Starting Highly Elliptical Geosynchronous Orbit and the Ending Circular Geosynchronous Orbit that Both Lie in the Earth-Moon Orbital Plane

The cost of this high-altitude conventional transfer is then compared to a traditional transfer. A conventional Hohmann-type transfer between the starting orbit and the ending orbit requires approximately 1.383 km/s of ΔV. This cost, in terms of ΔV, assumes the first burn is performed at apogee of the starting orbit. This tangent burn will place the spacecraft into an elliptical transfer orbit with an apogee altitude equal to the apogee altitude of the starting orbit and a perigee altitude equal to the altitude of the ending orbit. A second tangent burn is then performed at perigee of this orbit to complete the transfer. This ΔV calculation is a correction to Wilmer's calculations of the ΔV required to transfer between these two orbits using a Hohmann-type transfer [14]. Wilmer's calculations contain an error in the computation of the second burn of this transfer. Wilmer incorrectly uses the velocity at apogee of the transfer ellipse as the velocity at perigee of the transfer ellipse. This error results in a total ΔV of 3.129 km/s. However, the actual required ΔV to perform this transfer is 1.383 km/s. Wilmer also incorrectly calculates the ΔV required to perform a Hohmann-type transfer to the ending orbit that begins at the perigee of the starting orbit. Wilmer calculates a ΔV of 6.776 km/s, while the actual required ΔV to perform this transfer is 1.737 km/s.

3.1.2.2 Test Case 1B: Alternative High-Altitude Transfers from an Elliptical Geosynchronous Orbit that Lies in the Earth-Moon Orbital Plane to a Geostationary Orbit

In Test Case 1B, high-altitude transfers modeled in the Earth-Moon CR3BP between a geosynchronous elliptical orbit that lies in the Earth-Moon orbital plane and a geostationary orbit are investigated. The starting orbit lies in the Earth-Moon orbital plane, while the ending orbit lies in Earth's equatorial plane. Figure 34 shows a notional image of these two orbits. Since these two orbits lie in different planes with different inclinations, an inclination change will be required. Additionally, the Earth-Moon spatial CR3BP is utilized since both of these orbits do not lie in the plane of the primaries. Planar initial guesses are developed using a periapsis map of the invariant manifold approximations of a periodic orbit. Feasible solutions are then targeted through the implementation of a multiple-shooting algorithm. Finally, *fmincon* is implemented to search for a locally optimal solution in terms of ΔV.

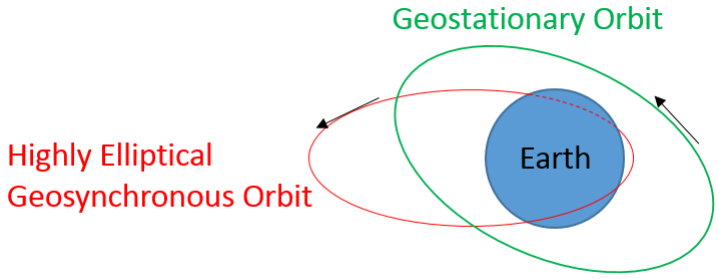

Figure 34. A Notional Depiction of the Starting Highly Elliptical Geosynchronous Orbit that Lies in the Earth-Moon Orbital Plane and the Ending Geostationary Orbit

The ΔV required to perform this alternative transfer is compared with a conventional transfer path. The cost of a conventional Hohmann-type transfer to perform this transfer is 1.526 km/s. The first burn of this transfer path utilizes a combined plane change at the apogee of the starting orbit to change inclination and transfer into an elliptical transfer orbit. The apogee altitude of this elliptical transfer orbit is

equal to the apogee altitude of the starting orbit, while the perigee altitude is equal to the altitude of the geostationary satellite. When the satellite is at perigee of this transfer ellipse, the second burn is performed to circularize the orbit and complete the transfer.

3.1.2.3 Test Case 1C: Alternative High-Altitude Transfers from an Elliptical Geosynchronous Orbit that Lies in the Earth-Moon Orbital Plane to a Tundra Orbit

In Test Case 1C, high-altitude transfers modeled in the Earth-Moon CR3BP between an elliptical orbit that lies in the Earth-Moon orbital plane and a Tundra orbit are explored. Figure 35 shows a notional depiction of these two orbits. Similar to Test Case 1B, an inclination change will be required to perform this transfer and the trajectories are modeled in the spatial Earth-Moon CR3BP. Planar initial guesses are developed using a periapsis map of the invariant manifold approximations of a periodic orbit. Feasible solutions are then targeted through the implementation of a multiple-shooting algorithm. Finally, *fmincon* is implemented to search for a locally optimal solution in terms of ΔV.

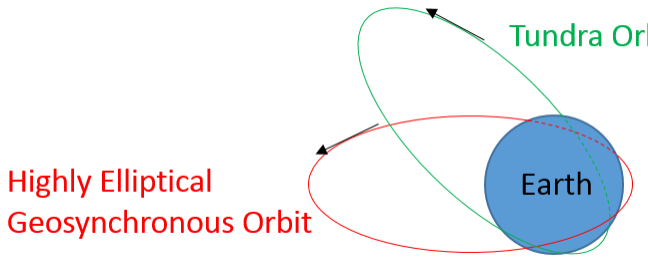

Figure 35. A Notional Depiction of the Starting Highly Elliptical Geosynchronous Orbit that Lies in the Earth-Moon Orbital Plane and the Ending Tundra Orbit

Next, the cost of this alternative transfer is compared to the cost of a conventional transfer. The required ΔV to perform this transfer using a conventional Hohmann-

type transfer is 2.989 km/s. The first burn of this transfer utilizes a combined plane change at the apogee of the starting orbit to change inclination and circularize the orbit. Then, a tangent second burn is performed at the apogee of the ending orbit to complete the transfer.

3.1.3 Test Case 2: The Application of High-Altitude Parking Orbits to Reconstitute Conventional Constellations

Conventional reconstitution methods require the launch of a new satellite to restore a degraded capability. Alternatively, in Test Case 2, the utility of a satellite in a high-altitude parking orbit as a source of reconstitution to each of the constellations of interest described in Section 3.1.1 is explored. A satellite in a high-altitude parking orbit would wait until it is tasked to reconstitute a constellation. Then, the spacecraft would perform a transfer to reconstitute the constellation. Reconstitution from a high-altitude parking orbit may be less detectable than a launch from the surface of the Earth. Additionally, the intent of the satellite in a high-altitude parking orbit may be unclear to an observer, while providing timely and cost-effective transfer opportunities to a desired capability. Candidate parking orbits in the current investigation are chosen after a multitude of planar resonant families were generated and the resonant families generated by other researchers were investigated. Vaquero and Howell provide many examples of resonant families in the Earth-Moon CR3BP [30, 31, 32]. From the generated resonant families, candidate parking orbits are selected because they possess the desirable characteristics, as defined by the current investigation. These desirable characteristics are listed and defined below.

1. Orbital instability and maneuverability of a spacecraft in the parking orbit

2. Proximity to the Moon during portions of the parking orbit

3. Proximity to geostationary altitude (35,786 km) during portions of the parking orbit

4. Ability to provide additional capability while in the high-altitude parking orbit waiting to be tasked with reconstitution

The first desired characteristic of a high-altitude parking orbit designed for reconstitution is orbital instability. While this characteristic may seem undesirable because stationkeeping requirements would be expected to be larger than an orbitally stable parking orbit, due to the sensitivity of this type of orbit to perturbations, a spacecraft in an orbitally unstable periodic orbit may be able to perform transfers for low ΔV. The invariant manifold approximations associated with the unstable periodic orbit may provide low-ΔV transfers to and from the periodic orbit. Geisel compares the ''maneuverability'' of a spacecraft in a sensitive region of the phase space to the added maneuverability of an unstable fighter aircraft [19]. The stability of a conventional civilian aircraft may make it simpler to design and operate, but the added maneuverability of an unstable aircraft may be desirable for military purposes. Actions are required to account for these instabilities, but additional maneuverability is possible. A spacecraft in a sensitive region of the phase space may require more nondeterministic ΔV for stationkeeping than a spacecraft in a less sensitive region of the phase space, but it may be able to perform low-ΔV maneuvers to alter the long term behavior of its trajectory. The invariant manifolds of a parking orbit may allow for these cost-effective maneuvers to be performed and to allow the timely reconstitution of conventional constellations. The second desired characteristic of this type of parking orbit is proximity to the Moon. This proximity may allow for a spacecraft to effectively exploit the gravitational effects of the Moon. This exploitation may be especially beneficial when performing inclination changes. The third desired characteristic is proximity to geostationary altitude (35,786 km). This proximity

may allow for nearly direct transfers from the parking orbit to the constellations of interest. In the current investigation, proximity to this altitude is considered desirable regardless of inclination. Additionally, this behavior may allow for the utilization of a resonant arc associated with the periodic orbit as an initial guess for a transfer path. Wilmer showcased the employment of a resonant arc of a periodic orbit as an initial guess for a high-altitude transfer to a geostationary orbit [14]. One potential downside of deploying a satellite into a high-altitude parking orbit for reconstitution purposes is that a satellite in this orbit is not performing its primary mission until the need for reconstitution arises. However, the satellite may be able to provide additional capability while waiting to be tasked with reconstitution. This ability to provide additional capability while in the parking orbit is the fourth desired characteristic of a parking orbit and is investigated further in Test Case 3.

Reconstitution from a high-altitude parking orbit may be implemented as an alternative to launching a new satellite to reconstitute a degraded capability. The cost, in terms of ΔV, to deploy a satellite into the high-altitude parking orbit and to transfer from the high-altitude parking orbit to the constellation of interest is compared with the cost of a Hohmann transfer from a 300 km LEO to a circular geosynchronous orbit in the Earth-Moon orbital plane. Both of these ΔV calculations neglect the cost, in terms of ΔV, to launch the satellite into the initial LEO; however, it is assumed that the launch ΔV to LEO for both scenarios are similar. Additionally, the timeliness of this alternative transfer is compared with an assumed launch-on-demand capability requiring 30 days lead time. This assumption is based on the assertion by *JP 3-14* that ‘‘current launch campaigns take weeks to months to generate and execute’’ assuming that both the satellite and launch vehicle are prepared and on site [1]. When comparing to a launch-on-demand capability, the current investigation

assumes that the satellite and launch vehicle are prepared and on site, but the launch campaign still requires 30 days lead time.

It should be noted that the reconstitution of a particular satellite requires the precise timing of transfers to ensure that the reconstituting satellite is able to rendezvous with the satellite that needs to be reconstituted. The precise timing of these transfers is not addressed in the current investigation. However, small ΔVs, or phasing maneuvers, may be performed after the transfers presented in the current investigation are completed. Such phasing maneuvers could be used to adjust the position of the reconstituting satellite to complete the rendezvous with the satellite that requires reconstitution.

3.1.3.1 Test Case 2A: The Reconstitution of A Constellation of Three Circular Geosynchronous Orbits That Lie in the Earth-Moon Orbital Plane from a High-Altitude Parking Orbit

In Test Case 2A, a satellite in a high-altitude parking orbit and its potential as a source of reconstitution of a constellation of three circular, geosynchronous orbits that lie in the Earth-Moon orbital plane are investigated. Figure 36 shows a notional image of the initial LEO and a circular geosynchronous orbit that both lie in the Earth-Moon Orbital Plane. Not depicted in this image is the high-altitude parking orbit where the satellite will wait until tasked with reconstitution. Initial guesses from the initial LEO to the parking orbit are developed using a periapsis Poincaré map of the stable and unstable manifolds of the periodic orbit. Feasible solutions are targeted through the implementation of a multiple-shooting targeting algorithm. Finally, *fmincon* is implemented to search for a locally optimal solution in terms of ΔV. Then, resonant arcs of a periodic, resonant orbit are input as initial guesses into a multiple-shooting algorithm to target a feasible transfer from the parking orbit to the constellation of

circular geosynchronous orbits. Again, *fmincon* is implemented to search for locally optimal transfers from the high-altitude parking orbit to the constellation.

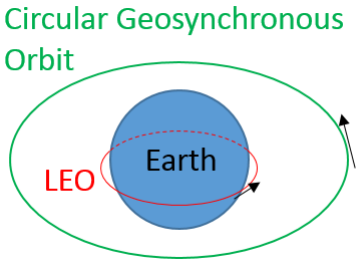

Figure 36. A Notional Depiction of the Starting LEO and the Ending Circular Geosynchronous Orbit that Both Lie in the Earth-Moon Orbital Plane

A traditional Hohmann transfer from LEO to a circular, geosynchronous orbit requires approximately 3.893 km/s of ΔV. This baseline ΔV is compared to the cost, in terms of ΔV, of reconstitution from the high-altitude parking orbit. The timeliness is then assessed by comparing the time to perform the alternative transfer with a launch-on-demand capability.

3.1.3.2 Test Case 2B: The Reconstitution of A Constellation of Three Geostationary Orbits from a High-Altitude Parking Orbit

In Test Case 2B, the exploitation of high-altitude orbits modeled in the Earth-Moon CR3BP as a source of reconstitution for a constellation of three equally spaced, geostationary orbits is investigated. Figure 37 shows the initial LEO that lies in the Earth-Moon orbital plane and a geostationary orbit. Not depicted in this image is the high-altitude parking orbit where the satellite will wait until tasked with reconstitution. Transfer paths from the high-altitude parking orbit to the geostationary orbits may not lie in the Earth-Moon orbital plane, so the spatial Earth-Moon CR3BP is implemented to model the dynamics of a transfer path between these orbits. Initial guesses are generated from a periapsis map of the invariant manifold approximations of the parking orbit. Feasible solutions are then targeted through the implementation of a

multiple-shooting algorithm. Finally, *fmincon* is implemented to search for locally optimal transfers in terms of ΔV.

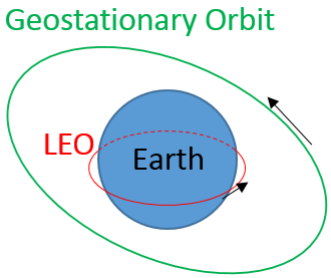

Figure 37. A Notional Depiction of the Starting LEO that Lies in the Earth-Moon Orbital Plane and the Ending Geostationary Orbit

The total ΔV of the reconstitution from a high-altitude parking orbit, which includes the ΔV from LEO to the parking orbit and from the parking orbit to the final orbit, is compared to the cost of a Hohmann-type transfer from a LEO that lies in the Earth-Moon orbital plane to a geostationary orbit. This conventional Hohmann-type transfer requires 4.145 km/s of ΔV. Additionally, the timeliness of the alternative reconstitution method from a high-altitude parking orbit is compared to a launch-on-demand capability.

3.1.3.3 Test Case 2C: The Reconstitution of A Constellation of Three Tundra Orbits from a High-Altitude Parking Orbit

In Test Case 2C, reconstitution of a constellation of three Tundra orbits from a high-altitude parking orbit is explored. Figure 38 shows a notional depiction of the initial LEO that lies in the Earth-Moon orbital plane and the final Tundra orbit. Not depicted in this image is the high-altitude parking orbit where the satellite will wait until tasked with reconstitution. Transfer paths from the high-altitude parking orbit to the Tundra orbits may not lie in the Earth-Moon orbital plane, so the spatial Earth-Moon CR3BP is again implemented to model the dynamics of a transfer path between

these orbits. In this test case, an initial guess is developed from the solution found in Test Case 1C. Feasible solutions are then targeted through the implementation of a multiple-shooting algorithm. Finally, *fmincon* is implemented to search for locally optimal transfers in terms of ΔV.

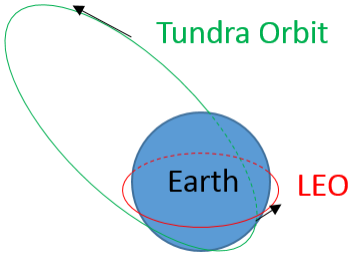

Figure 38. A Notional Depiction of the Starting LEO that Lies in the Earth-Moon Orbital Plane and the Ending Tundra Orbit

The total ΔV of the reconstitution from a high-altitude parking orbit is compared to the cost of a Hohmann transfer from LEO to a Tundra orbit. Note that in this case, the initial LEO does not lie in the Earth-Moon orbital plane. This difference is because from low-latitude launch sites, a satellite may be launched directly into a 63.4 degree inclination LEO, so a launch-on-demand capability would take advantage of this to reduce the required inclination change after launch. This conventional Hohmann-type transfer requires 2.955 km/s of ΔV. Additionally, the timeliness of the alternative reconstitution method from a high-altitude parking orbit is compared to a launch-on-demand capability.

3.1.4 Test Case 3: The Ability of a Satellite in a High-Altitude Orbit to Remotely Sense the Surface of the Earth

In Test Case 3, the ability of a satellite in high-altitude orbit to remotely sense the surface of the Earth is explored further. In Test Case 3A, high-altitude parking orbits waiting to be tasked for reconstitution are locally optimized in terms of their ability to remotely sense the surface of the Earth relative to a nominal satellite at

geostationary altitude. The ability of a satellite to remotely sense the surface of the Earth, while reconstituting a capability is investigated in Test Case 3B. Finally, in Test Case 3C, other high-altitude orbits, their performance in terms of the metrics defined in Section 3.5, and their applications are explored.

3.1.4.1 Test Case 3A: The Ability of a Satellite in a High-Altitude Parking Orbit to Remotely Sense the Surface of the Earth While It is Waiting to Be Tasked with Reconstitution

In Test Case 3A, the ability of a satellite to remotely sense the surface of the Earth while it is in a high-altitude parking orbit waiting to be tasked with reconstitution is investigated. Figure 39 shows a notional depiction of a satellite remotely sensing the surface of the Earth from a high-altitude parking orbit. In the current investigation,

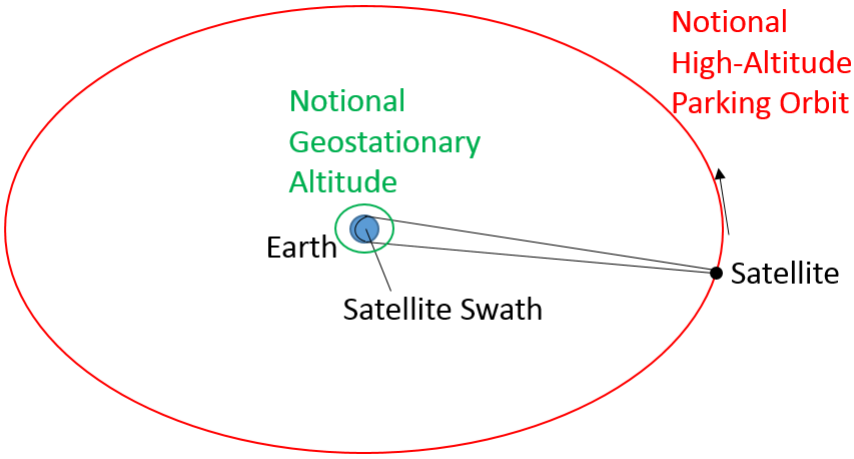

Figure 39. A Notional Depiction of a Satellite Remotely Sensing the Surface of the Earth from a Notional High-Altitude Parking Orbit

this performance is measured relative to a nominal satellite at geostationary altitude using the metric defined in Section 3.5.1. This metric quantifies the ability of a satellite in a high-altitude parking orbit to remotely sense the surface of the Earth. One of the downsides of deploying a satellite into a high-altitude parking orbit where

it will wait to be tasked with reconstitution is that this satellite must be launched but may never be deployed for reconstitution if the need never arises. However, if a satellite in such an orbit could add capability to an ongoing military mission while in a high-altitude parking orbit, then not only is mission assurance increased through the ability to reconstitute a capability, but a military capability is increased prior to the need for reconstitution. This additional capability is the focus of Test Case 3A. After finding a good candidate parking orbit for reconstitution, a locally optimal parking orbit, in terms of the average performance of this metric, is found.

3.1.4.2 Test Case 3B: The Ability of a Satellite in a High-Altitude Trajectory to Remotely Sense the Surface of the Earth While It is Reconstituting a Conventional Constellation

In Test Case 3B, the ability of a satellite to remotely sense the surface of the Earth as it is transferring from a high-altitude parking orbit to reconstitute a capability is investigated. Figure 40 shows a notional depiction of a satellite remotely sensing the surface of the Earth as it reconstitutes a notional constellation of interest from a notional high-altitude parking orbit. In this scenario, the capability of one of the constellations of interest has been degraded and the satellite in the high-altitude parking orbit has been tasked with the reconstitution of the degraded constellation. This test case investigates the ability of a satellite to remotely sense the specific region of the Earth's surface where the capability was lost while transferring from the high-altitude parking orbit to the constellation of interest. Once this transfer is complete, reconstitution of the degraded capability has been accomplished. To measure the ability to provide coverage of a degraded capability, another metric is defined in Section 3.5.2 that quantifies the ability of a satellite to remotely sense

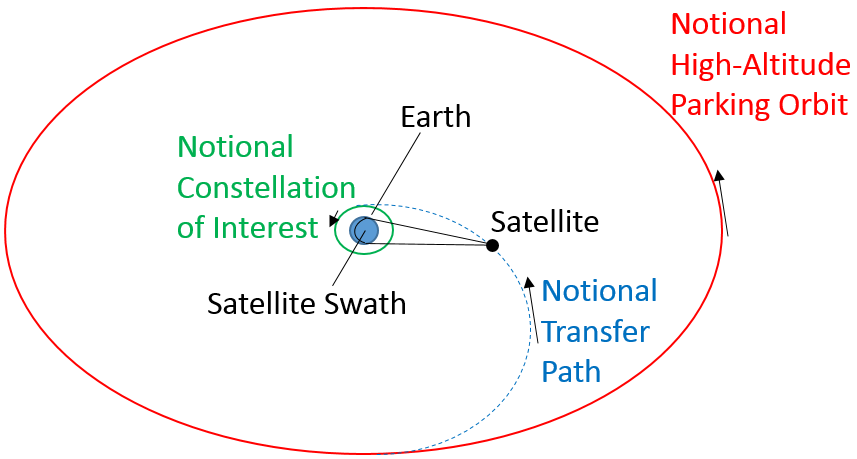

Figure 40. A Notional Depiction of a Satellite Remotely Sensing the Surface of the Earth as it Transfers from a Notional High-Altitude Parking Orbit to a Constellation of Interest

the surface of the Earth relative to a particular satellite. This performance is then compared to a launch-on-demand capability.

3.1.4.3 Test Case 3C: The Ability of a Satellite in a High-Altitude Trajectory to Remotely Sense the Surface of the Earth

In Test Case 3C, the ability of satellites in high-altitude orbits to remotely sense the surface of the Earth is investigated. Figure 41 shows a notional depiction of a satellite remotely sensing the surface of the Earth from a notional high-altitude trajectory. Unlike Test Cases 3A and 3B, this test case investigates the ability of a satellite in a high-altitude trajectory to remotely sense the surface of the Earth as a primary mission. Initial guesses for candidate periodic orbits are generated from a periapsis Poincaré map analysis. These initial guesses are then input into a single-shooting targeting algorithm to generate periodic orbits at a particular value of the Jacobi constant. The ability of a satellite in such an orbit to remotely sense the surface of the Earth is then measured using the metric defined in Section 3.5.1 that compares the trajectory to a nominal satellite at geostationary altitude. Then,

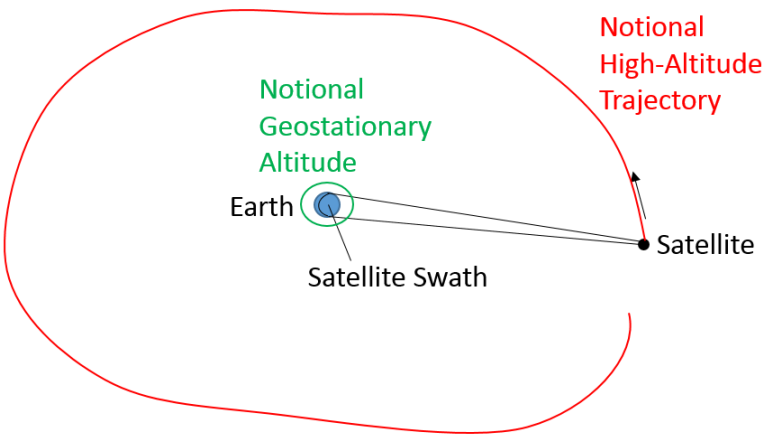

Figure 41. A Notional Depiction of a Satellite Remotely Sensing the Surface of the Earth from a Notional High-Altitude Trajectory

periodic orbits are input as initial guesses into an optimization algorithm that searches for locally maximum solutions in terms of the average performance of this metric. The ability to predict the long term behavior of a spacecraft's trajectory as it follows these trajectories is also discussed, as is the orbital stability.

3.1.5 Test Case 4: The Ability to Predict the Long Term Behavior of a Spacecraft's Trajectory Through the Utilization of a Periapsis Poincaré Map as a Visual Aid

In Test Case 4, the ability to predict the long term behavior of a spacecraft's trajectory through the utilization of a periapsis Poincaré map is investigated. First, in Test Case 4A, a periapsis Poincaré map is generated at a value of the Jacobi Constant equal to that of the high-altitude parking orbit investigated in Test Case 2 as a source of reconstitution. Then, in Test Case 4B, periapsis maps are generated at various values of the Jacobi Constant to demonstrate the qualitative changes in the Earth-Moon CR3BP as the value of the Jacobi Constant is changed. Additionally, a scenario is developed that illustrates the inability to predict the long term behavior of a spacecraft's trajectory that travels through chaotic regions of the phase space.

3.1.5.1 Test Case 4A: The Ability to Predict the Long Term Behavior of a Spacecraft's Trajectory in a High-Altitude Parking Orbit Waiting to Be Tasked with Reconstitution

In Test Case 4A, the ability to predict the long term behavior of a spacecraft's trajectory as it waits in a high-altitude parking orbit to be tasked with reconstitution is investigated. Specifically, the high-altitude parking orbit investigated in Test Case 2 is explored. First, a periapsis map is generated at the same value of the Jacobi Constant as the high-altitude parking orbit. These periapses are then color-coded based on the long term behavior associated with each periapse. In this test case, the long term behaviors include entering the vicinity of the Moon, collisions with the Earth or Moon, or a lack of these behaviors. In the current investigation, long term behavior is defined as the behavior of a spacecraft's trajectory over the next 100 nondimensional time units (approximately 1.19 years). After this analysis is performed, a periapsis Poincaré map of the invariant manifold approximations of the parking orbit are overlaid onto the periapsis Poincaré map depicting the long term behavior of a spacecraft's dynamics at this value of the Jacobi constant.

Since these two maps are generated at the same value of the Jacobi constant, a perfect overlap between two periapses implies that there is a zero-ΔV transfer that exists between the two trajectories. In the more likely case that two periapses are close to each other, but not overlapping, there may exist a low-ΔV transfer between these two trajectories. Of particular interest, in the current investigation, are periapses along the unstable manifold approximation associated with the parking orbit that are close to periapses that possess various long term behaviors. Regions that possess such behavior imply that a spacecraft in the periodic parking orbit could depart the periodic parking orbit for low ΔV along the unstable manifold approximations and perform a low-ΔV transfer to one of the periapses that possesses the desired long term

behavior. This possibility may allow for a spacecraft in the high-altitude parking orbit to alter the long term behavior of its trajectory for low ΔV. The long term behavior of such a spacecraft's trajectory may be deemed unpredictable.

3.1.5.2 Test Case 4B: The Ability to Predict the Long Term Behavior of a Spacecraft's Trajectory at Various Values of the Jacobi Constant

In Test Case 4B, the ability to predict the long term behavior of a spacecraft's trajectory at various values of the Jacobi constant is investigated. First, periapsis Poincaré maps are generated at various values of the Jacobi Constant. Then, the periapses on these maps are color-coded based on their long term behavior. Again, in the current investigation, long term behavior is defined as the next 100 nondimensional time units (approximately 1.19 years). The long term behaviors of interest in this test case are listed below.

- Trajectories that remain in the vicinity of the Earth.
- Trajectories that collide with the Earth.
- Trajectories that depart through the L_1 gateway and then depart through the L_2 gateway.
- Trajectories that depart through the L_1 gateway and then collide with the Moon.
- Trajectories that depart through the L_1 gateway and then return to the vicinity of the Earth.
- Trajectories that depart through the L_1 gateway, then depart through the L_2 gateway, and finally, return to the vicinity of the Earth through the L_1 gateway.

The evolution of the structures evident from these periapsis Poincaré maps is then analyzed. Then, the utilization of these maps as a mission designer is demonstrated through the design of a scenario where a satellite in a chaotic region of the phase space is able to alter the long term behavior of its trajectory through low-ΔV transfers. Additionally, the inverse of this question is proposed and the predictability of an observed spacecraft's trajectory is discussed.

3.2 Continuation Method

As discussed in Section 2.17, once a periodic orbit has been targeted within the convergence criteria, a continuation method may be implemented to generate a portion of a family of periodic orbits. This family of periodic orbits lies on a hodograph, which is a curve in the phase space that represents initial conditions for each member in the family. The first step to generating a portion of a family of periodic orbits in the CR3BP is to target an initial periodic orbit. Then, a continuation method may be implemented to attempt to follow along the hodograph of the family. The continuation method will provide an initial guess for the next member of the family. After that, the next periodic orbit in the family may be targeted by employing this initial guess. Once the desired convergence criteria is reached, another step along the hodograph may be taken.

One example of a continuation method is the single-parameter continuation method. First, a periodic orbit is targeted, resulting in the targeted initial state, $\vec{X}$, where $\vec{X} = [x,\ y,\ z,\ \dot{x},\ \dot{y},\ \dot{z}]^T$, and period T. Then, a step is taken along one of the initial states. For example, a step of length Δx may be taken in x, so an initial guess, $\vec{X}_i$, may be generated as $\vec{X}_i = [x + \Delta x,\ y,\ z,\ \dot{x},\ \dot{y},\ \dot{z}]^T$. Beginning with this initial guess from the previous periodic orbit, a new periodic orbit may be targeted. This continuation method may then be continued in both the $+\Delta x$ and $-\Delta x$ directions to

target a portion of a family of periodic trajectories. However, the implementation of single-parameter continuation method does possess limitations. For example, the user must choose which parameter to step along. In order to choose the proper parameter to step along, one may need to possess knowledge of the behavior of the periodic orbit family prior to targeting the members of the family. Without knowledge of the evolution of the family, one may step along a parameter that does not step along the hodograph of the periodic orbit family, resulting in a poor initial guess for the next member of the family. This poor initial guess may result in the targeting algorithm converging upon a periodic orbit that is not a member of the desired family or no convergence at all.

The continuation method utilized in the current investigation is a modified single-parameter continuation method that exploits symmetry in the Earth-Moon CR3BP. First, a trajectory with two perpendicular crossings of the $x-z$ plane is targeted with a single-shooting algorithm, as described in Section 2.15. The vector of independent variables, $\vec{X}$, and the constraint vector, $\vec{F}$, for this fixed-x single-shooting algorithm are described in equation (118), where τ is the integration time.

$$\vec{X} = \begin{Bmatrix} z(0) \\ \dot{y}(0) \\ \tau \end{Bmatrix} \qquad \vec{F} = \begin{Bmatrix} y(\tau) \\ \dot{x}(\tau) \\ \dot{z}(\tau) \end{Bmatrix} \tag{118}$$

The Jacobian of the constraint vector is then taken with respect to the vector of independent variables. Each of the partials in this Jacobian may then be described in terms of either the 6 X 6 state transition matrix of the trajectory, $\Phi(0,\tau)$, or the state derivatives as seen in equation (119).

$$D\vec{F} = \begin{bmatrix} \frac{\partial y(\tau)}{\partial z(0)} & \frac{\partial y(\tau)}{\partial \dot{y}(0)} & \frac{\partial y(\tau)}{\partial \tau} \\ \frac{\partial \dot{x}(\tau)}{\partial z(0)} & \frac{\partial \dot{x}(\tau)}{\partial \dot{y}(0)} & \frac{\partial \dot{x}(\tau)}{\partial \tau} \\ \frac{\partial \dot{z}(\tau)}{\partial z(0)} & \frac{\partial \dot{z}(\tau)}{\partial \dot{y}(0)} & \frac{\partial \dot{z}(\tau)}{\partial \tau} \end{bmatrix} = \begin{bmatrix} \Phi_{2,3}(0,\tau) & \Phi_{2,5}(0,\tau) & \dot{y}(\tau) \\ \Phi_{4,3}(0,\tau) & \Phi_{4,5}(0,\tau) & \ddot{x}(\tau) \\ \Phi_{6,3}(0,\tau) & \Phi_{6,5}(0,\tau) & \ddot{z}(\tau) \end{bmatrix} \tag{119}$$

Note that this Jacobian is square, so the inverse may be calculated in the update equation.

$$\vec{X}^{(i+1)} = \vec{X}^{(i)} - D\vec{F}^{-1}\vec{F}^{(i)} \tag{120}$$

In the current investigation, the update equation is iterated until $\varepsilon = 10^{-12}$, where $\varepsilon = ||\vec{F}||$. In the Earth-Moon CR3BP, this tolerance corresponds to a position error of 0.3844 mm and a velocity error of $1.024546856607337 \times 10^{-6}$ mm/s. The resulting trajectory represents one half of a symmetric periodic orbit in the Earth-Moon CR3BP. Additionally, the full-cycle monodromy matrix may be found using equation (109).

This continuation method then exploits the insight provided by the state transition matrix of the previous trajectory. First, a step of length Δx is added to the converged parameter $x(0)$. Also, steps of δz, $\delta \dot{y}$, and $\delta \tau$ will be added to the converged parameters $z(0)$, $\dot{y}(0)$, and τ, respectively. The length of step Δx is defined by the user, while the other lengths are described in terms of Δx. The constraint vector may then be approximated using a first-order Taylor series expansion about the previously converged trajectory as seen in equation (121).

$$\vec{F} \approx \begin{bmatrix} \Phi_{2,1}(0,\tau) \\ \Phi_{4,1}(0,\tau) \\ \Phi_{6,1}(0,\tau) \end{bmatrix} \Delta x + \begin{bmatrix} \Phi_{2,3}(0,\tau) & \Phi_{2,5}(0,\tau) & \dot{y}(\tau) \\ \Phi_{4,3}(0,\tau) & \Phi_{4,5}(0,\tau) & \ddot{x}(\tau) \\ \Phi_{6,3}(0,\tau) & \Phi_{6,5}(0,\tau) & \ddot{z}(\tau) \end{bmatrix} \begin{Bmatrix} \delta z \\ \delta \dot{y} \\ \delta \tau \end{Bmatrix} \tag{121}$$

Since it is desired to drive $\vec{F} \to \vec{0}$, equation (121) may be solved for each δ in terms of Δx.

$$\begin{Bmatrix} \delta z \\ \delta \dot{y} \\ \delta \tau \end{Bmatrix} = \begin{bmatrix} \Phi_{2,3}(0,\tau) & \Phi_{2,5}(0,\tau) & \dot{y}(\tau) \\ \Phi_{4,3}(0,\tau) & \Phi_{4,5}(0,\tau) & \ddot{x}(\tau) \\ \Phi_{6,3}(0,\tau) & \Phi_{6,5}(0,\tau) & \ddot{z}(\tau) \end{bmatrix}^{-1} \begin{bmatrix} \Phi_{2,1}(0,\tau) \\ \Phi_{4,1}(0,\tau) \\ \Phi_{6,1}(0,\tau) \end{bmatrix} (-\Delta x) \tag{122}$$

Then, the initial guess provided by this continuation method may be described as $\vec{X} + \delta\vec{X}$. Finally, this initial guess may be utilized in the same fixed-x single-shooting algorithm described above to converge upon the next member of the family. Figure 42 shows a portion of the 4:3 resonant orbit family in the Earth-Moon CR3BP.

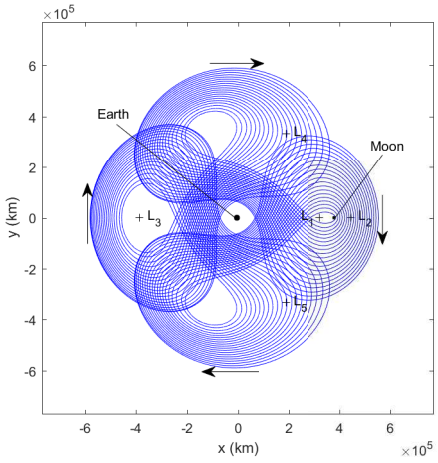

Figure 42. A Portion of the 4:3 Resonant Orbit Family in the Earth-Moon CR3BP Displayed in the Barycentric Rotating Frame

Figure 43 is an example of a portion of the hodograph of the 4:3 resonant orbit family displayed in Figure 42. Each point in Figure 43 represents the initial conditions of orbits in the 4:3 resonant family where $y = 0$, $z = 0$, $\dot{x} = 0$, and $\dot{z} = 0$.

The current investigation chose Δx to be equal to 0.01 nondimensional units (3,844 km). However, to continue the families through regions of the phase space where the final state is very sensitive to the initial state, an algorithm is developed to adjust Δx if needed. If a member of the family required more than six iterations of the update equation to converge, the algorithm returns to the previously converged trajectory

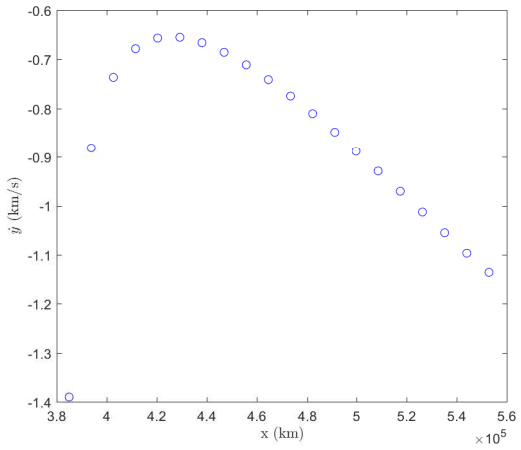

Figure 43. A Portion of the Hodograph associated with the 4:3 Resonant Orbit Family in the Earth-Moon CR3BP Displayed in Figure 42

and generates a new initial guess with $\Delta x = \Delta x/2$. This process is implemented until a new periodic orbit is found in less than six iterations.

3.3 Periapsis Poincaré Maps

Periapsis Poincaré maps are utilized as visual design aids in the current investigation. Instead of defining the hyperplane associated with a Poincaré map in terms of a position component, as seen in the $y = 0$ Poincaré map example shown in Figure 25, the hyperplane may be defined in terms of a velocity component. In the case of a periapsis map, a trajectory crosses the hyperplane each time a periapse occurs along a trajectory. Periapsis maps are implemented by Villac and Scheeres [34]. An apse in the 2BP occurs when the distance between two bodies modeled with two-body dynamics reaches a local minimum or local maximum. A local minimum is defined as a periapse, while a local maximum is defined as an apoapse. In the CR3BP, an apse is similarly defined when the distance between P_3 and a primary is at a local minimum or local maximum. An apse may be defined relative to the larger primary, P_1, or the smaller primary, P_2, in the CR3BP. Howell, Craig Davis, and Haapala

investigate the long term behavior of a spacecraft's trajectory in the vicinity of the smaller primary through the implementation of periapsis maps defined relative to the smaller primary [26, 27, 35, 36, 37]. On the other hand, Wilmer investigates the implementation of periapsis maps relative to Earth in the Earth-Moon CR3BP [14]. The current investigation is concerned with the periapsis Poincaré maps defined relative to Earth in the Earth-Moon planar CR3BP.

In the Earth-Moon planar CR3BP, a periapse occurs when the distance between the Earth and P_3 is at a local minimum. The following development follows that of Villac and Scheeres as well as Haapala [26, 34]. First, the position vector of P_3 relative to Earth is defined as $\vec{r}$ as seen in equation (123).

$$\vec{r} = [x + \mu,\ y]^T \tag{123}$$

Further, the magnitude of this relative position vector is defined as r. Then, according to the second-order sufficient conditions of a local minimum, if $\dot{r} = 0$ and $\ddot{r} > 0$, then r is at a local minimum [66]. Thus, the hyperplane of a periapsis map relative to the larger primary is defined as a one-sided hyperplane where $\dot{r} = 0$ and $\ddot{r} > 0$ [34]. On the other hand, when $\ddot{r} < 0$ an apoapse occurs, or when $\ddot{r} = 0$ an inflection point in the trajectory occurs. To evaluate these quantities, first the magnitude of $\vec{r}$ is evaluated.

$$r = ||\vec{r}|| = \sqrt{(x + \mu)^2 + y^2} \tag{124}$$

Next, the first derivative of the distance between Earth and P_3, $\dot{r}$, may be evaluated.

$$\dot{r} = \frac{(x + \mu)\dot{x} + y\dot{y}}{\sqrt{(x + \mu)^2 + y^2}} \tag{125}$$

Therefore, the first condition ($\dot{r} = 0$) is satisfied when equation (126) is true.

$$0 = (x + \mu)\dot{x} + y\dot{y} \tag{126}$$

Also, note that the right-hand side of equation (126) is equivalent to $\vec{r} \cdot \dot{\vec{r}}$. The quantity $\ddot{r}$ is then expressed in equation (127) [26].

$$\ddot{r} = \frac{\dot{\vec{r}} \cdot \dot{\vec{r}} + \vec{r} \cdot \ddot{\vec{r}}}{r} - \frac{(\vec{r} \cdot \dot{\vec{r}})^2}{r^3} \tag{127}$$

However, when the first condition ($\dot{r} = 0$) is met, equation (127) may be simplified.

$$\ddot{r} = \frac{\dot{\vec{r}} \cdot \dot{\vec{r}} + \vec{r} \cdot \ddot{\vec{r}}}{r} \tag{128}$$

Accordingly, the second condition ($\ddot{r} > 0$) for a periapse to occur is described in equation (129).

$$\vec{r} \cdot \ddot{\vec{r}} + \dot{\vec{r}} \cdot \dot{\vec{r}} > 0 \tag{129}$$

where $\dot{\vec{r}} \cdot \dot{\vec{r}} = v^2$.

Periapsis maps relative to Earth in the Earth-Moon CR3BP may be generated by plotting a point on the map each time a trajectory intersects this hyperplane. At a particular value of the Jacobi Constant, each periapse represents either a prograde or retrograde trajectory. To eliminate this ambiguity, the periapsis maps in the current investigation only include periapses associated with prograde behavior. This behavior is determined by performing a cross product between the position and velocity vector. If the z component of the cross product is positive, the trajectory is prograde. Alternatively, if the z component is negative, the trajectory is retrograde and not included on the map.

$$\left(\vec{r}\times\dot{\vec{r}}\right)\cdot\hat{z}=(x+\mu)\dot{x}-y\dot{x}\begin{cases}<0, & retrograde\\ =0, & neither\\ >0, & prograde\end{cases} \tag{130}$$

Unlike the Poincaré map example shown in Figure 25, a periapsis map may be plotted in the configuration space. Plotting the points in the configuration space may allow for a more intuitive understanding of the behavior of the dynamics. Additionally, the ZVCs may be plotted to separate the accessible and inaccessible regions.

In the current investigation, two methods are employed to generate periapsis maps. The first method is implemented to represent the stable and unstable manifolds associated with an orbitally unstable periodic orbit in the Earth-Moon planar CR3BP. The initial conditions for each manifold approximation are found using the method described in Section 2.19. The second method implements a grid to generate initial conditions for many trajectories in the vicinity of the Earth in the Earth-Moon planar CR3BP. First, a grid is defined with a desired denseness in the region of interest. The desired value of the Jacobi Constant is then chosen and the velocity of each grid point is calculated such that each point is a prograde apse at the desired value of the Jacobi Constant. Next, the grid points are inspected to ensure that no grid points lie in the inaccessible region. If any component of the velocity in the barycentric frame is calculated to be imaginary, the grid point was initialized in an inaccessible region and that point is discarded. Then, each grid point is examined further to ensure that each grid point is associated with a periapse by evaluating the second condition as defined in equation (129). If the grid point is not a periapse, it is discarded. An example of this grid is shown in Figure 44.

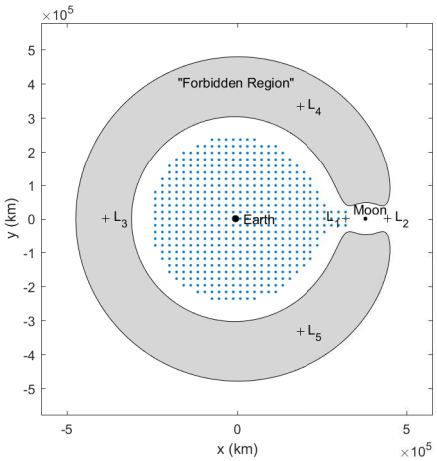

Figure 44. 498 Initialized Periapses in the Vicinity of the Earth at a Value of the Jacobi Constant Equal to 3.15

Finally, the state associated with each of the grid points is numerically integrated for the desired integration time. Figure 45 is an example of a periapsis map generated through an implementation of the grid method.

Multiple behaviors exist on the periapsis Poincaré map shown in Figure 45. Regions of regular (quasiperiodic) behavior appear as closed curves, while regions of chaos appear to be a ‘‘sea’’ of random points. At the ‘‘center’’ of these regular regions, orbitally stable (to in-plane perturbations) periodic orbits are expected. Figure 46 shows some examples of the periodic resonant orbits associated with some of the regular regions. Initial guesses are generated by selecting initial conditions near the ‘‘center’’ of an island structure and numerically integrating until a nearly perpendicular crossing of the x-axis. This trajectory is then utilized as an initial guess in a single-shooting algorithm that targets symmetric periodic orbits.

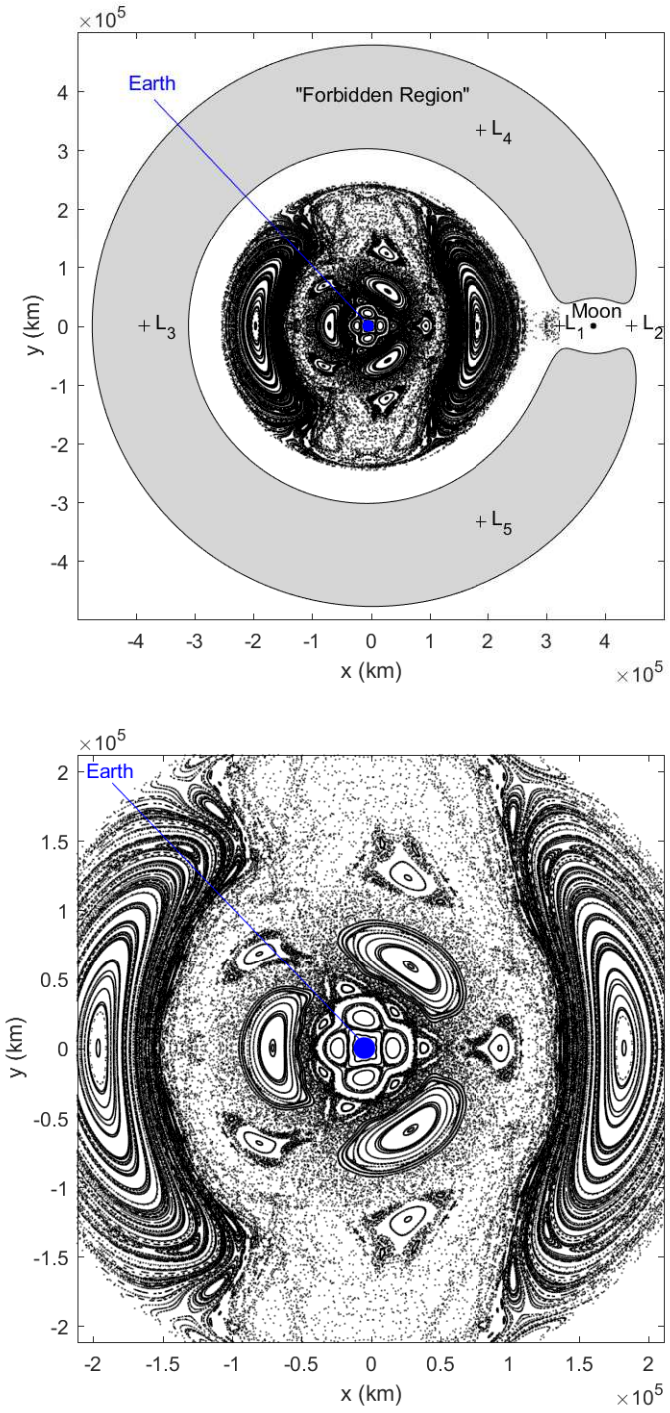

Figure 45. An Example of a Periapsis Poincaré Map Relative to Earth in the Earth-Moon Planar CR3BP With the Value of the Jacobi Constant Equal to 3.15, 498 Trajectories Numerically Integrated for 1,000 Nondimensional Units, 11.9 Years (Top: A Zoomed-Out View; Bottom: A Zoomed-In View in the Vicinity of the Earth)

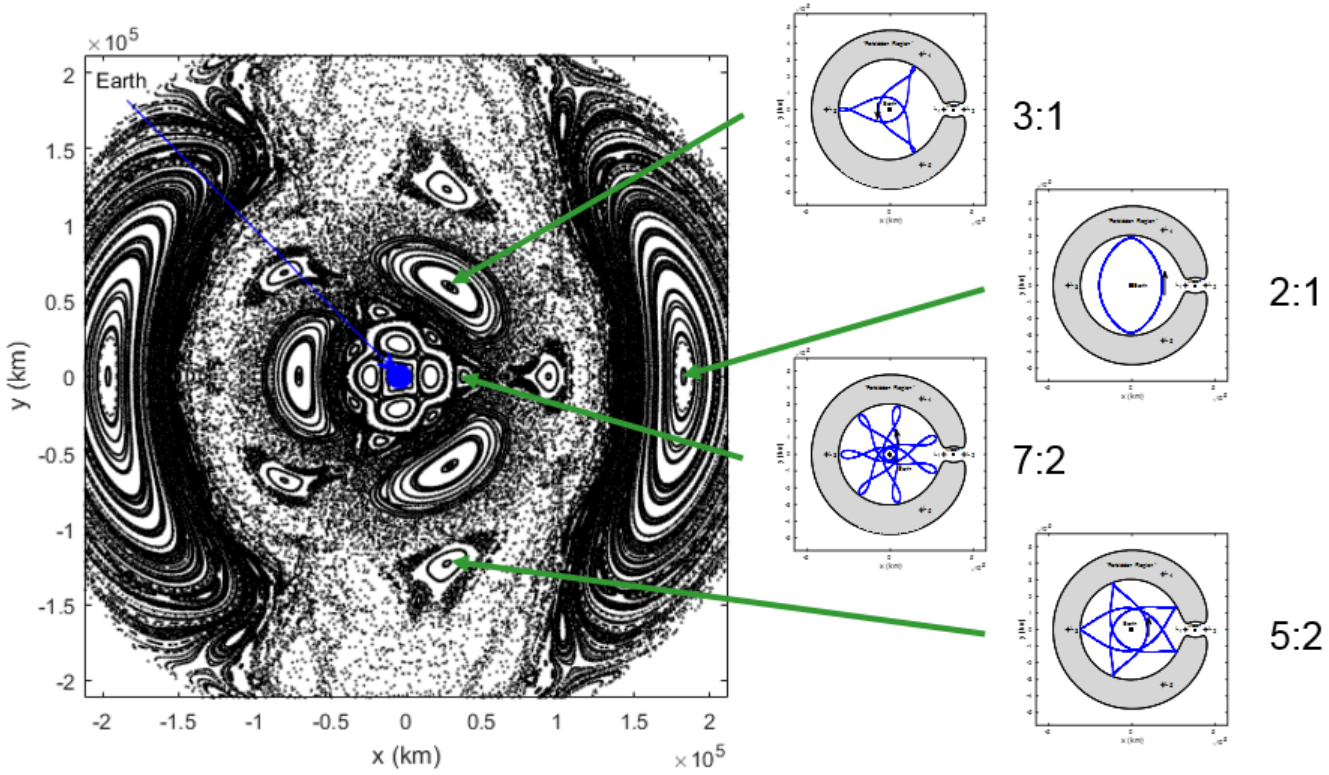

Figure 46. A Periapsis Poincaré Map at a Value of the Jacobi Constant Equal to 3.15 with Examples of Targeted Resonant Orbits Near the "Center" of the Island Structures

3.3.1 Supercomputer

The periapsis map shown in Figure 45 was generated by numerically integrating 498 trajectories for 1,000 nondimensional time units (about 11.9 years). This process is computationally expensive using MATLAB® and, without parallelization, requires about 10 hours in the current investigation. Because of the extensive time required to generate these maps, alternative methods of map generation are utilized. AFRL's High Performance Computer System Spirit is employed to aid in the generation of periapsis maps in the current investigation [100]. Each compute node of this supercomputer possesses 16 processors and 32 GB of memory. To generate a map, MATLAB® version 2015b is employed to numerically integrate 16 trajectories in parallel on a single node. This parallelization reduced the computation time of a single map from about 10 hours to about 45 minutes. This reduced computation time allows for more maps to be investigated, while simultaneously increasing the density of each map.

3.4 *fmincon* Options

Locally optimal solutions in the current investigation are found through the employment of *fmincon*, a function in the MATLAB® Optimization Toolbox [84]. The *fmincon* function allows for many user inputs. The first option involves selecting an appropriate algorithm to search for a locally optimal solution. In the current investigation, an interior-point algorithm is selected based on the recommendations in the MATLAB® documentation. Other options include the desired first-order optimality tolerance, the desired constraint tolerance, and the minimum step size to satisfy the KKT conditions described in Section 2.16. In the current investigation, the first-order optimality tolerance is chosen to be 10^{-6}, the constraint tolerance is chosen to be 10^{-12}, and the minimum step size is chosen to be 10^{-16}. In order for a locally optimal solution to be converged upon, the conditions described in equations

(103)-(104) must each be less than the chosen first-order optimality tolerance, while the conditions described in equations (105)-(107) must be satisfied within the constraint tolerance. Once these conditions are satisfied, a locally optimal solution has been converged upon and *fmincon* outputs an exit flag equal to one. This exit flag means that a local optimum has been found that satisfies the constraints. If *fmincon* begins taking steps that are less than the minimum step, but the current solution is feasible, an exit flag equal to two is output. This exit flag means that a locally optimal solution could not be converged upon, but a solution was found that satisfies the constraints. Both of these exit conditions may be considered valuable, and results presented in the current investigation are characterized based on this exit condition.

3.5 Metrics

Two metrics are defined in the current investigation to quantify the ability of a satellite in a given trajectory to provide coverage of the surface of Earth. The first metric measures the ability of a satellite to remotely sense the surface of the Earth relative to a nominal satellite at geostationary altitude (35,786 km). However, this metric does not measure the ability of a satellite to cover a particular region of the Earth and instead treats all regions of the Earth equally, so the rotation of the Earth does not affect this metric. On the other hand, the second metric is defined as the ability of a satellite to remotely sense the surface of the Earth relative to a particular satellite at geostationary altitude. This metric quantifies the ability of a satellite to provide coverage of a specific region on Earth. This specific region is defined by the region visible to a particular satellite, so, again, the rotation of the Earth does not affect this metric. Together these metrics are employed to track the performance of a satellite's trajectory. Both metrics are based on the square of the altitude of the satellite. This type of metric approximates the signal strength received by a satellite

from the surface of the Earth. Other metrics may exist and could be measured in a similar manner to the metrics defined by the current investigation.

3.5.1 The Performance of a Satellite Relative to a Nominal Satellite at Geostationary Altitude

The first metric utilized in the current investigation measures a satellite's ability to remotely sense the surface of the Earth along a trajectory relative to a satellite at geostationary altitude without regard to what region of the Earth's surface is covered. This metric is defined as the square of the ratio between the distance from a nominal satellite in a geostationary orbit to Earth's surface, R_{GEO}, and the distance from a satellite in a trajectory of interest to Earth's surface, $R(t)$. Note that these distances are altitudes not radii. The first distance, R_{GEO}, is constant, while the second distance, $R(t)$, is time dependent and evaluated at each time step along the trajectory of interest.

$$\Phi(t) = \left(\frac{R_{GEO}}{R(t)} \right)^2 \tag{131}$$

Additionally, this metric is restricted to always be less than or equal to one. If, at any time step, the metric is greater than one, the performance of the satellite in the trajectory of interest is set equal to one at that time step. The square of the ratio is taken to reflect the performance of remote sensing satellites. As the distance of the receiver from the transmitter increases, the power of the signal received decreases proportional to the inverse of the square of the distance [8]. For example, as the distance from Earth to the satellite increases, the metric decreases. Likewise, as the distance decreases, the performance increases. When the metric is equal to one, the satellite in the trajectory of interest performs just as well as a satellite at geostationary altitude. However, when the metric is less than one, a the satellite in the trajectory of interest performs less well than a satellite at geostationary altitude.

The metric, as defined, is evaluated at each time step. However, it is often convenient to discuss the metric in terms of a single scalar quantity. Accordingly, the time average of this metric, $\bar{\Phi}$, may be calculated.

$$\bar{\Phi} = \frac{\int_{t_1}^{t_2} \Phi(t) dt}{t_2 - t_1} \tag{132}$$

The integral of the performance of the metric is approximated with the trapezoidal rule. The resulting scalar quantity reflects the time average performance of a satellite with respect to its performance relative to a nominal satellite at geostationary altitude.

3.5.2 The Performance of a Satellite Relative to a Particular Satellite at Geostationary Altitude

The second metric utilized in the current investigation measures the ability of a satellite to remotely sense the surface of the Earth relative to a particular satellite at geostationary altitude. Unlike the first metric defined, this metric is concerned with the ability to provide coverage to a particular region on the surface of the Earth. First, the trajectory of the particular satellite at geostationary altitude and the trajectory of the satellite of interest are numerically integrated in the Earth-Moon CR3BP. Next, the square of the ratio between the distance from the particular satellite to Earth's surface, R_{GEO}, and the distance from a satellite in a trajectory of interest to Earth's surface, $R(t)$, is calculated. Again, note that these distances are altitudes not radii. Then, the ratio of swath area overlap on the surface of the Earth, $\varphi(t)$, is approximated at each time step. The yellow swath represents the ground swath of the particular satellite at geostationary altitude evaluated at time t. The area of this swath is defined as $A_{part}(t)$. The green swath represents the ground swath of a satellite in the orbit of interest evaluated at time t. The area of this swath is defined as $A(t)$. The area of overlap between these two ground swaths at time t is

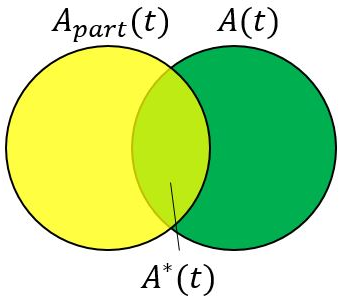

Figure 47. The Relationship and Overlap Between the Ground Swaths of a Satellite in the Trajectory of Interest and of a Particular Satellite

then defined as $A^*(t)$. The percentage of overlap between the two swaths is defined as $\varphi(t) = \frac{A^*(t)}{A_{part}(t)}$. By definition $\varphi(t)$ is always less than or equal to one. This value represents the percentage of ground swath area provided by the particular satellite at geostationary altitude that may be covered by a satellite in the trajectory of interest. A value of one implies that a satellite in the trajectory of interest is able to provide coverage to the entire ground swath area provided by the particular satellite. The performance of a satellite relative to a particular satellite may then be characterized by the metric $\Psi(t)$.

$$\Psi(t) = \left(\frac{R_{GEO}}{R(t)}\right)^2 \frac{A^*(t)}{A_{part}(t)} \tag{133}$$

Calculating the value of $\varphi(t)$ at each time step is not trivial. In the current investigation, the value is numerically approximated by first discretizing the surface of the Earth into 1,000 approximately equally spaced points [101]. Additionally, the surface of the Earth is assumed to be spherical with a radius of 6,378.135 km [3]. Figure 48 shows the discretization of Earth based on this spherical assumption.

At each time step along the trajectory of interest, the elevation angle is calculated from each of the discretized points to the particular satellite. If this elevation angle is greater than five degrees, then this point is assumed to be covered by the particular satellite. The number of points viewable from this particular satellite is defined as $N_{part}(t)$. It is important to note that these points are approximated at each time step

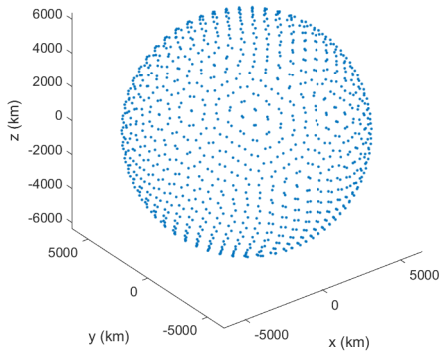

Figure 48. The Discretization of the Earth's Surface into 1,000 Approximately Equally Spaced Points

of the numerical integration, so the rotation of the Earth does not affect this metric. Then, the elevation angle from these $N_{part}(t)$ points to the satellite in the trajectory of interest is calculated. Again, if the elevation angle is greater than five degrees, the point is assumed to be covered by the satellite in the trajectory of interest. Of the $N_{part}(t)$ points, $N^*(t)$ of them are viewable from a satellite in the trajectory of interest. The area ratio $\varphi(t)$ may then be approximated as shown in equation (134).

$$\varphi(t) = \frac{A^*(t)}{A_{part}(t)} \approx \frac{N^*(t)}{N_{part}(t)} \tag{134}$$

It may be convenient to calculate the time average of this metric. This time average would provide a single, scalar quantity that describes the performance of an entire trajectory in terms of this metric. The time average of the performance of a satellite relative to a particular satellite is defined as $\bar{\Psi}$.

$$\bar{\Psi} = \frac{\int_{t_1}^{t_2} \Psi(t)dt}{t_2 - t_1} \tag{135}$$

Once again, the integral is approximated by the trapezoidal rule.

3.6 Chapter 3 Summary

This chapter provides an overview of the test plan and methodology developed to address the problem statement proposed in Section 1.5. First, the test plan is introduced and explained in detail. The three constellations of interest and the four test cases are defined. Test Case 1 consists of an investigation into the utility of high-altitude transfers modeled in the Earth-Moon CR3BP. Test Case 2 is an investigation into the utility of a satellite in a high-altitude parking orbit as a source of reconstitution. Then, in Test Case 3, the ability of a satellite to remotely sense the surface of the Earth while it is in a high-altitude orbit is explored. Finally, Test Case 4 investigates the implementation of periapsis Poincaré maps to predict the long term behavior of a satellite's trajectory.

After the test plan is defined, the methodology of the current investigation is introduced. The continuation method implemented to generate portions of families of periodic orbits is explained. Then, periapsis Poincaré maps and the methods employed to generate such maps are described. Next, the numerical optimization method applied in the current investigation is discussed. Finally, metrics are defined to quantify the ability of a satellite to remotely sense the surface of the Earth while it is in a high-altitude orbit.

4. Results and Analysis

This chapter presents the results and analysis of each of the test cases described by the test plan in Section 3.1. In Test Case 1, a periapsis Poincaré map is utilized as a visual aid to generate initial guesses for high-altitude, alternative transfers between conventional orbits. These initial guesses are then input into differential correction schemes to target feasible solutions. Finally, locally optimal solutions, in terms of ΔV, are found through the implementation of a numerical optimization process. Additionally, a trajectory is transitioned into an ephemeris model to demonstrate the need to validate these trajectories in a higher-fidelity model. After that, in Test Case 2, the ability of a spacecraft in a high-altitude parking orbit to reconstitute a conventional constellation is investigated. Initial guesses are generated from resonant arcs, the utilization of a periapsis map as a visual aid, and solutions from Test Case 1. Then, feasible solutions are targeted and input into an optimization algorithm to search for locally optimal solutions in terms of ΔV. Next, in Test Case 3, the ability of a spacecraft to remotely sense the surface of the Earth while it is in a high-altitude trajectory is investigated. First, the trajectories from Test Case 2 are analyzed. Then, other high-altitude trajectories are explored. Finally, in Test Case 4, the ability to predict the long term behavior of a spacecraft's trajectory is investigated. Periapsis Poincaré maps are generated at various values of the Jacobi Constant. After that, a scenario is developed to demonstrate the capability of a spacecraft traveling through chaotic regions of the phase space to alter its long term behavior for low ΔV.

4.1 Test Case 1: Results and Analysis of High-Altitude Transfers Between Conventional Orbits

In Test Case 1, high-altitude alternative transfers between conventional constellations are investigated. Each of these transfers begins in a highly elliptical, geosynchronous orbit that lies in the Earth-Moon orbital plane, as described in Section 3.1.2. Initial guesses are generated through the utilization of a periapsis Poincaré map of the invariant manifolds of a 4:3 resonant orbit. This periodic orbit is the same periodic orbit investigated in Test Case 2 as a candidate high-altitude parking orbit and is a result of the investigation in Test Case 3A. It is concluded that high-altitude transfers exist in a multi-body dynamical environment that may be performed for comparable, and in some case significantly less, ΔV than a Hohmann-type transfer. For example, when an inclination change is required, as is the case in Test Cases 1B and 1C, the ΔV required to perform one of the proposed high-altitude transfers is less than the required ΔV to perform a Hohmann-type transfer.

4.1.1 Test Case 1A: Results and Analysis of High-Altitude Transfers from an Elliptical, Geosynchronous Orbit to a Circular, Geosynchronous Orbit

In Test Case 1A, high-altitude transfers modeled in the Earth-Moon CR3BP between an elliptical geosynchronous orbit and a circular geosynchronous orbit that both remain in the Earth-Moon orbital plane are investigated. The COEs of both of these orbits are described in Tables 6 and 9. Initial guesses for this alternative transfer are developed from a periapsis map of the invariant manifold approximations of a 4:3 resonant orbit. Specifically, the chosen 4:3 resonant orbit is the same 4:3 resonant orbit utilized as a parking orbit in Test Case 2 and is a locally optimal solution based

on the analysis in Test Case 3A. Figure 49 shows periapsis Poincaré maps of the invariant manifold approximations of this resonant orbit.

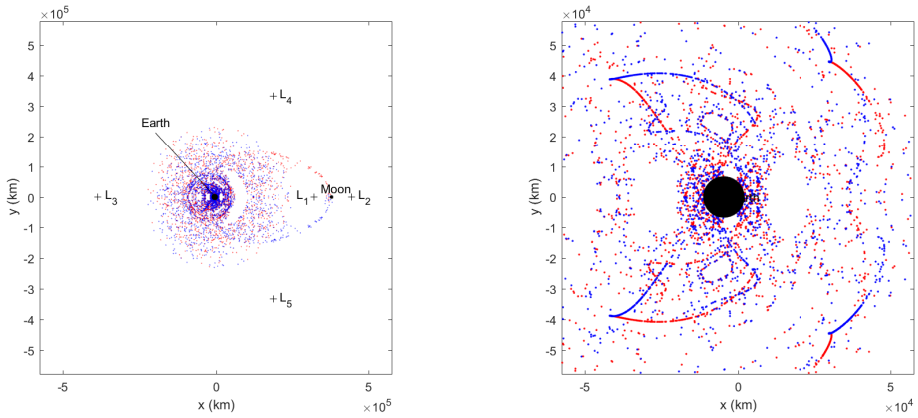

Figure 49. Invariant Manifold Approximations of a 4:3 Resonant Orbit in the Earth-Moon CR3BP: 200 Trajectories Approximating the Unstable Manifold Numerically Integrated for 1,000 Nondimensional Time Units (About 11.9 Years), Stable Manifolds Approximated Through a Reflection of the Unstable Manifolds Across the x-axis and Time (Blue: Stable Manifold Approximations; Red: Unstable Manifold Approximations)

Periapses on the map near the perigee of the initial elliptical orbit are selected and numerically integrated in forward time to generate potential transfer paths. Through an iterative process, an initial periapsis on the unstable manifold near the altitude of the perigee of the circular, geosynchronous orbit in the Earth-Moon orbital plane is chosen that is associated with a potential transfer path that possesses another periapse near the altitude of the destination orbit. Figure 50 shows one such trajectory.

A variable-time multiple-shooting algorithm is then implemented that requires position and velocity continuity at each of the patch points, while targeting a trajectory that begins at the perigee of the elliptical geosynchronous orbit and ends at the altitude of the circular geosynchronous orbit. The perigee altitude is selected as the initial point in the transfer trajectory in an attempt to maximize the Oberth effect [102]. This principle implies that a change in ΔV is most effective for changing the energy of a spacecraft when the ΔV is performed at the point where the spacecraft is traveling

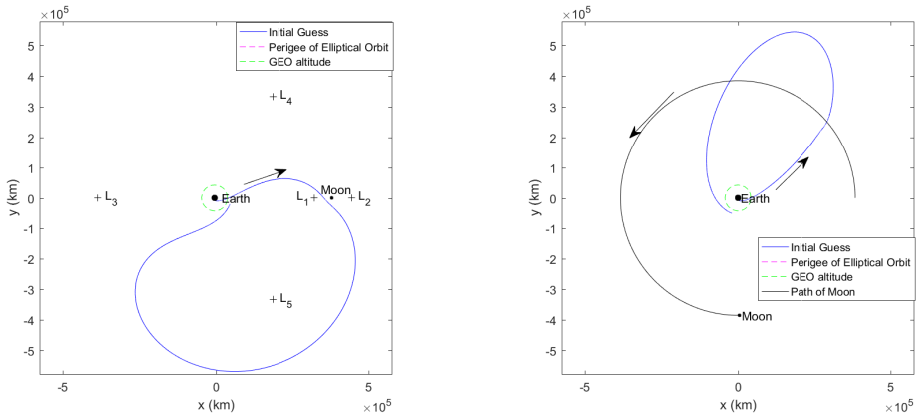

Figure 50. Initial Guess for a Transfer from an Elliptical Geosynchronous Orbit to a Circular, Geosynchronous Orbit Modeled in the Planar Earth-Moon CR3BP, Generated from a Periapsis Map (Left: Barycentric Rotating Frame; Right: Earth-Centered Inertial Frame)

at its fastest speed. Typically, higher speeds are present when a spacecraft is near periapse; however, unlike in the 2BP where periapses are global minima in radius, periapses in the CR3BP are local minima in radius. So, periapses in the CR3BP are associated with local maxima in speed. Therefore, by beginning the transfer at perigee of the elliptical orbit, the Oberth effect may be exploited. A converged, feasible solution resulting from this method utilizing the initial guess in Figure 50 is shown in Figure 51.

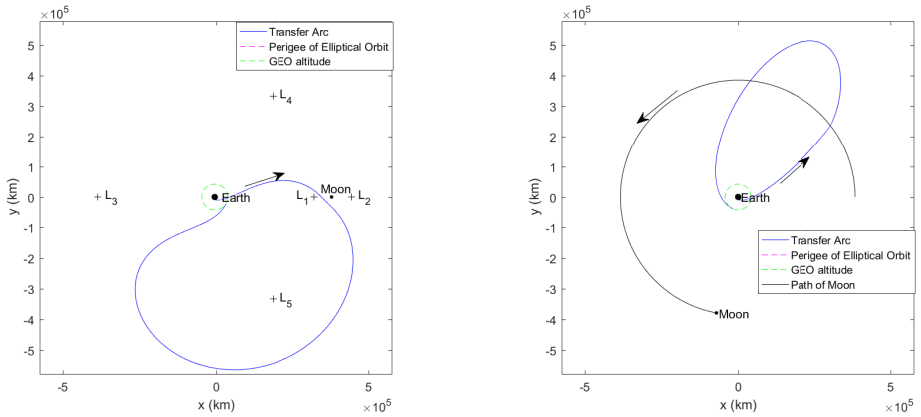

Figure 51. A Feasible Transfer from an Elliptical, Geosynchronous Orbit to a Circular Geosynchronous Orbit Modeled in the Planar Earth-Moon CR3BP (Left: Barycentric Rotating Frame; Right: Earth-Centered Inertial Frame)

This feasible solution requires approximately 1.657 km/s of ΔV to perform the transfer. However, the implementation of the differential corrections process made no effort to target an optimal solution. To perform an optimization, a multiple-shooting algorithm is set up within *fmincon* to search for a locally optimal solution, in terms of the total ΔV required to perform the transfer. The constraints enforce position and velocity continuity at each of the patch points while allowing a velocity discontinuity when a ΔV is performed. The cost function is the sum of the total ΔV throughout the trajectory. Figure 52 shows a locally optimal transfer in terms of ΔV from the initial elliptical geosynchronous orbit to the circular geosynchronous orbit.

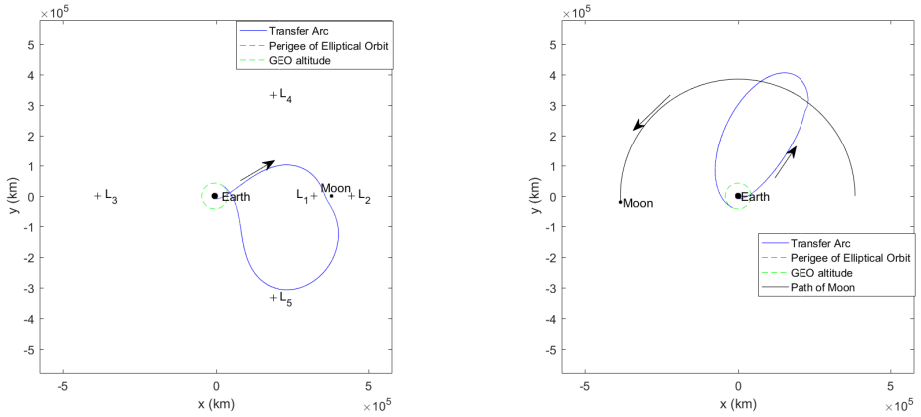

Figure 52. A Locally Optimal Transfer, in Terms of ΔV, from an Elliptical, Geosynchronous Orbit to a Circular, Geosynchronous Orbit Modeled in the Planar Earth-Moon CR3BP (Left: Barycentric Rotating Frame; Right: Earth-Centered Inertial Frame)

The optimization process implemented reduces the approximate total ΔV to 1.442 km/s. The time-of-flight of this locally optimal transfer is found to be approximately 13.9 days to perform this transfer. Additionally, this optimization process maintains the qualitative behavior of the feasible solution shown in Figure 51 that was utilized as the initial guess. However, like all solutions in the current investigation, this solution is not claimed to be globally optimal.

The cost, in terms of ΔV, to perform this transfer through the use of a Hohmann-type transfer is found in Section 3.1.2.1 to be 1.383 km/s. The cost, in terms of ΔV, of this high-altitude transfer is slightly larger than, but comparable to, a conventional transfer. Despite the small increase in ΔV, approximately 59 m/s, this transfer may provide other advantages. First, the intent of a spacecraft utilizing this transfer path may not be clear after the first burn. An observer viewing this trajectory from a two-body perspective may not expect the gravitational effects of the Moon to allow for an opportunity to transfer into a circular, geosynchronous orbit in the Earth-Moon orbital plane. The intent of a Hohmann-type transfer may be clear to an observer because it employs a direct transfer path.

As seen in Figure 52, significant insight is gained by observing this transfer in the Earth-Moon barycentric rotating frame. If an observer were strictly observing this transfer in the inertial frame, this transfer may appear to be perturbed two-body motion; however, the rotating frame clearly shows that the large perturbations from two-body motion occur near the apoapse of the transfer, when the spacecraft is close to the Moon. This conclusion is also evident when tracking the osculating, or instantaneous, COEs as a function of time as seen in Figure 53.

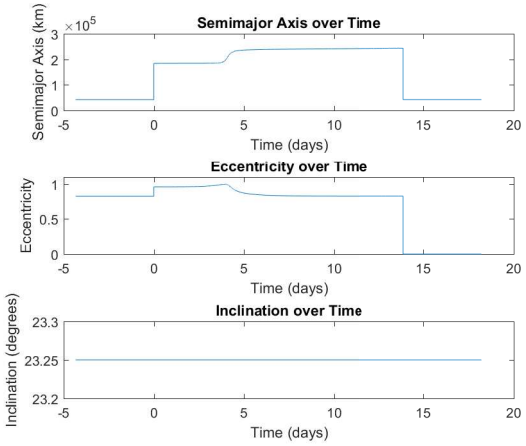

Figure 53. The Osculating COEs of a Locally Optimal Transfer, in Terms of ΔV, from an Elliptical, Geosynchronous Orbit to a Circular, Geosynchronous Orbit

When the time is equal to zero days, the first burn of the transfer is performed. This first burn requires approximately 0.360 km/s of ΔV. This impulsive change in velocity results in a discontinuity in the values of the semimajor axis and eccentricity, as seen in Figure 53. Then, approximately four days after the first burn, the gravitational effects of the Moon cause a large deviation in the semimajor axis and eccentricity. This third-body gravitational effect increases the semimajor axis and decreases the eccentricity of the trajectory. The spacecraft then returns to the Earth where the second burn is performed. An observer modeling this trajectory in a two-body dynamical model may not expect the increase in semimajor axis and decrease in eccentricity seen when modeling this trajectory in the Earth-Moon CR3BP. As expected, since the motion remains prograde in the Earth-Moon orbital plane, the inclination does not change.

Despite the successful preliminary design of this transfer, there may be some disadvantages to this design process. One such disadvantage is that no perturbations were included in this dynamical model. Perturbations from Earth's nonspherical mass distribution, solar gravity, solar radiation, and the elliptical orbit of the Moon (about the Earth) may perturb this trajectory in a higher-fidelity model. This preliminary design could be validated by utilizing this solution as an initial guess for a multiple-shooting algorithm in an ephemeris model that included perturbations. To illustrate the effects of transitioning into a higher-fidelity model, the locally optimal transfer shown in Figure 52 is transitioned into STK and propagated in forward time. STK's High Precision Orbit Propagator is utilized to numerically integrate the initial conditions in this dynamical environment. The settings employed in the current investigation are shown in Figure 54.

Initial conditions at 10 different points, equally separated in time, along this transfer path are input into the STK scenario that includes the gravitational effects of the Earth, Moon, and Sun, as well as other perturbations due to solar radiation, air drag,

and the nonspherical mass distribution of the Earth. The result of this propagation is seen in Figure 55. These initial conditions are found from the preliminary design of the transfer in the Earth-Moon CR3BP and are transitioned into the ephemeris model based on the position of the Moon according to ephemeris data from the Jet Propulsion Laboratory HORIZONS System web-interface [98]. The epoch time at the start of the transfer was chosen to be January 1st, 2020. This method for transitioning trajectories designed in the CR3BP to the ephemeris model follows the method described by Pavlak [28].

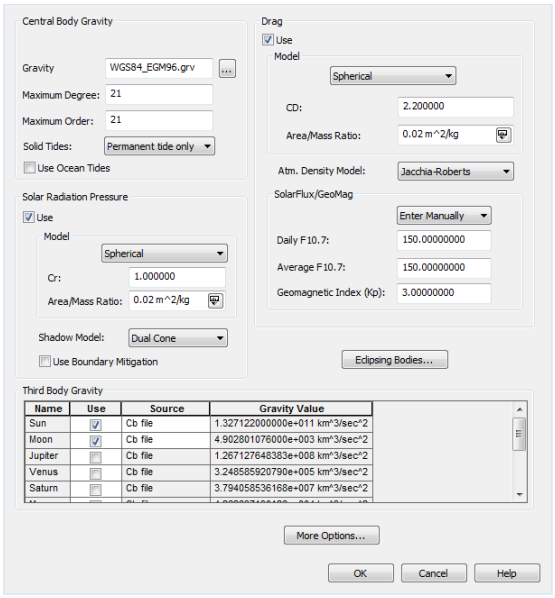

Figure 54. STK Screenshot of the Options Selected in STK's High Precision Orbit Propagator [99]

Figure 55 shows that this preliminary design process does not provide a solution in a higher-fidelity model, as expected, because the arcs are discontinuous. However, these arcs may be used as an initial guess in a differential corrections process to target a continuous transfer path. Specifically, a multiple-shooting algorithm could be implemented to attempt to target a feasible solution in the higher-fidelity model that may possess similar ΔV requirements as the preliminary design.

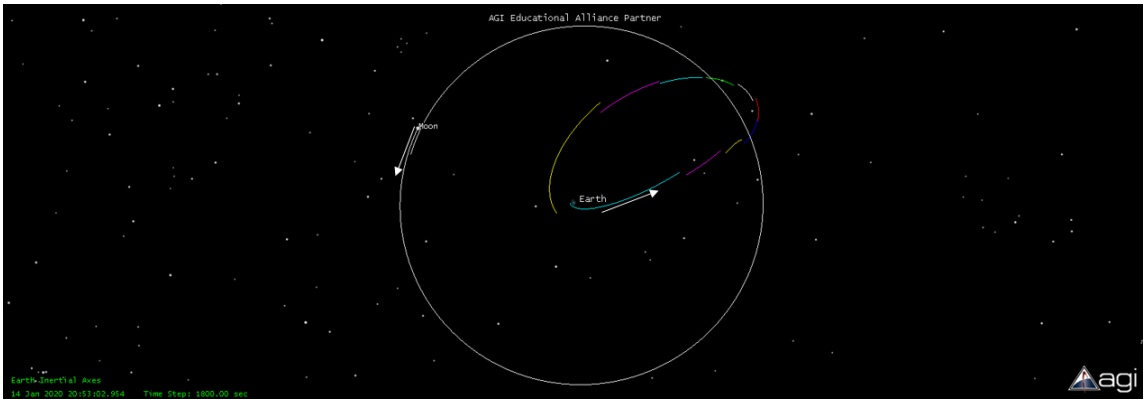

Figure 55. STK Screenshot of the Locally Optimal Transfer from an Elliptical, Geosynchronous Orbit to a Circular, Geosynchronous Orbit Modeled in STK in a Dynamical Environment that Includes the Gravitational Effects of the Sun, Earth, and Moon, as Well as the Effects of Air Drag, Solar Radiation Pressure, and the Nonspherical Mass Distribution of the Earth (Modeled Using 10 Arcs Equally Separated in Time) [99]

Additionally, this preliminary design does not include an investigation into the required nondeterministic ΔV to maintain the position of the spacecraft as it travels along this high-altitude transfer path. Position and velocity errors will accumulate as the spacecraft travels along this trajectory. These errors will require stationkeeping to be performed that will increase the amount of fuel required on-board the spacecraft.

4.1.2 Test Case 1B: Results and Analysis of High-Altitude Transfers from an Elliptical Geosynchronous Orbit that Lies in the Earth-Moon Orbital Plane to a Geostationary Orbit

In Test Case 1B, high-altitude alternative transfers are investigated from an elliptical geosynchronous orbit that lies in the Earth-Moon orbital plane to a geostationary orbit. The COEs of both of these orbits are described in Tables 7 and 9. Similar to Test Case 1A, planar initial guesses are generated from the periapsis Poincaré map, seen in Figure 49, of the invariant manifold approximations of a 4:3 resonant orbit. Through an iterative process of selecting periapses near the perigee of the initial elliptical orbit, the planar initial guess seen in Figure 56 is generated.

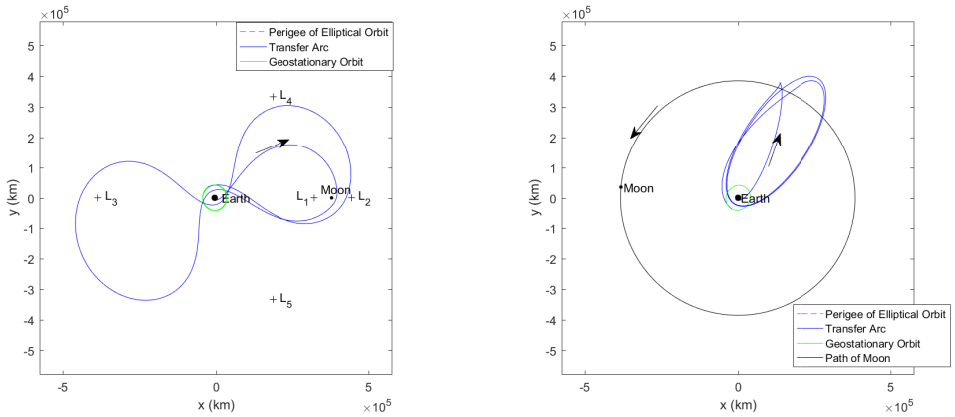

Figure 56. Initial Guess for a Transfer from an Elliptical Geosynchronous Orbit that Lies in the Earth-Moon Orbital Plane to a Geostationary Orbit Modeled in the Earth-Moon CR3BP, Generated from a Periapsis Map (Left: Barycentric Rotating Frame; Right: Earth-Centered Inertial Frame)

This initial guess is chosen because it allows the spacecraft to perform two fly-bys near the Moon. In Test Case 1B, this may be desirable because close lunar fly-bys may allow for the gravitational effects of the Moon to aid in the necessary inclination change. However, this initial guess only allows for two ΔVs: one to transfer from the elliptical orbit into the transfer path and one to transfer from the transfer path to the geostationary orbit. To add flexibility to the multiple-shooting algorithm, three additional velocity discontinuities equally separated in time are incorporated into this initial guess. A multiple-shooting algorithm is then implemented to search for a feasible solution based on this initial guess. Because the initial guess is generated in the plane of the primaries, the feasible solution remains in the plane of the primaries. This planar feasible solution is not a constraint but a result of the initial guess. However, this planar solution may not be an ideal solution because of the large inclination change required from the planar transfer orbit to the geostationary orbit. In fact, the total ΔV of this feasible solution is found to be approximately 3.133 km/s.

In the current investigation, the next step in the design process is to use this feasible solution as an initial guess in an optimization algorithm, as described in

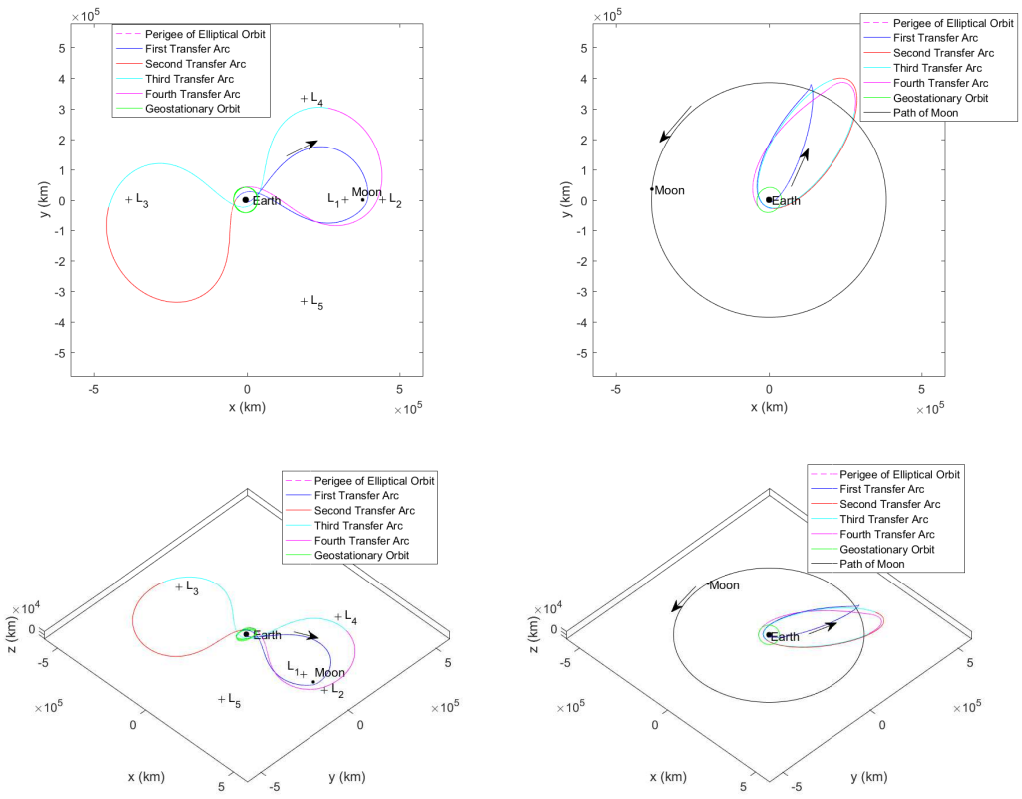

Figure 57. A Feasible Solution for a Transfer from an Elliptical Geosynchronous Orbit that Lies in the Earth-Moon Orbital Plane to a Geostationary Orbit Modeled in the Earth-Moon CR3BP (Top Left: View of $x-y$ Plane in the Barycentric Rotating Frame; Top Right: View of $x-y$ Plane in the Earth-Centered Inertial Frame; Bottom Left: 3D Perspective View in the Barycentric Rotating Frame; Bottom Right: 3D Perspective View in the Earth-Centered Inertial Frame)

Section 3.4. However, the implementation of *fmincon* using the initial guess described above does not result in a locally optimal solution. Instead, this algorithm outputs an exit flag of two, which means that a locally optimal solution could not be converged upon, but an improved feasible solution is found. Despite the lack of a local optimum, this algorithm did decrease the amount of required ΔV. This feasible solution output by *fmincon* can be seen in Figure 58.

The optimization process implemented reduces the required ΔV by approximately 52.7%, resulting in an approximate total ΔV of 1.480 km/s and a time-of-flight of

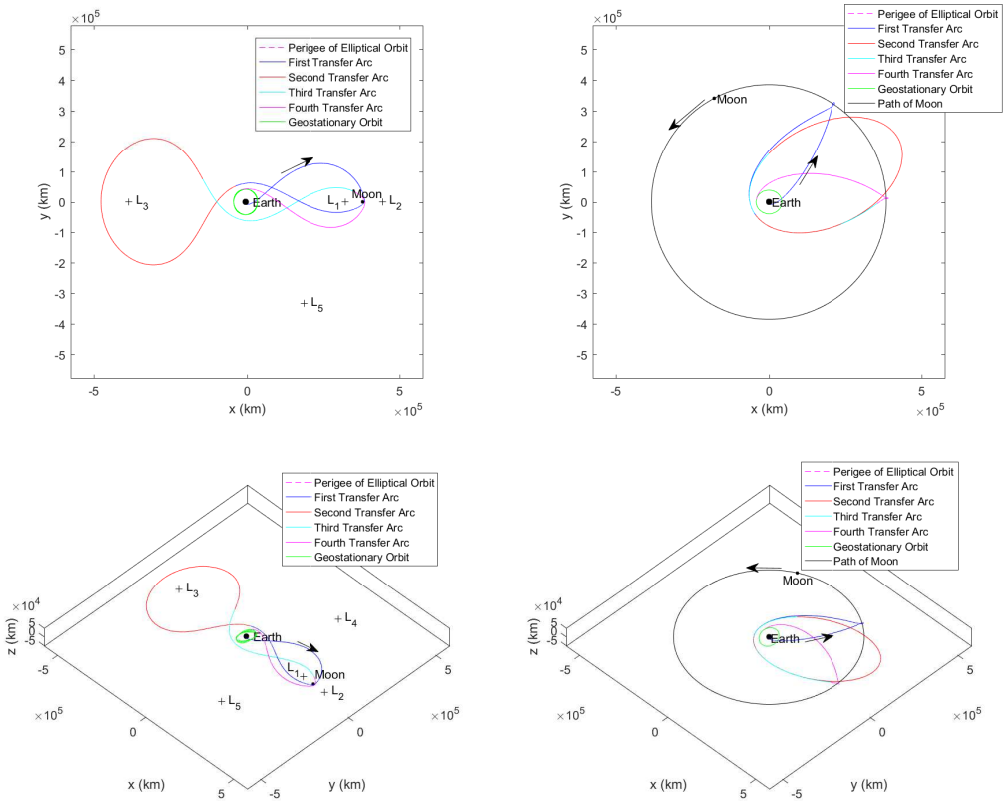

Figure 58. A Feasible Solution Output from *fmincon* for a Transfer from an Elliptical, Geosynchronous Orbit to a Geostationary Orbit Modeled in the Earth-Moon CR3BP (Top Left: View of $x-y$ Plane in the Barycentric Rotating Frame; Top Right: View of $x-y$ Plane in the Earth-Centered Inertial Frame; Bottom Left: 3D Perspective View in the Barycentric Rotating Frame; Bottom Right: 3D Perspective View in the Earth-Centered Inertial Frame)

approximately 31.9 days to perform this transfer. However, it is important to note that this is not a locally optimal solution.

The feasible solution output from *fmincon* requires 1.480 km/s of ΔV, while the cost to perform a transfer between these two orbits through the use of a conventional Hohmann-type transfer is found in Section 3.1.2.2 to be approximately 1.526 km/s. In this case, the ΔV required to perform this transfer using a high-altitude transfer orbit, is found to be less than the cost of a conventional transfer. Also, not only is a cost savings possible, but other advantages to this transfer path may exist. For example, the intent of a spacecraft in this trajectory may not be clear to an observer. The long

transfer time, high-altitude, and the multiple burns required by a spacecraft to perform this transfer may decrease the ability to predict the intent of a spacecraft's trajectory as the transfer is performed. Additionally, an observer viewing this trajectory in an inertial frame with a two-body perspective may be unable to predict the spacecraft's trajectory. Twice, the spacecraft's motion transitions from prograde to retrograde with respect to the revolution of the Moon about the Earth in the inertial frame and returns to prograde as it completes an orbit about the Moon. This behavior may be difficult to anticipate in the inertial frame; however, when viewed in the barycentric rotating frame, the spacecraft's behavior is clear as it performs close lunar fly-bys. Again, viewing the osculating COEs also provides insight into the complex behavior, as seen in Figure 59.

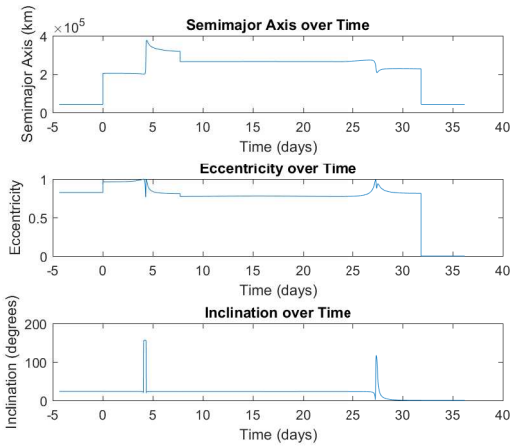

Figure 59. The Osculating COEs of a Feasible Transfer, Output from *fmincon*, from an Elliptical Geosynchronous Orbit that Lies in the Earth-Moon Orbital Plane to a Geostationary Orbit

Upon examination of the osculating COEs, multiple behaviors are evident. First, when time is equal to zero days, a ΔV is performed that instantaneously changes the semimajor axis and eccentricity. Then, after approximately 4 days, large disturbances in the semimajor axis, eccentricity, and inclination occur. These changes are due to the close lunar fly-by that changes the motion of the spacecraft from prograde to

retrograde. Again, at approximately 27 days, another large disturbance in the COEs occurs due to another lunar fly-by. This fly-by also changes the inclination to nearly zero. This exploitation of the gravitational effects of the Moon allows the spacecraft to perform its final ΔV from the transfer path to the final geostationary orbit without the need to perform a large plane change. A conventional Hohmann-type transfer is unable to take advantage of these effects and often requires a combined plane change to circularize the orbit and to adjust the inclination in order to complete the transfer.

4.1.3 Test Case 1C: Results and Analysis of High-Altitude Transfers from an Elliptical, Geosynchronous Orbit that Lies in the Earth-Moon Orbital Plane to a Tundra Orbit

In Test Case 1C, high-altitude transfers are investigated from an elliptical, geosynchronous orbit that lies in the Earth-Moon orbital plane to a Tundra orbit. Because of the high altitude of these transfers, the spacecraft's trajectory is modeled in the Earth-Moon CR3BP. The COEs of both of these orbits are described in Tables 8 and 9. Similar to Test Case 1B, planar initial guesses are generated from the periapsis map, seen in Figure 49, of the invariant manifold approximations of a 4:3 resonant orbit. Also, following the design process in Test Case 1B, velocity discontinuities are added to the initial guess to provide flexibility to the multiple-shooting algorithms. Through an iterative process of choosing periapses near the perigee of the initial elliptical orbit, the planar initial guess seen in Figure 60 is generated.

Similar to Test Case 1B, an initial guess is generated that performs two lunar fly-bys that may aid in the needed inclination change. A multiple-shooting algorithm is then implemented to target a feasible solution based on this initial guess. The feasible solution based on this initial guess can be seen in Figure 61. Because the initial guess is generated in the plane of the primaries, the feasible solution remains in

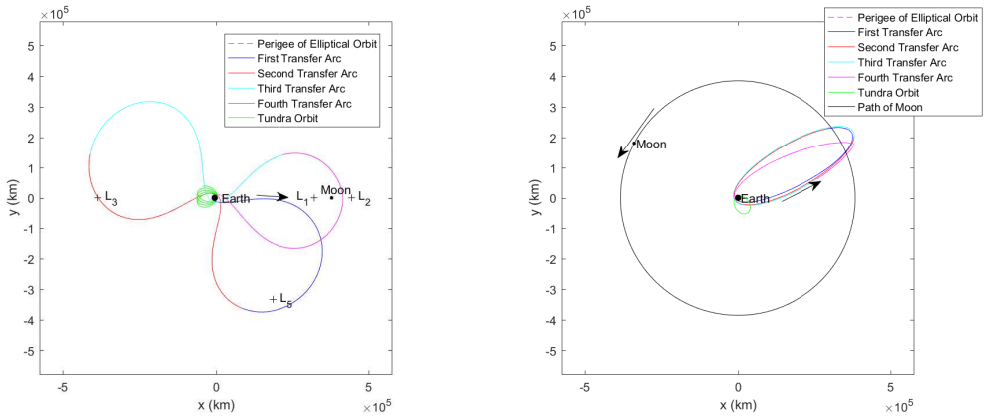

Figure 60. Initial Guess for a Transfer from an Elliptical, Geosynchronous Orbit that Lies in the Earth-Moon Orbital Plane to a Tundra Orbit Modeled in the Earth-Moon CR3BP, Generated from a Periapsis Map (Left: Barycentric Rotating Frame; Right: Earth-Centered Inertial Frame)

the plane of the primaries. Again, this solution may not be an ideal mission solution because of the large inclination change from the planar transfer orbit to the Tundra orbit.

Then, this feasible solution is utilized as an initial guess in an optimization algorithm. In this case, the optimization algorithm, *fmincon*, outputs an exit flag of two, which means that a locally optimal solution could not be converged upon, but a feasible solution is found. Despite the lack of a local optimum, this feasible solution does decrease the total ΔV required to perform this transfer. The ΔV of the feasible solution input into *fmincon* requires approximately 7.369 km/s of ΔV, while the output from *fmincon* only requires approximately 1.340 km/s of ΔV. The feasible solution output by *fmincon* can be seen in Figure 62.

The feasible solution output from *fmincon* requires approximately 1.340 km/s of ΔV, while the cost to perform a transfer between these two orbits through the employment of a conventional Hohmann-type transfer is found in Section 3.1.2.3 to be approximately 2.989 km/s. In this case, the ΔV required to perform this transfer using a high-altitude transfer orbit is found to be significantly less than the cost of a

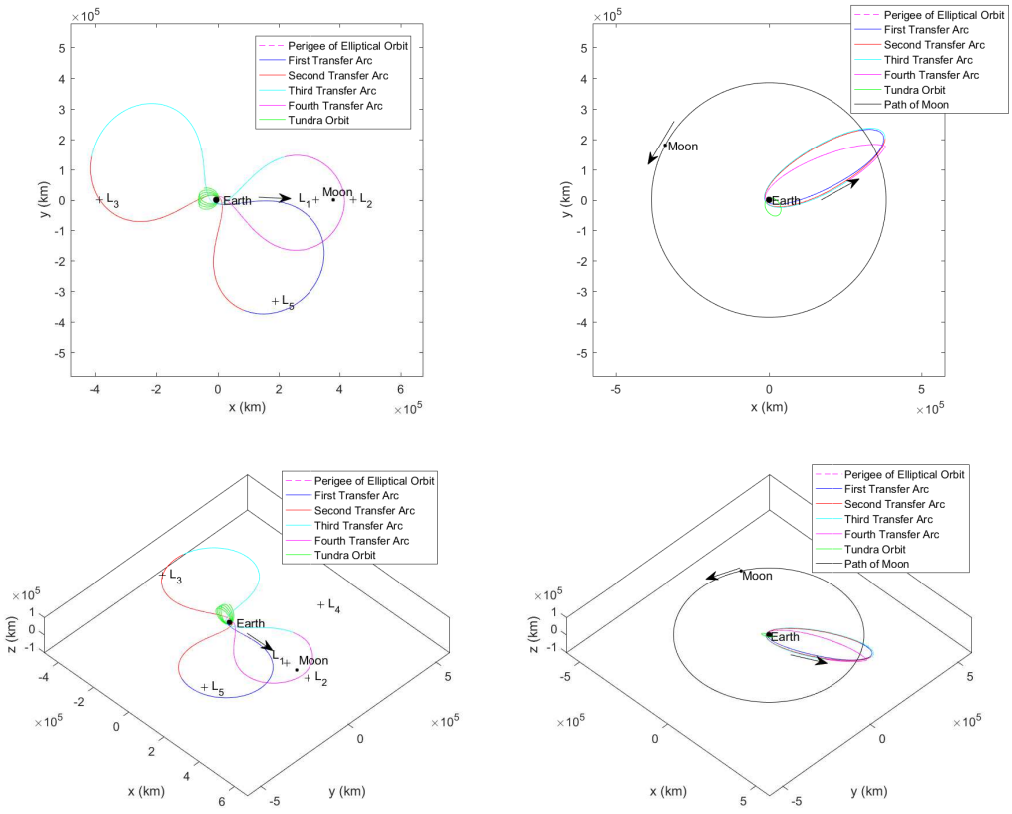

Figure 61. A Feasible Solution for a Transfer from an Elliptical, Geosynchronous Orbit that Lies in the Earth-Moon Orbital Plane to a Tundra Orbit Modeled in the Earth-Moon CR3BP (Top Left: View of $x-y$ Plane in the Barycentric Rotating Frame; Top Right: View of $x-y$ Plane in the Earth-Centered Inertial Frame; Bottom Left: 3D Perspective View in the Barycentric Rotating Frame; Bottom Right: 3D Perspective View in the Earth-Centered Inertial Frame)

conventional transfer. Additionally, the required time-of-flight to perform this transfer is about 41.9 days. Again, similar to the results in Test Case 1B, not only is a cost savings possible, but other advantages to this transfer path may exist. The intent of a spacecraft performing this transfer may be unclear to an observer in the inertial frame.

The COEs of this transfer path may be seen in Figure 63. These COEs illustrate multiple important behaviors. First, as seen in the previous two test cases, instantaneous changes to the COEs indicate ΔVs. Then, after about four days, the semimajor axis and eccentricity are disturbed as the spacecraft performs a lunar fly-by. However,

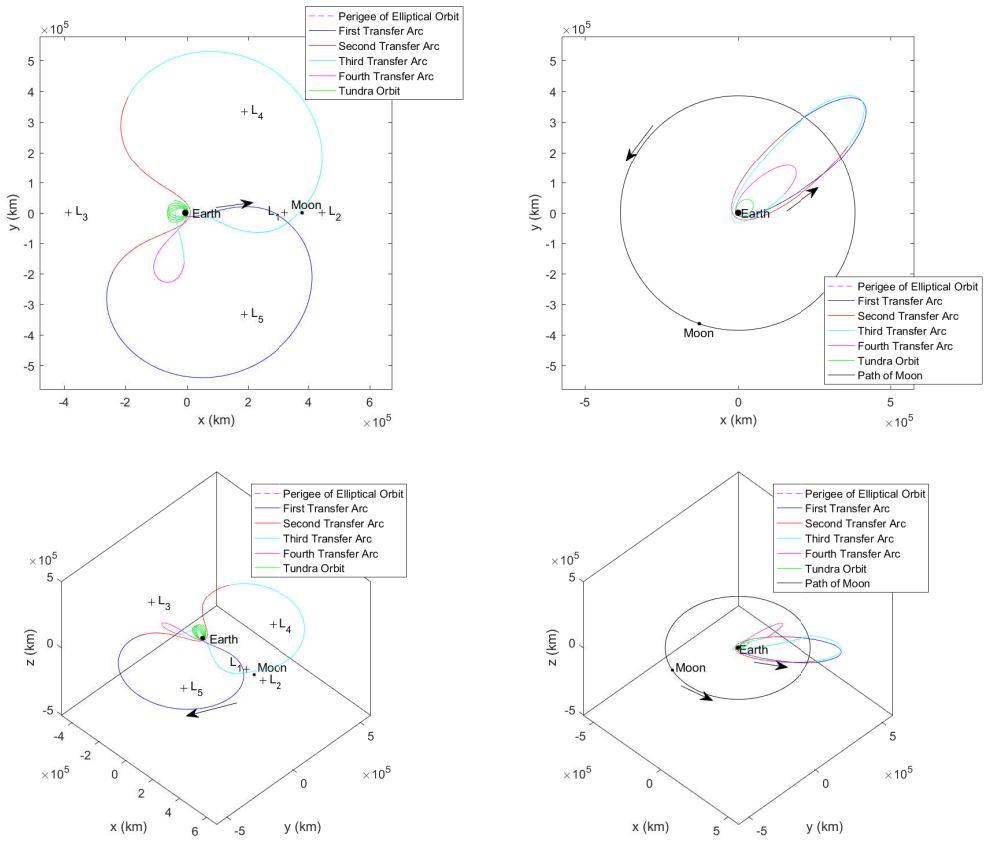

Figure 62. A Feasible Solution Output from *fmincon* for a Transfer from an Elliptical, Geosynchronous Orbit that Lies in the Earth-Moon Orbital Plane to a Tundra Orbit Modeled in the Earth-Moon CR3BP (Top Left: View of $x-y$ Plane in the Barycentric Rotating Frame; Top Right: View of $x-y$ Plane in the Earth-Centered Inertial Frame; Bottom Left: 3D Perspective View in the Barycentric Rotating Frame; Bottom Right: 3D Perspective View in the Earth-Centered Inertial Frame)

unlike Test Case 1B, the spacecraft remains in prograde motion with respect to the rotation of the Earth as it is near the Moon. Next, after approximately 32 days, the inclination is changed through the exploitation of another lunar fly-by. Only a small inclination change is required to be performed by the spacecraft. The majority of the inclination change occurs as a result of the second lunar fly-by. Finally, after about 42 days the spacecraft maneuvers into the destination Tundra orbit.

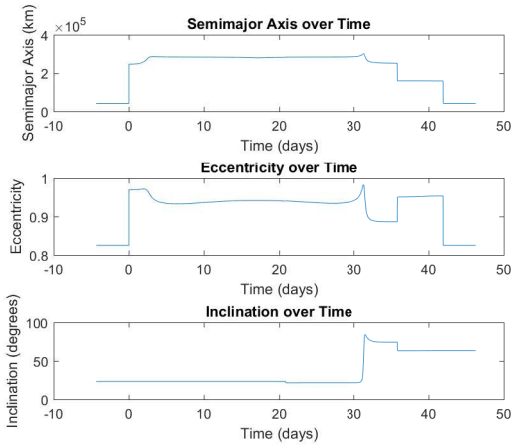

Figure 63. The Osculating COEs of a Feasible Transfer, Output from *fmincon*, from an Elliptical, Geosynchronous Orbit that Lies in the Earth-Moon Orbital Plane to a Tundra Orbit

4.1.4 Test Case 1: Discussion of Alternative, High-Altitude Transfers from a Planar Elliptical Geosynchronous Orbit to Conventional Constellations

In Test Case 1, the utilization of high-altitude transfers between conventional Earth-centric orbits is investigated. It is determined that the cost, in terms of ΔV, of these transfers is comparable, and in some cases significantly less, than the cost of a Hohmann-type transfer. In particular, when inclination changes are required, cost savings may exist. However, because of the high-altitude of these transfers, long times-of-flight were found. This result implies that there may be trade-offs between time-of-flight and the required ΔV. If a rapid transfer is desirable, a Hohmann-type transfer provides a direct transfer path between the conventional orbits. However, if a lower ΔV solution is desirable and an inclination change is required, it may be beneficial to utilize a high-altitude transfer. Another benefit of such a transfer is that the spacecraft's trajectory may be difficult to understand when viewing the trajectory in a two-body, inertial sense. Without viewing the transfers in the rotating frame of the Earth-Moon CR3BP, it may be difficult to anticipate the large deviations from

two-body motion. The rotating frame provides insight into the fly-bys performed and the gravitational effects of the Moon. Additionally, because of the high-altitude of the transfers, chaos may be present in these regions of the phase space. This chaos implies that for a low ΔV a transfer may be performed to alter the long term behavior of the spacecraft. So, these transfer paths may be considered less predictable to an observer. On the other hand, a Hohmann-type transfer provides a direct transfer between the two orbits, so the intent of a spacecraft may be known after a Hohmann-type transfer is begun.

The current investigation does possess some limitations. First, these trajectories only represent the preliminary design phase of an actual mission design. This preliminary design must be transitioned into an ephemeris model to validate the trajectories. This need is demonstrated in Section 4.1.1. Additionally, the ΔVs calculated only represent the deterministic ΔVs and do not include the required ΔV for stationkeeping. Analysis must be performed to account for the needed ΔV for stationkeeping.

4.2 Test Case 2: Results and Analysis of the Application of High-Altitude Parking Orbits to Reconstitute Conventional Constellations

In Test Case 2, the ability to reconstitute the conventional constellations of interest from a high-altitude parking orbit is investigated. In the current investigation, a planar 4:3 resonant orbit is selected as the high-altitude parking orbit. This parking orbit is chosen because it possesses desirable characteristics. First, this particular 4:3 resonant orbit is orbitally unstable to in-plane perturbations based on an eigenvalue analysis of the monodromy matrix. The invariant manifolds associated with this instability travel through desirable regions of the configuration space: near geostationary altitude (35,786 km) and LEO. This behavior may allow for low-cost transfers to and from the 4:3 resonant orbit. Additionally, the periapses of this parking orbit are near

geostationary altitude. These fly-bys near geostationary altitude may allow for direct transfers from the parking orbit to orbits with geostationary altitude. In the current investigation, fly-bys near this altitude are considered desirable regardless of inclination. Also, this 4:3 resonant orbit performs a lunar fly-by once per period in the barycentric rotating frame. This close encounter with the Moon may be beneficial when searching for cost-effective transfer paths that change the inclination of the satellite. Finally, the particular 4:3 resonant orbit explored in the current investigation is a locally optimal result of Test Case 3A, which searches for locally optimal parking orbits in terms of average performance relative to a nominal satellite at geostationary altitude. This characteristic may allow for a satellite in a high-altitude parking orbit to remotely sense the surface of the Earth while waiting to be tasked with reconstitution. A satellite on the ground waiting to be tasked with reconstitution would be unable to provide any additional capability. However, despite the desirable characteristics associated with this particular parking orbit, other parking orbits may exist that yield desirable results.

First, the cost, in terms of ΔV, to deploy a satellite into this 4:3 resonant orbit is calculated. An initial guess is generated from the invariant manifold approximations shown in Figure 49. A periapse from the stable manifold approximation near LEO is selected as an initial guess for a transfer from LEO to the parking orbit. Then, a multiple-shooting algorithm is implemented to target the feasible solution shown in Figure 64. The cost, in terms of ΔV, to perform this transfer based on the feasible solution presented in Figure 64 is found to be approximately 3.131 km/s. Then, this feasible solution is input as an initial guess into *fmincon* to search for a locally optimal solution, in terms of ΔV. The resulting locally optimal transfer is shown in Figure 65.

The cost of the locally optimal transfer presented in Figure 65 is found to be approximately 3.112 km/s. The locally optimal solution takes advantage of the Oberth

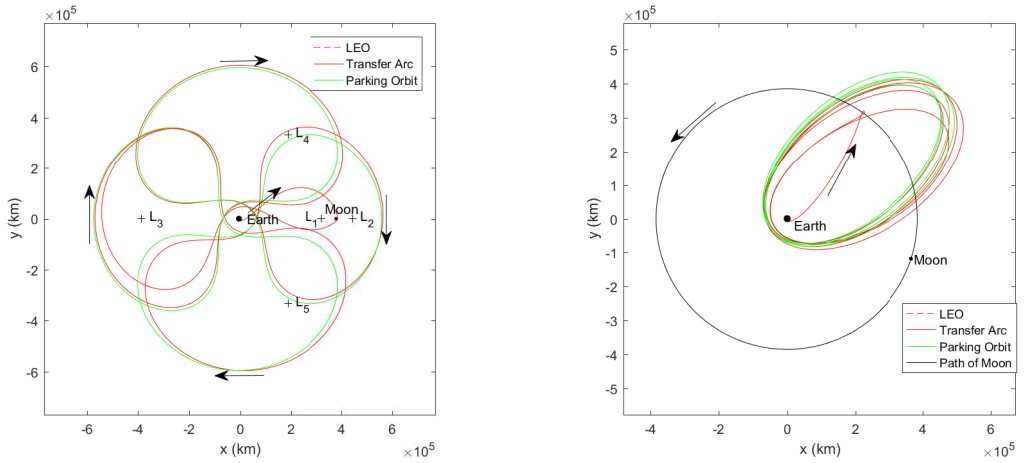

Figure 64. A Feasible Solution for a Transfer from LEO to the 4:3 Resonant Parking Orbit Modeled in the Earth-Moon CR3BP (Left: Barycentric Rotating Frame; Right: Earth-Centered Inertial Frame)

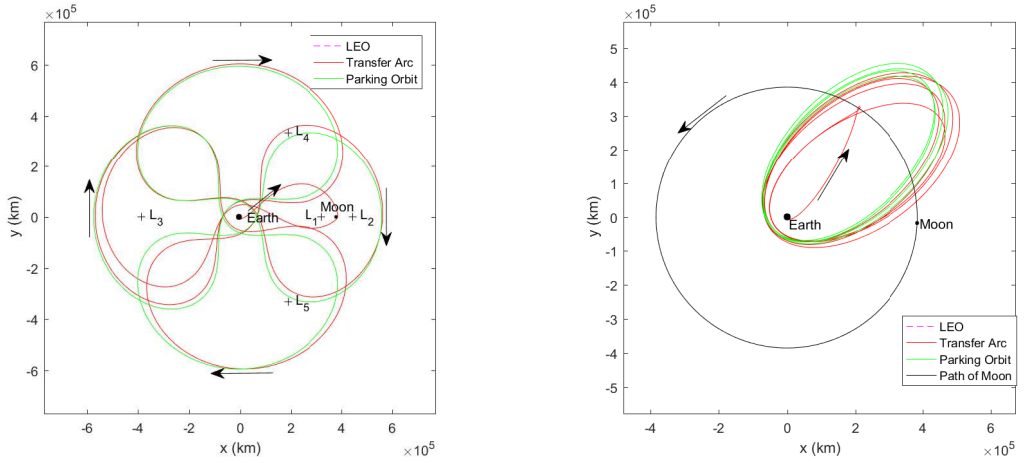

Figure 65. A Locally Optimal Solution, in Terms of ΔV, for a Transfer from LEO to the 4:3 Resonant Parking Orbit Modeled in the Earth-Moon CR3BP (Left: Barycentric Rotating Frame; Right: Earth-Centered Inertial Frame)

effect as the insertion point into the 4:3 resonant orbit is moved closer to a periapse in the locally optimal solution. Additionally, the time-of-flight of this transfer is found to be approximately 108.7 days.

4.2.1 Test Case 2A: Results and Analysis of the Reconstitution of A Constellation of Three Satellites in Circular Geosynchronous Orbits that Lie in the Earth-Moon Orbital Plane from a High-Altitude Parking Orbit

In Test Case 2A, the ability to reconstitute a constellation of circular geosynchronous satellites from a high-altitude parking orbit is investigated as an alternative to a launch-on-demand capability. Specifically, the 4:3 resonant orbit discussed above is investigated. In order to improve the timeliness of transfer paths, multiple transfer opportunities are investigated from the 4:3 resonant orbit to the constellation of interest. The multiple transfer opportunities from this parking orbit are analogous to the off-ramps of a highway. A satellite in the high-altitude orbit, based on the assumptions of the current investigation, must wait for the next transfer opportunity, or off-ramp, to depart the parking orbit. Only a small sample of the possible transfer paths are explored in the current investigation; however, other transfer paths, or off-ramps, may exist. Four initial guesses for transfer paths are generated from the resonant arcs of the 4:3 resonant orbit. Wilmer previously demonstrated the use of a 4:3 resonant arc as an initial guess to perform a transfer into a geostationary orbit from a geosynchronous transfer orbit [14]. However, the current investigation explores the employment of similar resonant arcs as initial guesses for transfer paths from the 4:3 resonant orbit to a constellation of circular geosynchronous orbits that lie in the Earth-Moon orbital plane. The four initial guesses shown in Figure 66 are generated from each of the four ‘‘loops’’ associated with the 4:3 resonant orbit [68]. The initial guesses each begin and end at a periapse associated with the 4:3 resonant orbit. These initial guesses are selected in an attempt to exploit the Oberth effect.

Each of these four initial guesses are utilized as an initial guess in a multiple-shooting algorithm that targets feasible transfers from the 4:3 resonant orbit to a

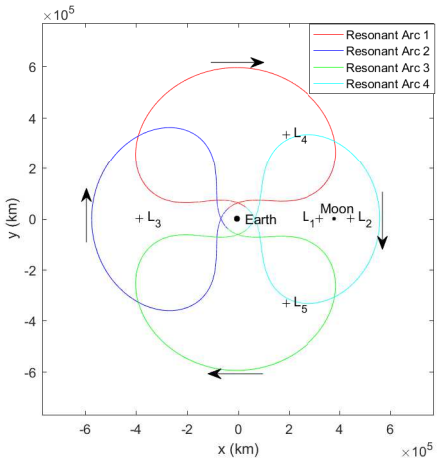

Figure 66. Four Initial Guesses for Transfers from a 4:3 Resonant Orbit to a Circular, Geosynchronous Orbit in the Earth-Moon Orbital Plane Modeled in the Earth-Moon CR3BP Displayed in the Barycentric Rotating Frame

circular, geosynchronous orbit. The resulting feasible solutions are shown in the rotating frame in Figure 67.

Then, these feasible solutions are input into *fmincon* as initial guesses to search for locally optimally transfers, in terms of ΔV. The four locally optimal transfers are shown in Figure 68. The cost, in terms of ΔV to perform each of these four locally optimal transfers ranges from 1.118 km/s to 1.169 km/s. The total ΔV to deploy a satellite into this high-altitude parking orbit, using the locally optimal transfer shown in Figure 65, and then to transfer to this constellation, using one of the locally optimal solutions shown in Figure 68, is found to range from 4.229 km/s to 4.281 km/s. Additionally, since there are only four locally optimal transfer opportunities, or locally optimal off-ramps, presented, a satellite in this 4:3 resonant orbit may be required to wait until it reaches an appropriate point in the resonant orbit, an off-ramp, to begin the transfer. Including these potential wait times, the maximum time it would take for a satellite to reach an appropriate point in the periodic orbit and to perform the transfer from the parking orbit to the circular geosynchronous orbit is approximately 41.3 days. Alternatively, it is possible that a satellite may not be required to wait

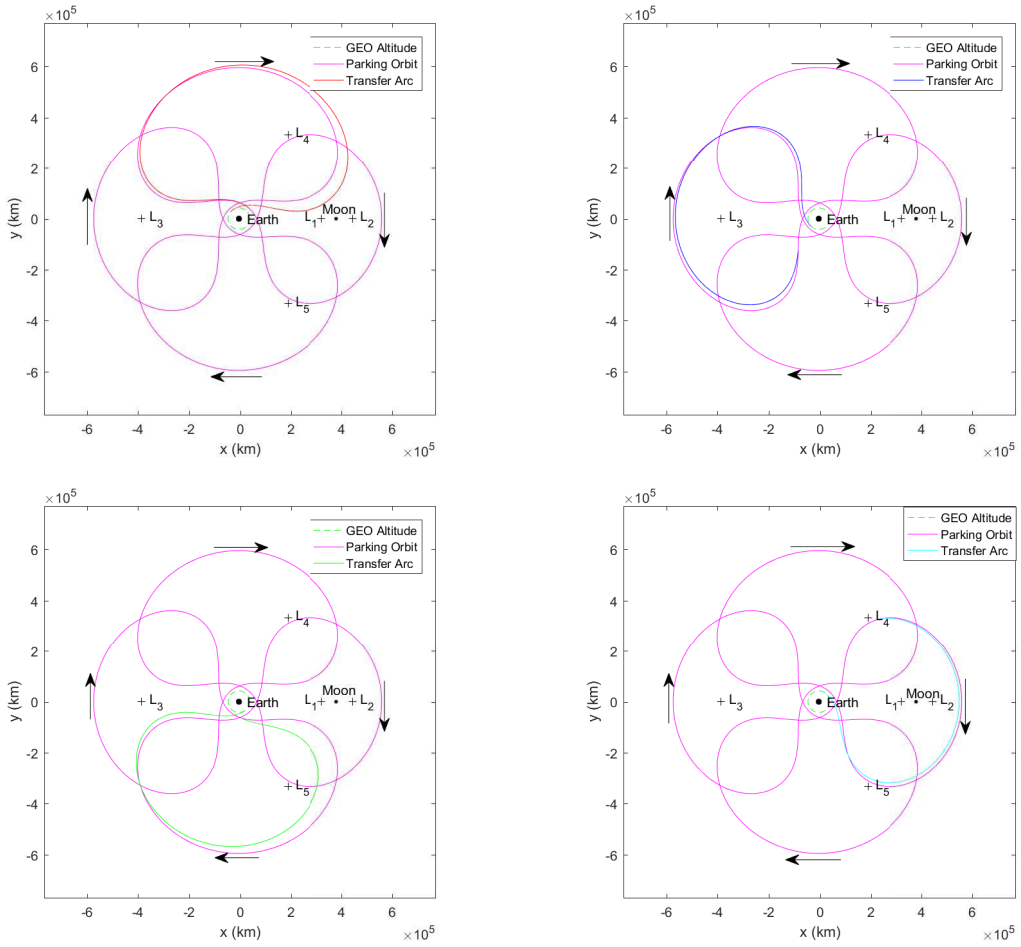

Figure 67. Four Feasible Transfers from a 4:3 Resonant Orbit to a Circular, Geosynchronous Orbit in the Earth-Moon Orbital Plane Modeled in the Earth-Moon CR3BP, Displayed in the Barycentric Rotating Frame (Top Left: Associated with Resonant Arc 1; Top Right: Associated with Resonant Arc 2; Bottom Left: Associated with Resonant Arc 3; Bottom Right: Associated with Resonant Arc 4)

when tasked with reconstitution. In this case, the minimum time to perform the transfer using one these four locally optimal solutions is 9.2 days. On average, the time until reconstitution is 23.0 days.

The four locally optimal solutions presented in Figure 68 are based on the initial guesses generated from the resonant arcs of the periodic parking orbit that begin and end near a periapse; however, not all of the locally optimal solutions begin near a periapse. The locally optimal solutions associated with the second, third, and fourth resonant arcs converge upon locally optimal transfers that begin near an apoapse of the

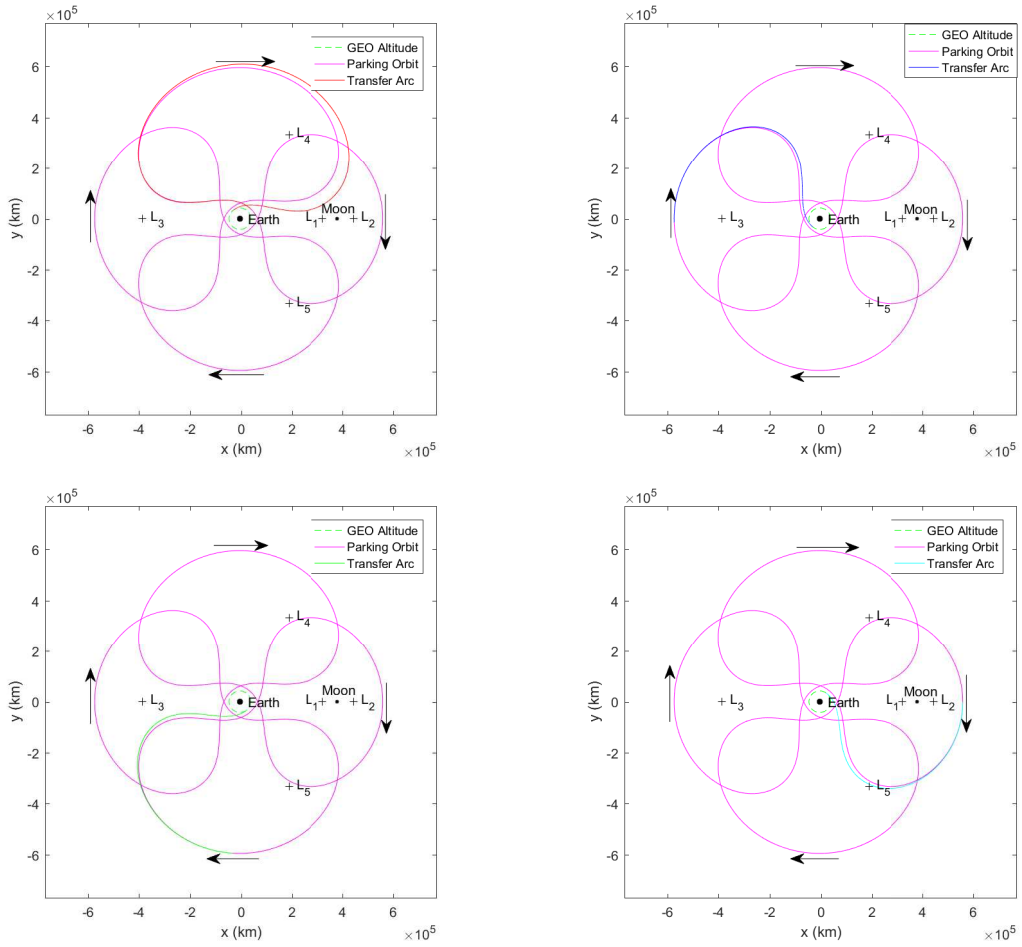

Figure 68. Four Locally Optimal Solutions, in Terms of ΔV, of Transfers from a 4:3 Resonant Orbit to a Circular, Geosynchronous Orbit in the Earth-Moon Orbital Plane Modeled in the Earth-Moon CR3BP Displayed in the Barycentric Rotating Frame (Top Left: Associated with Resonant Arc 1; Top Right: Associated with Resonant Arc 2; Bottom Left: Associated with Resonant Arc 3; Bottom Right: Associated with Resonant Arc 4)

4:3 resonant orbit. On the other hand, the locally optimal solution associated with the first resonant arc utilizes the entire resonant arc similar to the initial guess. However, since the locally optimal solution associated with this first resonant arc is different than the other three locally optimal solutions in that it begins near periapse, the longest wait time occurs when this transfer opportunity is missed and the spacecraft must wait until the starting point of the locally optimal solution associated with the second resonant arc. However, if another solution were found that began near the

apoapse of the first resonant arc, this maximum time until reconstitution could be reduced.

To attempt to reduce the maximum time until reconstitution, another initial guess is generated that begins at the apoapse of the first resonant arc and ends at the next periapse. Again, this initial guess is input into a multiple-shooting algorithm to target a feasible solution. The resulting feasible solution is shown in Figure 69.

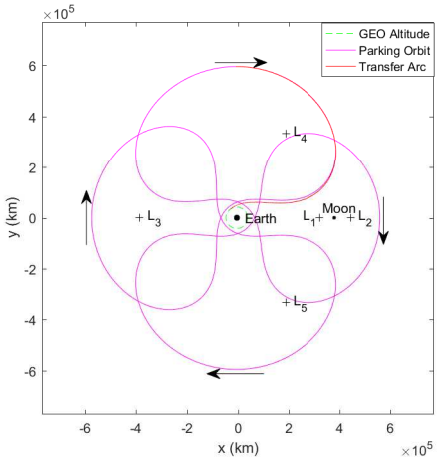

Figure 69. A Feasible Solution for a Transfer from a 4:3 Resonant Orbit to a Circular Geosynchronous Orbit in the Earth-Moon Orbital Plane Associated with an Initial Guess Beginning at the Apoapse of the First Resonant Arc Modeled in the Earth-Moon CR3BP Displayed in the Barycentric Rotating Frame

Then, in an attempt to find a locally optimal solution with similar behavior, this feasible solution is used as an initial guess in an optimization algorithm. However, the resulting locally optimal solution does not preserve the desired starting point of the transfer near the apoapse. Instead, the locally optimal solution found with *fmincon* is very similar to the locally optimal solution shown in Figure 68. This locally optimal solution is shown in Figure 70.

A satellite in this 4:3 parking orbit could utilize any of the feasible transfer paths, or off-ramps, presented above. Depending on where the satellite is in the parking orbit when a need for reconstitution occurs, the satellite may be tasked with transferring at the next available off-ramp. The eight transfer path options, or off-ramps, analyzed

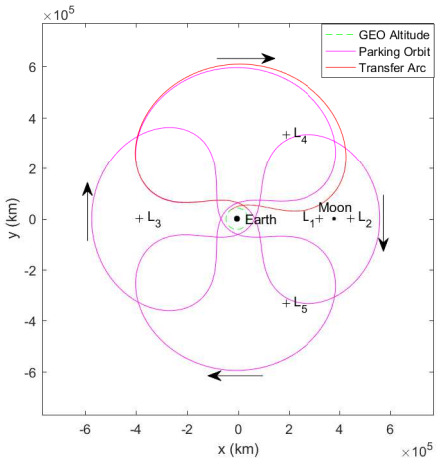

Figure 70. A Locally Optimal Solution, in terms of ΔV, for a Transfer from a 4:3 Resonant Orbit to a Circular, Geosynchronous Orbit in the Earth-Moon Orbital Plane Associated with an Initial Guess Beginning at the Apoapse of the First Resonant Arc Modeled in the Earth-Moon CR3BP Displayed in the Barycentric Rotating Frame

are the feasible solutions associated with the second, third, and fourth resonant arcs presented in Figure 67, the four locally optimal solutions presented in Figure 68, and the feasible solution presented in Figure 69. The feasible solution associated with the first resonant arc presented in Figure 67 and the locally optimal solution presented in Figure 70 are neglected in this analysis because of their similarity to the locally optimal solution associated with the first resonant arc in Figure 68. The time-of-flight and ΔVs associated with each of these transfer paths are shown in Table 10.

Together, these eight transfer paths, or off-ramps, consist of four feasible solutions and four locally optimal solutions. Additionally, four of the off-ramps begin near an apoapse of the 4:3 resonant orbit, while the other four begin near a periapse of the 4:3 resonant orbit. Figure 71 shows the nearest of the eight off-ramps to a satellite in the 4:3 resonant orbit depending on where the satellite is located when tasked with reconstitution. The feasible solutions are color-coded based on the resonant arc of the transfer path and are denoted with an "x." The locally optimal solutions are also color-coded based on the resonant arc of the transfer path and are denoted with an "o."

Table 10. The Approximate ΔV and Time-of-Flight Associated with Each of the Eight Transfer Paths

Resonant Arc	Type of Solution	Total ΔV (km/s)	Time-of-Flight (days)
1	Feasible	1.196	21.9
1	Locally Optimal	1.118	22.1
2	Feasible	1.295	18.4
2	Locally Optimal	1.155	9.9
3	Feasible	1.643	19.378
3	Locally Optimal	1.169	10.2
4	Feasible	1.302	14.248
4	Locally Optimal	1.169	9.2

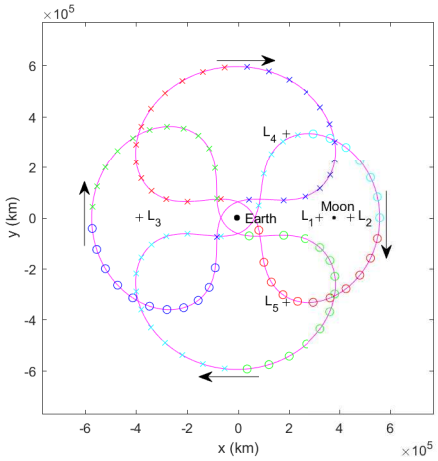

Figure 71. 100 Points Equally Spaced Along the 4:3 Resonant Parking Orbit Color-Coded Based on the Next Available Transfer Opportunity Using Eight Transfer Paths, Modeled in the Earth-Moon CR3BP and Displayed in the Barycentric Rotating Frame

Next, the associated ΔV and time until reconstitution associated with the nearest of the eight off-ramps from each of these points are shown in Figure 72. Based on this analysis, the average time until reconstitution from each of the points to a circular, geosynchronous orbit is 19.9 days. Additionally, the longest time-of-flight is 31.6 days. However, while the three feasible solutions associated with the second, third,

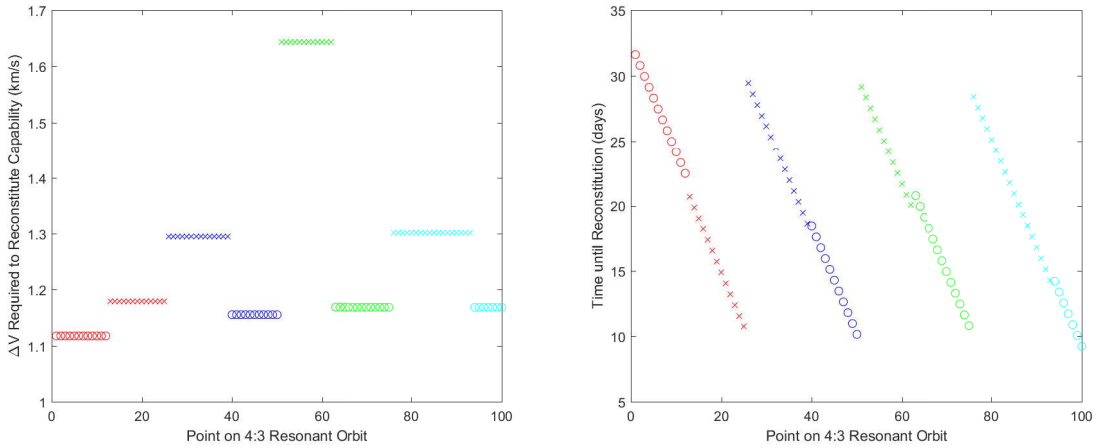

Figure 72. The ΔV and Time until Reconstitution Associated with the 100 Points Equally Spaced Along the 4:3 Resonant Parking Orbit Color-Coded Based on the Next Available Transfer Opportunity Using Eight Transfer Paths (Left: Approximate ΔV; Right: Approximate Time until Reconstitution)

and fourth arc may be the nearest off-ramp, they may not be the most cost-effective off-ramp. The maximum ΔV to utilize one of these eight off-ramps is found to be 1.643 km/s. The three feasible solutions associated with the second, third, and fourth resonant arcs are then eliminated from the analysis because of their cost, in terms of ΔV. This elimination results in a five off-ramp solution. After that, the same analysis is performed for this five off-ramp scenario. Figure 73 shows the nearest of these five off-ramps to a satellite as it travels through the 4:3 resonant orbit.

Again, the associated ΔV and time until reconstitution associated with the nearest off-ramp from each of these points are shown in Figure 74.

Figure 74 shows that the five off-ramp solution follows the same trends as the eight off-ramp solution, but with a lower maximum ΔV of 1.196 km/s. However, this five off-ramp scenario does result in a slightly increased average time until reconstitution of 20.3 days while the maximum time until reconstitution remains 31.6 days.

Next, a scenario of multiple satellites in the 4:3 resonant orbit is analyzed. One potential method for spacing the satellites in the 4:3 resonant orbit could be to equally space them in time throughout the entire orbit. In this 4:3 resonant orbit, this type

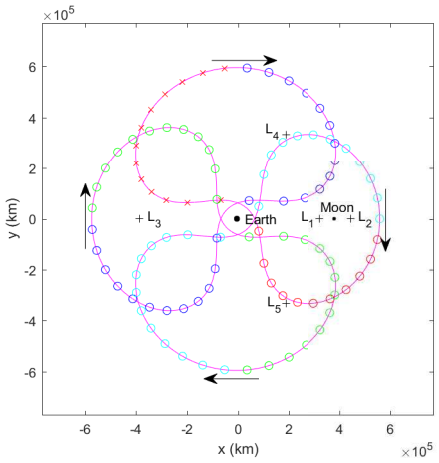

Figure 73. 100 Points Equally Spaced Along the 4:3 Resonant Parking Orbit Color-Coded Based on the Next Available Transfer Opportunity Using Five Transfer Paths, Modeled in the Earth-Moon CR3BP and Displayed in the Barycentric Rotating Frame

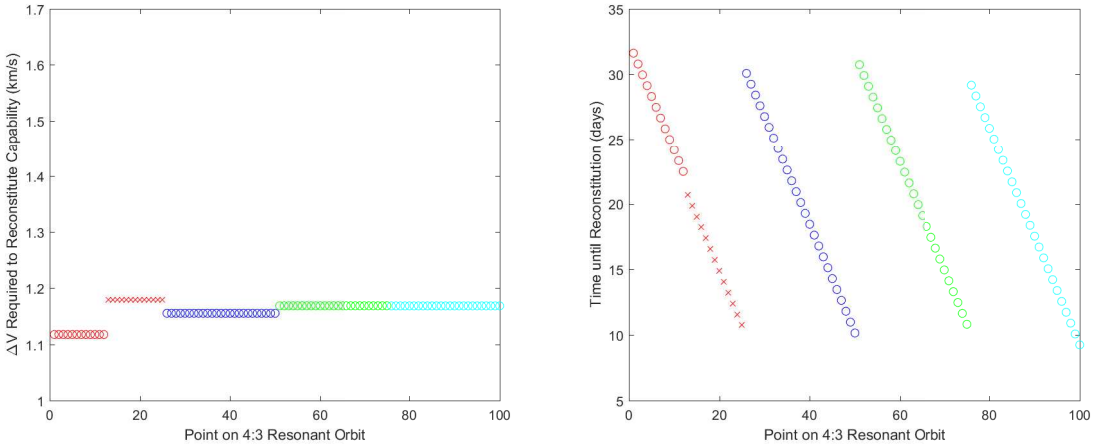

Figure 74. The ΔV and Time until Reconstitution Associated with the 100 Points Equally Spaced Along the 4:3 Resonant Parking Orbit Color-Coded Based on the Next Available Transfer Opportunity Using Five Transfer Paths (Left: Approximate ΔV; Right: Approximate Time until Reconstitution)

of spacing would correspond to the lead satellite being 41.1 days ahead of the second satellite. This arrangement would be beneficial for a satellite in a parking orbit with only one acceptable off-ramp; however, in the current scenario, this type of spacing is not desirable. For example, if a parking orbit were designed with two off-ramps that were equally spaced in time, equally spacing two satellites throughout the entire parking orbit would not reduce the wait time at all. Instead, both satellites would

arrive at different off-ramps at the same time. If the need for reconstitution occurred after both of these satellites just passed these off-ramps, the maximum wait time would still be one half of the period. Alternatively, it is more effective in terms of time until reconstitution to identify the longest wait time for a single satellite to reach an off-ramp and equally space the satellites along this time interval. This type of spacing is desirable because it staggers the satellite arrivals at off-ramps instead of spacing the satellites such that satellites arrive at different off-ramps at the same time.

In the current five off-ramp scenario, the longest wait time of 21.1 days occurs when the satellite misses the transfer opportunity associated with the locally optimal transfer associated with the second resonant arc and must wait until the locally optimal transfer associated with the third resonant arc. To effectively spread satellites in a multi-off-ramp scenario, the satellites should be equally spaced in time up to the longest wait time. For example, since the longest wait time presented was 21.1 days, the two satellite solution would be for the second satellite to be 10.5 days behind the lead satellite. Likewise, with three satellites, the second satellite should be 7.0 days behind the lead satellite and the third satellite should be 7.0 days behind the second satellite. Through the implementation of this spacing method, Figure 75 shows which of the five off-ramps possesses the shortest time until reconstitution for one of two satellites that are 10.5 days apart in the parking orbit. Note that Figure 75 plots the position of the lead satellite and is color-coded based on the shortest off-ramp solution associated with either satellite.

Interestingly, the locally optimal solution associated with the first resonant arc is never the shortest time until reconstitution transfer path when two satellites are spaced in this manner. This result is caused by the fact that when one of the two satellites is closest to this off-ramp, the other satellite is always near an off-ramp associated with a lower time until reconstitution. However, this transfer path may

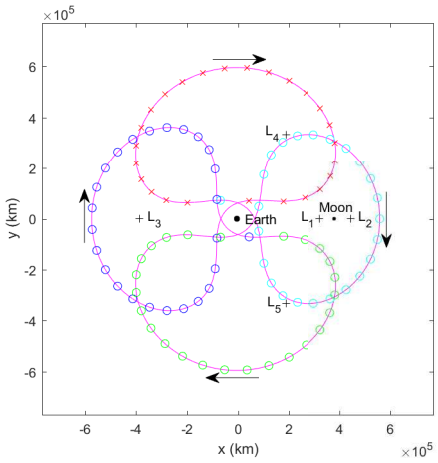

Figure 75. 100 Points Equally Spaced Along the 4:3 Resonant Parking Orbit Representing the Position of the Lead Satellite and Color-Coded Based on the Shortest Time until Reconstitution Transfer for One of the Two Satellites Using Five Transfer Paths, Modeled in the Earth-Moon CR3BP and Displayed in the Barycentric Rotating Frame

still be desirable to a decision-maker, as it requires the least ΔV. It may be desired to trade response time with the cost savings possible via this transfer option. Then, the associated ΔV and time until reconstitution associated with the shortest time-of-flight solution from each of these lead satellite positions are shown in Figure 76.

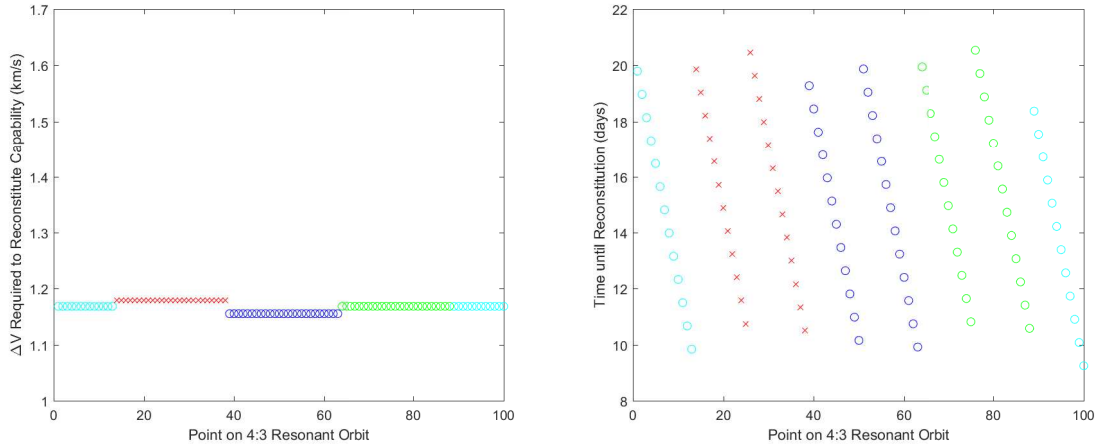

Figure 76. The ΔV and Time-of-Flight Associated with the 100 Points Equally Spaced Along the 4:3 Resonant Parking Orbit Color-Coded Based on the Shortest Time until Reconstitution Transfer for One of the Two Satellites Using Five Transfer Paths (Left: Approximate ΔV; Right: Approximate Time until Reconstitution)

Through the utilization of two satellites in this five off-ramp scenario, it is found that the maximum time until reconstitution is 20.5 days, while the average time until reconstitution is 15.0 days. Additionally, the maximum ΔV is found to be 1.169 km/s. Next, this analysis is extended to N satellites equally spaced in this manner.

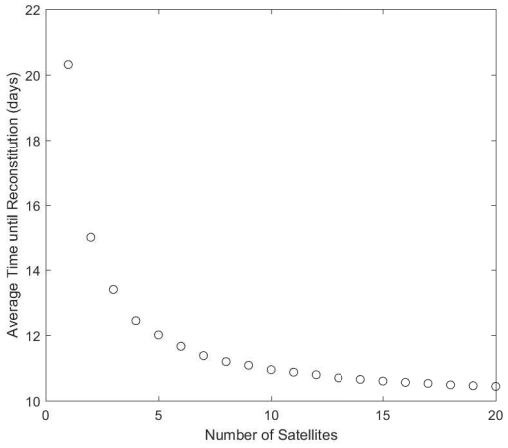

Figure 77. The Average Time until Reconstitution from the 4:3 Resonant Orbit as a Function of the Number of Satellites in the Orbit

Figure 77 shows that as the number of satellites increases, the average time until reconstitution decreases. However, as the number of satellites is increased further, an asymptotic limit is approached. This limit is associated with the average time required to actually complete one of these transfers. In other words, it is possible to increase the number of satellites to the point that one satellite is always at an off-ramp; however, since the off-ramp itself possesses a time-of-flight, it is not possible to increase the number of satellites such that the average time until reconstitution is zero.

In Test Case 2A, it is determined that transfers from a high-altitude parking orbit may be performed in a timely manner. With one satellite in the five off-ramp scenario, the average time until reconstitution is found to be 20.3 days, while the maximum time until reconstitution is found to be 31.6 days. On average, a single satellite in such an orbit provides a more timely transfer to the circular geosynchronous orbit

that lies in the plane of the primaries than a launch-on-demand capability requiring 30 days lead time. Additionally, through the addition of a second satellite, properly spaced with the lead satellite, the average time until reconstitution decreases to 15.0 days and the maximum time until reconstitution decreases to 20.5 days. Additionally, as the number of satellites in the parking orbit increases, it is concluded that the average time until reconstitution approaches an asymptotic limit.

It is also determined that the maximum transfer cost, in terms of ΔV, for the five off-ramp scenario is 1.196 km/s. In summation with the ΔV to deploy a satellite into the high-altitude orbit (3.112 km/s), it is found that the maximum total cost of such a mission is 4.308 km/s. To transfer directly from LEO to a circular, geosynchronous orbit that lies in the Earth-Moon orbital plane requires 3.893 km/s of ΔV. Therefore, this high-altitude transfer option provides a slightly larger but comparable cost, in terms of ΔV, to a launch-on-demand capability utilizing a Hohmann transfer. Since the cost, in terms of ΔV, is similar to a launch-on-demand capability, and the responsiveness is, on average, better than a launch-on-demand capability, it is concluded that a satellite in a high-altitude parking orbit may be an effective means of reconstitution for a circular, geosynchronous orbit that lies in the Earth-Moon orbital plane.

4.2.2 Test Case 2B: Results and Analysis of the Reconstitution of A Constellation of Three Geostationary Satellites from a High-Altitude Parking Orbit

In Test Case 2B, the ability of a satellite in a high-altitude parking orbit to reconstitute a constellation of geostationary satellites is investigated as an alternative to a launch-on-demand capability. The same 4:3 resonant orbit utilized in Test Case 2A is again selected as the candidate high-altitude parking orbit. An initial guess for

this transfer that remains in the Earth-Moon orbital plane is generated through an investigation of the periapsis Poincaré map of the invariant manifold approximations associated with this unstable periodic orbit. Then, a multiple-shooting algorithm is implemented to target a feasible solution from this initial guess. This feasible solution is shown in Figure 78.

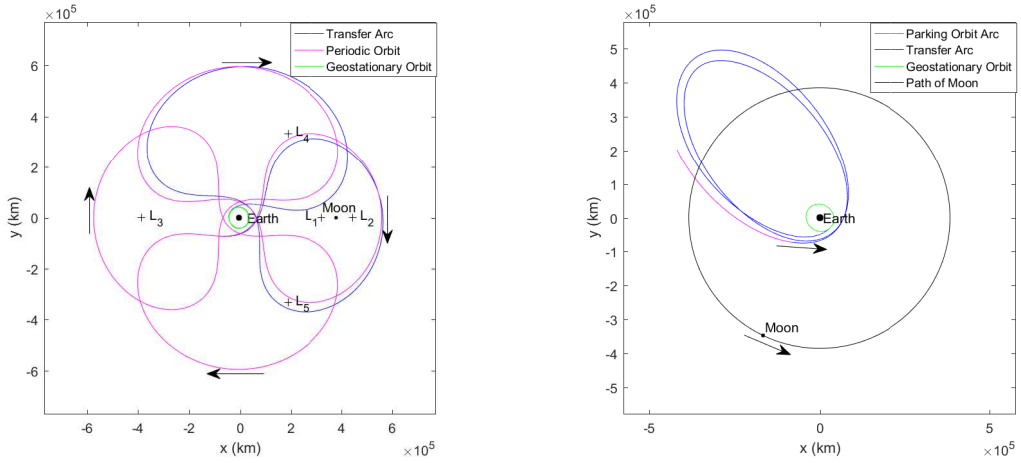

Figure 78. A Feasible Solution for a Transfer from a 4:3 Resonant Orbit to a Geostationary Orbit Modeled in the Earth-Moon CR3BP (Left: Barycentric Rotating Frame; Right: Earth-Centered Inertial Frame)

The differential corrections process converges upon a planar transfer from the high-altitude parking orbit to the geostationary orbit. However, this planar transfer resulted in a large ΔV of 1.883 km/s. Next, this feasible solution is input into *fmincon* to search for a locally optimal transfer in terms of ΔV. The resulting locally optimal transfer requires 1.273 km/s of ΔV and is shown in Figure 79.

The feasible solution begins the transfer near a periapse of the periodic orbit; however, *fmincon* converges upon a locally optimal solution that performs its first burn at a higher altitude. This change occurs because the locally optimal solution performs its inclination change while at a lower speed. It is more cost-effective to perform an inclination change when traveling at a slower speed than at a higher speed. This same effect is seen in Hohmann-type transfers from inclined LEO to geostationary

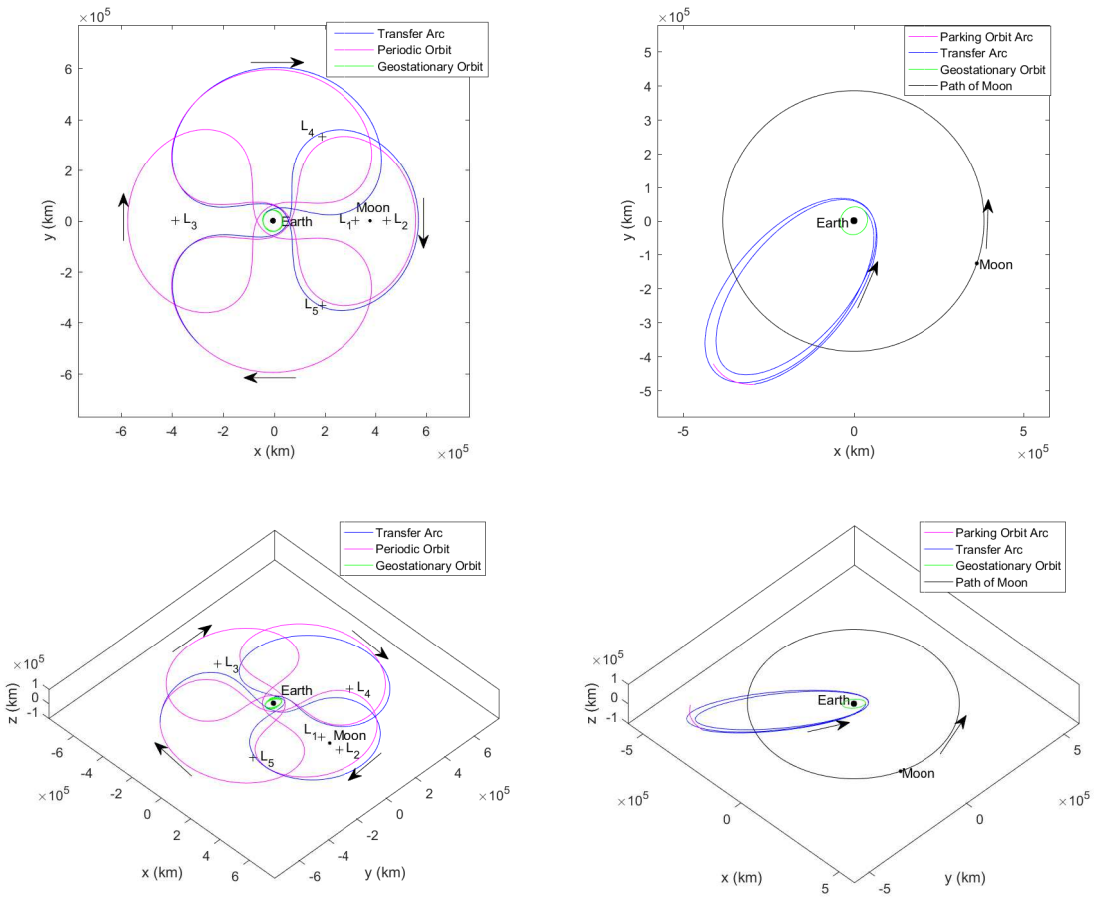

Figure 79. A Locally Optimal Solution, in Terms of ΔV, of a Transfer from a 4:3 Resonant Orbit to a Geostationary Orbit Modeled in the Earth-Moon CR3BP (Top Left: Barycentric Rotating Frame; Top Right: Earth-Centered Inertial Frame; Bottom Left: 3D Perspective of Barycentric Rotating Frame; Bottom Right: 3D Perspective of Earth-Centered Inertial Frame)

orbits. It is more cost-effective to perform the inclination change when traveling at slower speeds, so the combined plane change is typically performed at apogee of such a transfer orbit.

The locally optimal transfer presented above combined with the transfer from LEO into the parking orbit requires 4.385 km/s of ΔV. This cost, in terms of ΔV, is slightly larger than, but comparable, to a Hohmann-type transfer with a combined plane change from LEO, which requires 4.145 km/s of ΔV. However, the time-of-flight of this transfer from the 4:3 resonant orbit requires 48.8 days. This time-of-flight only

includes the amount of time it takes for the satellite to perform the transfer. It is possible that the satellite would be required to wait an entire period of the periodic parking orbit before the transfer could be started. In other words, only a single off-ramp is presented in this scenario. The time until reconstitution of a satellite in a geostationary orbit using this locally optimal transfer path could vary between 48.8 days and 130.9 days. It may be possible that this timeliness is satisfactory; however other options may also be considered to reduce the required time to reconstitute a capability. A similar analysis to Test Case 2A could be performed to increase the timeliness of reconstitution through the use of other transfer paths, or off-ramps. Alternatively, multiple satellites could be positioned in this high-altitude parking orbit. Since only one off-ramp was investigated in Test Case 2B, the maximum wait time to reach an off-ramp is one period of the 4:3 resonant orbit. Spacing two satellites employing the strategy described in Section 4.2.1 results in two satellites spaced one half-period apart. This reduces the maximum time until reconstitution from the periodic orbit to 89.8 days. Similar to Section 4.2.1, the average time until reconstitution is investigated as the number of satellites is increased. These results are shown in Figure 80. As the number of satellites is increased, the average time until reconstitution decreases until an asymptotic limit is reached.

In Test Case 2B, it is determined that the cost of transferring from a high-altitude parking orbit to a geostationary orbit is similar to the cost of performing a Hohmann-type transfer from LEO to a geostationary orbit. However, through the utilization of the single transfer path, or off-ramp, and a single satellite, the transfer may not be performed in less time than a 30-day launch-on-demand capability. Other transfer paths similar to the paths explored in Section 4.2.1 may exist that increase the timeliness of the transfer. Despite the increased time until reconstitution,

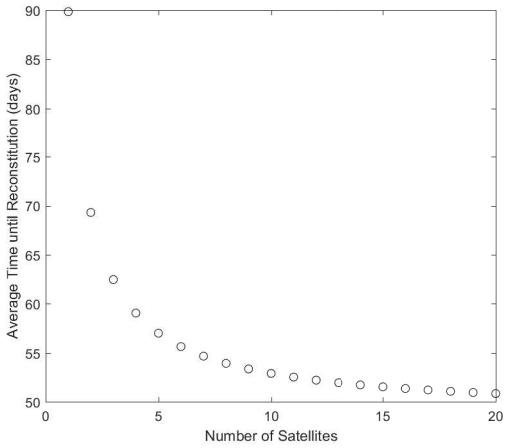

Figure 80. The Average Transfer Time to Reconstitute a Geostationary Constellation Using One Transfer Path as the Number of Satellites is Increased

reconstitution may still be effective, but less timely, from such a parking orbit with the single presented transfer path.

4.2.3 Test Case 2C: Results and Analysis of the Reconstitution of A Constellation of Three Tundra Satellites from a High-Altitude Parking Orbit

In Test Case 2C, the ability of a satellite in a high-altitude parking orbit to reconstitute a constellation of three Tundra satellites is investigated. Similar to the design process showcased in Test Cases 2A and 2B, first, an initial guess is generated. The feasible solution output from *fmincon* found in Test Case 1C, shown in Figure 62, is very effective in its exploitation of the gravitational effects of the Moon to aid in the necessary inclination change to transfer from the Earth-Moon orbital plane to the orbital plane of a Tundra orbit. Because of this demonstrated effectiveness, a portion of the transfer from Test Case 1C is utilized as an initial guess for a transfer from the 4:3 resonant orbit to a Tundra orbit. This initial guess is then input into a

multiple-shooting algorithm to target a feasible transfer from the high-altitude parking orbit to the Tundra orbit. This feasible transfer is shown in Figure 81.

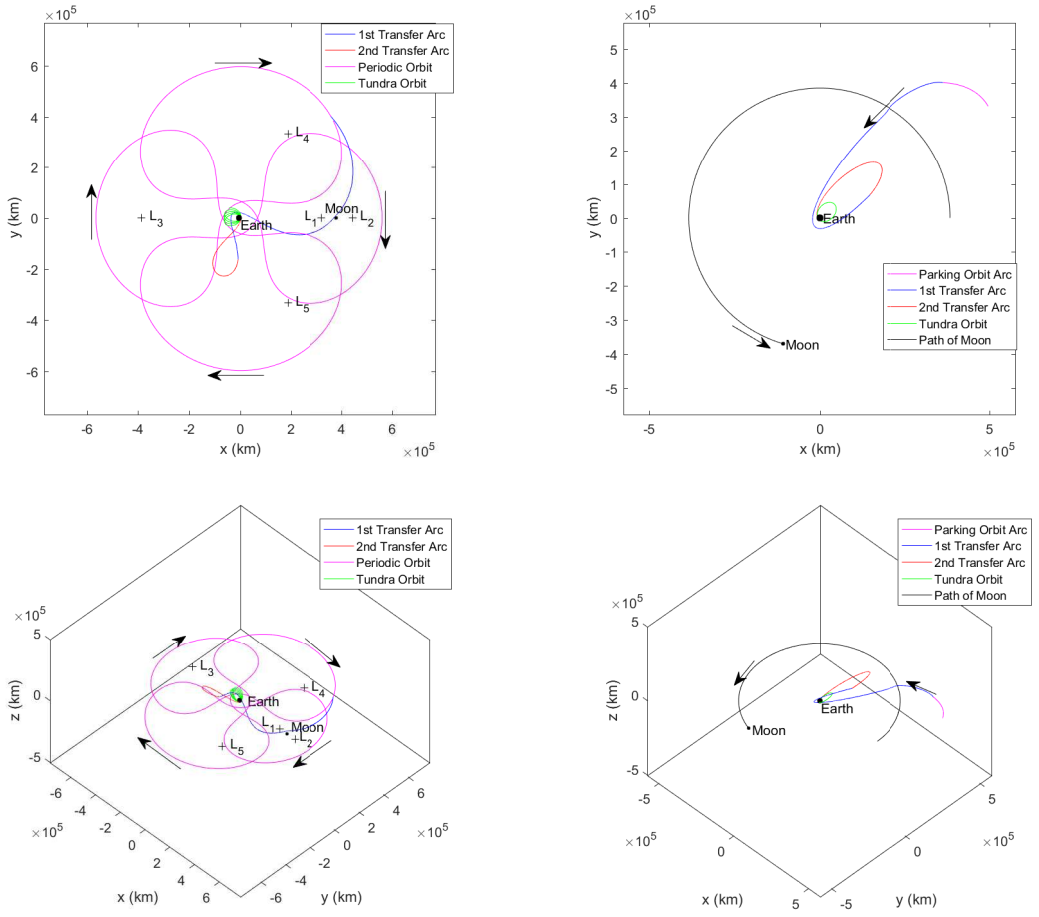

Figure 81. A Feasible Solution of a Transfer from a 4:3 Resonant Orbit to a Tundra Orbit Modeled in the Earth-Moon CR3BP (Top Left: Barycentric Rotating Frame; Top Right: Earth-Centered Inertial Frame; Bottom Left: 3D Perspective of Barycentric Rotating Frame; Bottom Right: 3D Perspective of Earth-Centered Inertial Frame)

Next, this feasible solution, which requires 1.201 km/s of ΔV, is utilized as an initial guess in an optimization algorithm. The resulting locally optimal solution, in terms of ΔV, requires 1.014 km/s of ΔV and is shown in Figure 82.

The optimization algorithm, *fmincon*, converged upon a transfer path that begins earlier in the parking orbit than the feasible solution. This result occurs because a more tangential burn is possible if the transfer is started earlier in the periodic orbit.

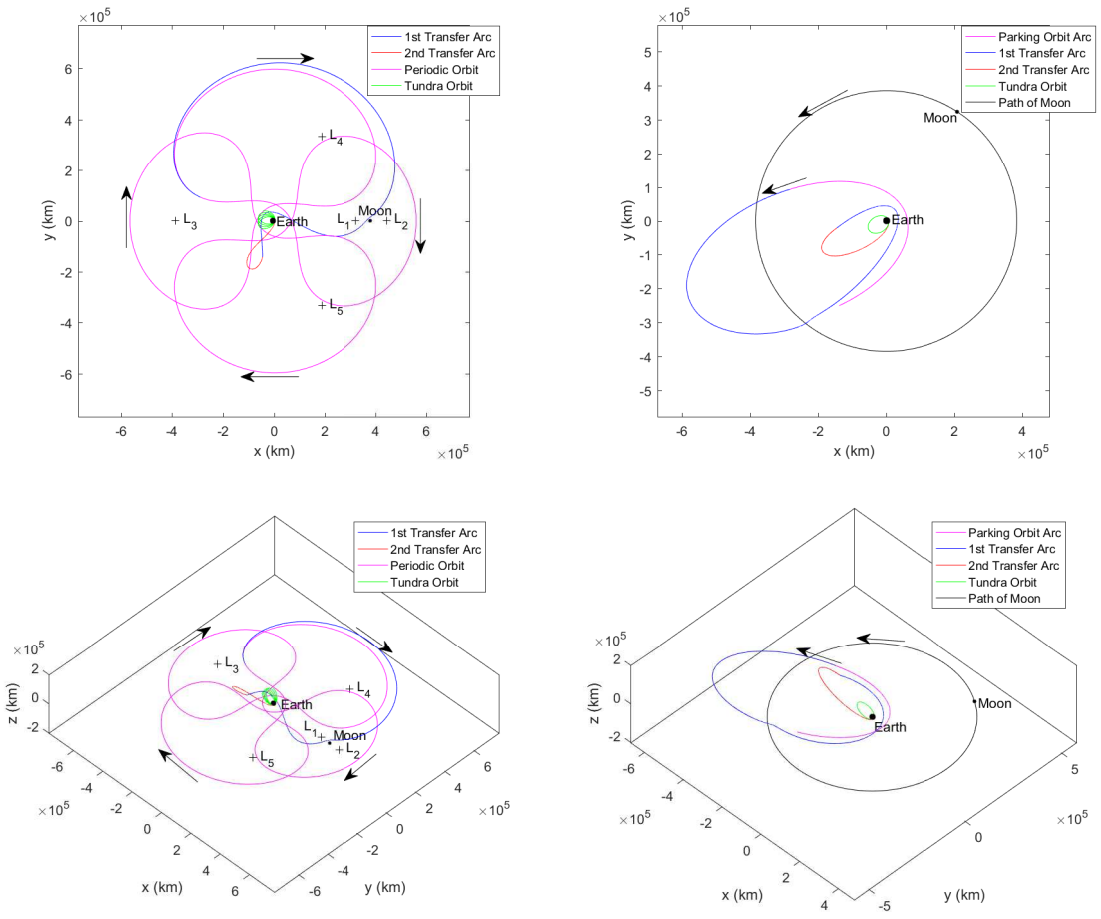

Figure 82. A Locally Optimal Solution, in Terms of ΔV, of a Transfer from a 4:3 Resonant Orbit to a Tundra Orbit Modeled in the Earth-Moon CR3BP (Top Left: Barycentric Rotating Frame; Top Right: Earth-Centered Inertial Frame; Bottom Left: 3D Perspective of Barycentric Rotating Frame; Bottom Right: 3D Perspective of Earth-Centered Inertial Frame)

This locally optimal transfer decreases the required ΔV but increases the transfer time to 27.3 days. Again, as in Test Case 2B, it is possible the spacecraft must wait an an entire period before the transfer may begin, resulting in a time range of 27.3 days to 109.4 days to reconstitute a Tundra orbit from a high-altitude parking orbit. However, similar to Test Case 2B, only one off-ramp is investigated and others may exist that decrease the time until reconstitution.

The total cost, in terms of ΔV, to perform a transfer from LEO to this parking orbit and from this parking orbit to a Tundra orbit is found to be 4.126 km/s. This

cost is substantially higher than the cost to transfer from LEO directly into a Tundra orbit through the employment of a Hohmann-type transfer, which is found to be 2.955 km/s. This cost increase results from the ability to launch directly from most launch sites into LEO with an inclination of 63.4 degrees. This ability eliminates the need to perform any inclination change. However, the increase in cost does not mean that reconstitution of a constellation of Tundra satellites from a high-altitude orbit possesses no military utility. Instead, this result demonstrates that a satellite in this high-altitude parking orbit possesses the operational agility to transfer to any of the three constellations of interest for comparable costs. Additionally, the intent of a satellite as it transfers from a high-altitude parking orbit to a Tundra orbit may not be clear to an observer viewing the transfer in an inertial frame. On the other hand, launching directly into an orbit with an inclination of 63.4 degrees may allow an observer to predict the intent of such a launch. Tracking the COEs over time of the transfer from the 4:3 resonant orbit to a Tundra orbit demonstrates the potential unpredictability.

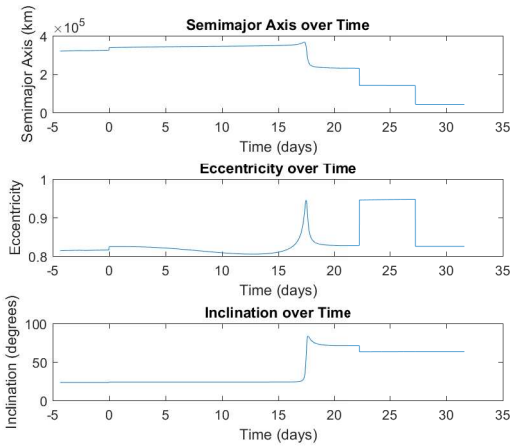

Figure 83. The COEs Associated with a Locally Optimal Transfer, in Terms of ΔV, of a Transfer from a 4:3 Resonant Orbit to a Tundra Orbit

The transfer begins at zero days where an instantaneous change in the COEs is seen. Then, at about 17 days, drastic changes in the COEs occur, without a ΔV being

performed, due to the gravitational effects of the Moon. The semimajor axis decreases, the eccentricity varies, and the inclination increases. Finally, a burn is performed to insert the satellite into a Tundra orbit. An observer expecting two-body motion may be unable to predict the intent of such a transfer.

4.2.4 Test Case 2: Discussion of the Application of High-Altitude Parking Orbits to Reconstitute Conventional Constellations

The results of Test Case 2 demonstrate that the timely and cost-effective, in terms of ΔV, reconstitution of conventional constellations may be possible. Additionally, a satellite in the selected high-altitude parking orbit is found to provide effective means of reconstitution to all three constellations of interest. This adaptability may increase the operational agility of a satellite while in this high-altitude orbit. A decision-maker may elect to transfer from this high-altitude orbit to various conventional constellations depending on the current needs. Additionally, this method of reconstitution does not require an available launch site when the need for reconstitution arises. Instead, a satellite may be launched into this high-altitude parking orbit well before the need for reconstitution occurs. Also, the period of highest risk in a satellite's life occurs during launch [103]. When relying on the conventional reconstitution method of launch-on-demand, a satellite must undergo the riskiest period of its life when the satellite is needed the most. Instead, by launching a satellite into a high-altitude parking orbit prior to the need for reconstitution, the obstacle of launch has already been overcome when the need for reconstitution arises. It is still possible that the launch of a satellite into a high-altitude parking orbit fails; however, in this case, another satellite could be launched into the high-altitude parking orbit without a degraded capability of the constellation. Another benefit of reconstitution via a high-altitude parking orbit is that the satellite may provide additional capability as

it waits to be tasked with reconstitution. This capability is investigated further in Test Case 3A. A satellite on the ground must constantly be prepared for launch, but does not provide any additional capability. On the other hand, a satellite waiting to reconstitute a constellation via launch-on-demand may have its hardware updated as it waits to be launched. The hardware on a satellite in a high-altitude orbit would typically not be maintained after it is launched.

One limitation of the current investigation is that the parking orbit and the associated transfer paths are not modeled in the ephemeris. As demonstrated in Section 4.1.1, a solution in the Earth-Moon CR3BP is not expected to be a solution in an ephemeris model but may serve as a good initial guess in the ephemeris model. The results presented in Test Case 2 need to be transitioned into an ephemeris model to validate the trajectories. Another limitation of this analysis is that only one candidate parking orbit is thoroughly investigated. Other parking orbits may exist that allow for even less costly and more timely transfers. A third limitation of the current investigation is that the precise timing required for a reconstituting satellite to rendezvous with a satellite that needs to be reconstituted is not addressed. Phasing maneuvers could be performed after the transfers presented to accomplish this rendezvous. A fourth limitation of this analysis is that the ΔV required for stationkeeping a satellite in an unstable high-altitude orbit is not approximated. This need for stationkeeping is demonstrated by the following example.

A satellite in the unstable 4:3 resonant orbit would require stationkeeping to correct its trajectory as it waits to be tasked with reconstitution. To demonstrate this need, an error of 1 km in position and 1 cm/s in velocity is added to each of the six states of the periodic parking orbit. These errors correspond to the $1-\sigma$ errors Pavlak used in the analysis of the Artemis trajectory [28]. The trajectory is then numerically integrated in forward time for 10 orbits as seen in Figure 84.

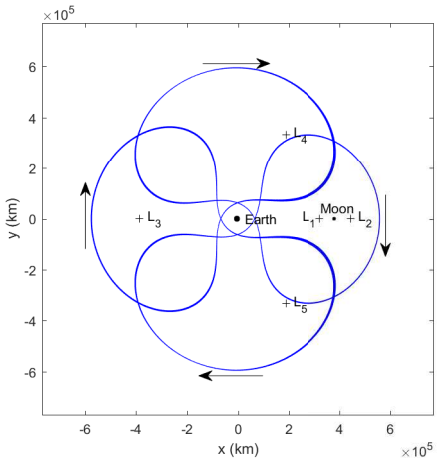

Figure 84. The 4:3 Resonant Orbit with Errors in Position and Velocity Added to the Initial State Numerically Integrated for 10 Orbits

This figure shows that without stationkeeping and in the presence of navigational errors, the trajectory is no longer periodic. The errors in position and velocity grow exponentially with each orbit as this trajectory is numerically integrated in forward time. This growth is seen in Figure 85.

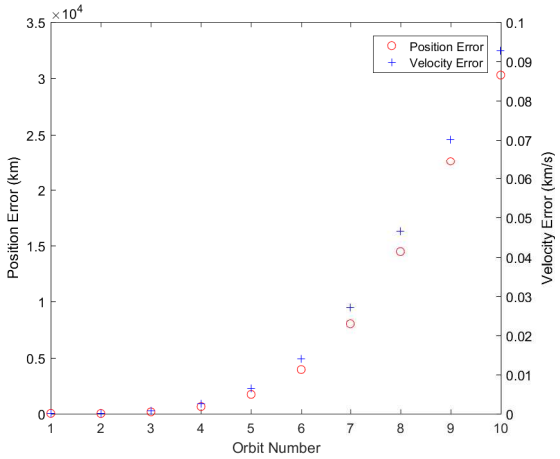

Figure 85. The Growth in the Errors in Position and Velocity of The 4:3 Resonant Orbit with Errors in Position and Velocity Added to the Initial State Numerically Integrated for 10 Orbits

The resulting error growth assumes that no stationkeeping is performed. However, it is possible to target a transfer from the initial state of the trajectory shown above

(which included initial navigational errors) to the actual periodic orbit. The periodic orbit itself is used as an initial guess for a transfer to perform this correction. A feasible solution is then targeted and input as an initial guess into *fmincon*. The resulting locally optimal transfer to correct the errors in position and velocity described above is shown in Figure 86, and the resulting ΔV to perform this transfer is 1.928 cm/s.

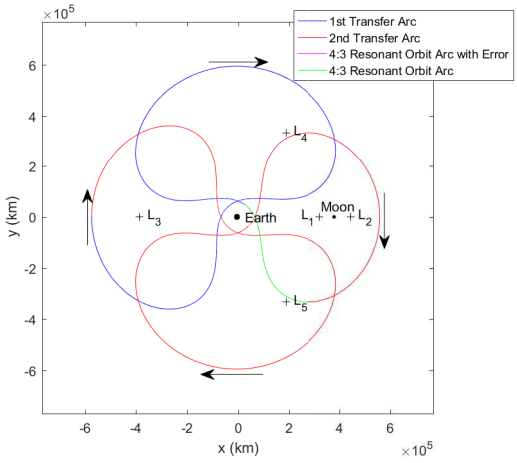

Figure 86. A Locally Optimal Transfer from the Initial State with Position and Velocity Errors Applied to the 4:3 Resonant Orbit Modeled in the Earth-Moon CR3BP

This brief analysis only provides one example of the required stationkeeping and is not representative of the actual stationkeeping required by a satellite in a high-altitude parking orbit. In order to accurately approximate the required ΔV for stationkeeping, a rigorous Monte Carlo simulation could be performed to approximate navigational errors and the cost, in terms of ΔV, to correct the errors over the lifetime of a satellite. Pavlak provides an example of this type of analysis for a trajectory modeled in the Earth-Moon CR3BP [28]. In addition to navigational errors in position and velocity, errors in the ΔV performed by a spacecraft should also be included in the analysis.

4.3 Test Case 3: Results and Analysis of the Ability of a Satellite in a High-Altitude Orbit to Remotely Sense the Surface of the Earth

In Test Case 3, the ability of a satellite to remotely sense the surface of the Earth while it is in a high-altitude orbit is investigated. First, the potential of a satellite to remotely sense the surface of Earth while it is in the high-altitude parking orbit waiting to be tasked with reconstitution is investigated in Test Case 3A. Then, the ability of a satellite to remotely sense a specific region on the surface of the Earth while it is performing a transfer to reconstitute a capability is investigated in Test Case 3B. Finally, in Test Case 3C, the potential of satellites in other high-altitude trajectories to remotely sense the surface of the Earth is investigated. Overall, it is concluded that the ability of a satellite to provide coverage of the surface of the Earth while it is in a high-altitude trajectory is low relative to a satellite at geostationary altitude. This result is based on the assumption that the performance of a satellite is inversely proportional to the square of the distance from the satellite to Earth's surface. However, despite the low performance of a satellite in a high-altitude orbit, other benefits may exist through the use of a satellite in a high-altitude orbit. A satellite in a high-altitude orbit may provide effective coverage at certain times during its orbit. And as discussed in Test Case 2, a high-altitude parking orbit may serve as an effective method of reconstitution. Additionally, as discussed in Test Case 4, it may be difficult to predict the long term behavior of a satellite's trajectory in certain regions of the phase space.

4.3.1 Test Case 3A: Results and Analysis of the Ability of a Satellite in a High-Altitude Parking Orbit to Remotely Sense the Surface of the Earth While It Is Waiting to Be Tasked with Reconstitution

In Test Case 3A, the ability of a satellite in a high-altitude parking orbit to remotely sense the surface of the Earth while it is waiting to be tasked with reconstitution is investigated. Specifically, the largest unstable 4:3 resonant orbit found is investigated because of its desirable characteristics according to Section 3.1.3. Figure 42 shows a portion of the 4:3 resonant family investigated. Then, the 4:3 resonant orbit is input as an initial guess into a numerical optimization algorithm that searches for a locally optimal parking orbit in terms of the average performance relative to a nominal satellite at geostationary altitude as discussed in Section 3.5.1. The initial parking orbit and the locally optimal parking orbit output by *fmincon* are shown in Figure 87.

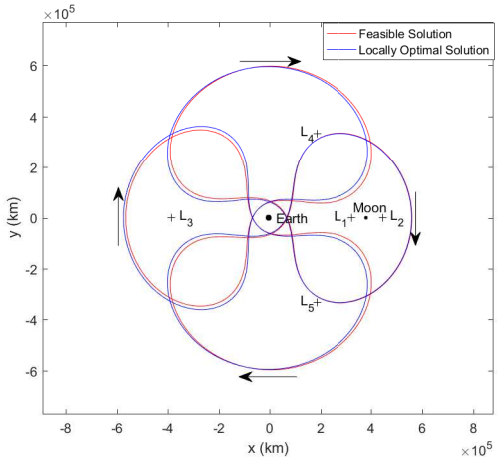

Figure 87. A Feasible Parking Orbit and a Locally Optimal Parking Orbit Based on a Satellite's Average Performance Relative to a Nominal Satellite at Geostationary Altitude Modeled in the Earth-Moon CR3BP

The average performance of a satellite in this locally optimal parking orbit is found to be 3.2% of that of a nominal satellite at geostationary altitude. This performance is relatively low; however, at times during the periodic orbit, significant additional capability may be provided by a satellite in this parking orbit. These spikes in

coverage can be seen in Figure 88. During these spikes, a satellite's performance is near 60% to 70% of a nominal satellite at geostationary altitude. The persistence of a satellite in the high-altitude orbit is defined by the current investigation as the ratio of the amount of time the performance is greater than 10% to the period of the orbit. This value of 10% approximately corresponds to the performance of a satellite at an altitude three times greater than geostationary altitude and is assumed to be a reasonable limit. This percentage is chosen to showcase the analysis method employed by the current investigation, but may be adjusted to satisfy a user's requirements. The persistence of a single satellite in this high-altitude parking orbit is found to be 6.5%. Additionally, the width of each period of performance greater than 10% is found to be about 1.3 days. Further, an average revisit rate is defined as the frequency of peaks. A single satellite in this locally optimal parking orbit possesses a revisit rate of 0.049 days^{-1}.

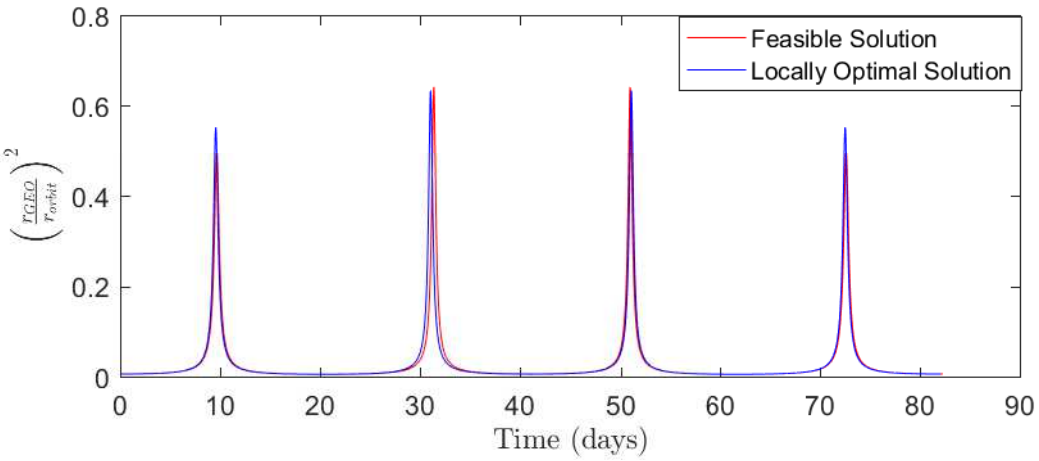

Figure 88. A Feasible Parking Orbit and a Locally Optimal Parking Orbit Based on a Satellite's Average Performance Relative to a Nominal Satellite at Geostationary Altitude Modeled in the Earth-Moon CR3BP

This capability may be beneficial to a ground user. During these coverage spikes, the satellite may be able to provide an additional capability to a conventional constellation. Additionally, since a satellite in such an orbit is not fixed in position

relative to the rotating Earth, it may be able to provide capability to regions of the Earth that are not typically covered by the conventional constellation. On the other hand, since the satellite does not remain over the same region of the Earth during these close approaches, long term coverage is not possible from the satellite. Throughout the majority of the parking orbit, negligible performance is provided because the performance is inversely proportional to the distance from Earth squared. However, despite the low average performance, the primary purpose of a satellite in this high-altitude parking orbit is to serve as a reconstitution option, so any additional capability provided by a satellite in this high-altitude orbit contributes to the overall military utility of such a high-altitude parking orbit.

As discussed in Section 4.2.1, it may be desirable to position multiple satellites in the high-altitude parking orbit to decrease the time-of-flight required to perform the reconstitution of a capability. Utilizing the same two satellite and five off-ramp scenario discussed in Section 4.2.1, the combined capability of the satellites may be assessed based on its performance relative to a nominal satellite at geostationary altitude. Recall that in this scenario, the second satellite is positioned 10.5 days behind the lead satellite. Figure 89 shows the combined performance of two such satellites over time. This combined performance is the summation of the performance of the individual satellites.

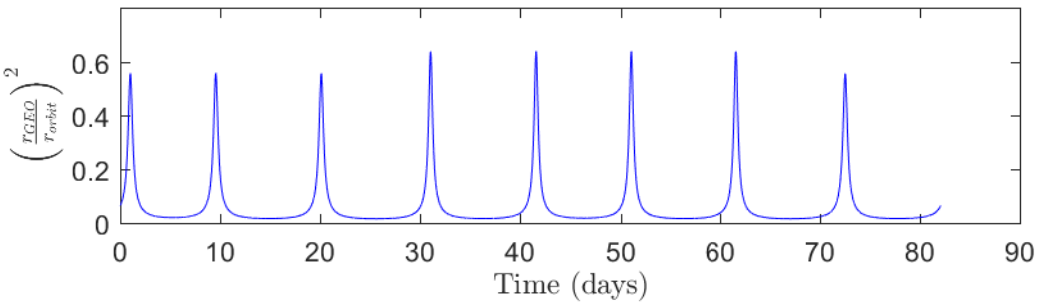

Figure 89. The Combined Performance of Two Satellites Positioned in the High-Altitude Parking Orbit Spaced 10.5 Days Apart Relative to a Nominal Satellite at Geostationary Altitude

The average combined performance of these two satellites is found to be 6.3% of that of a nominal satellite at geostationary altitude. As expected, since the combination of the performance of two satellites involved a summation, the average combined performance is twice the average performance of a single satellite. The combined persistence of these satellites is found to be 13.6%. Likewise, the combined revisit rate is found to be 0.097 days^{-1}. As the number of satellites is increased in the same manner as Test Case 2A, the combined average performance will continue to increase. Additionally, the combined average revisit rate will also increase. The combined persistence will also increase until the number of satellites allows for at least one satellite to provide 10% capability regardless of where the lead satellite is in the parking orbit. Figure 90 shows how the average combined performance, the combined persistence, and the combined average revisit rate increase as the number of satellites is increased.

In order for a launch-on-demand capability to exist, a satellite and rocket must be prepared at all times. The satellite provides no capability while on the ground; however, a satellite deployed into the high-altitude orbit does provide some capability, based on the above analysis. Both reconstitution methods also present the possibility that the need for reconstitution never occurs. In this case, a satellite that is deployed into a high-altitude parking orbit is able to provide some capability while in the parking orbit. On the other hand, the satellite waiting on the ground to be tasked with reconstitution via launch-on-demand provides no military utility if there is never a need for reconstitution.

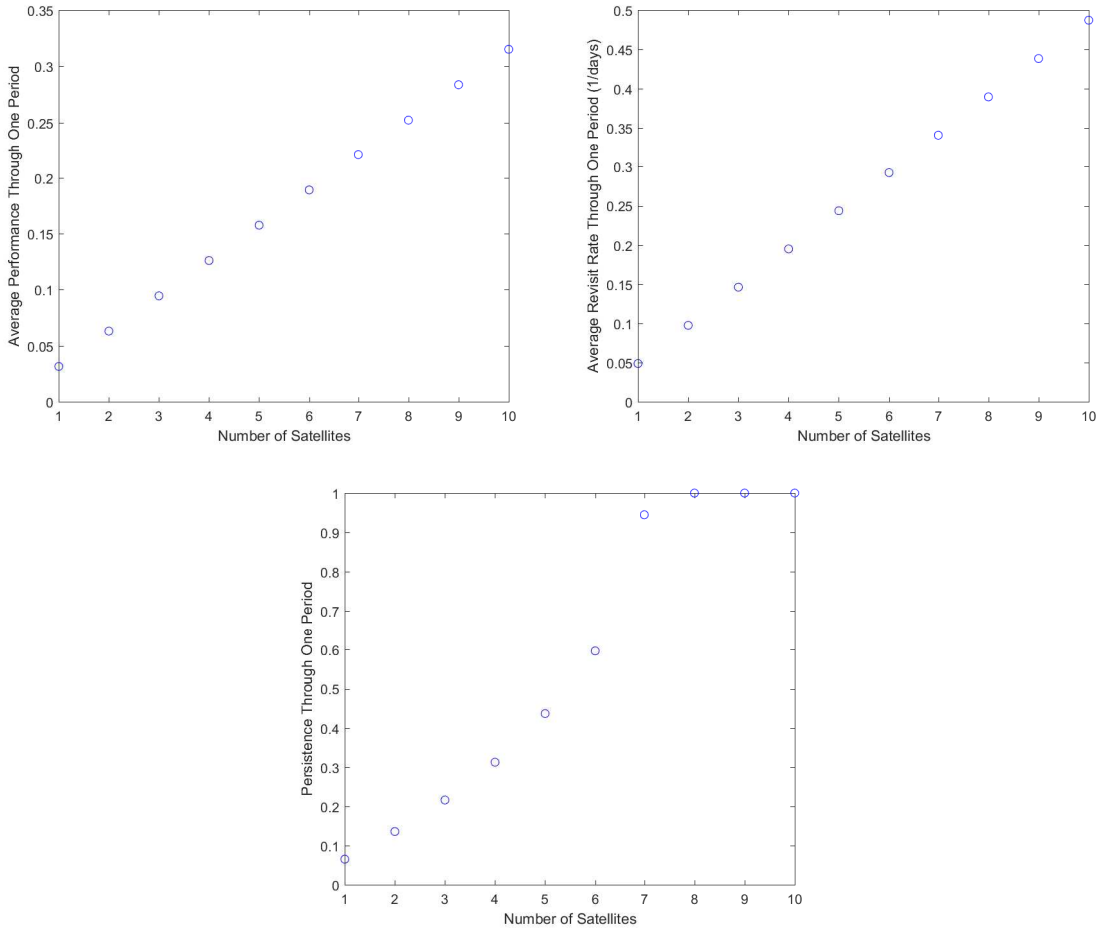

Figure 90. The Ability of Satellites in the High-Altitude 4:3 Resonant Orbit to Provide Coverage of the Surface of the Earth as a Function of the Number of Satellites (Top Left: The Combined Average Performance Relative to a Nominal Satellite at Geostationary Altitude; Top Right: The Combined Average Revisit Rate; Bottom: The Combined Persistence

4.3.2 Test Case 3B: Results and Analysis of the Ability of a Satellite in a High-Altitude Parking Orbit to Remotely Sense the Surface of the Earth While It Is Reconstituting a Conventional Constellation

In Test Case 3B, the ability of a satellite to remotely sense a specific region on the surface of the Earth as it is reconstituting a capability from a high-altitude parking orbit is investigated. In the scenario described in Test Case 3A, the constellation

of interest was fully operational, so additional coverage of anywhere on the Earth is considered an increase in capability; however, in Test Case 3B, a need for the reconstitution of a capability exists, so only coverage of the degraded capability is considered increased performance. This requirement led to the development of the metric defined in Section 3.5.2, which measures the performance of a satellite relative to a particular satellite of interest. The performance of this metric is tracked over time and compared to a launch-on-demand capability requiring 30 days of lead time.

The performance of a single satellite utilizing the five transfer paths from Test Case 2A is analyzed. Specifically, the worst case transfer and the best case transfers, in terms of time-of-flight, based on the five transfer paths discussed in Section 4.2.1, are explored. These five transfer paths, or off-ramps, include the feasible solution shown in Figure 69 and the four locally optimal transfer paths shown in Figure 68. The performance of the worst case transfer, in terms of time to reconstitution, is seen in Figure 91.

The average performance of the reconstitution path via the high-altitude orbit over the first 30 days of the transfer in the worst case scenario is found to be 1.6%. The launch-on-demand capability's average performance of the same metric is found to be 0% over the same time interval because the launch-on-demand capability is assumed to require 30 days of lead time. In the worst case scenario for the reconstitution of the constellation from the high-altitude parking orbit, a launch-on-demand capability requires 1.6 less days to reconstitute the capability. However, the worst case scenario reconstitution via a high-altitude parking orbit does provide a spike in coverage near 10 days. This increase in coverage reaches 60% performance relative to a particular satellite and persists above 10% for 0.9 days. Again, persistence is defined as a period of continuous capability greater than 10%. This temporary increase in performance may allow for a mission essential function to be performed. Such a function may not

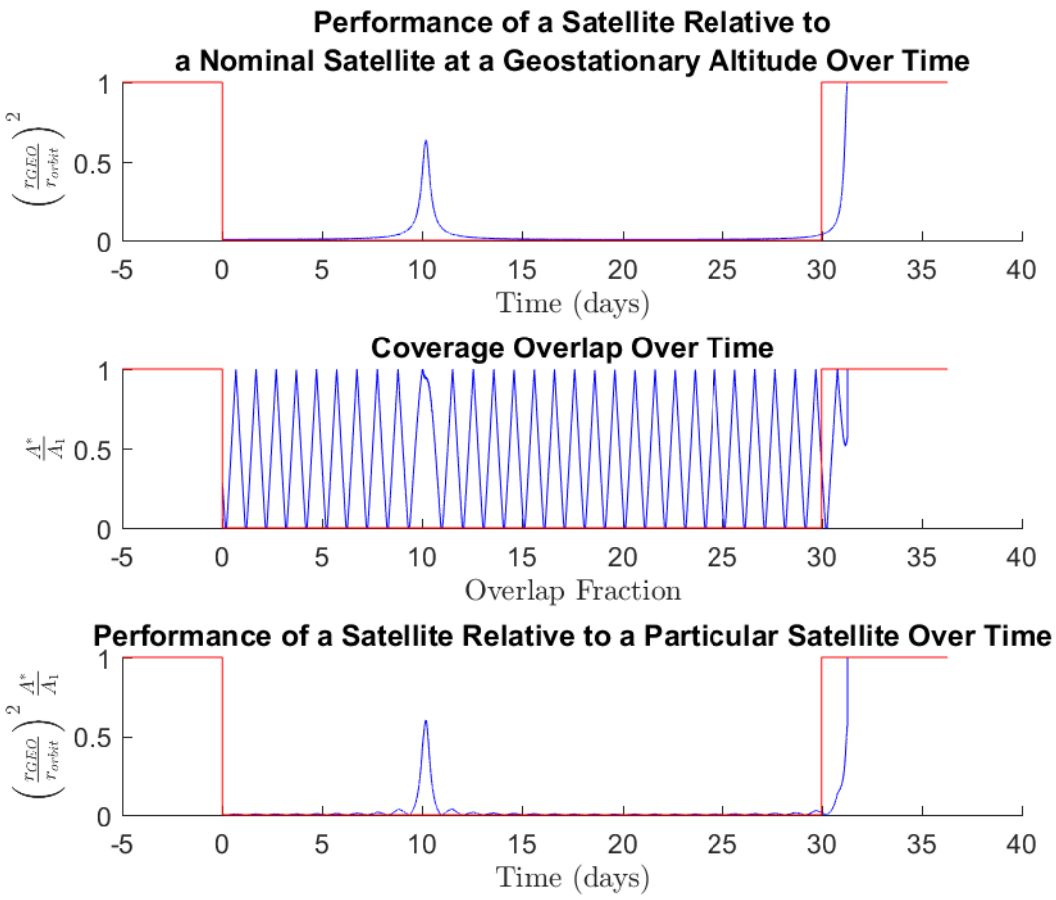

Figure 91. The Performance of the Worst Case Scenario Transfer from the High-Altitude Parking Orbit (Blue) Compared to the Performance of a Launch-On-Demand Capability of 30 Days (Red)

be performed during reconstitution via a launch-on-demand capability. Next, the performance of the best case transfer, in terms of time to reconstitution, is investigated and shown in Figure 92.

The average performance of the reconstitution path via the high-altitude orbit over the first 30 days after the need for reconstitution occurred based on the performance relative to a particular satellite is found to be 69.8%. On the other hand, the average capability of a satellite that reconstitutes the constellation via a launch-on-demand capability provides an average performance of 0% over the same 30 day interval. However, the vast majority of the increased performance occurs after the constellation

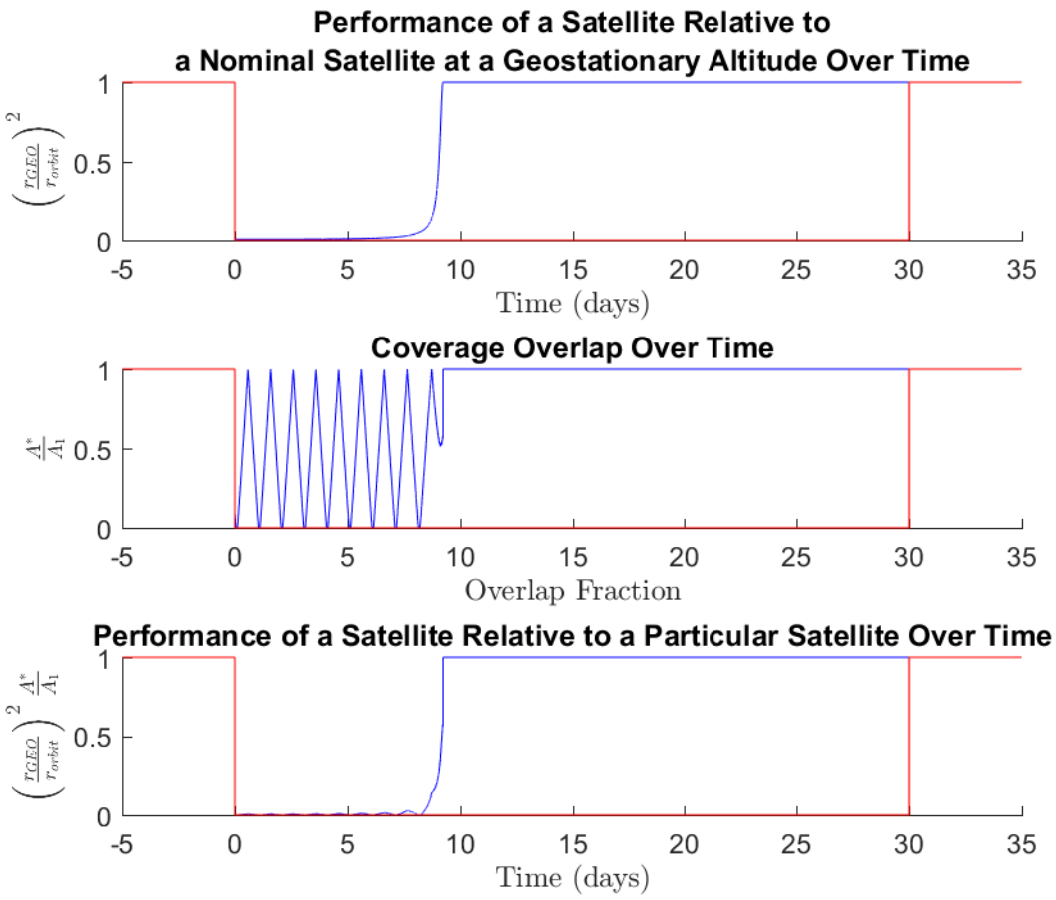

Figure 92. The Performance of the Best Case Scenario Transfer from the High-Altitude Parking Orbit (Blue) Compared to the Performance of a Launch-On-Demand Capability of 30 Days (Red)

is reconstituted via the high-altitude parking orbit. In general, due to the high-altitude of these transfer paths, low performance is provided by a satellite while it reconstitutes a capability from a high-altitude parking orbit. Therefore, the primary consideration when comparing performance between the two reconstitution methods is the timeliness of the transfers.

Next, the average performance of a single satellite in the five off-ramp scenario discussed in Section 4.2.1 is assessed based on where the satellite is in the parking orbit when tasked with reconstitution. Figure 93 shows the average performance of a satellite performing a transfer from each of the 100 points shown in Figure 73.

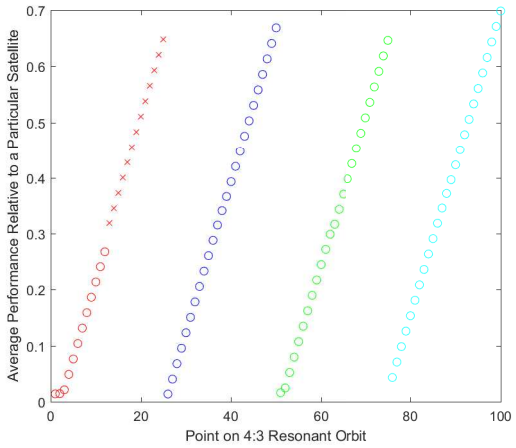

Figure 93. The Average Performance of a Single Satellite Relative to a Particular Satellite at Geostationary Altitude Corresponding to the 100 Equally Spaced Points Shown in Figure 73

As the time-of-flight decreases, the average performance increases. This result further demonstrates that the most important factor in the average performance of a satellite relative to this metric is the timeliness of the reconstitution. However, it is also shown that, in some cases, a satellite may be able to provide coverage over the specific region prior to its ability to reconstitute the capability. This ability may reach 60% and persist above 10% for 0.9 days. This temporary coverage as a capability is being reconstituted may provide enough persistence to perform a mission essential function that would not be possible with a launch-on-demand capability.

4.3.3 Test Case 3C: Results and Analysis of the Ability of a Satellite in a High-Altitude Trajectory to Remotely Sense the Surface of the Earth

In Test Case 3C, the ability of satellites in high-altitude trajectories to remotely sense the surface of the Earth is investigated. In this test case, unlike Test Cases 3A and 3B, the primary purpose of a satellite in one of these high-altitude trajectories is not reconstitution, but military utility. To perform this investigation, candidate orbits

are generated at a particular value of the Jacobi Constant. Their ability to remotely sense the surface of the Earth is then calculated relative to a nominal satellite at geostationary altitude. Note that this metric is not concerned with what region of the Earth is covered by the satellite. To generate initial guesses for candidate periodic orbits, a periapsis Poincaré map analysis is performed at a specific value of the Jacobi Constant as seen in Figure 94.

In the periapsis Poincaré map shown in Figure 94, two regions of interest are selected. The first region (right) is associated with a regular region of the phase space. In this region, one portion of a quasiperiodic island chain exists. This island chain consists of seven islands, or seven returns to the map per period. An initial guess from near the ‘‘center’’ of this island on the x-axis is numerically integrated in forward time until another nearly perpendicular crossing occurs. This trajectory is then input as an initial guess into a single-shooting algorithm that exploits symmetry to target a planar symmetric resonant orbit. This differential corrections process results in the orbitally stable, in the linear sense, 7:2 resonant orbit shown in Figure 95.

This resonant orbit is expected to be orbitally stable, in the linear sense, to in-plane perturbations because the initial guess is generated from the ‘‘center’’ of an island structure. However, no indication of the orbital stability to out-of-plane perturbations exists from this map. The resonant orbit is found to be orbitally stable to out-of-plane perturbations based on a linear stability analysis examining the eigenvalues of the monodromy matrix. Additionally, seven revolutions of Earth in the inertial frame per period is also expected because seven islands existed in the island chain on the map. The second region (left) displayed on the map in Figure 94 is not associated with regular behavior, but instead with chaotic behavior. However, this region does exist between two of the island structures associated with the orbitally stable, in the linear sense, 7:2 resonant orbit. Because unstable periodic orbits are expected to

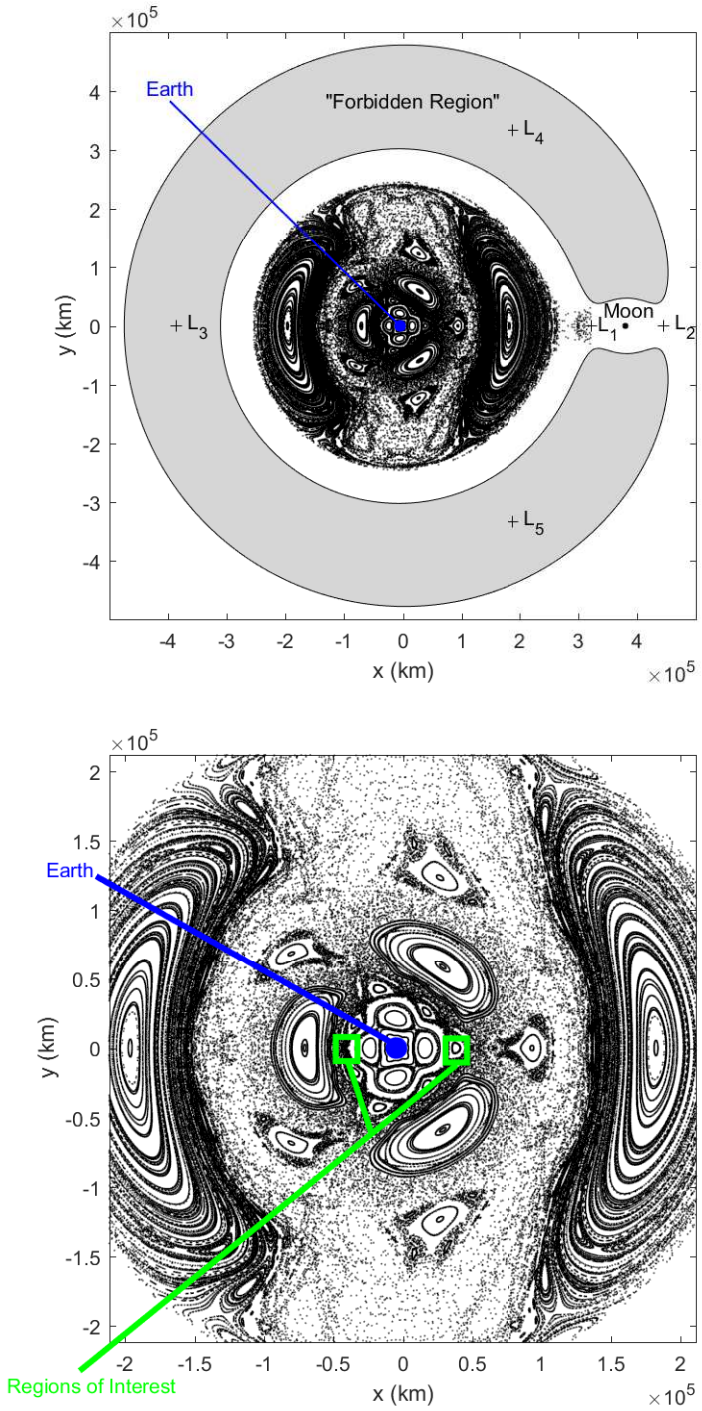

Figure 94. A Periapsis Poincaré Map at a Value of the Jacobi Constant Equal to 3.15 Nondimensional Units in the Earth-Moon CR3BP with Regions of Interest Labeled (Top: A Zoomed-Out View; Bottom: A Zoomed-In View with Regions of Interest Labeled)

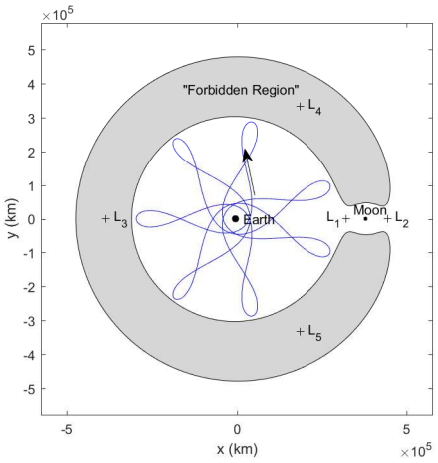

Figure 95. An Orbitally Stable, in the Linear Sense, 7:2 Resonant Orbit Modeled in the Earth-Moon CR3BP Displayed in the Barycentric Rotating Frame

occur between the island structures of stable periodic orbits, near the middle of this second region, an orbitally unstable 7:2 resonant orbit is expected to exist. An initial guess near the middle of this region of interest on the x-axis is numerically integrated in forward time for one revolution of the primaries, because a 7:2 resonant orbit is expected. Then, this trajectory is input as an initial guess into the single-shooting algorithm to target an orbitally unstable, in the linear sense, 7:2 resonant orbit. This orbit is expected to be orbitally unstable to in-plane perturbations; however, no information about the orbital stability to out-of-plane perturbations exists on the map. In this case, the orbit is found to be orbitally stable, in the linear sense, to out-of-plane perturbations.

Next, the performance of both of these trajectories is investigated relative to a nominal satellite at geostationary altitude. The average performance of the orbitally stable 7:2 resonant orbit is found to be 9.7%, while the average performance of the orbitally unstable 7:2 resonant orbit is found to be 9.8%. Both of these average performances represent an increase in performance relative to the parking orbit investigated as a source of reconstitution. However, the performance is still low

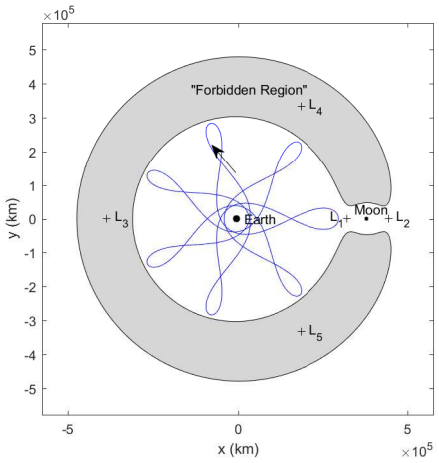

Figure 96. An Orbitally Unstable 7:2 Resonant Orbit Modeled in the Earth-Moon CR3BP Displayed in the Barycentric Rotating Frame

relative to a satellite at geostationary altitude. The performance of this metric over time in both orbits is seen in Figure 97.

At times during these trajectories, the performances are near 100%; however, during the majority of the trajectory, the performances are negligible. These regions of negligible performance are due to the inverse proportionality between performance and the square of the distance from Earth. The persistence of a single satellite in each of these orbits, using the same definitions as in Section 4.3.1, is found to be 18.0% and 17.9% for the orbitally stable and unstable 7:2 resonant orbits, respectively. Next, the average revisit rates are found to both be about 0.128 days^{-1}. While providing some performance, the long term behavior of a satellite's trajectory in the orbitally unstable 7:2 resonant orbit may also be difficult to predict because this trajectory travels through chaotic regions of the phase space and is associated with invariant manifolds. These manifolds may allow a spacecraft in this orbit to depart the orbit for low ΔV.

As the number of satellites in the orbitally stable, in the linear sense, 7:2 resonant orbit is increased, the combined average performance, combined persistence, and

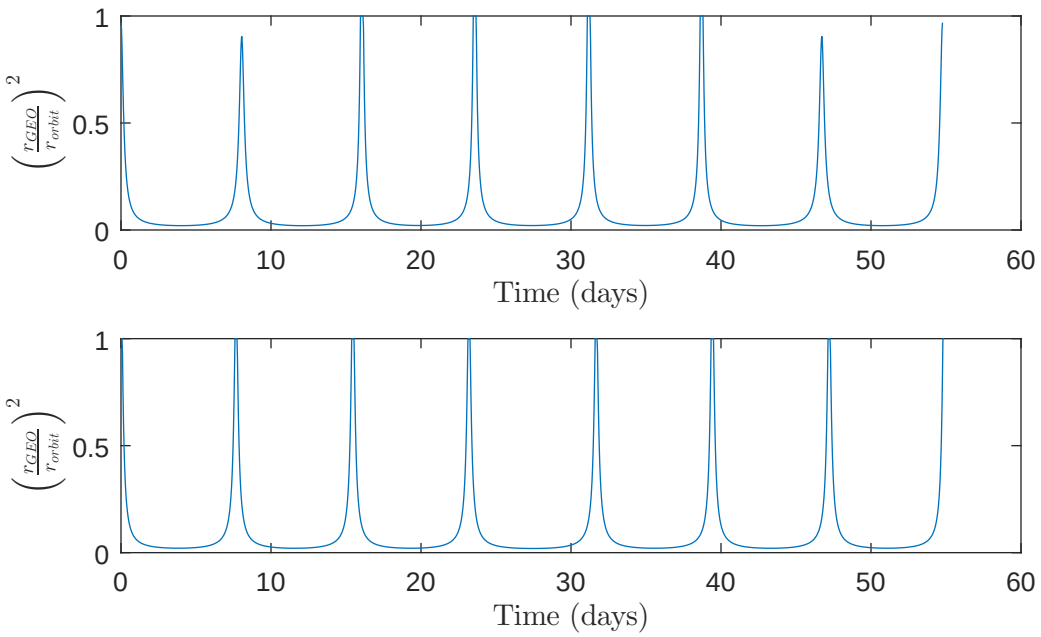

Figure 97. The Performance of the 7:2 Resonant Orbits Targeted from the Periapsis Poincaré Map shown in Figure 94 (Top: The Orbitally Stable, in the Linear Sense, 7:2 Resonant Orbit; Bottom: The Orbitally Unstable 7:2 Resonant Orbit)

combined average revisit rate increase and follow the same trends seen in Section 4.3.1. Figure 98 demonstrates these trends.

The persistence reaches unity with four satellites. Therefore, this parking orbit requires less satellites to achieve continuous persistence than the 4:3 resonant orbit investigated in Section 4.3.1. However, the orbit investigated in Section 4.3.1 is chosen because of its desirable characteristics for a parking orbit, while the orbits in the current test case are explored because of their potential military utility.

Next, the orbitally stable 7:2 resonant orbit is input as an initial guess into a numerical optimization algorithm that searches for a locally optimal, symmetric periodic orbit based on the average performance of the trajectory relative to a nominal satellite at geostationary altitude. The locally optimal solution that was converged upon is an orbitally stable 13:1 resonant orbit at a much higher value (lower ‘‘energy’’ level) of the Jacobi Constant ($JC = 6.276$). This locally optimal solution output from *fmincon* is shown in Figure 99.

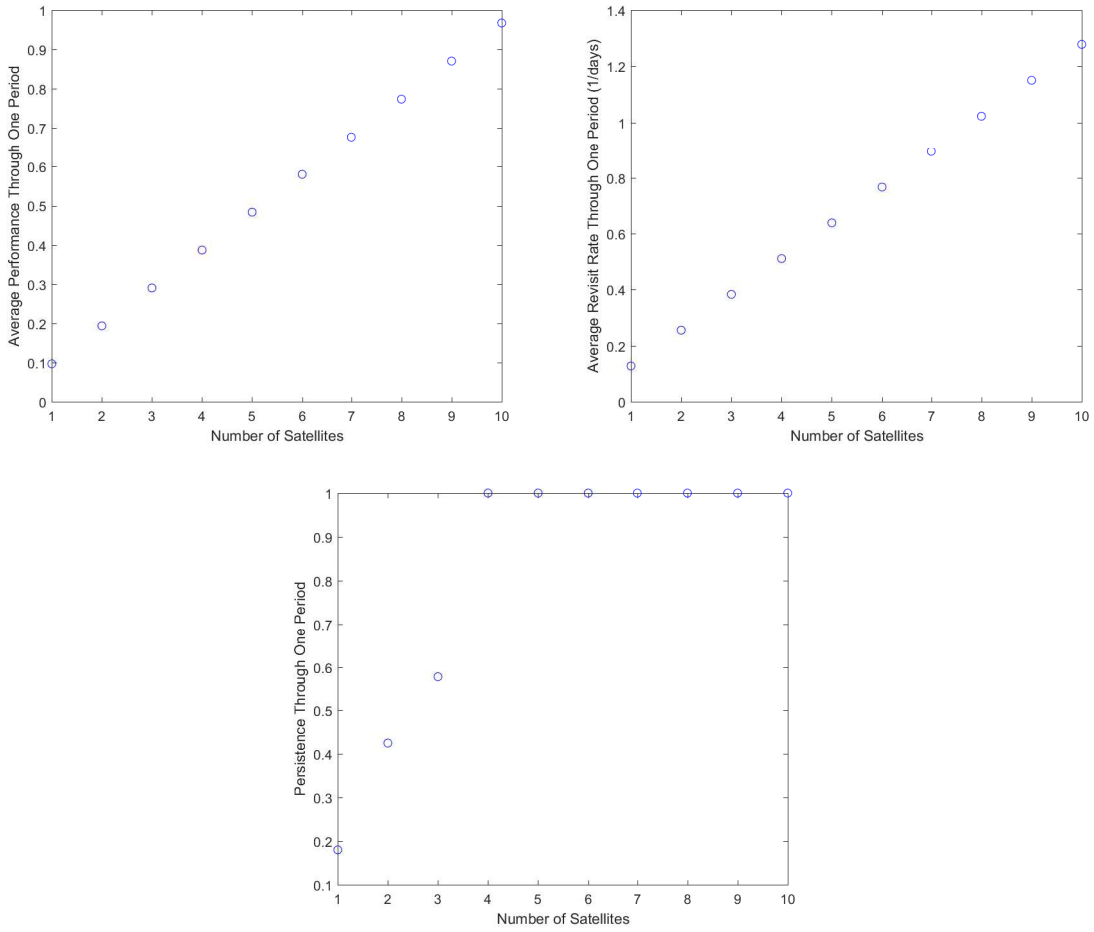

Figure 98. The Ability of Satellites in a High-Altitude 7:2 Resonant Orbit to Provide Coverage of the Surface of the Earth as a Function of the Number of Satellites (Top Left: The Combined Average Performance Relative to a Nominal Satellite at Geostationary Altitude; Top Right: The Combined Average Revisit Rate; Bottom: The Combined Persistence)

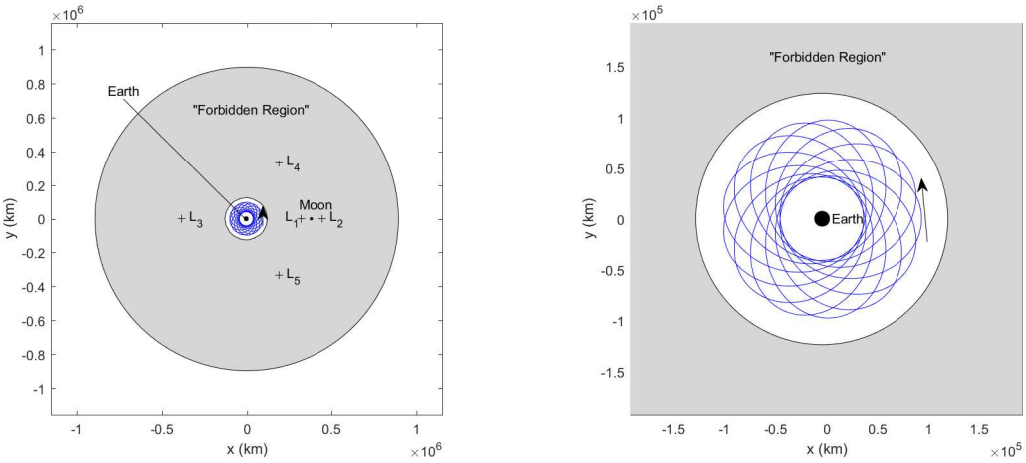

Figure 99. A Locally Optimal 13:1 Resonant Orbit, in Terms of Average Performance, Modeled in the Earth-Moon CR3BP and Displayed in the Barycentric Rotating Frame (Left: A Zoomed-Out View; Right A Zoomed-In View)

This locally optimal, symmetric periodic orbit possesses an average performance of 40.4%. However, in exchange for performance, the high-altitude nature of the trajectory was lost. This performance over time is shown in Figure 100.

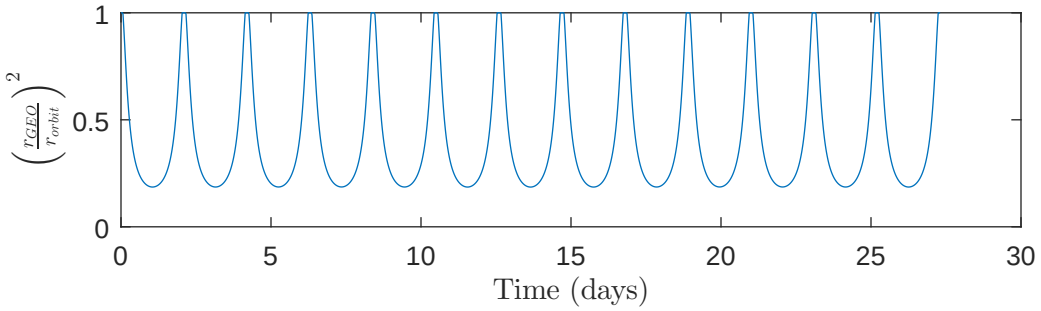

Figure 100. The Performance of the 13:1 Resonant Orbit Relative to a Nominal Satellite at Geostationary Altitude Over Time

Furthermore, the ZVSs now bound the trajectory to a lower altitude. This low-altitude, relative to the original 7:2 resonant orbit, results in higher performance, but may result in an increase in the predictability of the long term behavior of the satellite's trajectory. Since the predictability is lost, this trajectory may not be useful for military purposes as the performance of the satellite could increase to 100% by positioning the satellite in an actual circular, geosynchronous orbit.

In summary, there is a trade-off between predictability of the long term behavior of a spacecraft's trajectory and the ability of a satellite in a high-altitude orbit to remotely sense the surface of the Earth. At high-altitudes, unpredictable orbits may exist, but due to the high altitudes the ability of a satellite in such an orbit to remotely sense the surface of the Earth is relatively low compared to a satellite at geostationary altitude for the majority of the trajectory. However, a satellite in a high-altitude orbit may provide effective coverage at certain times during its orbit. Alternatively, at lower altitudes, the performance may be increased, but the unpredictability is sacrificed.

4.3.4 Test Case 3: Discussion of the Ability of a Satellite in a High-Altitude Orbit to Remotely Sense the Surface of the Earth

Overall, in Test Case 3, it is concluded that the overall capability of a satellite to remotely sense the surface of the Earth while in a high-altitude orbit is relatively low compared to a satellite at geostationary altitude. On the other hand, periods of increased performance may exist, indicating that a satellite in such an orbit may remotely sense the surface of the Earth with performance comparable to a satellite at geostationary altitude during these time intervals. In Test Case 3A, the average performance of a single satellite in the high-altitude orbit investigated in Test Case 2 waiting to be tasked with reconstitution is found to be 3.2%. However, intervals of increased capability do exist where this performance can reach over 60%. During these spikes in coverage (when performance is above 10%) that are found to last about 1.3 days, the satellite may be able to provide an additional remote sensing capability to a conventional constellation. Additionally, as the number of satellites in this parking orbit increases, using the spacing described in Section 4.2.1, the combined average performance, combined persistence, and combined revisit rate of these satellites also

increases. Similar results are found in Test Case 3B, where it is determined that little military capability may be provided by a satellite as it is performing the reconstitution of a capability through the use of the transfer paths found in Test Case 2; however, spikes in coverage may exist, allowing for an increase in capability. Additionally, it is determined that the primary factor in the performance provided by a satellite as it transfers to the constellation is the transfer time. As the timeliness of the transfer is increased, performance compared to a launch-on-demand capability increases. This further justifies the utilization of multiple satellites in a high-altitude parking orbit to decrease the maximum transfer times. Finally, in Test Case 3C, it is determined that there is a trade-off between the unpredictability of the long term behavior of a satellite's trajectory and the ability of such a satellite to remotely sense the surface of the Earth. In high-altitude trajectories, the predictability of the long term behavior of a spacecraft's trajectory may be decreased, but so is the ability to provide coverage of the surface of the Earth. The inverse is true for lower-altitude trajectories.

4.3.4.1 Alternative Applications of Satellites in High-Altitude Trajectories

Alternative applications of satellites may favor satellites in high-altitude trajectories. As an example, the IBEX mission utilized a high-altitude 3:1 resonant orbit to take measurements of the termination shock [88, 89]. The termination shock is where solar wind particles slow down as they reach the interstellar medium [90]. To increase the military practicality of the high-altitude trajectories presented in Test Case 3, scientific observations could be performed while at high-altitudes. Resonant orbits in the Earth-Moon system may be ideal for observing Earth's magnetosphere and solar wind at high altitudes [104]. For example, in Test Case 3A, instead of a satellite providing additional capability to a conventional constellation while waiting

to be tasked with reconstitution, the satellite could perform scientific observations as a secondary mission. Then, when the spacecraft was tasked with reconstitution, the scientific mission would end and the primary mission of reconstitution would begin. Likewise, in Test Case 3C, a dual-purpose satellite could be deployed into a high-altitude orbitally unstable resonant orbit. In such an orbit, a satellite could perform scientific observations when at high altitudes, while remotely sensing the surface of the Earth while at lower altitudes. In both cases, the cooperative effort may increase the overall cost of the satellite, but may be more cost-effective than two independently performed missions. However, this cooperative effort would likely increase the complexity of both the design and operation of such a satellite.

4.4 Test Case 4: Results and Analysis of the Ability to Predict the Long Term Behavior of a Spacecraft's Trajectory Through the Utilization of Periapsis Poincaré Maps as Visual Aids

In Test Case 4, the utilization of periapsis Poincaré maps as visual aids to predict the long term behavior of a spacecraft's trajectory is investigated. In the current investigation, the long term behavior of a spacecraft's trajectory is defined as the behavior of the trajectory for the next 100 nondimensional time units (approximately 1.19 years). First, the long term behavior of a spacecraft's trajectory that is in the 4:3 resonant orbit investigated in Test Case 2 as a high-altitude parking orbit is explored in Test Case 4A. Then, in Test Case 4B, the predictability of the long term behavior of a spacecraft's trajectory at other values of the Jacobi Constant is investigated. Additionally, a scenario is developed to demonstrate the ability of a satellite in a chaotic region of the phase space to alter the long term behavior of its trajectory through the utilization of low-ΔV transfers. Overall, it is seen that periapsis Poincaré maps are an effective visual aid to distinguish between regular and chaotic regions of

the phase space. This fact allows for the utilization of periapsis Poincaré maps by a mission designer to develop initial guesses for trajectories that are able to alter their long term behavior for low ΔV. Additionally, the color-coding of periapses on such a map to categorize the long term behavior of a spacecraft's trajectory may also be exploited by a mission planner to design trajectories with desired long term behaviors. Alternatively, these maps are also beneficial to an observer as a method to categorize the long term behavior of a spacecraft's trajectory or to determine that the spacecraft is traveling through a chaotic region of the phase space and may be maneuvered for low ΔV to alter the long term behavior of the spacecraft.

4.4.1 Test Case 4A: Results and Analysis of the Ability to Predict the Long Term Behavior of a Spacecraft's Trajectory in a High-Altitude Parking Orbit Waiting to be Tasked with Reconstitution Through the Utilization of a Periapsis Poincaré Map as a Visual Aid

In Test Case 4A, the ability to predict the long term behavior of a spacecraft's trajectory as it waits in a high-altitude parking orbit to be tasked with reconstitution is investigated. Specifically, the high-altitude parking orbit from Test Case 2 is investigated. To conduct this investigation, first, a periapsis Poincaré map is generated at the same value of the Jacobi Constant as the 4:3 resonant high-altitude parking orbit. The periapses are then color-coded based on the long term behavior of their associated trajectories. This color code is listed below.

- Cyan: Trajectories that enter the vicinity of the Moon.
- Yellow: Trajectories that collide with the Earth or the Moon.
- Green: Trajectories that do not possess either of the other behaviors.

Then, the periapsis map of the invariant manifolds associated with the 4:3 resonant orbit (Figure 49) is overlaid on top of the original map (described above). These periapses are also color-coded based on whether the periapse is associated with the stable or unstable manifold approximations. This color code is listed below.

- Blue: Trajectories that are on the stable manifold approximations of the 4:3 resonant orbit.
- Red: Trajectories that are on the unstable manifold approximations of the 4:3 resonant orbit.

Figure 101 shows a zoomed-in view of the overlay of these periapsis Poincaré maps, as well as an identified region of interest and a zoomed-in view of this region of interest. This region of interest is identified as such because periapses associated with various long term behaviors and periapses associated with the invariant manifold approximations exist in proximity to each other within this region. Because of this proximity, and the fact that these periapsis Poincaré maps were generated at the same value of the Jacobi Constant, it is implied that low-ΔV transfers may exist between these trajectories. This possibility is demonstrated in Section 4.4.2.

Within this region of interest, periapses exist within proximity of each other that possess various characteristics. First, a cyan periapse associated with a trajectory that enters the vicinity of the Moon is present. Second, a green periapse associated with a trajectory that does not enter the vicinity of the Moon or collide with the Earth or the Moon (within approximately the next 1.19 years) is also present. In fact, the green periapses may be associated with the chain of islands structure seen near the region of interest. At the ‘‘center’’ of these islands are periapses associated with a 9:6 resonant orbit that is expected to be orbitally stable, in the linear sense, to in-plane perturbations. Additionally, both blue and red periapses, associated with trajectories

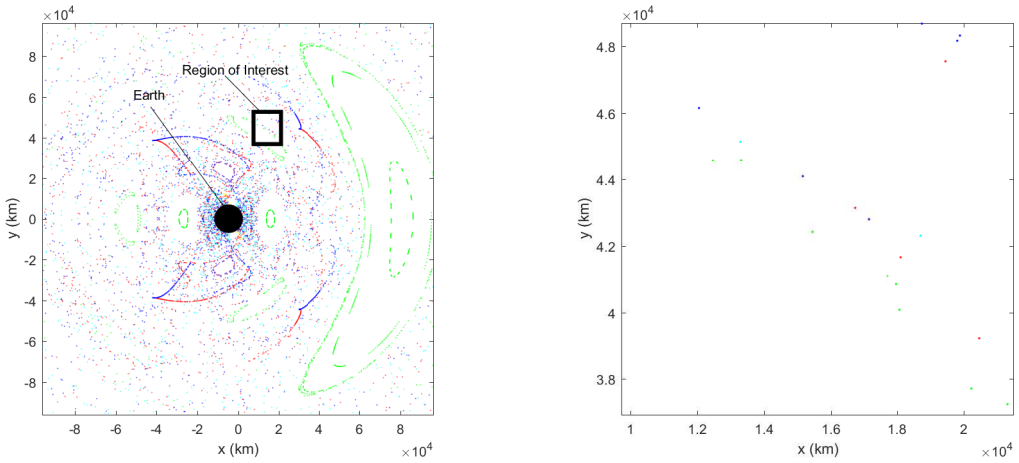

Figure 101. An Overlay of a Periapsis Poincaré Map of the Invariant Manifold Approximations of the 4:3 Resonant Orbit with a Periapsis Poincaré Map Generated at the Same Value of the Jacobi Constant with the Associated Long Term Behaviors Color-Coded—Cyan: Trajectories that Enter the Vicinity of the Moon; Yellow: Trajectories that Collide with the Earth or the Moon; Green: Trajectories that do not Possess Either of These Behaviors; Blue: Trajectories that are on the Stable Manifold Approximations; Red: Trajectories that are on the Unstable Manifold Approximations (Left: a View of the Maps in the Vicinity of the Earth with an Identified Region of Interest; Right: A Zoomed-In View of the Region of Interest)

on the stable and unstable manifold approximations, respectively, are present in this region.

The proximity of the aforementioned periapses implies that low-ΔV transfers may exist between these trajectories. A spacecraft in the 4:3 resonant orbit waiting to be tasked with reconstitution could travel through this region of interest for theoretically zero ΔV along the unstable manifold; however, this transfer would also require infinite time. Instead, for low ΔV, the spacecraft could transfer from the 4:3 resonant orbit to the unstable manifold. This trajectory could be followed until the spacecraft travels near the region of interest. Then, because the periapses in the region of interest exist in proximity, the spacecraft may be able to transfer from the unstable manifold to one of these other trajectories for low ΔV. Alternatively, the spacecraft could transfer from the unstable manifold to the stable manifold and return to the periodic orbit for

low ΔV. Examples of transfers between periapses that are in proximity to each other are demonstrated in Section 4.4.2.

A spacecraft in an orbitally unstable high-altitude periodic orbit waiting to reconstitute a constellation is able to maneuver through chaotic regions of the phase space to alter the long term behavior of the spacecraft's trajectory for low ΔV. Because of this, the long term behavior of a spacecraft's trajectory in such an orbit may be unpredictable to an observer. This knowledge may be exploited by a mission designer to design a trajectory that travels through chaotic regions of the phase space. Alternatively, an observer may utilize the same periapsis Poincaré map to determine the predictability of a spacecraft's trajectory. This knowledge may provide insight into the intent of such a satellite.

4.4.2 Test Case 4B: Results and Analysis of the Ability to Predict the Long Term Behavior of a Spacecraft's Trajectory at Various Values of the Jacobi Constant Through the Utilization of Periapsis Poincaré Maps as Visual Aids

In Test Case 4B, the ability to predict the long term behavior of a spacecraft's trajectory through the utilization of periapsis Poincaré maps is investigated. First, multiple periapsis maps are generated at various values of the Jacobi Constant. The periapses are color-coded based on the long term behavior of the associated trajectory using the following color-coding scheme.

- Green: Trajectories that remain in the vicinity of the Earth.
- Red: Trajectories that collide with the Earth.
- Blue: Trajectories that depart through the L_1 gateway and then depart through the L_2 gateway.

- Red: Trajectories that depart through the L_1 gateway and then collide with the Moon.

- Cyan: Trajectories that depart through the L_1 gateway and then return to the vicinity of the Earth.

- Magenta: Trajectories that depart through the L_1 gateway, then depart through the L_2 gateway, and finally, return to the vicinity of the Earth through the L_1 gateway.

More diverse long term behaviors are possible in Test Case 4B than in Test Case 4A because the ZVCs partially bound the motion. In Test Case 4A, because of the value of the Jacobi Constant of the parking orbit, the ZVSs do not intersect the Earth-Moon orbital plane, so motion in the Earth-Moon orbital plane is unbounded. Figure 102 displays periapsis Poincaré maps generated at various values of the Jacobi Constant.

As the value of the Jacobi Constant is changed, the structures in the periapsis Poincaré maps evolve. As the value of the Jacobi Constant is increased, the island structures associated with quasiperiodic trajectories increase in size. Periodic trajectories that are orbitally stable, in the linear sense, to in-plane perturbations are expected inside these island structures. Consequently, the irregular regions of chaos, which are identified on the maps as the ''dusty'' regions, decrease in size as the value of the Jacobi Constant is increased (the ''energy'' level is decreased) [9]. Additionally, at lower values of the Jacobi Constant (higher ''energy'' levels), large islands, associated with quasiperiodic trajectories, on the left and right side of the map are not connected. At the ''center'' of these islands is a 2:1 resonant orbit that is orbitally stable, in the linear sense, to in-plane perturbations. As the value of the Jacobi Constant is increased (lower ''energy'' levels), these islands begin to merge at the top and bottom of the map. Another interesting structure visible on these maps is the emergence of

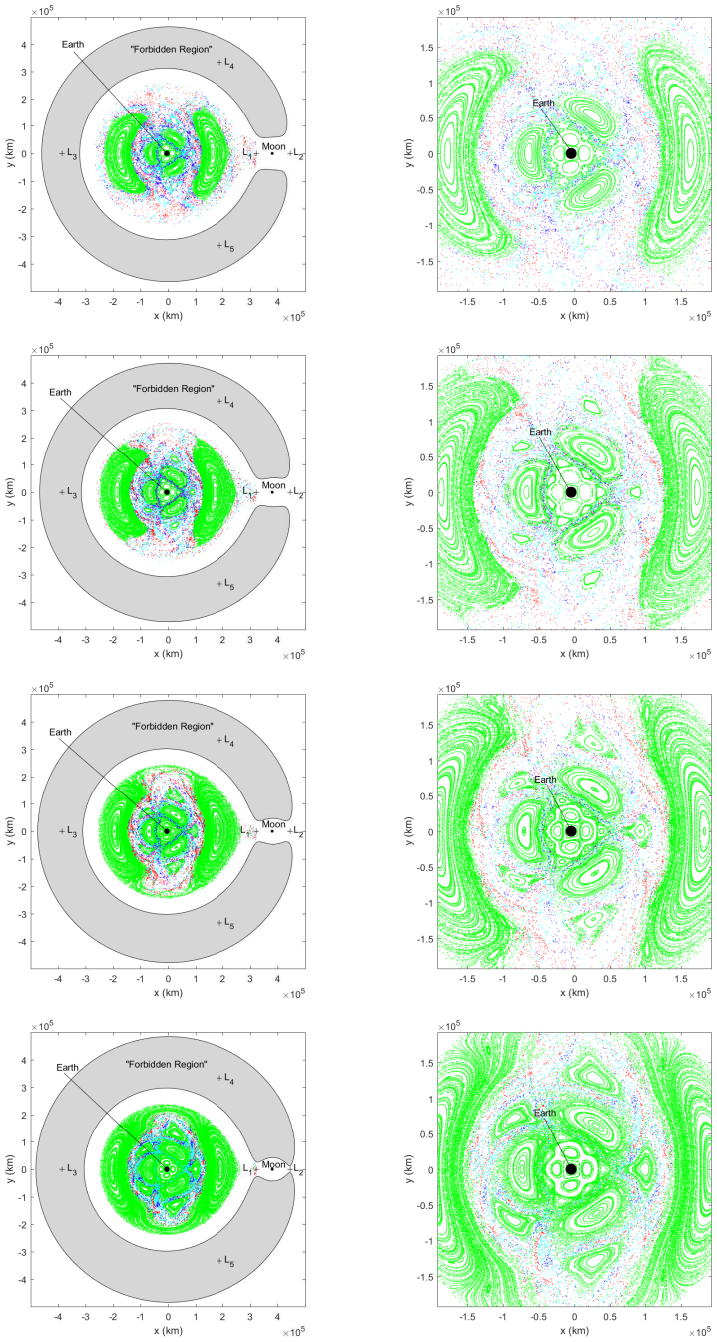

Figure 102. Periapsis Poincaré Maps Generated in the Earth-Moon CR3BP at Various Values of the Jacobi Constant Color-Coded Based on the Long Term Behavior of the Trajectory Associated with Each of the Periapses (First Row: JC=3.11; Second Row: JC=3.13; Third Row: JC=3.15; Fourth Row: JC=3.17)

an island chain that consists of five islands, or five returns to the map per period. A 5:2 resonant orbit that is orbitally stable, in the linear sense, to in-plane perturbations

exists near the ‘‘center’’ of this island chain. When the value of the Jacobi Constant is equal to 3.11, this island chain is not visible. However, as the value of the Jacobi Constant is increased, this island structure becomes visible and continues to grow as the value of the Jacobi Constant is increased even further.

An observer may exploit one of these maps to attempt to predict the long term behavior of a spacecraft's trajectory. A spacecraft observed to be traveling through the green regions on one of the maps above may be associated with a trajectory that will remain in the vicinity of the Earth. Additionally, since these green islands are surrounded by other green periapses, except at the coast line, it may be costly, in terms of ΔV, to change the long term behavior of such a spacecraft's trajectory. On the other hand, the long term behavior of a spacecraft's trajectory may be considered unpredictable if the spacecraft is observed traveling through a chaotic region of the phase space. To demonstrate this, the map associated with a value of the Jacobi Constant equal to 3.15 is investigated further. In Figure 103, a region of interest associated with chaotic behavior is identified and a zoomed-in view is shown.

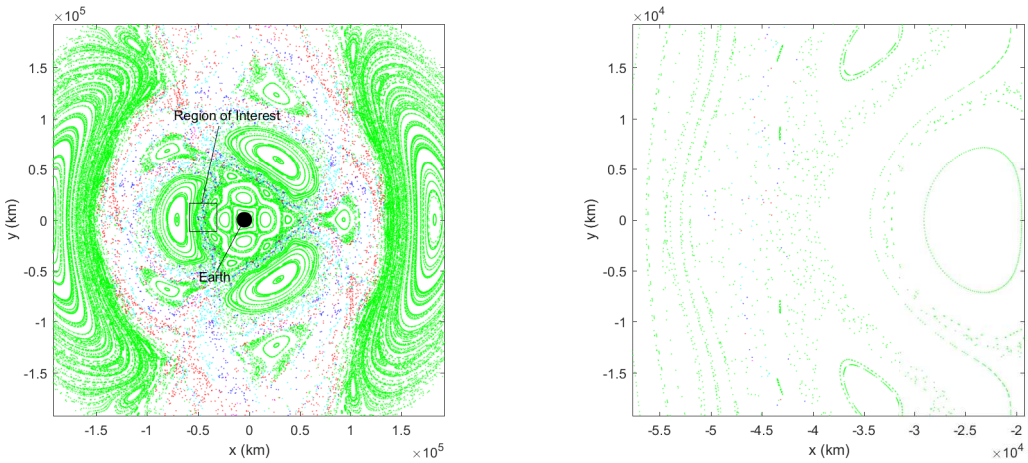

Figure 103. A Periapsis Poincaré Map Generated at a Value of the Jacobi Constant of 3.15 in the Earth-Moon CR3BP Color-Coded Based on the Long Term Behavior of the Trajectory associated with each of the Periapses with a Region of Interest Identified (Left: A View of the Map in the Vicinity of the Earth; Right: A Zoomed-in View of the Region of Interest)

The zoomed-in view shown in Figure 103 is determined to not be a dense enough map to understand the behavior in this region of the phase space. So, this region is gridded using the method described in Section 3.3 to produce a denser map in this region of the phase space. The resulting map is shown in Figure 104.

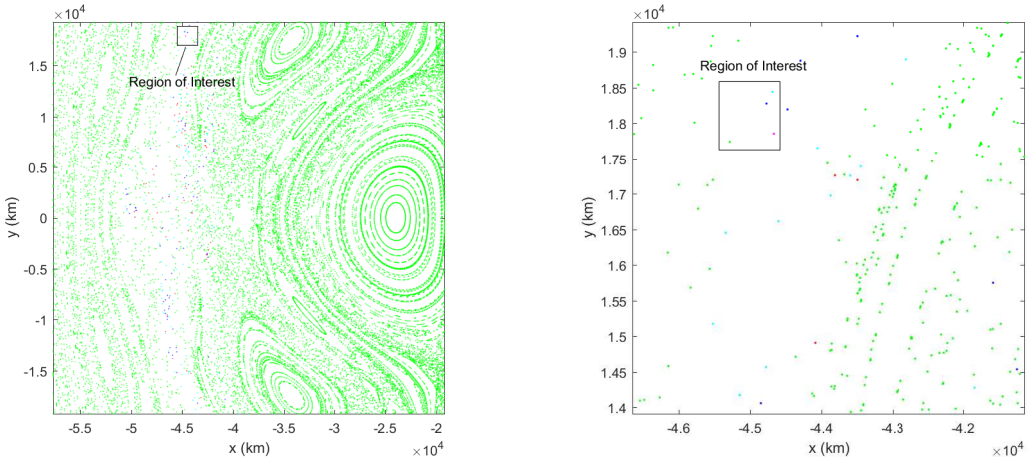

Figure 104. An Increased Density Periapsis Poincaré Map Generated at a Value of the Jacobi Constant of 3.15 in the Earth-Moon CR3BP Color-Coded Based on the Long Term Behavior of the Trajectory associated with each of the Periapses with Another Region of Interest Identified (Left: The Region of Interest Identified in Figure 103; Right: A Zoomed-In View of Another Region of Interest)

The region of interest identified in Figure 104 possesses periapsis with various long term behaviors. Each of these long term behaviors is then numerically integrated in forward time to illustrate these different behaviors that begin near each other in the phase space. A trajectory that remains in the vicinity of the Earth and is associated with the green periapse from the region of interest is shown in Figure 105. Next, a trajectory that departs through the L_2 gateway and is associated with a blue periapse from the region of interest is shown in Figure 106. After that, a trajectory that departs through the L_1 gateway and returns to the vicinity of the Earth and is associated with the cyan periapse from the region of interest is shown in Figure 107. Finally, a trajectory that departs through the L_2 gateway and returns to the vicinity of the

Earth and is associated with the magenta periapse from the region of interest is shown in Figure 108.

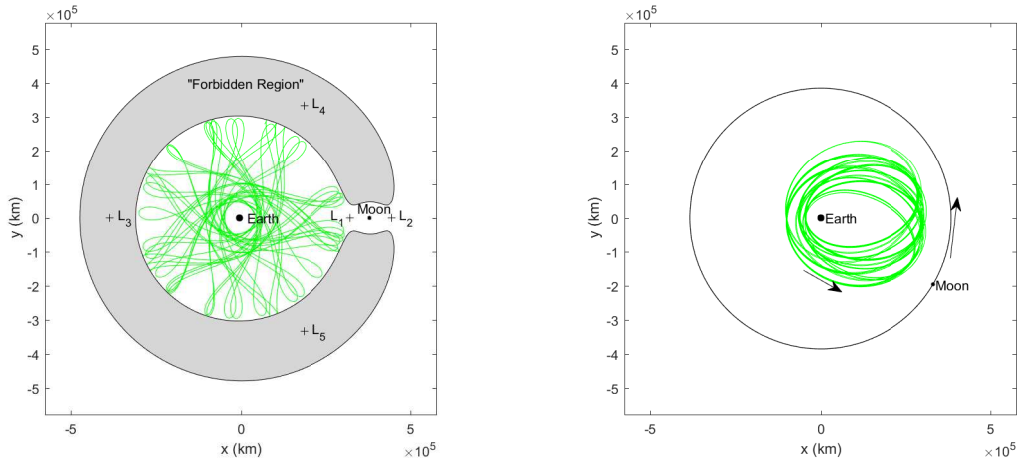

Figure 105. The Long Term Behavior of a Trajectory Associated with the Green Periapse Identified in the Region of Interest in Figure 104 Modeled in the Earth-Moon CR3BP (Left: The Barycentric Rotating Frame; Right: The Earth-Centered Inertial Frame)

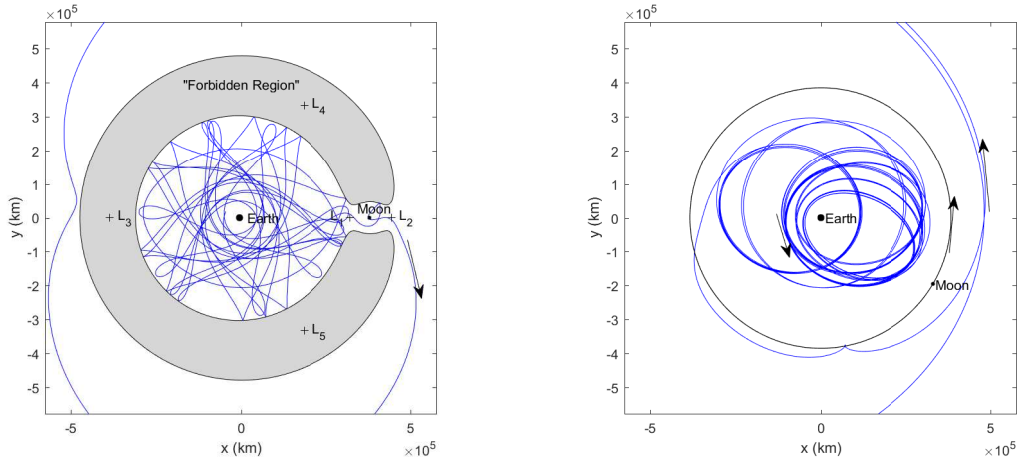

Figure 106. The Long Term Behavior of a Trajectory Associated with the Blue Periapse Identified in the Region of Interest in Figure 104 Modeled in the Earth-Moon CR3BP (Left: The Barycentric Rotating Frame; Right: The Earth-Centered Inertial Frame)

Each of these four trajectories possess different long term behaviors even though the initial states associated with each of these trajectories are located in the same region of the phase space. Because of the proximity of these initial periapses, as seen

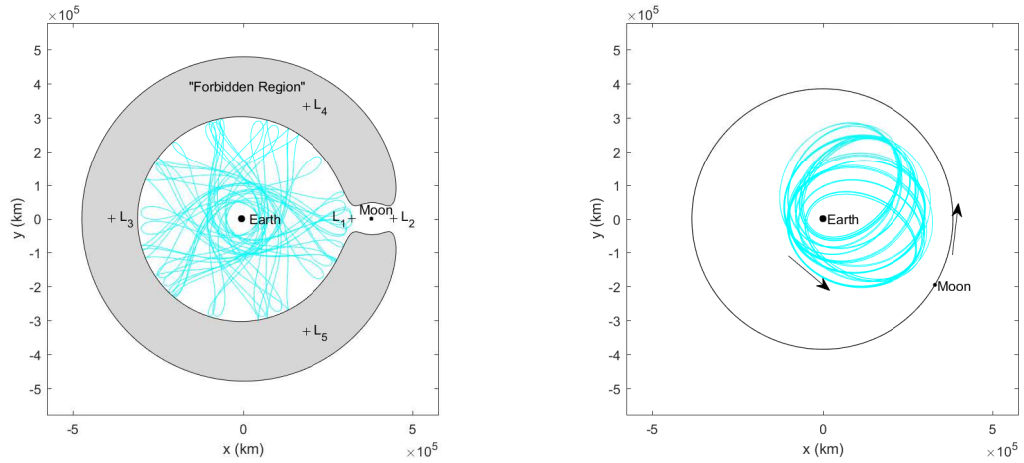

Figure 107. The Long Term Behavior of a Trajectory Associated with the Cyan Periapse Identified in the Region of Interest in Figure 104 Modeled in the Earth-Moon CR3BP (Left: The Barycentric Rotating Frame; Right: The Earth-Centered Inertial Frame)

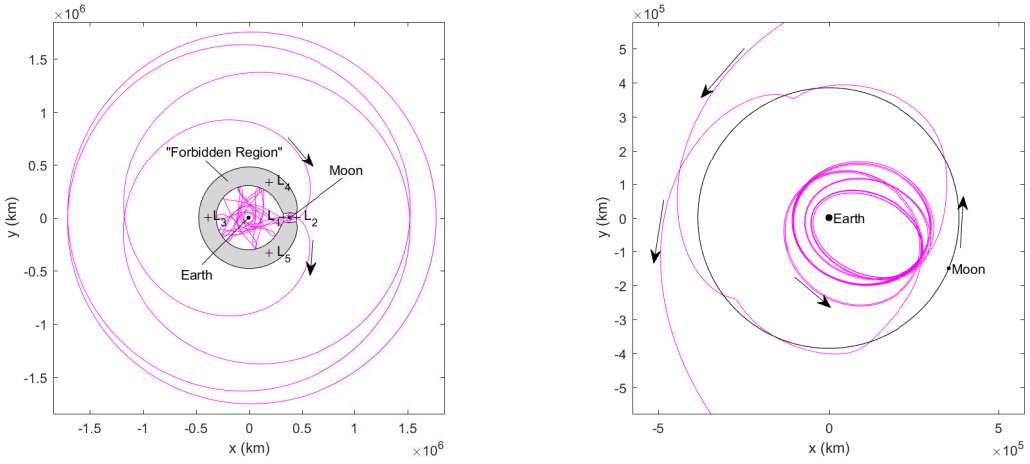

Figure 108. The Long Term Behavior of a Trajectory Associated with the Magenta Periapse Identified in the Region of Interest in Figure 104 Modeled in the Earth-Moon CR3BP (Left: The Barycentric Rotating Frame; Right: The Earth-Centered Inertial Frame)

in Figure 104, low-ΔV transfers may exist between these trajectories that allow a spacecraft to alter the long term behavior of its trajectory. To demonstrate the low costs, in terms of ΔV, to perform these transfers, a transfer scenario is developed. In this scenario, the spacecraft begins along the green trajectory, which is associated with a trajectory that remains in the vicinity of the Earth for the next 1.19 years.

Next, transfers are investigated from this initial trajectory to each of the other three trajectories. First, an initial guess for each transfer is developed. The initial state associated with the green periapse is numerically integrated in reverse time until the next apoapse. This arc is selected as the initial guess for a transfer from the green trajectory to each of the other trajectories. Then, a multiple-shooting algorithm is implemented to target a feasible solution. Finally, this feasible solution is input as an initial guess into *fmincon* to search for a locally optimal solution, in terms of ΔV. The resulting locally optimal transfers are shown in Figure 109.

Each of the three locally optimal transfers converged upon similar transfers. These similarities are a result of the proximity of these trajectories in the phase space. The cost, in terms of ΔV, to perform the locally optimal transfer from the green trajectory to the blue trajectory is 3.541 m/s. The cost to perform the locally optimal transfer to the cyan trajectory is found to be 4.115 m/s. Finally, the cost to transfer to the magenta trajectory is 4.258 m/s. As expected, these transfer costs are very low because these trajectories are in proximity to each other in the phase space. A mission designer could utilize these low-cost transfers to alter the long term behavior of the spacecraft's trajectory.

If the periapsis Poincaré map is utilized as a visual aid to predict the long term behavior of a spacecraft's trajectory, a spacecraft following the initial green trajectory may be expected to remain in the vicinity of the Earth; however, this analysis demonstrates that spacecraft in chaotic regions of the phases space may be able to alter the long term behavior of their trajectory for low cost, in terms of ΔV. Thus, it is determined that the long term behavior of such a spacecraft's trajectory is unpredictable. Alternatively, a spacecraft with a periapse observed within one of the island structures seen in Figure 103 may be determined to be traveling within a regular region of the phases space by utilizing a periapsis Poincaré map as a visual aid.

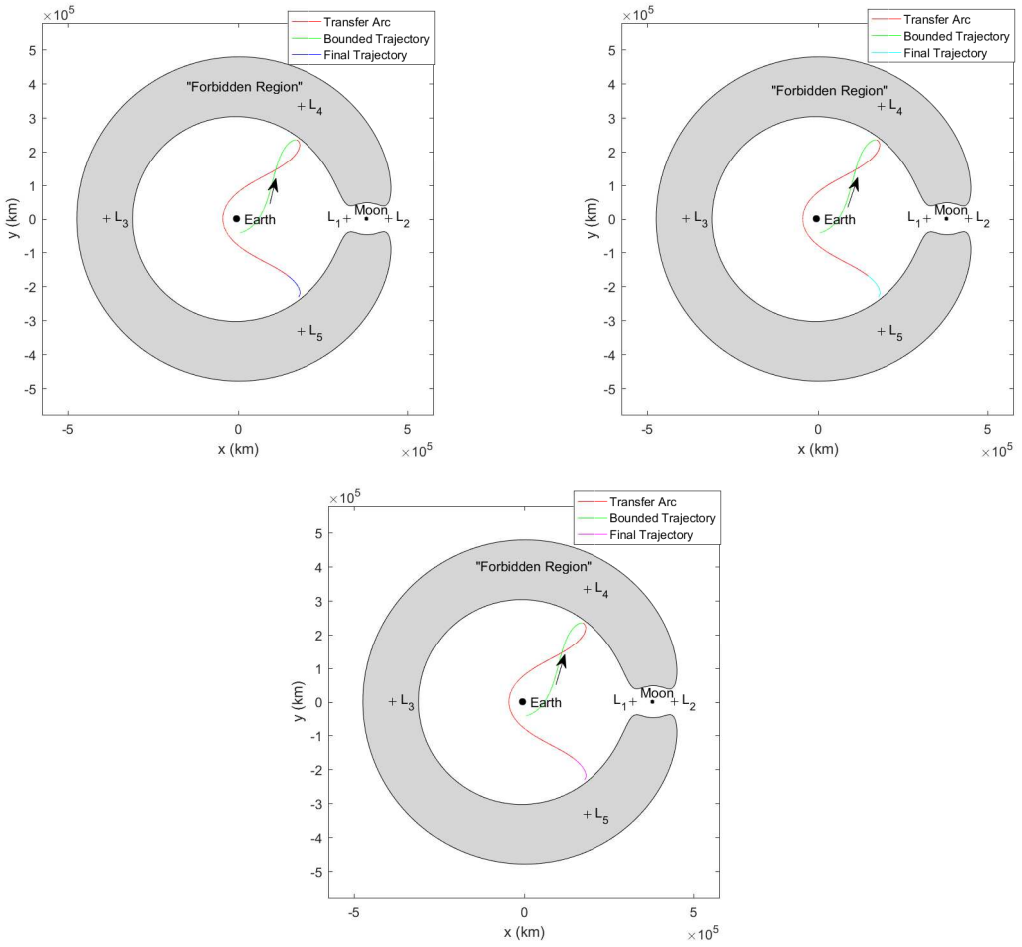

Figure 109. Locally Optimal Transfers Between the Trajectories with Different Long Term Behaviors as Identified in the Region of Interest in Figure 104 Modeled in the Earth-Moon CR3BP and Displayed in the Barycentric Rotating Frame (Top Left: A Transfer from the Trajectory Associated with the Green Periapse to the Trajectory Associated with the Blue Periapse; Top Right: A Transfer from the Trajectory Associated with the Green Periapse to the Trajectory Associated with the Cyan Periapse; Bottom Center: A Transfer from the Trajectory Associated with the Green Periapse to the Trajectory Associated with the Magenta Periapse)

A spacecraft in such a trajectory may be unable to maneuver into trajectories with other long term behavior for low cost. Thus, the long term behavior of a spacecraft's trajectory in this region of the phase space may be determined to be predictable. This knowledge may be exploited by a mission planner to design a trajectory with desired characteristics or by an observer to identify the ability of a spacecraft to alter the long term behavior of its trajectory.

4.4.3 Test Case 4: Discussion of the Ability to Predict the Long Term Behavior of a Spacecraft's Trajectory Through the Utilization of a Periapsis Poincaré Map as a Visual Aid

In Test Case 4, it is determined that the utilization of periapsis Poincaré maps as visual aids provides insight into the predictability of the long term behavior of a spacecraft's trajectory. The ability of a spacecraft to alter the long term behavior of its trajectory may be assessed by determining if the trajectory travels through chaotic or regular regions of the phase space. If the spacecraft travels through chaotic regions of the phase space, the long term behavior of the trajectory may be altered for low ΔV. Such an orbit may be deemed unpredictable. Alternatively, if the spacecraft travels through regular regions of the phase space, it may be costly to maneuver the spacecraft into a trajectory with a different long term behavior, so the long term behavior of this type of trajectory may be deemed predictable. This information may be exploited in the design process or in an observation process. A mission planner may utilize a periapsis Poincaré map as a visual aid to design trajectories with desired characteristics, or to design transfers between trajectories with different long term behaviors as demonstrated in Section 4.4.2. An observer may exploit such a map to determine the predictability of a satellite to gain insight into the satellite's purpose.

One limitation of this analysis is that due to the cost in terms of the time required to generate maps using MATLAB®, limitations on the denseness of the periapsis Poincaré maps exist. A denser map may provide more insight into the possible island structures and other chaotic regions. Additionally, the coast lines of such islands may be more well-defined by denser maps. However, there may also be an upper limit to the resolution provided by a periapsis Poincaré map. Because this tool is utilized as a visual aid, at some point a human may no longer benefit from an increase in the density of a Poincaré map. Distinct behaviors may not be distinguishable by a human

on a very dense Poincaré map. Another limitation of the current investigation is that due to the need for numerical integration, periapses on the map that are plotted near the end of a trajectory's numerical integration may be less trustworthy than earlier periapses. The error accumulation grows as the numerical integration time is increased. A third limitation of this analysis is that only a few long term behaviors are distinguished. For example, it may be possible that some periapses depart through the L_2 gateway and return to Earth twice within 1.19 years. However, increasing the number of potential long term behaviors increases the number of distinct colors needed to represent each behavior. This increase in the number of colors may inhibit the ability of a user to distinguish between different behaviors.

4.5 Chapter 4 Summary

In Test Case 1, it is demonstrated that the invariant manifolds of a resonant orbit provide good initial guesses for transfers between conventional constellations. Additionally, through the utilization of a periapsis Poincaré map of these manifolds as a visual aid, the complex nature of the manifolds could be better understood to generate initial guesses for potential transfer trajectories. Also, in some cases, transfer paths are found that required less ΔV than conventional Hohmann-type transfers. However, note that no solutions in the current investigation are claimed to be globally optimal. In addition to the potential cost savings, because of the high-altitude of these trajectories, the intent of these transfer paths may be unpredictable to an observer viewing the trajectories in the inertial frame. However, the design method employed does possess some limitations. First, the trajectories are modeled in the Earth-Moon CR3BP and, while this model may be more representative of the true dynamics than a two-body model, the trajectories must still be validated in an ephemeris model. Also, the deterministic ΔV of each transfer was calculated; however, these calculations did

not include the ΔV required to stationkeep a spacecraft as it travels through the multi-body environment. Additionally, transitioning this visual aid into the spatial CR3BP, which possesses a six-dimensional phase space, may not be trivial. A Poincaré map in the spatial CR3BP requires four dimensions, which may be challenging to visualize.

In Test Case 2, the reconstitution of a conventional constellation by a satellite in a high-altitude parking orbit is demonstrated. The utilization of periapsis maps to generate initial guesses for transfer trajectories is again illustrated. Additionally, it is demonstrated that resonant arcs can be effective initial guesses for transfers. The ΔVs required to perform the reconstitution of constellations are found to be comparable to the cost of a Hohmann-type transfer. Also, in some cases, the reconstitution of a conventional constellation is found to be more timely than a launch-on-demand capability requiring 30 days of lead time. Multi-satellite scenarios are investigated as well, including proper spacing methods, and are found to reduce the average time until reconstitution as the number of satellites is increased. Eventually, as the number of satellites is increased further, an asymptotic limit is approached. Another benefit associated with reconstitution from a high-altitude parking orbit is that no launch site is required when the need for reconstitution occurs. Instead, the satellite may be launched into the parking orbit well before the need for reconstitution occurs. Further, the period of highest risk in a satellite's life occurs during launch [103]. Through the deployment of a satellite into a high-altitude parking orbit, this risk may be overcome when a critical need for reconstitution is not present. On the other hand, a satellite on the ground waiting to reconstitute a capability via a launch-on-demand capability may have its hardware updated as it waits to be launched. Hardware updates may not be possible for a satellite in a high-altitude parking orbit. Again, some limitations are present in the current investigation. The need for a stationkeeping analysis is

demonstrated and, since the trajectories are modeled in the Earth-Moon CR3BP, the trajectories must be validated in an ephemeris model. Additionally, the precise timing required for a reconstituting satellite to rendezvous with a satellite that needs to be reconstituting is not addressed. To accomplish this rendezvous, phasing maneuvers could be performed after the transfers presented in the current investigation are completed.

In Test Case 3, the ability of a satellite to remotely sense the surface of the Earth while it is in a high-altitude orbit is found to be relatively low compared to a satellite at geostationary altitude. On the other hand, a satellite in a high-altitude orbit may be able to effectively remotely sense the surface of the Earth at times during its orbit. In particular, in resonant orbits, it is found that there are brief periods of increased performance. Additionally, increasing the number of satellites in a high-altitude orbit increases the combined average performance, combined persistence, and combined revisit rate. These periods of increased capability may allow for a satellite to perform a critical remote sensing mission. In order to improve the performance of a single satellite in such a orbit, the altitude must be decreased. However, this decrease in altitude is found to reduce the ability of a satellite to alter its long term behavior for low ΔV. Because of this, the long term behavior of a lower-altitude satellite may be more predictable. These findings resulted in the conclusion that there is a trade-off between the performance of a satellite and the predictability. Alternatively, the current investigation is interested in Earth-centric observations; however, there are scientific applications that may benefit from a satellite in a high-altitude resonant orbit. Therefore, dual-use satellites, as discussed in Section 4.3.4.1, should be considered in future investigations.

In Test Case 4, the ability to identify the long term behavior of a satellite is demonstrated. The utilization of periapsis Poincaré maps as visual aids is shown to

be an effective method of distinguishing between regular and chaotic regions of the phase space. Additionally, the color-coding of a periapsis Poincaré map based on the long term behavior is found to be an effective method of understanding the long term behavior of various trajectories. A spacecraft in a chaotic region of the phase space is shown to be able to alter its long term behavior for little ΔV, while regular regions of the phase space were found to contain trajectories that may be unable to do so. This knowledge may be exploited by a mission designer to generate a trajectory that possesses desired characteristics. Alternatively, an observer may utilize such a map to determine the predictability of a spacecraft. One limitation of this analysis is that the utilization of the Poincaré maps as a visual aid is not easily transitioned into the spatial CR3BP. Such a map would require four dimensions and may be difficult to visualize/analyze.

5. Conclusions and Future Work

The current investigation demonstrates the implementation of numerical methods and methods from dynamical systems theory to analyze the behavior of a spacecraft in a multi-body dynamical environment. Trajectory design is performed to illustrate the potential applications of high-altitude alternative trajectories (traveling well above the altitude of a geostationary orbit). Additionally, the ability of a satellite in a high-altitude trajectory to remotely sense the surface of the Earth is investigated. Finally, the utilization of periapsis Poincaré maps as visual aids to predict the long term behavior of a spacecraft's trajectory is explored. The results and analysis of the test cases presented in the current investigation lead to a number of conclusions as well as recommendations for future work.

5.1 The Invariant Manifolds Associated with Orbitally Unstable Resonant Orbits in the Earth-Moon CR3BP Provide Good Initial Guesses for High-Altitude Transfers Between Conventional Constellations

The generation of the invariant manifold approximations of an orbitally unstable resonant orbit provides insight into the behavior of trajectories at a given value of the Jacobi Constant. This insight may be exploited by a mission planner to design high-altitude trajectories that allow for cost-effective transfers between conventional constellations. These manifolds may be utilized to naturally alter the spacecraft's trajectory by exploiting the gravitational effects of the Moon. In the current investigation, this possibility is demonstrated in Section 4.1.1. Additionally, even though these invariant manifolds are generated in the planar Earth-Moon CR3BP, the trajectories may still be effectively applied to transfers in the spatial Earth-Moon CR3BP. In this case, the invariant manifolds may be applied as a planar initial guess for a transfer

between two constellations. When plane changes are required, initial guesses that perform lunar fly-bys may be desirable. Then, a numerical optimization algorithm, such as *fmincon*, may be applied to search for locally optimal solutions, in terms of ΔV. This design process proves to be very successful in Test Cases 1B and 1C where transfers are found that require less ΔV than a Hohmann-type transfer. The numerical optimization algorithm tends to converge upon a trajectory that exploited the gravitational effects of the Moon. For example, in Test Case 1C, only a small inclination change is required by the spacecraft. Then, a lunar fly-by is performed that greatly changes the inclination of the trajectory with respect to the Earth's equatorial plane. However, this process is found to be very dependent on the initial guess provided by the user. Initial guesses that do not allow for the numerical optimization algorithm to exploit the gravitational effects of the Moon may result in higher costs, in terms of ΔV. It should be noted that this design process possesses some limitations. First, trajectories are modeled in the Earth-Moon CR3BP, which does not fully represent the dynamical behavior of a spacecraft. Because of this limitation, trajectories must be validated in an ephemeris model. Also, the ΔV required for stationkeeping is not quantified. This cost may not be trivial as the trajectory is traveling through chaotic regions of the phase space or as Wiesel states, ''the stable manifold of the unstable periodic orbit might itself be unstable'' [9].

5.2 Orbitally Unstable Resonant Orbits in the Earth-Moon CR3BP Provide Good Candidates for High-Altitude Parking Orbits from which a Satellite may Reconstitute a Conventional Constellation

In Test Case 2, the ability of a satellite in a high-altitude orbit to reconstitute a conventional constellation is investigated. It is discovered that a satellite in the orbitally unstable 4:3 resonant orbit proved to be a viable reconstitution option for

each of the three constellations of interest. These constellations of interest each consist of three satellites; however, the results of the current investigation are not affected by the number of satellites in each constellation. It is found that resonant arcs may provide good initial guesses for transfers from the resonant orbit to the constellations of interest. Alternatively, the invariant manifolds associated with the resonant orbit provided low-ΔV transfer opportunities from the parking orbit to the constellations of interest. In some cases, these transfers provided a more timely response than a launch-on-demand capability that requires 30 days of lead time. Additionally, because of the low value of the Jacobi Constant (high ''energy'' level), the manifolds were able to travel near LEO. This characteristic is not present in all orbitally unstable periodic orbits, but is desirable for designing low cost transfers from LEO to the parking orbit. Other orbitally unstable resonant orbits may exist in the Earth-Moon CR3BP that provide a satellite with the ability to reconstitute conventional constellations for low ΔV. In particular, orbitally unstable resonant orbits that do not lie in the Earth-Moon orbital plane may also be effective for reconstituting constellations that do not lie in the Earth-Moon orbital plane. Moreover, multi-satellite scenarios are found to potentially further reduce the time until reconstitution. The current investigation found that the proper method for spacing multiple satellites in a high-altitude parking orbit is to identify the longest wait time until a transfer path and to equally space the satellites along this time interval. Other benefits of reconstitution from a high-altitude parking orbit include the lack of need for a launch when the need for reconstitution occurs. Launch sites may not always be available for a launch-on-demand capability to be performed, and the period of highest risk in a satellite's lifetime occurs during launch. A satellite in a high-altitude parking orbit may be launched when the launch site is available and may overcome the riskiest period of its lifetime when a critical need for reconstitution is not present. On the other hand, a satellite waiting to

reconstitute a capability via a launch-on-demand capability may have its hardware updated, while a satellite in a high-altitude parking orbit may not. Again, limitations of the current investigation include the need to validate the proposed trajectories in an ephemeris model and to quantify the required nondeterministic ΔV for stationkeeping. The latter limitation is particularly important to verify the feasibility of maintaining a satellite in a high-altitude parking orbit because a satellite may be required to wait in this parking orbit for a long period of time. Another limitation is that the precise timing of transfers required for a reconstituting satellite to rendezvous with a satellite that needs to be reconstituted is not addressed. However, phasing maneuvers could be performed after the transfers from the high-altitude parking orbit are completed to accomplish a rendezvous between the reconstituting satellite and the satellite that requires reconstitution.

5.3 Intervals of High Performance Regarding the Ability of a Satellite to Remotely Sense the Surface of the Earth Are Found to Exist

The overall capability of satellites in such high-altitude orbits to remotely sense the surface of the Earth is found to be low relative to that of a satellite at geostationary altitude; however, intervals of high performance are found, indicating that a satellite in such an orbit may effectively perform remote sensing of the Earth's surface at specific times during the satellite's trajectory. In Test Case 3, the average performances of a satellite in a high-altitude orbit are found to be less than 10% of that of a satellite at geostationary altitude. On the other hand, periods of high performance do exist that can, in some cases, reach almost 100% that of a satellite at geostationary altitude. During these spikes in coverage, a satellite may be able to provide a critical remote sensing capability. Additionally, through the analysis of multi-satellite scenarios, it is found that as the number of satellites in the high-altitude parking orbit is increased the

combined average performance, combined persistence, and combined revisit rate are also increased. One limitation of the current investigation is that satellite performance was only based on its ability to remotely sense the surface of the Earth. There may be other military applications of a satellite that would benefit from a high-altitude trajectory.

5.4 There is a Trade-Off Between the Ability of a Satellite in a High-Altitude Parking Orbit to Provide Coverage of the Surface of the Earth and the Predictability of the Long Term Behavior of the Satellite's Trajectory

In the current investigation, it is concluded that as the altitude of a parking orbit is increased, the predictability of the long term behavior may be decreased. This decrease in predictability is a result of the lower value of the Jacobi Constant (higher "energy" level) associated with the trajectory. At lower values of the Jacobi Constant, larger regions of chaos are present than at higher values of the Jacobi Constant. The long term behavior of a spacecraft's trajectory in a chaotic region of the phase space may be deemed unpredictable, as demonstrated in Section 4.4.2. However, not all trajectories at low values of the Jacobi Constant travel through chaotic regions of the phase space. Nevertheless, traveling through chaotic regions of the phase space may allow for the long term behavior of a spacecraft's trajectory to be altered for very low ΔV. On the other hand, because of the high-altitude nature of such a trajectory, the ability of a satellite to remotely sense the surface of the Earth is decreased. A satellite in a lower-altitude trajectory allows for an increase in the ability to remotely sense the surface of the Earth, but the regions of chaos are smaller at these higher values of the Jacobi Constant. Additionally, as the value of the Jacobi Constant is increased further ("energy" level decreased), the regions of chaos will diminish in

size. A spacecraft's trajectory at such a value of the Jacobi Constant would possess regular behavior and may be deemed predictable. A mission designer must trade the unpredictability associated with high-altitude trajectories with the performance provided by a satellite in a lower-altitude trajectory. However, as previously noted, not all high-altitude trajectories possess this unpredictability. A mission designer must identify chaotic regions of the phase space to design such a trajectory. One method to identify such regions is the utilization of a Poincaré map as a visual aid.

5.5 The Utilization of Periapsis Poincaré Maps as Visual Aids Provides Insight into the Potential Behaviors at Particular Values of the Jacobi Constant

The current investigation demonstrates the implementation of methods from dynamical systems theory to aid in the design and analysis of high-altitude trajectories modeled in the Earth-Moon CR3BP. Specifically, periapsis Poincaré maps are generated and effectively exploited in various manners to gain insight into the dynamical behavior at particular values of the Jacobi Constant. First, it is demonstrated that periapsis Poincaré maps provide an effective method for viewing the invariant manifolds of an orbitally unstable periodic orbit. Such maps provide insight into the regions of the phase space that a satellite in the orbitally unstable periodic orbit may travel to for low ΔV. Additionally, because the hyperplane chosen was a periapsis condition, these maps provide initial guesses for transfers to conventional constellations with nearly tangential burns. These tangential burns may allow for low-ΔV transfers to conventional constellations to exist. Then, it is demonstrated that periapsis Poincaré maps are desirable for generating initial guesses for resonant orbits in the Earth-Moon CR3BP. Orbitally stable, in the linear sense, resonant orbits are fixed points on the maps surrounded by island structures consisting of quasiperiodic trajectories.

Additionally, the corresponding orbitally unstable periodic orbits exist in between these island structures. Finally, periapsis Poincaré maps are demonstrated to be an effective means for categorizing the long term behavior of a spacecraft's trajectory. These maps may be exploited by an observer to characterize the predictability of the long term behavior of an observed spacecraft's trajectory. On the other hand, a mission planner may exploit such a map to design a trajectory that possesses desired characteristics. One limitation of the current investigation is the cost, in terms of time, associated with the generation of a dense periapsis Poincaré map using MATLAB®. The current investigation overcame this obstacle through the employment of AFRL's supercomputing resources. Another limitation of the current investigation is that Poincaré maps are only generated in the planar CR3BP. The generation and analysis of Poincaré maps in the spatial CR3BP is more complex because of the four-dimensional nature of such maps. However, these maps may be more applicable to the analysis of real world trajectories.

5.6 Limitations of the Current Investigation

The current investigation possesses some limitations that must be noted and are listed below.

- The highly elliptical geosynchronous starting orbit investigated in Test Case 1 and the 4:3 parking orbit investigated in Test Case 2 both lie in the Earth-Moon orbital plane. These planar orbits are chosen due to their simplicity in the Earth-Moon CR3BP. Since these orbits lie in the Earth-Moon orbital plane, analysis may be performed in the planar Earth-Moon CR3BP, which possesses a four-dimensional phase space rather than the six-dimensional phase space present in the spatial Earth-Moon CR3BP. This four-dimensional phase space allows for the generation and analysis of two-dimensional Poincaré maps.

These two-dimensional Poincaré maps are much simpler to analyze than the four-dimensional Poincaré maps associated with the spatial Earth-Moon CR3BP.

- Only the ability of a satellite to remotely sense the surface of the Earth is investigated in Test Case 3. There are many other applications of satellites in high-altitude parking orbits that could be investigated.

- Trajectories developed through preliminary design in the Earth-Moon CR3BP are not transitioned and converged in an ephemeris model. This transition would be the next step in the design process to ensure that the trajectories developed are feasible in the ephemeris.

- The nondeterministic ΔV required to stationkeep a satellite in a high-altitude parking orbit is not quantified. The trajectories developed in the current investigation may travel through chaotic regions of the phase space or be in orbitally unstable periodic orbits. Because of this, such trajectories may be sensitive to perturbations and require a substantial amount of nondeterministic ΔV for stationkeeping.

- The precise timing of transfers required for a reconstituting satellite to rendezvous with a satellite that needs to be reconstituted is not investigated. Phasing maneuvers could be performed after the transfers presented in the current investigation are completed to accomplish a rendezvous between the reconstituting satellite and the satellite that requires reconstitution.

- The radiation environment present at high-altitudes is not considered during the preliminary design and analysis of trajectories in the current investigation. This environment may influence the design of satellites and their missions and needs to be assessed before a mission is performed.

- The command and control of a satellite in a high-altitude trajectory is not considered and may present challenges to the operation of such satellites.

- Due to the cost, in terms of time, to generate Poincaré maps using MATLAB®, the denseness of such maps is sacrificed. A denser map may provide further insight into the trajectories present at a particular value of the Jacobi Constant. On the other hand, an upper limit may exist where a human may no longer benefit from an increase in the density of a Poincaré map because distinct behaviors may not be distinguishable if too many points are shown.

- Only periapsis maps are generated in the current investigation. Other maps, such as apoapsis maps, may also provide insight into potential transfers. These apoapsis maps may be beneficial for generating initial guesses where inclination changes are required. Performing an inclination change at apoapse may be desirable because it is less costly, in terms of ΔV, to change the direction of motion when traveling at lower speeds.

- All trajectories in the Earth-Moon CR3BP are numerically integrated. The numerical integrators employed introduce errors into the trajectories. As a result, trajectories integrated for short periods of time may be reliable, but trajectories integrated for long periods of time may not reflect the behavior of the true trajectory. However, numerical integration is required in the CR3BP because this muti-body dynamical environment does not possess a known closed-form analytical solution.

5.7 Future Work

The current investigation provides many opportunities for future research. Some recommendations for future research are presented in the following section; however,

these examples are not inclusive of all of the future research that may be performed. These recommendations for future work would extend the results and analysis of the current investigation as well as address the limitations of the current work.

5.7.1 Validate the Effectiveness of a Satellite in a High-Altitude Parking Orbit to Reconstitute Conventional Constellations by Performing a Higher-Fidelity Analysis

The feasible solutions of the current investigation are solutions to the Earth-Moon CR3BP. However, this model only provides an approximation of the dynamics of a spacecraft. This method may be valid for preliminary design, but trajectories must be transitioned into an ephemeris model to validate the designs. The ephemeris model could include the gravitational effects of Earth's nonspherical mass distribution, solar radiation pressure, air drag, and the gravitational effects of the Earth, Moon, and Sun based on their ephemeris locations. Once the preliminary design is transitioned into the ephemeris model, a multiple-shooting algorithm could be implemented to target a feasible solution in this higher-fidelity model. The need for this targeting process is demonstrated in Section 4.1.1. A solution in the Earth-Moon CR3BP may not be a solution in an ephemeris model, but may be a good initial guess for such a solution. Once a feasible solution is targeted in the ephemeris model, an optimization algorithm could then be implemented to search for a locally optimal solution in terms of ΔV.

In addition to the need to transition feasible trajectories into an ephemeris model, the nondeterministic ΔV required for stationkeeping must be approximated. Without stationkeeping, errors in navigation may grow exponentially for a spacecraft in an orbitally unstable periodic orbit. An example of this error growth is demonstrated in Section 4.2.4. Pavlak provides a method for approximating the required ΔV for stationkeeping of periodic orbits in the Earth-Moon CR3BP [28].

The current investigation considers resonant orbits in the Earth-Moon CR3BP that lie in the Earth-Moon orbital plane and their applications as high-altitude parking orbits. However, resonant orbits also exist in the spatial CR3BP that do not lie in the Earth-Moon orbital plane. These spatial resonant orbits may also be good candidates for high-altitude parking orbits in the Earth-Moon CR3BP, especially for constellations that do not lie in the Earth-Moon orbital plane. Vaquero provides some examples of these spatial resonant orbits [31]. Lower cost transfers than the solutions presented in the current investigation may exist from such an orbit to conventional constellations that do not lie in the Earth-Moon orbital plane such as geostationary or Tundra orbits. However, the invariant manifolds of such orbits may be more difficult to analyze. These manifolds would not remain in the Earth-Moon orbital plane, so a planar periapsis Poincaré map may not be sufficient to understand the dynamical behavior of these manifolds. Instead, a four-dimensional Poincaré map could be generated to attempt to understand these manifolds. The generation and analysis of this type of map would not be trivial, but may be effective for generating initial guesses for low-cost transfers to and from the spatial resonant orbit. Additionally, it may be challenging to generate families of resonant orbits in the spatial Earth-Moon CR3BP. The continuation method implemented in the current investigation is able to effectively generate of families of planar resonant orbits. However, the modified single-parameter continuation method possesses limitations. For example, knowledge of the evolution of the family is required to step along the appropriate parameter. It is possible that families found in the current investigation may be continued further with a more robust continuation method. One such method may be the pseudo-arclength continuation method [14,27,31]. This continuation method steps in the direction of the null space of the Jacobian vector instead of a physical parameter. Pseudo-arclength continuation does not require knowledge of the evolution of the family and may

provide a more efficient method to generate families of resonant orbits in the spatial Earth-Moon CR3BP.

5.7.2 Expand the Analysis of Reconstitution Scenarios

The current investigation demonstrates that reconstitution from a high-altitude parking orbit is viable. However, only a limited analysis is performed. Future work could include the analysis of reconstitution from a high-altitude parking orbit involving other parking orbits and even other constellations. Additionally, the current investigation demonstrates an appropriate spacing method for multiple satellites in a parking orbit that could be employed in other reconstitution scenarios. The analysis of multiple off-ramps could be continued to potentially further reduce the time until reconstitution from a high-altitude parking orbit. The current investigation only explores multiple off-ramps for the reconstitution of one constellation; however, the reconstitution of other constellations of interest may also benefit from multiple off-ramps. Additionally, it may be possible for the cost, in terms of ΔV, to be traded with time until reconstitution when designing transfers. This trade may also be possible when an off-ramp is just missed. In the current investigation, if an off-ramp is missed, the satellite must wait until the next off-ramp to begin a transfer. On the other hand, transfers may exist that begin after the locally optimal off-ramps investigated. A satellite may be able to utilize one of these transfers, even if more ΔV is required, to decrease the time until reconstitution. Also, the current investigation does not address the precise timing required for a reconstituting satellite to rendezvous with a satellite that needs to be reconstituted. Future research could investigate different methods to accomplish this precise timing. One method could be to perform phasing maneuvers after a satellite in the high-altitude parking orbit has completed a transfer to the constellation. These phasing maneuvers would be used to adjust the

reconstituting satellite's position in the orbit until a successful rendezvous with the satellite requiring reconstitution is accomplished. Another method could be to perform phasing maneuvers during the transfer from the high-altitude parking orbit to the constellation of interest to rendezvous with the satellite that requires reconstitution at the completion of the transfer. A third method to accomplish this precise timing could be to perform the phasing maneuvers while the satellite in the high-altitude parking orbit is waiting to reach an off-ramp. These three methods could be employed individually or potentially used together depending on the specific scenario.

5.7.3 Explore Operational Scenarios Involving the Remote Sensing Capability of Satellites in High-Altitude Trajectories

In the current investigation, only the ability to remotely sense the Earth's surface is investigated regardless of where on the Earth's surface this capability is provided. Future research could investigate the specific regions on Earth that may be remotely sensed during spikes in coverage. Additionally, the percentage of the Earth covered during a spike in coverage could be measured as well. In some cases spikes in performance are observed to persist above 10% of that of a satellite at geostationary altitude for about 1.3 days. A spacecraft may be able to remotely sense a large portion of the Earth during these intervals. This proposed investigation would require the refining of the metrics developed in the current investigation, but similar analysis may be performed.

5.7.4 Investigate Alternative Applications of Satellites in High-Altitude Orbits

The current investigation explores the ability of a satellite in a high-altitude trajectory to remotely sense the surface of the Earth. However, many other applications

of such a trajectory may exist. For example, some scientific observations can only be performed from a high-altitude trajectory. Metrics could be developed to determine the ability of a satellite in such an orbit to perform one of these applications. Additionally, an investigation into the potential application of a dual-purpose satellite, as discussed in Section 4.3.4.1, could be performed. Such a satellite could be in a high-altitude parking orbit waiting to be tasked with reconstitution while simultaneously performing a mission that benefits from high-altitudes. A dual-purpose satellite could incorporate two military missions, or could involve a cooperative effort between two distinct organizations. This type of cooperative mission may increase the complexity of both the design and operation of such a satellite, but may be more cost-effective than two independently performed missions. Alternatively, a satellite in a high-altitude orbit could potentially be used for space-based space situational awareness.

5.7.5 Extend the Categorization of Periapses Based on the Long Term Behavior of the Trajectory to the Spatial CR3BP

The current investigation generates periapsis Poincaré maps in the planar Earth-Moon CR3BP and color-codes the periapses based on the long term behavior of the trajectory. However, these maps are only useful for analyzing the behavior of trajectories that lie in the Earth-Moon orbital plane. It is possible that similar analysis techniques may be extended into the spatial Earth-Moon CR3BP. This analysis would require the generation and analysis of four-dimensional Poincaré maps, but perhaps these maps could be effectively utilized as visual aids in a similar manner as a two-dimensional periapsis Poincaré map. Visualization techniques similar to those discussed by Geisel to analyze these maps may be employed [19]. Also, Geisel employed a ‘‘space-plus-color’’ method to represent the four dimensions of such a map, while Haapala utilized glyphs to represent the fourth dimension [19, 27]. It may

be useful to view a periapsis map in the spatial CR3BP through the implementation of this ‘‘space-plus-color’’ method with glyphs denoting the long term behavior of the trajectory. This map may then be utilized as a visual aid by a mission designer or observer to understand the potential dynamical behaviors at a specific value of the Jacobi Constant.

5.8 Chapter 5 Summary

This chapter discusses the overall conclusions of the current investigation. Next, some limitations of the investigation are discussed. Finally, recommendations for future work are discussed in detail.

Bibliography

1. U. S. Joint Chiefs of Staff, ''Space Operations,'' *Joint Publication 3-14*, 2013. [Online]. Available: http://www.dtic.mil/doctrine/new_pubs/jp3_14.pdf [Accessed 2016-12-01].

2. Los Angeles Air Force Base, ''Advanced Extremely High Frequency (AEHF) System,'' 2012, *losangeles.af.mil*. [Online]. Available: http://www.losangeles.af.mil/About-Us/Fact-Sheets/Article/343735/advanced-extremely-high-frequency-aehf-system [Accessed 2016-11-28].

3. W. Wiesel, *Spaceflight Dynamics*, 3rd ed. Beavercreek, OH: Aphelion Press, 2010.

4. E. Howell, ''What is a Geosynchronous Orbit?'' 2015, *space.com*. [Online]. Available: http://www.space.com/29222-geosynchronous-orbit.html [Accessed 2016-12-06].

5. B. Iannotta and T. Malik, ''U.S. Satellite Destroyed in Space Collision,'' 2009, *space.com*. [Online]. Available: http://www.space.com/5542-satellite-destroyed-space-collision.html [Accessed 2016-11-28].

6. C. Moskowitz, ''Space Junk Problem is More Threatening than Ever, Report Warns,'' 2011, *space.com*. [Online]. Available: http://www.space.com/12801-space-junk-threat-orbital-debris-report.html [Accessed 2016-11-28].

7. D. Vallado, *Fundamentals of Astrodynamics and Applications*, 3rd ed. Hawthorne, CA: Microcosm Press, 2007.

8. J. Wertz, D. Everett, and J. Puschell, *Space Mission Engineering: The New SMAD*, 1st ed. Hawthorne, CA: Microcosm Press, 2011.

9. W. Wiesel, *Modern Astrodynamics*, 2nd ed. Beavercreek, OH: Aphelion Press, 2010.

10. Executive Office of the President, ''National Space Policy of the United States of America,'' 2010, *obamawhitehouse.gov*. [Online]. Available: https://obamawhitehouse.archives.gov/sites/default/files/national_space_policy_6-28-10.pdf [Accessed 2017-03-08].

11. Office of the Assistant Secretary of Defense for Homeland Defense and Global Security, ''Space Domain Mission Assurance: A Resilience Taxonomy White Paper,'' 2015, *Federation of American Scientists*. [Online]. Available: https://fas.org/man/eprint/resilience.pdf [Accessed 2016-12-01].

12. U.S. Department of Defense, ‘‘Air Force Future Operating Concept,’’ 2015, *af.mil*. [Online]. Available: http://www.af.mil/Portals/1/images/airpower/AFFOC.pdf [Accessed 2016-12-01].

13. C. Ocampo, ‘‘Trajectory Analysis for the Lunar Flyby Rescue of AsiaSat-3/HGS-1,’’ *Annals of the New York Academy of Sciences*, vol. 1065, no. 1, pp. 232–253, 2005.

14. M. Wilmer, *Military Applications of High-Altitude Satellite Orbits in a Multi-Body Dynamical Environment Using Numerical Methods and Dynamical Systems Theory*, Master's thesis, Air Force Institute of Technology, 2016.

15. V. Szebelehy, *Theory of Orbits*. New York, NY: Academic Press, 1967.

16. B. Dunford, ‘‘ISEE-3/ICE: In Depth,’’ *nasa.gov*. [Online]. Available: http://solarsystem.nasa.gov/missions/iseeice/indepth [Accessed 2016-10-16].

17. E. Grayzek, ‘‘ISEE 3,’’ 2016, *nasa.gov*. [Online]. Available: http://nssdc.gsfc.nasa.gov/nmc/spacecraftDisplay.do?id=1978-079A [Accessed 2016-10-11].

18. National Research Council, *Continuing Kepler's Quest: Assessing Air Force Space Command's Astrodynamics Standards*. Washington DC: National Academies Press, 2012. [Online]. Available: https://www.nap.edu/download/13456# [Accessed 2016-12-01].

19. C. Geisel, *Spacecraft Orbit Design in the Circular Restricted Three-Body Problem Using Higher-Dimensional Poincaré Maps*, Ph.D. dissertation, Purdue University, 2013. [Online]. Available: https://engineering.purdue.edu/people/kathleen.howell.1/Publications/Dissertations/2013_Geisel.pdf [Accessed 2016-12-01].

20. S. Wiggins, *Introduction to Applied Nonlinear Dynamical Systems and Chaos*. New York, NY: Springer-Verlag, 1990.

21. K. Howell, B. Barden, R. Wilson, and M. Lo, ‘‘Trajectory Design Using A Dynamical Systems Approach With Application To Genesis,’’ in *AAS/AIAA Astrodynamics Specialists Conference*, 1997. [Online]. Available: https://engineering.purdue.edu/people/kathleen.howell.1/Publications/Conferences/1997_AAS_HowBarWilLo.pdf [Accessed 2016-03-28].

22. M. Lo, B. Williams, W. Bollman, D. Han, Y. Hahn, J. L. Bell, E. A. Hirst, R. Corwin, P. Hong, K. Howell, B. Barden, and R. Wilson, ‘‘Genesis Mission Design,’’ *The Journal of Astronautical Sciences*, vol. 49, no. 1, pp. 169–184, 2001. [Online]. Available: https://engineering.purdue.edu/people/kathleen.howell.1/Publications/Journals/2001_JAS_Genesis.pdf [Accessed 2016-10-11].

23. W. Koon, M. Lo, J. Marsden, and S. Ross, ''Heteroclinic Connections between Periodic Orbits and Resonance Transitions in Celestial Mechanics,'' *Chaos: An Interdisciplinary Journal of Nonlinear Science*, vol. 10, no. 2, pp. 427–469, 2000. [Online]. Available: http://scitation.aip.org/content/aip/journal/chaos/10/2/10.1063/1.166509 [Accessed 2016-07-11].

24. M. Lo and J. Parker, ''Unstable Resonant Orbits near Earth and Their Role in Planetary Missions,'' *AIAA/AAS Astrodynamics Specialist Conference*, no. August, pp. 1–29, 2004. [Online]. Available: http://arc.aiaa.org/doi/pdf/10.2514/6.2004-5304 [Accessed 2016-08-31].

25. G. Gómez, W. S. Koon, M. W. Lo, J. E. Marsden, J. J. Masdemont, and S. D. Ross, ''Connecting Orbits and Invariant Manifolds in the Spatial Restricted Three-Body Problem,'' *Nonlinearity*, vol. 17, no. 5, pp. 1571–1606, 2004. [Online]. Available: http://iopscience.iop.org/0951-7715/17/5/002 [Accessed 2016-08-12].

26. A. Haapala, *Trajectory Design Using Periapse Maps and Invariant Manifolds*, Master's thesis, Purdue University, 2010. [Online]. Available: https://engineering.purdue.edu/people/kathleen.howell.1/Publications/Masters/2010_Haapala.pdf [Accessed 2016-07-08].

27. A. Haapala, *Trajectory Design in the Spatial Circular Restricted Three-Body Problem Exploiting Higher-Dimensional Poincaré Maps*, Ph.D. dissertation, Purdue University, 2014. [Online]. Available: https://engineering.purdue.edu/people/kathleen.howell.1/Publications/Dissertations/2014_Haapala.pdf [Accessed 2016-09-24].

28. T. Pavlak, *Trajectory Design and Orbit Maintenance Strategies in Multi-Body Dynamical Regimes*, Ph.D. dissertation, Purdue University, 2013. [Online]. Available: https://engineering.purdue.edu/people/kathleen.howell.1/Publications/Dissertations/2013_Pavlak.pdf [Accessed 2016-12-03].

29. K. Davis, R. Anderson, and G. Born, ''Preliminary Study of Geosynchronous Orbit Transfers from LEO using Invariant Manifolds,'' *The Journal of the Astronautical Sciences*, vol. 58, no. 3, pp. 295–310, 2011. [Online]. Available: http://ccar.colorado.edu/geryon/papers/Misc/BornSymposiumPreprint.pdf [Accessed 2016-09-14].

30. M. Vaquero and K. C. Howell, ''Leveraging Resonant-Orbit Manifolds to Design Transfers Between Libration-Point Orbits,'' *Journal of Guidance, Control, and Dynamics*, vol. 37, no. 4, pp. 1143–1157, 2014. [Online]. Available: http://arc.aiaa.org/doi/abs/10.2514/1.62230 [Accessed 2016-08-31].

31. T. Vaquero Escribano, *Spacecraft Transfer Trajectory Design Exploiting Resonant Orbits in Multi-body Environments*, Ph.D. dissertation, Purdue University, 2013. [Online]. Available: https://engineering.purdue.edu/people/kathleen.howell.1/Publications/Dissertations/2013_Vaquero.pdf [Accessed 2016-12-13].

32. T. Vaquero Escribano, *Poincaré Sections and Resonant Orbits in the Restricted Three-Body Problem*, Master's thesis, Purdue University, 2010. [Online]. Available: https://engineering.purdue.edu/people/kathleen.howell.1/Publications/Masters/2010_Vaquero.pdf [Accessed 2016-12-13].

33. M. Henon, ''Numerical Exploration of the Restricted Three-body Problem,'' in *The Theory of Orbits in the Solar System and in Stellar Systems*. Proceedings from Symposium no. 25 held in Thessaloniki, August 17-22, 1964, Academic Press, London, 1966, pp. 157–169. [Online]. Available: http://adsabs.harvard.edu/full/1966IAUS...25..157H [Accessed 2016-08-09].

34. B. Villac and D. Scheeres, ''On the Concept of Periapsis in Hill's Problem,'' *Celestial Mechanics and Dynamical Astronomy*, vol. 90, no. January 2004, pp. 165–178, 2004. [Online]. Available: https://www.researchgate.net/publication/225231299_On_The_Concept_Of_Periapsis_In_Hill%27s_Problem [Accessed 2016-07-11].

35. D. Craig Davis, *Multi-body Trajectory Design Strategies Based on Periapsis Poincare Maps*, Ph.D. Dissertation, Purdue University, 2011. [Online]. Available: https://engineering.purdue.edu/people/kathleen.howell.1/Publications/Dissertations/2011_CraigDavis.pdf [Accessed 2016-08-02].

36. D. Craig Davis and K. Howell, ''Characterization of Trajectories Near the Smaller Primary in Restricted Problem for Applications,'' *Journal of Guidance, Control, and Dynamics*, vol. 35, no. 1, pp. 116–128, 2012. [Online]. Available: https://engineering.purdue.edu/people/kathleen.howell.1/Publications/Journals/2012_JGCD_DavHow.pdf [Accessed 2016-09-14].

37. K. Howell, D. Craig Davis, and A. Haapala, ''Application of Periapse Maps for the Design of Trajectories Near the Smaller Primary in Multi-Body Regimes,'' *Mathematical Problems in Engineering*, 2012. [Online]. Available: http://www.hindawi.com/journals/mpe/2012/351759/ [Accessed 2016-07-11].

38. MathWorks, ''MATLAB®,'' Natick, MA, 2015, version R2015b.

39. L. Meirovitch, *Methods of Analytical Mechanics*. Mineola, NY: Dover, 2003.

40. R. Bate, D. Mueller, and J. White, *Fundamentals of Astrodynamics*, 1st ed. New York, NY: Dover Publications, 1971.

41. The NIST Reference on Constants, Units and Uncertainty, ''Newtonian Constant of Gravitation,'' *National Institute of Standards and Technology*. [Online]. Available: http://physics.nist.gov/cgi-bin/cuu/Value?bg [Accessed 2016-12-03].

42. V. Chobotov, *Orbital Mechanics*, 3rd ed. Reston, VA: American Institute of Aeronautics and Astronautics, 2002.

43. J. Prussing and B. Conway, *Orbital Mechanics*. New York, NY: Oxford University Press, 1993.

44. V. Szebelehy, *Adventures in Celestial Mechanics*, 1st ed. Austin, TX: University of Texas Press, 1989.

45. J. Barrow-Green, *Poincaré and the Three Body Problem*, 1st ed. American Mathematical Society, 1997.

46. S. Wolfram, ''Some Historical Notes,'' 2002, *wolframscience.com*. [Online]. Available: https://www.wolframscience.com/reference/notes/972d [Accessed 2016-12-03].

47. H. Franz, P. Sharer, K. Ogilvie, and M. Desch, ''WIND nominal mission performance and extended mission design,'' *AIAA/AAS Astrodynamics Specialist Conference and Exhibit*, 1998. [Online]. Available: http://arc.aiaa.org/doi/10.2514/6.1998-4467

48. B. Fleck, ''SOHO Fact Sheet,'' Greenbelt, MD, 2003, *nasa.gov*. [Online]. Available: https://sohowww.nascom.nasa.gov/about/docs/SOHO_Fact_Sheet.pdf [Accessed 2016-10-12].

49. K. Fox, ''ACE, Workhorse Of NASA's Heliophysics Fleet, Is 15,'' 2012, *nasa.gov*. [Online]. Available: http://www.nasa.gov/mission_pages/sunearth/news/ace-15th.html [Accessed 2016-10-12].

50. E. Christian and A. Davis, ''Advanced Composition Explorer (ACE) Mission Overview,'' 2012, *caltech.edu*. [Online]. Available: http://www.srl.caltech.edu/ACE/ace_mission.html [Accessed 2016-10-16].

51. A. Meyer, ''Genesis Search for Origins,'' 2009, *nasa.gov*. [Online]. Available: http://genesismission.jpl.nasa.gov/gm2/mission/history.htm [Accessed 2016-10-16].

52. E. Wollack, ''WMAP Mission Overview,'' 2016, *nasa.gov*. [Online]. Available: http://map.gsfc.nasa.gov/mission/ [Accessed 2016-10-16].

53. J. Nelson, ‘‘Herschel Space Observatory,’’ *nasa.gov*. [Online]. Available: http://www.jpl.nasa.gov/missions/herschel-space-observatory/ [Accessed 2016-12-22].

54. European Space Agency, ‘‘Planck,’’ *esa.int*. [Online]. Available: http://www.esa.int/Our_Activities/Space_Science/Planck/Journey [Accessed 2016-10-16].

55. M. Woodard, D. Folta, and D. Woodfork, ‘‘ARTEMIS: The First Mission to the Lunar Libration Orbits,’’ 2007, *nasa.gov*. [Online]. Available: http://artemis.igpp.ucla.edu/pubs/2009_nonrefereed/artemis_woodward.pdf [Accessed 2016-10-12].

56. B. Dunbar, ‘‘THEMIS Overview,’’ 2015, *nasa.gov*. [Online]. Available: http://www.nasa.gov/mission_pages/themis/mission/index.html [Accessed 2016-10-16].

57. D. Greenwood, *Classical Dynamics*. Mineola, NY: Dover, 1997.

58. H. Schaub and J. Lunkins, *Analytical Mechanics of Space Systems*, 2nd ed. Reston, VA: American Institute of Aeronautics and Astronautics, 2009.

59. C. Geisel, ‘‘MECH532 Graduate Course: Introductory Spaceflight Dynamics,’’ Wright-Patterson Air Force Base, OH: Air Force Institute of Technology, 2016.

60. M. Bruno and H. Pernicka, ‘‘Tundra Constellation Design and Stationkeeping,’’ *Journal of Spacecraft and Rockets*, vol. 42, no. 5, pp. 902–912, 2005. [Online]. Available: http://arc.aiaa.org/doi/pdf/10.2514/1.7765 [Accessed 2017-01-14].

61. T. Parker and L. Chua, *Practical Numerical Algorithms for Chaotic Systems*. New York, NY: Springer-Verlag, 1989.

62. MathWorks, ‘‘ode45,’’ 2016, *mathworks.com*. [Online]. Available: https://www.mathworks.com/help/matlab/ref/ode45.html?s_tid=srchtitle [Accessed 2016-04-29].

63. L. Shampine and M. Reichelt, ‘‘The MATLAB ODE Suite,’’ *SIAM Journal on Scientific Computing*, vol. 18, no. 1, pp. 1–22, 1997. [Online]. Available: https://www.mathworks.com/help/pdf_doc/otherdocs/ode_suite.pdf [Accessed 2016-04-29].

64. R. Hamming, *Numerical Methods for Scientists and Engineers*. New York, NY: McGraw-Hill Book Company, 1962.

65. K. Meyer and G. Hall, *Introduction to Hamiltonian Dynamical Systems and the N-Body Problem*. New York, NY: Springer-Verlag, 1992.

66. J. Nocedal and S. Wright, *Numerical Optimization*, 2nd ed. New York, NY: Springer-Verlag, 2006.

67. M. Hirsch, S. Smale, and R. Devaney, *Differential Equations, Dynamical Systems and an Introduction to Chaos*, 2nd ed. San Diego, CA: Academic Press, 2004.

68. C. Murray and S. Dermott, *Solar System Dynamics*. New York, NY: Cambridge University Press, 1999.

69. K. Howell, ''Three-Dimensional, Periodic, 'Halo' Orbits,'' *Celestial Mechanics and Dynamical Astronomy*, vol. 32, no. 1, pp. 53–71, 1984. [Online]. Available: https://engineering.purdue.edu/people/kathleen.howell.1/Publications/Journals/1984_CM_How.pdf [Accessed 2016-12-03].

70. E. Doedel, V. Romanov, R. Paffenroth, H. Keller, D. Dichmann, J. Galán-Vioque, and A. Vanderbauwhede, ''Elemental Periodic Orbits Associated with the Libration Points in the Circular Restricted 3-body Problem,'' pp. 2625–2677, 2007. [Online]. Available: http://www.worldscientific.com/doi/pdf/10.1142/S0218127407018671 [Accessed 2016-12-03].

71. D. Arrowsmith and C. Place, *Ordinary Differential Equations*, 1st ed. New York, NY: Chapman and Hall Ltd, 1982.

72. E. Weisstein, ''Restricted Three-Body Problem,'' 2007, *wolfram.com*. [Online]. Available: http://scienceworld.wolfram.com/physics/RestrictedThree-BodyProblem.html [Accessed 2016-10-30].

73. R. Burden and J. Faires, *Numerical Analysis*, 8th ed. Belmont, CA: Thomson Brooks/Cole, 2005.

74. A. Roy, *The Foundations of Astrodynamics*. New York, NY: Macmillan Company, 1965.

75. C. Lanczos, *The Variational Principles of Mechanics*, 4th ed. New York, NY: Dover, 1986.

76. C. Marchal, *The Three-body Problem*, 1st ed. New York, NY: Elsevier, 1990.

77. T. Vincent and W. Grantham, *Nonlinear and Optimal Control Systems*. New York, NY: John Wiley and Sons, INC, 1997.

78. E. Kreyszig, *Advanced Engineering Mathematics*, 10th ed. New York, NY: Wiley, 2011.

79. E. Tedesco, ‘‘Trojan Asteroid,’’ 2016, *Encyclopedia Britanica*. [Online]. Available: https://www.britannica.com/topic/Trojan-asteroid [Accessed 2016-12-15].

80. N. Atkinson, ‘‘Earth Has a Companion Asteroid With a Weird Orbit,’’ 2015, *universetoday.com*. [Online]. Available: http://www.universetoday.com/84652/earth-has-a-companion-asteroid-with-a-weird-orbit/ [Accessed 2016-12-15].

81. D. Arrowsmith and C. Place, *An Introduction to Dynamical Systems*. Cambridge: Cambridge University Press, 1990.

82. T. Pavlak, *Mission Design Applications in the Earth-Moon System: Transfer Trajectories and Stationkeeping*, Master's thesis, Purdue University, 2010. [Online]. Available: https://engineering.purdue.edu/people/kathleen.howell.1/Publications/Masters/2010_Pavlak.pdf [Accessed 2016-12-03].

83. D. Lay, *Linear Algebra*, 4th ed. Boston, MA: Pearson, 2012.

84. MathWorks, ‘‘Constrained Nonlinear Optimization Algorithms,’’ *mathworks.com*. [Online]. Available: https://www.mathworks.com/help/optim/ug/constrained-nonlinear-optimization-algorithms.html#brnpd5f [Accessed 2016-12-01].

85. C. Goudas, ‘‘Three-Dimensional Periodic Orbits and Their Stability,’’ *Icarus*, vol. 2, pp. 1–18, 1963.

86. E. Campbell, *Bifurcations from Families of Periodic Solutions in the Circular Restricted Problem with Application to Trajectory Design*, Ph.D. Dissertation, Purdue University, 1999. [Online]. Available: https://engineering.purdue.edu/people/kathleen.howell.1/Publications/Dissertations/1999_Campbell.pdf [Accessed 2016-12-13].

87. A. Roy, *Orbital Motion*, 2nd ed. Bristol: Adam Hilger Ltd, 1982.

88. J. Carrico, D. Dichmann, L. Policastri, J. Carico, T. Craychee, J. Ferreira, M. Intelisano, R. Lebois, M. Loucks, T. Schrift, and R. Sherman, ‘‘Lunar-Resonant Trajectory Design for the Interstellar Boundary Explorer (IBEX) Extended Mission,’’ *Advances in the Astronautical Sciences*, vol. 142, pp. 771–789, 2012. [Online]. Available: http://www.applieddefense.com/wp-content/uploads/2012/12/2011-ADS-Lunar_Resonant_Trajectory_Design.pdf [Accessed 2016-08-31].

89. National Aeronautics and Space Administration, ‘‘NASA's Interstellar Boundary Explorer Mission,’’ pp. 1–2, 2008, *nasa.gov*. [Online]. Available: http://www.nasa.gov/pdf/280255main_IBEXFactSheetOct08.pdf [Accessed 2016-10-12].

90. Southwest Research Institute, ‘‘What is the termination shock?’’ *swri.edu*. [Online]. Available: http://ibex.swri.edu/students/What_is_the_termination.shtml [Accessed 2017-02-14].

91. M. Ritsko, ‘‘TESS - Transiting Exoplanet Survey Satellite.’’ [Online]. Available: https://tess.gsfc.nasa.gov/overview.html [Accessed 2016-10-16].

92. J. Guckenheimer and P. Holmes, *Nonlinear Oscillations, Dynamical Systems, and Bifurcations of Vector Fields*. New York, NY: Springer-Verlag, 1983.

93. L. Perko, *Differential Equations and Dynamical Systems*. New York, NY: Springer-Verlag, 1991.

94. K. Howell and E. Campbell, ‘‘Three-Dimensional Periodic Solutions that Bifurcate from Halo Families in the Circular Restricted Three-Body Problem,’’ in *AAS/AIAA Spaceflight Mechanics Meeting*, Breckenridge, CO, 1999. [Online]. Available: https://engineering.purdue.edu/people/kathleen.howell.1/Publications/Conferences/1999_AAS_HowCam.pdf [Accessed 2016-12-13].

95. C. Geisel, ‘‘MECH699 Graduate Course: Orbit Design in Multi-Body Environments,’’ Wright-Patterson Air Force Base, OH: Air Force Institute of Technology, 2016.

96. A. Zurita, *Minimum-Fuel Trajectory Design in Multiple Dynamical Environments Utilizing Direct Transcription Methods and Particle Swarm Optimization*, Master’s thesis, Air Force Institute of Technology, 2016.

97. R. Rausch, *Earth To Halo Orbit Transfer Trajectories*, Master’s thesis, Purdue University, 2005. [Online]. Available: https://engineering.purdue.edu/people/kathleen.howell.1/Publications/Masters/2005_Rausch.pdf [Accessed 2016-12-19].

98. Jet Propulsion Laboratory Solar System Dynamics Group, ‘‘HORIZONS Web-Interface,’’ 2017, *nasa.gov*. [Online]. Available: http://ssd.jpl.nasa.gov/horizons.cgi [Accessed 2017-09-03].

99. Analytical Graphics Inc., ‘‘Systems Tool Kit® (STK),’’ Exton, PA, 2015, version 10.

100. Air Force Research Laboratory (AFRL), ‘‘SGI Ice X (Spirit) User Guide,’’ *afrl.hpc.mil*. [Online]. Available: https://www.afrl.hpc.mil/docs/spiritUserGuide.html [Accessed 2017-01-02].

101. J. Bowman, ‘‘psphere,’’ 2000. [Online]. Available: https://www.mathworks.com/matlabcentral/newsreader/view_thread/21747 [Accessed 2017-01-03].

102. R. Adams and G. Richardson, ‘‘Using the Two-Burn Escape Maneuver for Fast Transfers in the Solar System and Beyond,’’ in *46th AIAA/ASME/SAE/ASEE Joint Propulsion Conference & Exhibit*, Nashville, TN, 2010. [Online]. Available: http://arc.aiaa.org/doi/abs/10.2514/6.2010-6595 [Accessed 2017-01-17].

103. E. M. Pawlikowski, ‘‘Mission Assurance—A Key Part of Space Vehicle Launch Mission Success,’’ pp. 1–10, 2008. [Online]. Available: http://www.nro.gov/news/articles/2008/2008-05.pdf [Accessed 2017-02-04].

104. D. McComas, J. Carrico, B. Hautamaki, M. Intelisano, R. Lebois, M. Loucks, L. Policastri, M. Reno, J. Scherrer, N. Schwadron, M. Tapley, and R. Tyler, ‘‘A New Class of Long-Term Stable Lunar Resonance Orbits: Space Weather Applications and the Interstellar Boundary Explorer,’’ *Space Weather*, vol. 9, no. 11, pp. 1–9, 2011. [Online]. Available: http://onlinelibrary.wiley.com/doi/10.1029/2011SW000704/epdf [Accessed 2017-01-10].

REPORT DOCUMENTATION PAGE

Form Approved
OMB No. 0704–0188

1. REPORT DATE *(DD–MM–YYYY)*	2. REPORT TYPE	3. DATES COVERED *(From — To)*
23–03–2017	Master's Thesis	Aug 2015–Mar 2017

4. TITLE AND SUBTITLE

Military Space Mission Design and Analysis in a Multi-Body Environment: An Investigation of High-Altitude Orbits as Alternative Transfer Paths, Parking Orbits for Reconstitution, and Unconventional Mission Orbits

5a. CONTRACT NUMBER

5b. GRANT NUMBER

5c. PROGRAM ELEMENT NUMBER

6. AUTHOR(S)

Brick, John N., 2d Lt, USAF

5d. PROJECT NUMBER

5e. TASK NUMBER

5f. WORK UNIT NUMBER

7. PERFORMING ORGANIZATION NAME(S) AND ADDRESS(ES)

Air Force Institute of Technology
Graduate School of Engineering and Management (AFIT/EN)
2950 Hobson Way
WPAFB OH 45433-7765

8. PERFORMING ORGANIZATION REPORT NUMBER

AFIT-ENY-MS-17-M-246

9. SPONSORING / MONITORING AGENCY NAME(S) AND ADDRESS(ES)

AFRL Space Vehicles Directorate
3550 Aberdeen Avenue
Kirtland AFB NM 87117-5776
POC: N/A

Principal DoD Space Advisor Staff
1670 Air Force Pentagon
Washington DC 20330-1670C
703-693-5799
POC: Lt Col Stuart A. Stanton

10. SPONSOR/MONITOR'S ACRONYM(S)

AFRL/RV

11. SPONSOR/MONITOR'S REPORT NUMBER(S)

12. DISTRIBUTION / AVAILABILITY STATEMENT

Distribution Statement A. Approved for public release; Distribution Unlimited.

13. SUPPLEMENTARY NOTES

14. ABSTRACT

High-altitude satellite trajectories are analyzed in the Earth-Moon circular restricted three-body problem. The equations of motion for this dynamical model possess no known closed-form analytical solution; therefore, numerical methods are employed. To gain insight into the dynamics of high-altitude trajectories in this multi-body dynamical environment, periapsis Poincaré maps are generated at particular values of the Jacobi Constant. These maps are employed as visual aids to generate initial guesses for orbital transfers and to determine the predictability of the long term behavior of a spacecraft's trajectory. Results of the current investigation demonstrate that high-altitude transfers may be performed for comparable, and in some cases less, ΔV than conventional transfers. Additionally, transfers are found that are more timely than a launch-on-demand capability that requires 30 days lead time. The ability of satellites in such orbits to provide remote sensing coverage of the surface of the Earth is also assessed and found to be low relative to that of a satellite at geostationary altitude (35,786 km); however, intervals of high performance exist. The current investigation demonstrates not only the potential utility of high-altitude satellite trajectories for military applications but also an effective implementation of methods from dynamical systems theory.

15. SUBJECT TERMS

Orbital Transfer, Multi-body dynamical environment, Invariant manifolds, Dynamical Systems Theory, Lunar fly-by, Poincaré map, Periapsis, Circular restricted three-body problem, Reconstitution, Predictability, Mission Assurance

16. SECURITY CLASSIFICATION OF:			17. LIMITATION OF ABSTRACT	18. NUMBER OF PAGES	19a. NAME OF RESPONSIBLE PERSON
a. REPORT	b. ABSTRACT	c. THIS PAGE			Lt Col Christopher D. Geisel, Ph.D.,AFIT/ENY
U	U	U	UU	283	19b. TELEPHONE NUMBER *(include area code)* (937)255-3636 x4237; christopher.geisel@afit.edu